Insights into antibiotic inactivation by β-lactamases from multiscale simulations

By

Viivi Heidi Annukka Hirvonen

School of Biochemistry

University of Bristol

A dissertation submitted to the University of Bristol in accordance with the requirements for award of the degree of Doctor of Philosophy in the Faculty of Life Sciences.

June 2021

Word count: 40,461 words

Abstract

In Gram-negative bacteria, resistance against β-lactam antibiotics arises most often in the form of β-lactamase enzymes. β-Lactamases inactivate these antibiotics by hydrolysing their β-lactam pharmacophore. In this thesis, enzymatic drug modification by selected serine β-lactamases is studied using combined quantum mechanics/molecular mechanics (QM/MM) simulations.

Carbapenem breakdown by class A β-lactamases is inspected using so-called "computational assays". The assays are simplified simulation protocols, which are still accurate enough to distinguish between active and inhibited enzymes. By limiting the simulation time and conformational sampling, a >99% reduction in required computational resources was achieved (compared to the original protocols), whilst still preserving the predictive power of the computational assay.

Further studies focus on class D β-lactamases, in particular the OXA-48 family. Most OXA-48 β-lactamases, including the wildtype OXA-48, are carbapenemases with specific preference for imipenem, but some variants have acquired activity against expanded-spectrum oxyimino cephalosporins. Ceftazidime breakdown for OXA-48-like enzymes is simulated to elicit the origins behind this enhanced cephalosporinase activity. Active site hydration was observed to correlate with the energy barriers for the rate-limiting reaction step. In addition to ceftazidime breakdown, carbapenem inactivation by OXA-48 is compared for imipenem and meropenem. QM/MM simulations are used to identify the preferred substrate orientation for deacylation, and to further illustrate that the difference in carbapenem hydrolysis comes from a subtle change in the active site hydrogen bonds.

Lastly, two suggested inhibition mechanisms of the non-β-lactam β-lactamase inhibitor avibactam against OXA-48 are compared to deduct the most plausible acylation pathway. The QM/MM potential energy profiles show that avibactam most likely utilises a similar mechanism to β-lactam substrates, where a carboxylated Lys73 acts as a proton acceptor in acylation. Based on these data, it is hypothesised that the avibactam inhibition most likely results from post-acylation decarboxylation of Lys73, which prevents any further reactivity.

Author’s declaration

I declare that the work in this dissertation was carried out in accordance with the requirements of the University's *Regulations and Code of Practice for Research Degree Programmes* and that it has not been submitted for any other academic award. Except where indicated by specific reference in the text, the work is the candidate's own work. Work done in collaboration with, or with the assistance of, others, is indicated as such. Any views expressed in the dissertation are those of the author.

SIGNED: ..... DATE:.....

Acknowledgements

First and foremost, I would like to thank my supervisor Marc van der Kamp for his support and guidance during my whole PhD. In addition to being one of the kindest people I have had the pleasure of working with, he has continuously supported my research career and given me the freedom to pursue the kind of projects I have desired. I would further like to thank my co-supervisors Jim Spencer and Adrian Mulholland for their advice and discussions, which have helped to elucidate many questions along the way.

A very special thank you goes to all my colleagues in the van der Kamp research group, with whom I have shared my time in Bristol. I would also like to thank Michelle Southey and my other colleagues at Evotec for organising my industrial placement, which was a great experience teaching me a lot. I thank the GW4Biomed Doctoral Training Program for funding my research and my industrial placement. Nanna and Kajsa, thank you for proofreading my thesis.

Finally, I would like to thank all my friends, who have been a part of this journey. A tremendous thank you goes to my family, who have been there to support me.

Table of Contents

Chapter 1 - An introduction to antibiotic resistance

1.1 The Antimicrobial Resistance Crisis

Antimicrobial resistance (AMR) conveys all different mechanisms, with which pathogens, such as bacteria, viruses, and parasites, resist medical treatments designed to cure infections. AMR develops naturally over time through changes in the genetic code, but the overuse of antimicrobials in healthcare and agriculture, poor hygiene, lack of proper sanitation, as well as lower-quality healthcare accelerate it.[1] These factors point strongly towards low- and middle-income countries, for example in Asia and Africa, where AMR continues to be a constant burden.[2-5] However, AMR is also a growing problem in the western world. According to the Centers of Disease Control and Prevention (CDC), in the United States alone more than 2.8 million antibiotic resistant bacterial infections are diagnosed annually, resulting in more than 35 000 fatalities.[6] Furthermore, according to the English Surveillance Programme for Antimicrobial Utilisation and Resistance report from 2019 to 2020 (published by Public Health England), there has been an estimated 32% increase in antibiotic resistant blood stream infections from 2015 to 2019. This increase is despite the decreased consumption of antibiotics during the same time interval, going from 19.4 to 17.9 defined daily doses per 1000 inhabitants.[7]

Evidently, there is a need to combat the evolving AMR problem, and multiple global and national initiatives have been propagated to this end. In 2015, a global action plan on AMR was established at the World Health Assembly.[8] The aims of this plan are focused on spreading AMR awareness, endorsing research concerning AMR, strengthening surveillance, optimising the use of antimicrobials, and sustainably investing in countering AMR. The World Health Organization (WHO) has also multiple additional initiatives: the World Antimicrobial Awareness Week (annually between November 18th and 24th),[9] the Global Antimicrobial Resistance Surveillance System (GLASS),[10] and the Global Antibiotic Research and Development Partnership (GARDP), to mention a few. In addition to global initiatives, most countries have national strategies for controlling the spread of AMR. For example, the UK has currently a five-year action plan between 2019-2024 for tackling AMR with three key aims: reducing the need and unnecessary exposure to antimicrobials, optimising the use of antimicrobials, and investing in new innovations, supply, and access in this field.[11] As expected, these aims are well aligned with the overall aims in the WHO global action plan,

with the overarching national goal being containing and controlling the spread of AMR by 2040.[11]

One central aspect in most action plans is ensuring the research and development work necessary for discovering new and effective antibiotics, against which bacteria have not yet developed resistance mechanisms. After the considerable successes in antibiotic drug discovery in the 20th century, when most currently available antibiotics were first introduced into clinical practice, the antibiotic pipeline has dried out. This so-called "antibiotic discovery void" is due to the inherent difficult nature of drug discovery and development, as well as the reluctance of big pharmaceutical companies to engage in antibiotic research. Many antibiotic classes were originally derived from natural products, such as tetracyclines from soil *Actinomycetes* or penicillin from fungi,[12, 13] though purely synthetic antibiotic classes, such as quinolones, also exist.[14] Currently, mining natural sources has mainly led to the re-discovery of already existing antibiotics. Additionally, finding possible sources for new antibiotics would require assembling and screening a huge library, which is a laboursome and costly task.[13] Antibiotic development is a difficult task, as the drug candidate needs to be potent enough to cure the bacterial infection, whilst being non-toxic for humans. Other aspects, such as the drug being preferably in an orally bioavailable form, should be considered as well. One bottleneck seems to be the lack of compounds able to enter the bacterial cell through the cell envelope.[15] Finally, after the time-consuming development and clinical testing process involved for any new drug, any possible profits from the approved antibiotic are most likely to be less than the development costs.[16]

1.2 β-Lactam antibiotics

β-Lactam antibiotics were first discovered in 1929 by Alexander Fleming,[17] and the large-scale production of these drugs began in the 1940s. Despite their relatively old age, β-lactams are still the most prescribed group of antibiotics globally due to their non-toxicity in human patients and general broad-spectrum antibacterial activity.[18] β-Lactams are categorised into four classes: penicillins, cephalosporins, carbapenems, and monobactams (Figure 1.1). The scaffold in all four groups involves a four-atom β-lactam ring, which is the pharmacophore responsible for drug binding. In the first three groups, the β-lactam ring is fused to a second ring: thiazolidine in penicillins, dihydrothiazone in cephalosporins, and pyrroline in

carbapenems. Monobactams are monocyclic and the β-lactam ring stands alone (with other substituents attached to it). Penicillin antibiotics were initially isolated among the natural products of the *Penicillium* fungi,[12] but most commercially available penicillin antibiotics today are synthetic penicillin derivatives.[19] Cephalosporins are divided into generations based on their antibacterial properties. Especially the newer third and fourth generations have broad activity against Gram-negative bacteria,[20] whilst some fifth generation cephalosporins have additional activity against methicillin-resistant *Staphylococcus aureus*.[21, 22] Currently, the only commercially available monobactam antibiotic is aztreonam.[23] Carbapenems are the newest group of β-lactam drugs, and often referred to as "last-resort antibiotics" due to their general potency and wider spectrum of use, with respect to cephalosporins and penicillins.[24]

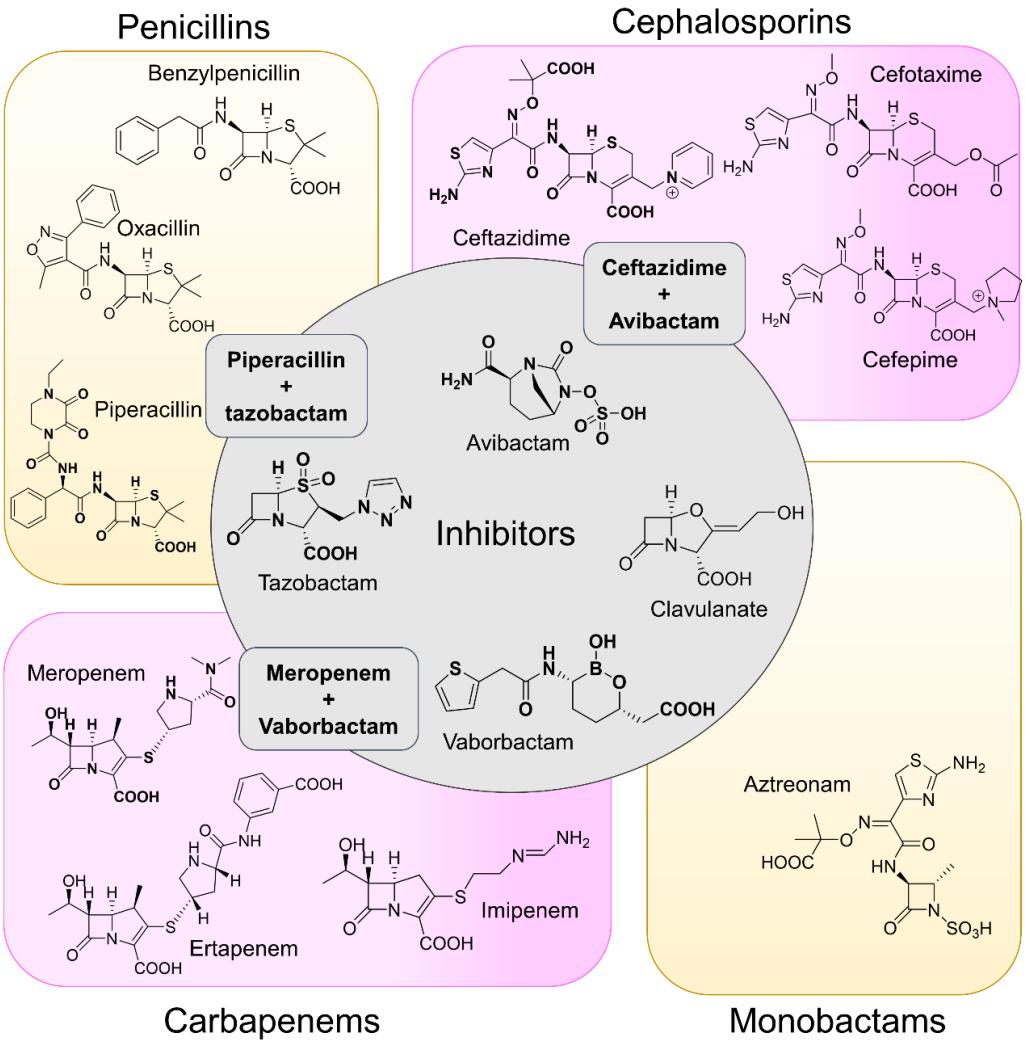

Figure 1.1 Some clinically used β-lactam antibiotics and β-lactamase inhibitors. Examples of approved β-lactam antibiotic/β-lactamase inhibitor combinations are listed in rectangular grey boxes with bold text.

To combat growing antibiotic resistance against β-lactam drugs, an antibiotic may be administered together with a β-lactamase inhibitor (some combinations presented in Figure 1.1).[25] This so-called "combination therapy" is often reserved for multi-drug resistant bacterial infections with only limited treatment possibilities. The treatment power of combination therapy is illustrated by the WHO model list of essential medicines, which categorises necessary drugs into access, watch, and reserve groups. Different examples of β-lactam/β-lactamase inhibitor combinations are listed in all three aforementioned groups of medicine.[26] β-Lactamase inhibitors essentially block enzymes responsible for β-lactam antibiotic inactivation (as outlined in following sections), which allows for the actual antibiotic to bind to its ultimate target.[27] They can be mechanism-based inhibitors including a β-lactam ring, or belong to another functional group. Examples of mechanism-based antibiotic/inhibitor combinations include amoxicillin/clavulanic acid (tradename Augmentin or Clavulin),[28] ampicillin/sulbactam (Unasyn),[29] and piperacillin/tazobactam (Tazocin, Zosyn),[30] which have inhibitory activity mainly against some class A penicillinases and extended-spectrum β-lactamases (ESBLs). As these β-lactam-based β-lactamase inhibitors do not possess very broad-spectrum activity, new inhibitor classes including diazabicyclooctanones (DBOs) and cyclic boronates have been introduced to the market in the last decade. Avibactam[31, 32] was the first DBO inhibitor approved in clinical use in combination with ceftazidime (FDA approved in 2015, tradename Avycaz),[33] and it shows broad inhibition against serine β-lactamases (introduced in the following sections).[34] Beyond avibactam, the DBO scaffold is undergoing extensive research to provide inhibitors with more broad-spectrum activity.[35-39] Cyclic boronates also show promise as possible broad-spectrum β-lactamase inhibitors.[40, 41] The first FDA approved cyclic boronate inhibitor was vaborbactam,[42] which is approved in clinical use together meropenem (Vabomere).[43] Boronate inhibitors are also undergoing extensive research, and some clinical candidates show promise of ultrabroad-spectrum inhibition against all β-lactamases (such as taniborbactam and QPX7728).[44, 45] The market for β-lactam antibiotics together with β-lactamase inhibitors is growing, with a size of over $27 million in 2018 and a projected rise to over $34 million by 2028.[46]

1.3 β-Lactamase-mediated antibiotic resistance

Antibiotic resistance is a natural phenomenon, which has been observed since the introduction of modern antibiotics: penicillin-resistant *Staphylococcus aureus* was identified only a year after the clinical introduction of penicillin.[47] Antibiotic resistance in bacteria is manifested in different ways, which include both chromosomal changes (such as efflux pumps) and extrachromosomal elements (such as resistance plasmids).[48] Focusing on Gram-negative bacteria, the main resistance mechanism is enzymatic drug modification by β-lactamase enzymes.[49] β-lactam compounds mimic the tertiary structure of D-ala-D-ala, which is the natural substrate of penicillin-binding proteins (PBPs). PBPs are essential in bacterial cell wall biosynthesis, as the D-ala-D-ala-end of pentapeptides is a precursor for peptidoglycan formation in the cell wall.[50] β-Lactam binding and subsequent long-lived covalent complex formation with PBPs inhibits cell wall renewal and eventually leads to bacterial death.[51] Therefore, the sole purpose of β-lactamases is to inactivate β-lactam antibiotics before they bind to PBPs, ensuring the survival of the bacteria. β-Lactamases are often encoded on plasmids,[52-56] which makes for efficient spread of the resistance genes; however, chromosomally-encoded β-lactamases exist as well.[57-60] The CDC categorises many Gram-negative bacteria expressing β-lactamases as urgent threats, including carbapenem-resistant *Acinetobacter* and *Enterobacterales* as well as ESBL-producing *Enterobacterales*.[6] The number and variety of identified β-lactamases has increased exponentially after β-lactams were introduced as antibacterials,[61] and the sequences of over 7000 enzymes are listed in the β-lactamase database in 2021 (with structural data available for over 1300).[62]

β-Lactamases are divided into serine β-lactamases and metallo-β-lactamases based on their catalytic mechanism. According to the Ambler classification, serine β-lactamases are further grouped into classes A, C, and D, whilst all metallo-β-lactamases comprise class B. The Ambler classification is based on sequence similarity between enzymes.[63] Serine β-lactamases are distant relatives to PBPs,[64] and even when the sequence homology between different groups of serine β-lactamase is limited, the tertiary structure across the classes is similar (Figure 1.2). Generally, penicillin-recognising enzymes (including β-lactamases and PBPs) have a conserved Ser-X-X-Lys moiety in their active site, which includes the catalytic serine and a lysine (X-X can be any amino acid); the residue numbering is Ser70 in class A, Ser64 in class C, and Ser70 or Ser79 in class D, depending on the enzyme. Further, two triads near the active site consisting of Lys-Thr-Gly and Ser-Asp-Asn are conserved across most penicillin-

recognizing enzymes.[65] All serine β-lactamases have an Ω-loop near their active site, even though the loop residues and location differs between classes. β-Lactamases in classes A and D are widely distributed globally and confer broad-spectrum resistance against cephalosporins, carbapenems, and β-lactamase inhibitors.[49] The work in this thesis is focused on studying selected enzymes from these classes. Class C β-lactamases are mainly chromosomally encoded and do not inherently possess activity against the most potent carbapenem antibiotics, as their carbapenemase activity is suggested to be a result of reduced permeation into the cell.[66] Class B β-lactamases are also a clinically significant part of widespread multidrug resistance,[67] but they have a distinct hydrolytic mechanism utilising zinc cofactors instead of a nucleophilic serine.[68]

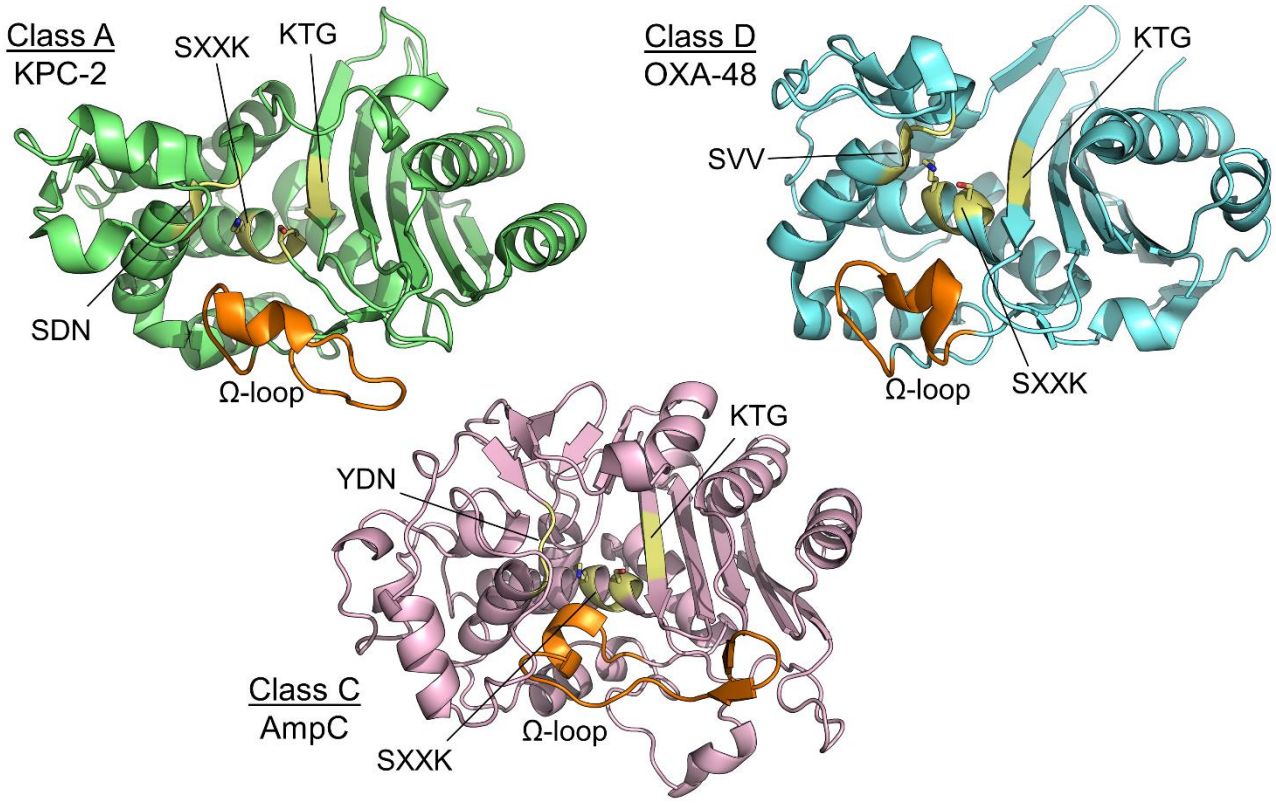

Figure 1.2 Crystal structures of three unliganded serine β-lactamases (PDB IDs: KPC-2 2OV5[69], AmpC 2BLS[70], OXA-48 6P96[71]). Conserved motifs in the tertiary structure highlighted in yellow and the Ω-loops in orange. The active site serine and lysine residues (part of the SXXK motif) are indicated in sticks.

In serine β-lactamases, antibiotic inactivation relies on forming a covalent intermediate with the drug via the catalytic serine residue. The reaction mechanism follows the general mechanism of serine proteases (to which serine β-lactamases belong) illustrated in Figure 1.3. First, the nucleophilic serine is activated via proton transfer to a general base in acylation. This involves tetrahedral intermediate formation leading to a covalent acylenzyme complex.[72] Subsequently, the covalent acylenzyme undergoes deacylation, where a water acts a nucleophile, again leading to tetrahedral intermediate formation. Finally, the hydrolysed antibiotic is cleaved. The tetrahedral intermediate formation in both reaction steps is aided by the so-called "oxyanion hole",[73] which is formed by the backbone amides of two active site residues (the catalytic serine and another one). Hydrogen bonds in the oxyanion hole stabilise the negatively charged transition state and subsequent tetrahedral intermediate, which accounts for most of the catalytic effect of serine β-lactamases, and serine proteases in general.[73] The specific residues participating in the hydrolysis reaction vary between different classes. The mechanism for class A β-lactamases is described in Section 1.3.1, whereas the mechanism for class D β-lactamases is covered in Chapter 4. The mechanism in class C β-lactamases differs from classes A and D, as they most likely use a tyrosine residue as the general base in β-lactam hydrolysis.[74]

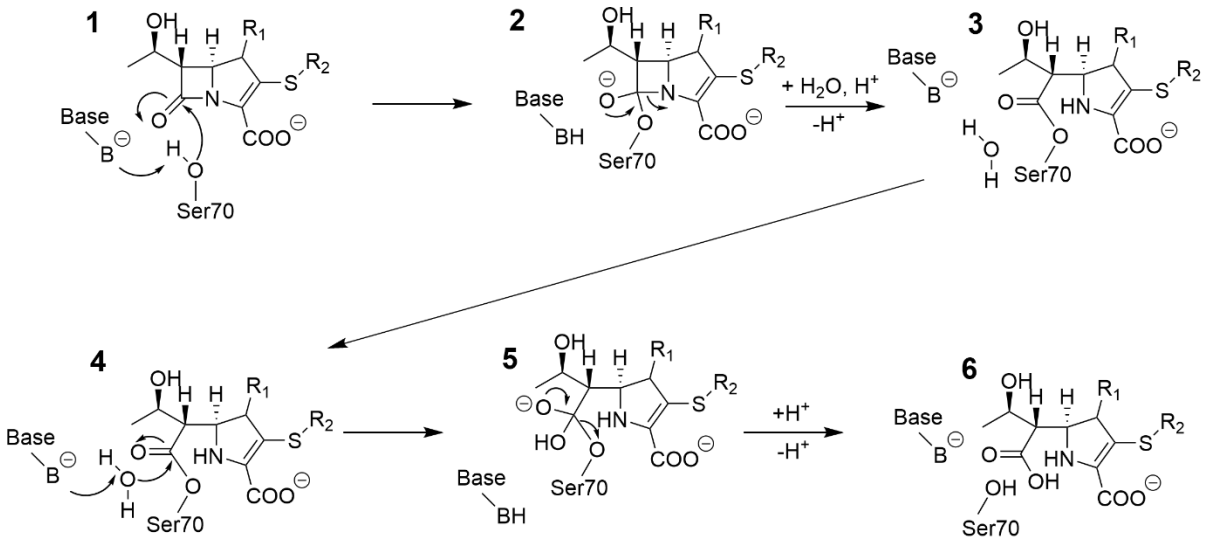

*Figure 1.3 General hydrolysis scheme for serine β-lactamases for a carbapenem substrate. Starting from the non-covalent Michaelis' complex (1), in acylation the catalytic serine nucleophile is activated via proton transfer to a general base. This leads to tetrahedral intermediate formation (**1 → 2**), which collapses to form the covalent acylenzyme (**2 → 3**). In deacylation a water nucleophile is activated to form a new tetrahedral intermediate (**4 → 5**), which yields the final hydrolysis product (**6**). The carbapenem substrate depicted as the Δ^2-tautomer.*

1.3.1 Class A β-lactamases

Class A β-lactamases are perhaps the most studied group of serine β-lactamases, even though some controversies concerning e.g. their catalytic mechanism still remain (discussed further below). These enzymes are traditionally characterised as penicillinases, meaning they exhibit efficient penicillin breakdown, but a growing array of enzymes capable of cephalosporin and carbapenem hydrolysis have emerged. Most encountered class A β-lactamase families in clinical settings include the TEM (originally identified in Greece in a patient named Temoneira),[75] SHV (sulfhydryl variant),[59] CTX-M (cefotaximase),[76] and KPC (*Klebsiella pneumoniae* carbapenemase)[77] enzymes. The TEM and SHV families inactivate primarily penicillin substrates, although some of their variants have acquired activity against oxyimino cephalosporins (e.g. cefotaxime) through point mutations.[78] β-Lactamases exhibiting activity against broad-spectrum cephalosporins are referred to as extended-spectrum β-lactamases (EBSLs),[79] and as the name cefotaximase suggests, CTX-M enzymes belong to this group as well. Moreover, CTX-M enzymes are specifically named in the CDC Antibiotic Resistance Threats report under ESBL-producing *Enterobacterales*.[6] Another concerning direction exhibited by some class A β-lactamases is carbapenemase activity, i.e. the ability to inactivate potent carbapenem antibiotics, which severely limits treatment options.[80] Examples of class A carbapenemases include e.g. the previously mentioned KPCs, SME (*Serratia marcescens* enzyme),[81] NMC-A (non-metallocarbapenemase A),[82] and SFC-1 (*Serratia fonticola* carbapenemase)[83]. KPC enzymes are among the most commonly identified carbapenemases in *Enterobacterales*, and they confer resistance against most carbapenem and cephalosporin antibiotics.[84] As an example, KPC enzymes accounted for 12.5% of confirmed carbapenemase-producing *Enterobacterales* samples in England according to the 2019 ESPAUR report.[7] Alarmingly, KPC-2 point mutants have also demonstrated resistance against new inhibitors such as avibactam,[85] and mutants with activity against the ceftazidime/avibactam combination have been observed in a laboratory setting.[86]

The hydrolysis mechanism in class A β-lactamases follows the general mechanism presented in Figure 1.3. However, the residue acting as the general base in acylation remains disputed. Two main reaction mechanisms have been proposed in the literature. In the first proposal, the serine nucleophile is activated via proton transfer to Glu166 using a bridging water molecule, which yields the tetrahedral intermediate. The second proposed mechanism

involves Ser70 nucleophile activation by a proton transfer to Lys73 instead of a water molecule, which would require Lys73 in its neutral protonation state. In both proposals, a proton is subsequently transferred from Glu166 to Ser130 via Lys73, as Ser130 protonates the β-lactam ring nitrogen in the second acylation step, which ultimately yields the covalent acylenzyme intermediate. This intermediate is cleaved using a water nucleophile, which is activated by a proton transfer to Glu166 (analogous to acylation). Evidence for Glu166 as the (primary) general base in acylation is based on information derived both from computational modelling and experimental studies.[87-89] The proposed role of Lys73 as the general base instead of Glu166 is based on site-directed mutation studies, as mutants of TEM-1 at position 166 are able to undergo acylation, albeit with greatly reduced rates.[90] Further studies indicate that Lys73 would be in its neutral form if Glu166 is mutated,[91] and that proton transfer to Lys73 could be feasible.[92, 93] However, is it possible that the absence of Glu166 shifts the pK_a of Lys73, enabling it to be deprotonated and to act as a base, and that the primary base in the wildtype enzyme is Glu166.

1.3.2 Class D β-lactamases

The class D β-lactamases studied in this thesis, namely OXA-48 enzymes, are presented in a minireview comprising Chapter 4.

1.4 Summary of this thesis

In this thesis, I will present my work on simulating antibiotic breakdown by selected serine β-lactamases. This research has two main goals:

1. Establishing efficient computational protocols, which still accurately distinguish between active and inhibited β-lactamases.
2. Deducting structural and/or mechanistic features contributing to efficient catalysis.

Computational methods utilised in this thesis, and the theory behind them, are briefly introduced in Chapter 2. Chapter 3 focuses on investigating carbapenem hydrolysis by class A β-lactamases. This work introduces the term "computational assay", which accurately distinguishes between carbapenemases and carbapenem-inhibited enzymes whilst employing relatively straightforward and fast simulation protocols. Chapters 4 to 7 focus on class D β-

lactamases. Chapter 4 consists of a minireview summarising recent research concerning class D OXA-48 enzymes. Chapters 5 to 7 are focused on simulating β-lactam degradation by OXA-48s. Cephalosporin inactivation by OXA-48 and its variants is presented in Chapter 5, whilst Chapter 6 discusses carbapenem hydrolysis by OXA-48. Finally, studies on OXA-48 inhibition by avibactam are summarised in Chapter 7. Chapters 5 to 7 concentrate on the second goal, where atomistic simulations are used for elucidating the determinants behind different hydrolysis phenotypes.

Chapter 2 - Computational methods

Computational chemistry has paved its way into modern chemical research, as it is routinely used in many different applications ranging from materials research to catalyst design to studying biological systems.[94-98] In this chapter, different computational chemistry methods are presented, covering theory from more simplistic molecular mechanics description of atoms to computationally more demanding quantum chemical wavefunction-based methods and density-functional theory. Semi-empirical methods are also briefly introduced. The theory behind biased reaction simulations and the standard techniques used in biomolecular modelling are described in the end.

2.1 Molecular mechanics

Due to the relatively large system sizes (ranging usually from tens of thousands to millions of atoms) encountered when simulating biological systems, methods based on quantum mechanics become too computationally expensive to apply for practical use. Instead, a system can be described using molecular mechanics,[99] where the general potential energy function *V(total)* for the system includes contributions from both intramolecular and intermolecular terms:

Eq. 2.1

$$V(total) = V(bonds) + V(angles) + V(dihedrals) + V(vdW) + V(el)$$

where *V(bonds)*, *V(angles)*, and *V(dihedrals)* form the intramolecular energy contribution from bonds, angles, and dihedrals, and the Van der Waals interactions *V(vdW)* together with the electrostatic interaction term *V(el)* form the intermolecular component.

The energy contribution arising from bonds between atoms has the following form:

Eq. 2.2

$$V(bonds) = \sum k_b(r - r_0)^2$$

where k_b corresponds to the bond force constant and r_0 the reference bond length. The harmonic form of the bond energy expression prohibits bonds from breaking and ensures bond lengths staying near the reference value.

The energy expression for angles is analogous to the energy contribution arising from bonds, and is:

Eq. 2.3

$$V(angles) = \sum k_0(\theta - \theta_0)^2$$

where k_0 is the force constant, and θ_0 the reference angle value.

The intramolecular energy expression for the dihedrals is slightly more complicated than the previous two:

Eq. 2.4

$$V(dihedrals) = \sum k_\phi(1 + \cos(n\phi - \delta))$$

where k_ϕ is the force constant, and n the number of rotational minima between 0° and 360°.

Additionally, the force field energy expression can include a term for improper torsions. These involve four atoms that can form out-of-plane torsions:

Eq. 2.5

$$V(impropers) = \sum k_\phi(\phi - \phi_0)^2$$

where again k_ϕ is a force constant, and ϕ_0 the reference improper value.

Intermolecular energy terms describe interactions between non-bonded atoms. For the Van der Waals component, the interaction energy is often modelled using a 12-6 Lennard-Jones-type potential:

Eq. 2.6

$$V(vdW) = \sum_{i<j} \frac{A_{ij}}{R_{ij}^{12}} - \frac{B_{ij}}{R_{ij}^{6}}$$

where A_{ij} and B_{ij} are atom-pair specific parameters included in the force field, and R_{ij} the distance between non-bonded atoms i and j. A 12-6 potential ensures that the interaction energy increases steeply as two atoms come too close together (R^{12} term) and is lowered when they are further apart (R^6 term).

Electrostatic interaction between two atoms is described by a Coulomb potential:

Eq. 2.7

$$V(el) = \sum_{i<j} \frac{q_i q_j}{\epsilon R_{ij}}$$

where q_i and q_j are point charges on atoms i and j, R_{ij} the distance between the atoms, and ϵ the effective dielectric constant for the solvent.

The specific parameter set used when calculating the individual energy terms for a certain system configuration is called a force field. In this thesis, the Amber ff14SB force field was used in all calculations.[100]

2.2 Basics of quantum mechanics

Molecular mechanics is a convenient approach for simulating large systems. However, quantum mechanics provides a more appropriate description of system behaviour at the molecular level. In the heart of quantum mechanics is the Schrödinger equation,[101] which tells how a system with a state wavefunction $\psi(t)$ evolves with time:

Eq. 2.8

$$\mathrm{i}\hbar \frac{\partial}{\partial \mathrm{t}} \psi(r,t) = \hat{\mathrm{H}}\, \psi(r,t)$$

Here, $\psi(t)$ is the time-dependent wavefunction of the system, and $\hat{H}$ the Hamiltonian operator corresponding to the total energy of a system. If the Hamiltonian is assumed to be time-independent, the Schrödinger equation can be written as:

Eq. 2.9

$$\hat{H}\, \psi(r) = E\psi(r)$$

where E is the total energy of a system. The total energy is a sum of kinetic and potential energy terms for electrons and nuclei, and the molecular Hamiltonian takes the form:

Eq. 2.10

$$\hat{\mathrm{H}} = -\frac{1}{2}\sum_i \nabla_i^2 - \frac{1}{2}\sum_a \frac{1}{m_a}\nabla_a^2 + \sum_{ij} \frac{1}{r_{ij}} + \sum_{ab} \frac{Z_a Z_b}{r_{ab}} - \sum_{ai} \frac{Z_a}{r_{ia}}$$

where the first and second terms describe the kinetic energies of electrons and nuclei (respectively), the third term electron repulsion, the fourth nuclei repulsion, and the last one attractive interaction between electrons and nuclei. However, often nuclei are considered as fixed point charges in space. This is due to the large mass difference between electrons and nuclei. When this so-called Born-Oppenheimer approximation[102] is applied, the electronic Hamiltonian is obtained:

Eq. 2.11

$$\hat{\mathrm{H}} = -\frac{1}{2}\sum_{i}\nabla_i^2 + \sum_{ij}\frac{1}{r_{ij}} - \sum_{ai}\frac{Z_a}{r_{ia}}.$$

Even with the Born-Oppenheimer approximation, the Schrödinger equation is possible to solve analytically only for a hydrogen atom or hydrogen-like molecules (with only one electron). Further approximations for obtaining the system energy include separating the full electron wavefunction into a product of single-electron wavefunctions:

Eq. 2.12

$$\psi(\boldsymbol{r}) = |\psi_1\psi_2 \ldots \psi_n|$$

As electrons are fermions with a half-integer spin, the Pauli exclusion principle[103] states that the wavefunction must be antisymmetric with respect to interchanging two electrons (fermions), and it is hence described as a determinant.

Molecular orbitals for a given system are often constructed from atomic orbitals (AOs). In the LCAO approximation (linear combination of atomic orbitals), one-electron AOs $\chi_1,\ldots,\chi_n$ are used for describing a MO ϕ_i:

Eq. 2.13

$$\phi_i = c_{1i}\chi_1 + c_{2i}\chi_2 + \ldots + c_{ni}\chi_n$$

where coefficients c_{ni} correspond to the individual weights of the AOs in the linear combination for a particular MO. The AOs used are often referred to as basis functions, which comprise the basis set (discussed later in more detail). The system wavefunction can then be constructed by finding the AO weights which yield the lowest energy. However, solving the Schrödinger equation and obtaining the total energy even using this LCAO-MO wavefunction would require

knowing the individual AO weights in advance, and hence the weights are solved in an iterative way using trial weights as a starting guess. This procedure is called a self-consistent field (SCF) calculation.[104]

2.3 *Ab Initio* methods

Ab initio translates from Latin as "from first principles". The oldest *ab initio* method is the Hartree-Fock (HF) method, which is alternatively called the self-consistent field method.[105] Within HF theory, the system wavefunction is expressed as single Slater determinant, and the system energy is solved in practice using the Hartree-Fock-Roothan equations.[106, 107] The HF method scales cubically with respect to system size, i.e. N^3. HF formulation follows the variational principle, which states that when using a trial wavefunction for finding the energy of a ground state, the true ground state energy is never higher than the one obtained with the trial wavefunction. Therefore, the HF energy is always an upper-bound limit for the real energy. The shortcomings of HF theory include neglecting electron correlation, as the movement of a single electron is independent of the other electrons (except for the repulsion arising from the average electron positions). The only correlation considered is Fermi correlation, which means that the probability of finding two parallel spin electrons in the same point in space is zero. This is not true for antiparallel spin electrons, though. Secondly, the single-determinant approach is often a poor description of many-body systems. These are also referred to as dynamical and statistical correlation, respectively. Neglecting electron correlation is a big approximation, which can lead to wrong system descriptions and large deviations of computed values from experimentally determined ones.[108-111]

Building on the HF theory, the so-called post-HF methods have been developed to address the shortcomings of the original formulation, e.g. by adding more dynamical correlation. The Møller–Plesset perturbation theory (MP)[112] incorporates electron correlation through perturbation theory. The Hamiltonian operator is expressed as a sum of the unperturbed operator and a small perturbation, and the corresponding energies can be calculated up to the second (MP2), third (MP3), or fourth (MP4) order. The first order (MP1) energy equals the Hartree-Fock energy (which is also the zeroth order energy with an unperturbed Hamiltonian, as the first order correction is zero). Among the different levels of MP theory, MP2 remains perhaps as the most utilised method as it is least costly computationally (scaling N^5) and progressing to MP3 or beyond does not necessarily guarantee better convergence of the

calculated energies towards a certain value.[113] The steep scaling of MP2 can be partly overcome by utilising the resolution of identity (RI) approximation.[114] In the RI approximation, the computationally expensive four index two-electron integrals are approximated as a linear combination of three-index integrals; this procedure can be applied to both the SCF part and the MP2 correction. One drawback of the MP theory is that it is not variational, i.e. it overestimates system stability by underestimating their energies. On the other hand, this can be used as an upper bound for stability. One easy way to improve the calculated energies is to incorporate empirical scaling factors for energy contributions from same-spin and opposite-spin electrons, as is done in spin-component-scaled MP2 method (SCS-MP2).[115]

Further post-Hartree-Fock *ab initio* methods include the configuration interaction (CI)[116] and the coupled cluster (CC)[117] methods. Especially the CC method combined with perturbation theory (named CCSD(T))[118] is currently regarded as the "gold standard" in quantum chemistry. However, calculations utilising CCSD(T) are limited to very small molecules or only single-point energies, where initial structure optimisation is done using a lower level of theory, due to its expensive scaling behaviour of computational time with respect to system size (N^7). A promising development regarding CC methods is utilising the locality of electron correlation. The DLPNO-CCSD(T) (domain based local-pair natural orbital) is a linear-scaling method with respect to the system size,[119] and based on benchmarking, it is able to recover over 99% of the CCSD(T) correlation energy.[120] In this thesis, benchmarking of semi-empirical methods is most often done against (SCS-)MP2 results for very small gas-phase model systems, as routinely utilising *ab initio* methods for system sizes in biomolecular simulations becomes unfeasible.

2.4 Density functional theory

Ab initio methods rely on finding the energy of a molecular system by constructing a wavefunction to describe the system and solving the Hamiltonian eigenvalue problem. Density functional theory (DFT) approaches the same problem from another angle, as the electron density ρ of a system is used for obtaining system energies. DFT is originally built on the Hohenberg-Kohn theorems, which state that 1. the ground state electron density of a system uniquely determines its energy (and other properties), and 2. only the ground state electron density minimises the energy functional for a system.[121] In other words, determination of ground-state properties depends only on three spatial coordinates for electron positions, and

the DFT formulation follows the variational principle. However, modern DFT formulation is based on later Kohn-Sham equations,[122] where the electron density of the full, interacting system is matched with the electron density of a fictious, non-interacting system. The total energy is then expressed as a sum:

Eq. 2.14

$$E_{DFT}[\rho] = T_e[\rho] + \mathrm{V_{ne}}[\rho] + \mathrm{V_{ee}}[\rho] + \mathrm{E_{XC}}[\rho]$$

where T_e is the kinetic energy of non-interacting electrons, V_{ne} the attractive Coulomb potential between electrons and nuclei, and V_{ee} the repulsive potential between electrons. All the unknown interactions terms are grouped into the last E_{XC} term, which is the so-called exchange-correlation functional. The exchange-correlation functional can be further decomposed into separate exchange and correlations terms: the exchange term can be calculated exactly as in the HF method. Notably, the theory of DFT is exact, i.e. it yields the exact electronic energy of a system. In reality, however, the exact form of the E_{XC} functional is unknown, and some approximations need to be introduced.

As many different approximations have been developed for tackling the problem of the unknown exchange-correlation functional, DFT cannot be systematically improved. Nonetheless, the Jacob's ladder framework (proposed by Perdew) rationalises the approaches taken in constructing various DFT functionals, as progressing higher on the successive levels should improve the functional (and bring the performance closer to the "heaven of chemical accuracy").[123] The first rung is the local density approximation (LDA), which is originally derived for homogeneous electron gas (electron density identical at every point in space).[121] The energy of a system is given by the electron density at certain point in space, and the density is assumed to vary slowly. However, LDA functionals are not widely applied to molecular systems as their electron density is often far from spatially uniform. Functionals incorporating the generalised gradient approximation (GGA) build on the LDA, but also include the gradient of electron density in the E_{XC} functional.[124-126] Analogously, meta-GGA functionals include the second derivative of electron density, and examples of meta-GGA functionals include e.g. TPSS[127] and M06-L[128]. On the ladder towards the heaven of chemical accuracy, GGA and meta-GGA functionals comprise the second and third rung, respectively. On the fourth and fifth rungs are hybrid and double hybrid functionals, respectively. Hybrid functionals incorporate a certain amount of the exact HF exchange energy into their E_{XC} functional,[129] whereas double hybrid functionals also include a certain fraction of MP2 correlation energy.

B3LYP[130-133] is still perhaps the most widely applied hybrid functional, other popular hybrids include functionals in the M06 suite[134] and the ωB97 family[135, 136]. Examples of double hybrid functionals include B2PLYP[137] and ωB97X-2[138]. A known drawback of most DFT methods is the incorrect description of long-range dispersion interactions,[139-142] and corrections can be added to address this.[143] Common ways to account for this error include van der Waals density functionals (vdW-DF), where a non-local energy term for dispersion interactions is added to the E_{XC} functional.[144] Another example are the semiclassical DFT-D corrections, where the dispersion energy is calculated pair-wise in an additive fashion for all atoms and simply added to the Kohn-Sham energy.[145]

In this thesis, DFT was mainly used for benchmarking purposes due to the computational cost of using DFT in conformational sampling for large biomolecular systems. The performance of semi-empirical methods in QM/MM calculations was compared against DFT results both for model gas-phase systems of the enzyme active site, and for energy corrections for structures optimised using semi-empirical methods. Mainly hybrid functionals were used, the most utilised one being the meta-GGA hybrid M06-2X.[134] M06-2X includes 54% HF exchange in its E_{XC} formulation, and it is parametrised only for non-metals. Based on previously published benchmarking data, M06-2X performs well for thermochemistry and barrier heights,[134, 146] but may lack proper description of non-covalent interactions.[147] Another functional of choice was the long-range corrected hybrid GGA ωB97X,[135] either as its initial formulation or as ωB97X-D[136] with dispersion corrections.

2.5 Basis sets

Functions used for constructing the electronic wavefunction are called basis functions, and together the functions form a basis set. Approaching the complete basis set limit, i.e. the perfect description of a wavefunction, would require an infinite amount of basis functions; in practise a finite number of functions is included in each basis set. Basis sets are often constructed using AOs, which are combined to yield MO descriptions (as introduced in section 2.2). Slater-type orbitals (STOs) can be used for describing AOs, as these functions are analytical solutions for the Schrödinger equation for one-electron systems. However, evaluation of two-electron integrals using STOs can be difficult; therefore, STOs are often approximated using a combination of Gaussian-type orbitals (GTOs). Minimal basis sets follow the format STO-*n*G, where *n* tells the number of GTOs used for constructing one STO.

Even when minimal basis sets are computationally efficient, results obtained using them are often crude as only one STO is used per orbital. Pople's split-valence basis sets follow format X-YZG, where X tells how many GTOs comprise every core AO, and Y and Z how many primitive gaussian are used for the valence orbitals.[148] For example, in 3-21G basis set every core AO is a linear combination of three primitive gaussians, while the two valence AOs consist of two and one primitive gaussians. With split-valence basis, at least two STOs are used for each valence electron, which yields a better description of the system than provided by STO-nG basis sets. Polarisation is indicated by a star after the basis set name and is incorporated by including higher angular momentum orbitals in the basis set (for example 1p orbitals for hydrogen). Diffuse functions are indicated by a +, and they are used for describing regions further away from the nucleus (often called the tail regions). Dunning basis sets,[149] or the so-called correlation-consistent basis sets, are designed to approach the complete basis set limit upon adding more basis functions. They follow the format cc-pVnZ, where the prefix cc-p indicates the set to be correlation-consistent polarised, and the suffix VnZ tells how many functions (n) are used for describing each valence electron. Diffuse functions can be added with the aug- suffix. The Karlsruhe def2 basis sets (also named Ahlrichs basis sets) follow the same format, where e.g. def2-SVP denotes split valence (two AOs per valence electron) polarised.[150]

2.6 Semi-empirical methods

Semi-empirical quantum chemical methods are based on the HF theory, but skip many computationally intensive steps by introducing additional approximations or parametrisation. Any parameters used in the formulation are usually empirically derived, i.e. the goal is to fit the computed results to match some existing empirical data. Many semi-empirical methods employ the neglect of diatomic differential overlap (NDDO) approach, where the simplified idea is to reduce the computational overhead by ignoring the two-electron integrals,[151] and treating remaining one-electron integrals approximately e.g. through parametrisation.[152] These methods often employ minimal basis sets with only valence electrons, which further speeds up the calculations. Popular semi-empirical methods include AM1 (Austin Model 1)[153], PMx (Parametric Method, x=3,6,7)[154-156], and OMx methods (Orthogonalization-corrected Methods, x=1,2,3)[157]. As some methods are formulated against empirical data, they are able to recover some electron correlation (unlike HF). However, the limited number of systems used in the

parametrisation procedure combined with valence-only and minimal basis set approaches limits their applicability, and their performance for a given problem should be tested against higher-level methods.

In addition to finding approximate ways to speed up HF-based calculations, density functional tight-binding (DFTB) schemes aim to do the same for DFT methods. The electron density ρ for a system is expressed as a sum of a reference density and a small fluctuation $\rho = \rho_0 + \delta\rho$ (ρ_0 being the superposition of neutral atomic densities). The energy expression can now be expanded as a Taylor series around the reference density. Including only the first order terms in the expansion yields the DFTB1 method (alternatively just DFTB), whereas including the second order term yields DFTB2. DFTB2 is also called SCC-DFTB, as it introduces calculating atomic partial charges self-consistently.[158] DFTB3 includes terms up to third order.[159] As the DFTB1 method is not self-consistent,[160] it is advised to be used only for systems where charge transfer between atoms is small.[161] Both DFTB2 and DFTB3 have been applied widely in simulating biological systems,[162, 163] and are the semi-empirical methods of choice also in this thesis.

2.7 Hybrid quantum mechanics/molecular mechanics methods

State-of-the-art reaction simulations of large biomolecular systems often utilize a combined quantum mechanics/molecular mechanics (QM/MM) approach, where a small portion of the system is modelled using quantum mechanics, whilst the rest are described by molecular mechanics.[164] The QM subsystem often consists of ligand and some key active site residues (e.g. participating in the catalysed reaction or transition stabilisation). QM/MM methods allow simulating chemical reactions within the enzyme, as the bonding situation is not fixed, unlike in simulations based on molecular mechanics.

The total energy for a given system in QM/MM simulations is generally calculated using either the additive or subtractive approach.[165] In an additive scheme, the total energy consists of three terms:

Eq. 2.15

$$E(add, total) = E(MM) + E(QM) + E(QM - MM)$$

where energies for the MM and QM parts of the system are described by E(MM) and E(QM), respectively), and the two systems are coupled by the interface energy E(QM-MM). On the other hand, in a subtractive QM/MM scheme the total energy is expressed as:

Eq. 2.16

$$E(sub, total) = E(MM, whole) + E(QM) - E(MM\ for\ QM)$$

where first the MM energy is calculated for the whole system (E(MM,whole), including the QM region) and QM energy for the QM subsystem (E(QM)). From this total energy, the MM energy contribution for the QM region (E(MM for QM)) is then subtracted. The Amber software suite utilises the additive scheme in its QM/MM implementation, therefore it shall be discussed more in depth below.[166]

In an additive QM/MM implementation, calculating energies for the QM and MM regions is relatively straightforward, whilst calculating the interaction energy (E(QM-MM)) for energy contributions spanning over the two subsystems remains more complicated. In the QM/MM implementation in the sander program (part of the Amber software package[166], used for all QM/MM calculations in this thesis), point charges in the MM system polarise the QM system but not vice versa, as this would require a polarisable force field. This approach is also referred to as electrostatic embedding. Electrostatics often dominate in the QM-MM interaction energy contribution, but also Van der Waals interactions between QM and MM atoms are included in the QM-MM interaction energy function. Van der Waals interactions are calculated using the 12-6 potential as for MM atoms as discussed in Section 2.1 (equation 2.6). If there are no covalent bonds between the QM and MM regions, the interface energy is simply a sum of the electrostatic and van der Waals interactions. However, more terms must be included if covalent bonds are "cut" when partitioning the system into QM and MM parts. Often the link atom approach[165] is used for these "broken" covalent bonds (as is done in sander).[166] A link atom (hydrogen) is added as a cap to any covalent bonds between QM and MM regions to fill open valences. It is placed on the bond vector between the bonded QM and MM atoms, therefore introducing no new degrees of freedom (as the link atom coordinates depend on the QM and MM atom coordinates). In Amber, the link atom bond length is set to the equilibrium distance of a methyl C-H bond 1.09 Å. Electrostatics for link atoms are calculated the same way as for other QM atoms excluding the MM link pair atoms, whilst no Van der Waals interactions are calculated. Additionally, the MM terms for bonds spanning over the QM and MM systems are calculated using force field terms as usual. In addition to careful formulation

of the QM/MM energy function, care must be taken when partitioning the system into QM and MM regions. Generally, polar bonds should not be broken, and the QM-MM partitioning is thus best done across C-C bonds. A compromise between QM system size, accuracy of calculated energetics/properties, and computational power needed should be considered.

2.8 System preparation

The starting point for biomolecular simulations is often an experimentally determined structure for the system of interest, either unliganded or with a ligand. Structural techniques, such as X-ray crystallography, yield the positions of heavy atoms, but the resolution is still often too low for observing hydrogens. Hence, hydrogens need to be added to the structure prior to performing any calculations, and many simulation programs have an automated way of doing this (such as tleap in the Amber suite[166]). The protonation states as well as residue tautomers need to be determined in advance as well, as standard molecular dynamics techniques do not allow for bonding changes (e.g. proton transfers). In this thesis, the protonation states of ionisable residues are based on empirically predicted pK_a values using the propKa3.1 software.[167] Determining the tautomeric states of histidine residues was done using reduce as part of Ambertools 19[166].

The parameters used for standard protein residues to calculate the system energy (according to equation 2.1) are included in a force field. For any ligands or non-standard residues, new force field parameters and atomic partial charges need to be derived. Specific parameter sets are designed to cover most of the chemical space of small organic molecules, such as gaff and gaff2,[168] which can be used for assigning force field parameters for most small-molecule organic ligands. For non-covalent ligands, calculating atomic partial charges is rather straightforward using e.g. the restrained electrostatic potential (RESP)[169] or AM1-BCC charges[170, 171]. However, deriving accurate charges for non-standard residues, which form a part of the protein backbone, is not as trivial. Charges for all non-standard residues in this thesis are derived using the R.E.D Server,[172] which offers an automated way for fragment charge derivation using intramolecular charge constraints during charge fitting (the charges on the capping groups around the desired non-standard residues are set to zero). Any missing force field parameters were taken from the gaff force field.

2.9 Water models

To make the simulations more realistic, enzyme models are often solvated in water. The applied water model depends on the particular purpose, and generally one can utilise either an implicit or an explicit solvent method. Implicit solvents mimic solvation effects by approximating the solvent as a continuous medium, whilst in explicit solvent methods actual solvent molecules are added around the studied system. Explicit solvation allows for calculating e.g. possible active site interactions with solvent, but this model also largely increases the number of atoms in the system. Vice versa, implicit solvent models often enhance conformational sampling due to smaller system sizes, but do not offer information of protein interactions with water.

With explicit solvation, the solvent molecules tend to "drift off" from their original starting positions during the simulation. Therefore, so-called periodic boundary conditions (PBCs) are applied, where the simulated system consists of an infinite number of simulation cells. Once a solvent molecule exits the original cell from one side, a new solvent molecule enters the cell from the opposing side. PBCs ensure that possible surface effects of water are avoided, and that the number of particles in the system stays fixed.

The choice of water model is also important in explicit solvent simulations. These can be divided into three-site, four-site, and five-site interaction models. Three-site models (such as TIP3P[173], SPC[174], and SCP/E[175]) have three interactions points on the three atoms in water, and the geometry of water is often rigid. All three atoms have fixed point charges, and the oxygen atom has Lennard-Jones parameters for calculating van der Waals interactions. In four-site models (TIP4P[173] and its successors, OPC[176], BF[177]), a dummy atom with a negative charge is added next to the oxygen atom on the axis bisecting the HOH angle. Often the geometry of solvent molecules is again kept fixed. Correspondingly, five-site water models (TIP5P[178] and its successors, BNS[179], ST2[179]) mimic the tetrahedral geometry of oxygen lone pairs in water. Five-site models tend to have a higher computational cost in simulations, and hence have only been developed further in the recent decades.

All molecular dynamics simulations in this thesis are done using an explicit solvation using the TIP3P water model with PBCs, except for the simulation in Chapter 3, where the four point TIP4P-Ew was used.

2.10 Energy minimization

The variation of system energy as a function of atom coordinates can be described as a potential energy surface (PES). As a system consisting of N atoms has $3N$-6 degrees of freedom, PESs are often quite complex. Local minima on the PES respond to stable configurations, whereas the global minimum is the overall lowest energy structure. The geometry of a system can be optimised when the energy is minimised, which does not necessarily yield the global minimum energy structure as the system is optimised to a near-by local minimum. This is especially true for large biomolecular systems, where finding the global minimum energy structure is impossible.

Minimisation algorithms often rely on following the gradient of the PES. In the steepest descent method only the gradient of the energy is calculated.[180] As the net force acting on the system is the opposite of the gradient, the atoms are moved parallel to the net force towards the nearest PES minimum. A pre-defined step size indicates how far the system is displaced. Steepest descent is often combined with another minimisation method to avoid oscillating around the energy minimum. The conjugate gradient algorithm is similar to steepest descent, but uses additionally information of the previous steps to speed up convergence.[180] More advanced (and often computationally expensive) minimisation methods can also employ second derivatives of the PES, as is done in the Newton-Raphson method.

2.11 Molecular dynamics simulations

To study the time-dependent behaviour of biomolecular systems, molecular dynamics (MD) simulations can be performed. Theory behind the equations used in MD simulations starts from the Newton's second law of motion:

Eq. 2.17

$$F = ma$$

where F is the force acting on a particle, m the mass of a particle, and a acceleration. As force is also the gradient of potential energy and acceleration the second gradient of position, equation 2.17 can be written as

Eq. 2.18

$$\frac{\partial V}{\partial r} = m\frac{\partial^2 r}{\partial t^2}$$

where *V(r)* is the potential energy of the system, *r(t)* the position (in Cartesian coordinates), and *t* time. Combining equations 2.17 and 2.18 yields the expression:

Eq. 2.19

$$F_i = m_i\frac{\partial^2 r}{\partial t}$$

where F_i is the force acting on atom i and m_i its mass. Integrating this equation at certain timesteps yields new atomic positions and shows how the system evolves dynamically with time.

As the potential energy is a function of all *3N* atom coordinates, the differential equation cannot be solved analytically. Different numerical integration algorithms exist, such as the Verlet[181], velocity Verlet[182], and leapfrog[183] schemes. In the Verlet algorithm, the new atom positions at timepoint $t+\delta t$ are calculated using information from the two previous timepoints, *t* and $t-\delta t$:

Eq. 2.20

$$r(t+\delta t) = 2r(t) - r(t-\delta t) + a(t)\delta t$$

where *a(t)* is the second derivative of position with respect to time (acceleration). The expression is derived by combining two Taylor expansions for $r(t+\delta t)$ and $r(t-\delta t)$ and ignoring higher than the third order terms. As seen in equation 2.20, atom velocities are not explicitly solved when using the Verlet algorithm for numerical integration. Instead, they are often calculated as a first order central difference based on the atom positions at timepoints $t-\delta t$ and $t+\delta t$:

Eq. 2.21

$$v(t) = \frac{r(t+\delta t) - r(t-\delta t)}{2\delta t}$$

The velocity Verlet algorithm is similar to the Verlet algorithm, but incorporates atom velocities explicitly in the integration scheme. In this scheme, only the positions and velocities

at the previous timepoint *t* are needed (instead of positions at two previous timepoints, as in Verlet). In the leapfrog algorithm, positions and velocities are updated in a "staggered" fashion after each other at certain timepoints. For any integration scheme, the timestep δt needs to be shorter than the fastest timescale for system movement to allow for generating a stable trajectory. Often a timestep between 0.5-1 fs is used, but it can be increased to 2 fs if stretching vibrations of bonds involving hydrogens are restrained.

System configurations obtained in a molecular dynamics trajectory correspond to a certain statistical ensemble. A "standard" simulation with no temperature or pressure control is in the microcanonical (*NVE*) ensemble, where the number of particles *N*, the volume *V*, and the system energy *E* stay constant. The canonical (*NVT)* ensemble corresponds to constant temperature, and the isothermal-isobaric (*NPT*) simulation to constant temperature and pressure simulations. The temperature is often controlled by coupling the system to an external heat bath, which acts as a thermostat (such as in the Berendsen algorithm[184]). Analogously, a barostat is required to control the system pressure.

Simulations in this thesis were performed in the *NPT* ensemble using Langevin dynamics for temperature scaling. In Langevin dynamics, the energy expression is modified by neglecting some system degrees of freedom, and by introducing the so-called friction and random force terms. The friction term mimics system viscosity, and the random force term the stochasticity of the system. The Berendsen barostat was used to control the pressure. When using the Berendsen barostat, the equations of motion for atoms are scaled according to the desired reference pressure, which results in slight changes in the corresponding periodic box size.

2.12 Umbrella sampling simulations

To simulate chemical reactions within enzyme active site, often biased simulation techniques are applied. In umbrella sampling (US), a biasing potential is added along one or two reaction coordinates to force the system to undergo a transition (e.g. a chemical reaction).[185] Reaction coordinates are parameters describing the system change from its initial (reactant) state to the final (product) state and can include for example bond distances or torsions. These two end states are connected via a series of intermediate states, which are referred to as US windows. A MD simulation is done in each window to sample structures near

the restrained reaction coordinate values, and the US windows are placed so that the sampled reaction coordinate distribution in each window overlaps with distributions in the adjacent windows. To ensure sampling near a desired value for reaction coordinate ξ in the US window i, a harmonic biasing potential ω_i is added to the overall energy function:

Eq. 2.22

$$\omega_i(\xi) = K(\xi - \xi_i^{ref})$$

where K is a force constant, ξ the reaction coordinate value at a certain time point, and ξ_i^{ref} the reference reaction coordinate value in ith US window. Care must be taken when choosing a value for the force constant K, as its value should both ensure conformational sampling around the chosen US window minimum, as well as allow for sufficient overlap of sampled reaction coordinate values between adjacent windows.

With this approach, a biased potential mean force (PMF) along a reaction coordinate(s) is obtained. To study the unbiased PMF, the system is assumed to be ergodic (ensemble averages for reaction coordinate distribution equal to time averages for the distribution during the simulation), and the free energy expression takes the form:

Eq. 2.23

$$A_i(\xi) = -(1/\beta)\ln P_i^b(\xi) - \omega_i(\xi) + F_i$$

where $\beta=1/k_BT$, P_i^b is the biased distribution for ξ in window i, ω_i is the biasing potential, and F_i a term to combine free energy distributions from US windows to one global PMF:

Eq. 2.24

$$F_i = -(1/\beta)\ln\left(\sum P(\xi)e^{-\beta\omega_i(\xi)}\right)$$

As F_i cannot be directly estimated from US simulations, another method needs to be used for analysing the simulations. The weighted histogram analysis method (WHAM) is a popular one,[186] where the unbiased distribution is calculated based on a weighted average of individual windows. Because F_i depends on the distribution $P(\xi)$, and the given weights depend on F_i, the WHAM procedure requires iterating the calculations until convergence. Other methods for analysing US simulations are for example the dynamic histogram analysis method (DHAM)[187] and umbrella integration (UI)[188].

Chapter 3 – An efficient computational assay for β-lactam antibiotic breakdown by class A β-lactamases

This chapter consists of a communication article titled "An efficient computational assay for β-lactam antibiotic breakdown by class A β-lactamases", which was published in Journal of Chemical Information and Modelling in 2019.[189] This article continues the work by E. I. Chudyk *et al.* published in 2014,[190] and builds on the original computational assays by reducing both the sampling time and the conformational sampling along the free energy surface. By shortening the sampling time from 20 to 2 ps and sampling only along an approximate reaction free energy path, the required computational power is reduced by more than 99% (compared against the original assays). I performed and analysed all calculations in the new, shortened assays, and wrote the manuscript with help from my supervisors. Section 3.6 consists of the data included as the Supporting Information for this article.

3.1 Abstract

Class A β-lactamases cause clinically relevant resistance to β-lactam antibiotics. Carbapenem degradation is a particular concern. We present an efficient QM/MM molecular simulation protocol that accurately predicts the activity of β-lactamases against carbapenems. Simulations take <24 CPU hours, a >99% reduction, and do not require fitting against experimental data or significant parameterization. The computational assay reveals mechanistic details of β-lactam breakdown, and should assist in evaluating emerging β-lactamase variants and developing new antibiotics.

3.2 Introduction

Antibiotic resistance is one of the most concerning phenomena of the 21st century.[191, 192] To some extent, this resistance occurs naturally, but in recent decades its spread has been accelerated by the excessive use of antibiotics.[61] β-lactam drugs are one of the largest groups of commercially available antibiotics and they remain the most prescribed ones,[18] but they also

suffer from increasing clinical resistance.[193] The key source for this resistance, especially in Gram-negative bacteria, are the β-lactamase enzymes.[49, 194, 195]

β-lactamases can be divided into four different classes based on their primary amino acid sequence homology (Ambler classification): classes A, C, and D are serine β-lactamases with an active site serine residue, whilst class B are metallo-β-lactamases with active site zinc ion(s).[63] Of the four classes class A β-lactamases are the largest, with many clinically significant enzymes. They can inactivate a broad range of β-lactam substrates: in addition to hydrolyzing penicillins and cephalosporins, some family members can also mediate resistance against carbapenems.[27, 196, 197] Carbapenems are mainly used as 'last resort' antibiotics or for difficult infections,[24] hence the Centers for Disease Control and Prevention (CDC) have categorized the clinical importance of carbapenemase-producing Enterobacteriaceae (the group of Gram-negative bacteria including *Escherichia coli* and *Klebsiella pneumoniae*) as "an immediate public health threat that requires urgent and aggressive action".[198]

β -lactamases inactivate β-lactam antibiotics by hydrolyzing the β-lactam amide (Figure 3.1). In serine β-lactamases, this consists of two consecutive reactions: acylation, resulting in formation of a covalently-bound acylenzyme, and deacylation.[49] In acylation, a nucleophilic attack by the active site serine upon the β-lactam carbonyl carbon occurs to form the acylenzyme, via a tetrahedral intermediate.[199] Deacylation is analogous to acylation including a tetrahedral intermediate (TI), but the nucleophile is an active site water molecule (the deacylating water, DW). In class A enzymes, both nucleophiles are activated via proton abstraction by an active site glutamate residue (Glu166 in the class A β-lactamase numbering scheme).[200, 201] β-lactamases are typically inhibited when the acylenzyme intermediate is long-lived due to slow deacylation rates.[190] For many β-lactam drugs, including carbapenems, TI formation in deacylation of the acylenzyme is most likely the rate-limiting step.[24] Therefore, to determine the carbapenemase activity of class A β-lactamases, only this reaction needs to be modelled.

Previously, a quantum mechanics/molecular mechanics (QM/MM) protocol for modelling TI formation in the deacylation step for class A enzymes with meropenem was shown to correctly distinguish between carbapenemases and non-carbapenemases.[190] Using the proposed protocol, carbapenem-inhibited enzymes showed deacylation barriers of 17.0-18.9 kcal/mol, whilst for carbapenem-hydrolyzing enzymes the values were 7.5-10.5 kcal/mol. A similar computational protocol has been used to study class A β-lactamase inhibition by clavulanate, which identified the covalent clavulanate complex responsible for irreversible β-

lactamase inhibition.[202] Despite the promising results of these protocols, the carbapenem assay requires significant computational resources due to extensive sampling of the free energy surface. Hence, it cannot be used for more rapid, computationally efficient, screening of a variety of different enzyme-antibiotic combinations.

Starting from our previous work, here we present and validate a more rapid computational assay that can discriminate between carbapenemase activities using only limited computational resources. The resources are minimized first by limiting the area on the free energy surfaces (FES) to be sampled, and then by reducing the sampling time. We demonstrate that this reduced protocol, requiring less than 1 % of the computational resources of the original assay, can still correctly distinguish between carbapenemases and carbapenem-inhibited class A β-lactamases. It therefore provides an efficient computational diagnostic towards *in silico* screening of β-lactamase activity.

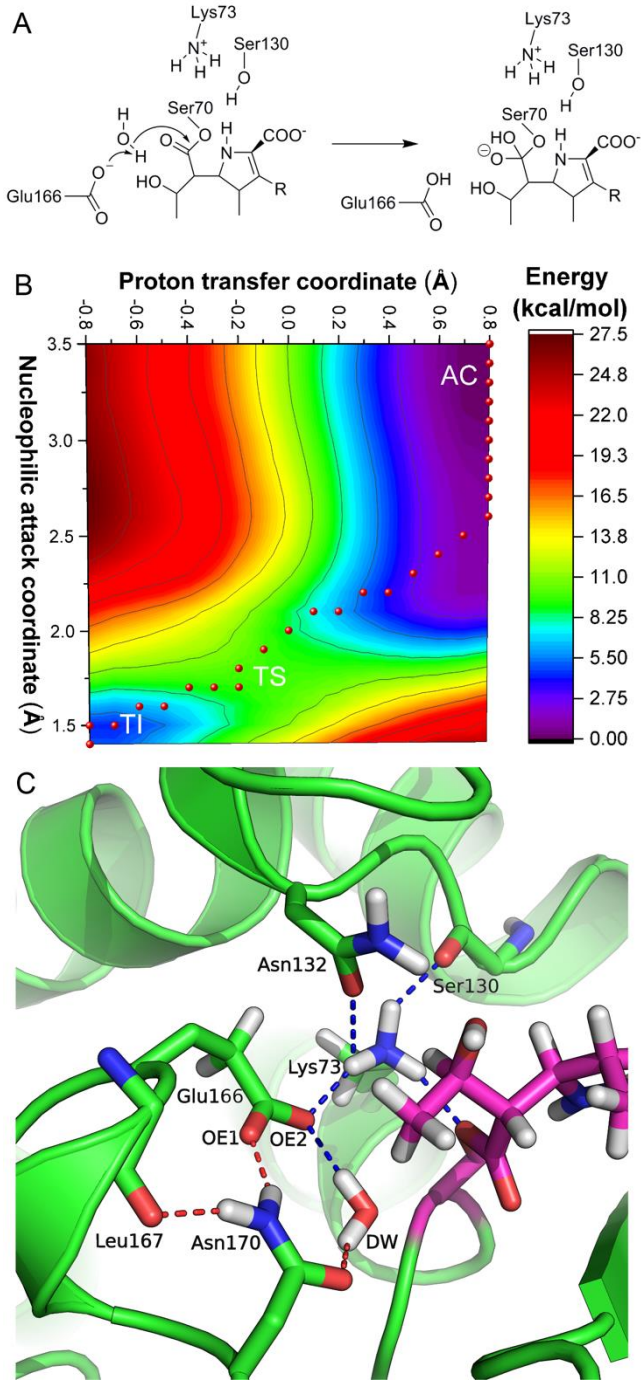

Figure 3.1 A) First step of deacylation in class A β-lactamases. Glu166 acts as a proton acceptor allowing the deacylating water to perform nucleophilic attack on the acylenzyme (1), which results in tetrahedral intermediate formation (2). B) Full free energy surface of deacylation for KPC-2 with meropenem. Red circles show the positions of umbrella sampling windows along the approximate "standard" minimum free energy path (MFEP) used for all enzymes. AC = acylenzyme, TS = approximate transition state, TI = tetrahedral intermediate. C) Active site of KPC-2 highlighting the hydrogen bonds between Glu-166 OE1 and OE2 and relevant residues. Meropenem in magenta.

3.3 Methods

We investigate eight class A β-lactamases, including the widely distributed *K. pneumoniae* carbapenemase (KPC), and the TEM, SHV and CTX-M enzymes (Table 3.1), selected for their clinical relevance and their ability (or inability) to hydrolyze carbapenems. Acylenzyme systems were prepared as described previously (details in ESI, Section 3.6).[190] Briefly, structures were solvated in water and minimized, followed by heating to 300 K in 50 ps. Starting structures for umbrella sampling (US) were then taken after at least 50 ps of unrestrained QM/MM MD (with starting points for repeat simulations at least 15 ps apart). Two reaction coordinates are used for umbrella sampling: one for the proton transfer between DW and Glu166, and one the nucleophilic attack of DW on the acylenzyme carbonyl. The DFTB2 method was used for the QM region.[162] All calculations were performed with sander from AmberTools16.[203] The weighted-histogram analysis method (WHAM)[186] was used to analyze US results and to obtain calculated barriers for each reaction ($\Delta^{\ddagger}G_{calc}$). Three independent US simulations were run for each acylenzyme to test convergence of $\Delta^{\ddagger}G_{calc}$ (details in the ESI in Section 3.6; meropenem parameters at DOI 10.6084/m9.figshare.8158097).

3.4 Results and discussion

Several modifications to the protocol were evaluated in order to improve computational efficiency. First, the amount of sampling was reduced by sampling only at those US windows corresponding to the approximate minimum free energy path (MFEP) on the FES. Based on our earlier work,[190] the calculated MFEPs on full FESs across all eight studied β-lactamases are similar, which implies that only a partial FES needs to be calculated to compare the deacylation rates between studied enzymes. The "standard" MFEP used for partial sampling along the FES is presented in Figure 3.1 (and in the ESI, Section 3.6). Sampling only in windows along this MFEP reduces the number of US calculations from the original 374 to 28 per (partial) surface. The more limited sampling along the surface does not change the resulting $\Delta^{\ddagger}G_{calc}$ values significantly, with the largest calculated change between full and partial surface calculations being 2.5 kcal/mol (Table 3.1). Despite some changes in $\Delta^{\ddagger}G_{calc}$ values for all enzymes, the correct division into two groups is maintained. Carbapenemases (KPC, SFC, SME and NMC) have $\Delta^{\ddagger}G_{calc}$ values between 7.8-10.4 kcal/mol, and carbapenem-inhibited enzymes (SHV, TEM, BlaC and CTX-M) between 15.5-16.8 kcal/mol. This suggests that the

standard MFEP describes deacylation sufficiently well for differentiating between different carbapenem-hydrolyzing abilities.

Even when the amount of US windows is significantly reduced, the computational time for each window remains high. Hence, the possibility of utilizing shorter sampling times was first tested using the original 20 ps US results. This was done by using only the first 0.5, 1, 2, 5 or 10 ps of each 20 ps US window to calculate $\Delta^{\ddagger}G_{calc}$ values (Table S2 in Section 5.6). This differs from sampling each window for a shorter time only, since the system is still allowed to equilibrate for 20 ps before changing the reaction coordinate restraints. Nonetheless, this preliminary analysis can be used to study the effects of shorter sampling. The results indicate that sampling for only a fraction of 20 ps is enough to distinguish between the two groups of β-lactamases. In most cases, the preliminary shorter sampling times yield somewhat higher barriers (<2.5 kcal/mol), which is expected due to reduced sampling of the phase space. However, this does not affect the distinction between carbapenemases and non-carbapenemases. When reducing sampling to 1 ps per window or less, more significant increases of the barrier heights (up to 20%) become common. We thus decided to use 2 ps US sampling per window. Sampling for 2 ps also ensures enough overlap between sampling in adjacent US windows.

Table 3.1 Comparison of experimental ($\Delta^{\ddagger}G_{exp}$) and calculated free energies of activation ($\Delta^{\ddagger}G_{calc}$) for the first step of deacylation of meropenem by eight enzymes using different protocols.

β-lactamase	**k_{cat} (s^{-1})** [a]	**$\Delta^{\ddagger}G_{exp}$ (kcal/mol)** [b]	**$\Delta^{\ddagger}G_{calc}$ (kcal/mol)** [c]		
			Full [a]	MFEP (20ps)	MFEP (2ps)
KPC-2	3.6	16.8	10.5 (0.9)	8.5 (2.2)	9.1 (1.1)
SFC-1	6.5	16.6	10.9 (0.9)	10.4 (1.2)	9.9 (1.3)
SME-1	3.2	16.9	10.3 (2.8)	7.8 (0.2)	9.5 (1.4)
NMC-A	12.0	16.1	7.5 (0.4)	8.8 (0.4)	10.4 (0.7)
SHV-1	0.0013	21.6	17.0 (0.4)	16.1 (1.0)	19.5 (0.5)
TEM-1	0.0023	22.7	17.1 (0.4)	16.3 (2.2)	23.6 (1.4)
BlaC	0.0017	21.5	17.9 (0.1)	15.5 (2.2)	24.7 (1.1)
CTX-M-16	0.0042	20.8	18.9 (1.1)	16.8 (1.5)	17.2 (1.6)
Computer resource (%) [d]			100	7.5	0.75

a) Values taken from ref. 19.

b) Calculated from experimental rate constants using the Eyring equation, see ref. [202].

c) Barriers are calculated from three simulations using WHAM as described in the ESI, standard deviations in parenthesis.

d) Computer resources required are estimated by extrapolating the time needed for all required QM/MM simulations from 2 ps calculations: 374 umbrella sampling windows for the whole surface and 20 ps per window (374 x 20) for "Full", 28 windows x 20 ps for "MFEP (20ps)" and 28 windows x 2 ps for "MFEP (2ps)".

Sampling for only 2 ps per window along the MFEP gives similar overall results to sampling for 20 ps (Table 3.1). With the shorter protocol, carbapenemases have $\Delta^{\ddagger}G_{calc}$ values of 9.1-10.4 kcal/mol, whilst carbapenem-inhibited enzymes have $\Delta^{\ddagger}G_{calc}$ values of 17.2-24.7

kcal/mol. Shorter US gives higher deacylation $\Delta^{\ddagger}G_{calc}$ values for all enzymes, with most significant increases seen for carbapenem-inhibited enzymes (0.4-9.2 kcal/mol) when compared to calculations using 20 ps sampling along the MFEP. However, the increased deacylation barriers do not change the division of the enzymes into the two distinct groups. Furthermore, the shortened protocol enables all running calculations on modest computing resources (e.g. on a desktop with one CPU) in a reasonable time. For the largest system (SFC-1, containing 54.9k atoms), US takes on average 23 hours to finish on one 2.6 GHz CPU. In general, the more efficient assay requires less than 1 % of the computer resources needed for the original assay (Table 3.1).

The efficient assay we have developed can be used to study specific mechanistic details of carbapenem hydrolysis. Glu166, the general base in deacylation, has two chemically inequivalent carboxylate oxygens: one that forms a hydrogen bond with Asn170 (OE1), and one that interacts with Lys73 (OE2) (Figure 3.1C). The DW hydrogen bonds with OE2 in all MD simulations, and the US calculations have been performed using this oxygen as the proton acceptor. However, proton transfer to OE1 might also be relevant for deacylation. We thus used our new, efficient protocol to compare the two possible proton acceptors. When forcing the proton transfer to OE1, the $\Delta^{\ddagger}G_{calc}$ values increase by >3 kcal/mol for the carbapenemases (Table S3, Section 3.6). Significant increases also incur for the carbapenem-inhibited enzymes (especially if the barrier with proton transfer to OE2 was not very high already). This consistent increase implies that the most probable proton transfer pathway in carbapenem hydrolysis is via Glu166:OE2 that interacts with Lys73, thus indicating an important role for this residue.

Preference for a certain carboxylate oxygen as the general base has been observed also in other enzymes.[204] For the β-lactamases, DW is primarily hydrogen bonded with OE2 in the acylenzyme MD simulations and this interaction is thus present in all starting structures for US calculations. The preference for OE2 acting as the base can be explained by inspecting the additional hydrogen bonds formed by the Lys73 and Asn170 side chains. Lys73 interacts with Glu166:OE2 as well as Asn132, Ser70, meropenem and the Ser130 backbone carbonyl oxygen, whilst Asn170 interacts only with Glu166:OE1 and the backbone carbonyl of Leu167. Upon a proton transfer, other residues can balance the weakening interaction of Lys73 with Glu166:OE2, whereas Asn170 has fewer other interactions for such stabilization.

3.5 Conclusions

In conclusion, the carbapenemase activity of eight class A β-lactamases was assayed *in silico* using QM/MM reaction simulations with an optimized, efficient computational protocol. Assays based on computational simulation are increasingly common and can complement traditional experimental assays.[98] Assay efficiency is obtained here by using the semi-empirical DFTB2 method and by limiting both conformational space and time sampled. Distinction between four enzymes known to efficiently hydrolyze carbapenems, and four enzymes that do not, can be made within a day with very modest computer resources (e.g. one CPU per enzyme). Additionally, this efficient assay can be used to inspect mechanistic aspects of carbapenem inactivation; exemplified here by comparing the $\Delta^{\ddagger}G_{\text{calc}}$ values of the first deacylation step for two possible proton transfer pathways. The short computational assay time with moderate computer resources now makes this assay attractive for more rapid *in silico* activity screening of different class A β-lactamase – antibiotic combinations. This will assist assessment and understanding of resistance to β-lactam drugs as conferred by β-lactamases, e.g. the effect of acquired point mutations on drug hydrolysis. As access to genome sequences of pathogen isolates becomes more routine, such information could be used in guiding prescription decisions. Furthermore, elucidation of mechanistic details of acyl-enzyme hydrolysis, as identified in simulations, may guide the development of new β-lactams or β-lactamase inhibitors designed to evade the activity of broad-spectrum and carbapenem-hydrolyzing β-lactamases.

3.6 Computational details

This section comprises the Supporting Information data for the above publication.

System set-up

Acylenzyme structures were built on available crystal structures (Table S1). For SHV-1 and BlaC, acylenzyme structure with meropenem was available, for SFC-1 the Glu166Ala structure was used (mutated back to wild-type enzyme based on SFC-1 Ser70Ala and meropenem structure, PDB: 4EUZ). TEM-1 with meropenem was generated by minimizing

the crystal structure with imipenem, and then changing the substrate to meropenem. Acylenzymes for CTX-M-16, NMC-A, KPC-2, and SME-1 were built by aligning the available apoenzyme structures with the SFC-1 and meropenem complex, and by combining the coordinates of the antibiotic substrate with the enzyme.

Table S1. Accession codes for acylenzyme structures used in model generation.

Enzyme	**PDB code**
KPC-2	2OV5
SFC-1 (E166A)	4EV4
NMC-A	1BUE
SME-1	1DY6
CTX-M-16	1YLW
SHV-1	2ZD8
BlaC	3DWZ
TEM-1	1BT5

Protonation states were calculated using the propKA3.1 program, and hydrogen atoms like implemented in tLeap. All crystallogprahic water molecules were deleted from the structures excluding the deacylating water, and the structures were solvated in a 10 Å box of TIP4P-Ew water. Existing charges were neutralized by adding sodium ions.

Computational methods

Systems were minimized, heated and equilibrated as described in the ESI of ref. [190].

QM/MM Free energy calculations

All QM/MM umbrella sampling (US) calculations were done using two reaction coordinates: one for describing the nucleophilic attack (NA, d[DW:O - ACA:C]), and one for describing the proton transfer (PT, d[Glu:O-DW:H] - d[DW:O-DW:H]).[190] Reaction coordinate values for the standard MFEP (in Å):

PT	0.8	0.8	0.8	0.8	0.8	0.8	0.8	0.8	0.8	0.8	0.7	0.6	0.5	0.4	0.3	0.2
NA	3.5	3.4	3.3	3.2	3.1	3.0	2.9	2.8	2.7	2.6	2.5	2.4	2.3	2.2	2.2	2.1

PT	0.1	0.0	-0.1	-0.2	-0.2	-0.3	-0.4	-0.5	-0.6	-0.7	-0.8	-0.8
NA	2.1	2.0	1.9	1.8	1.7	1.7	1.7	1.6	1.6	1.5	1.5	1.4

where PT and NA describe the values for the proton transfer and nucleophilic attack reaction coordinates, respectively. The range of both RCs was kept same as in ref. 190.

Outputs from US calculations were analysed using the weighted histogram analysis (WHAM)[186] program using 17 bins for PT and 22 bins for NA reaction coordinates. The convergence criterium was set to 0.0000000000001. This analysis was done separately for all three starting structures, and lastly by combining all three results into one WHAM calculation for calculating the overall reaction barrier (as opposed to taking the average of three snapshots). However, especially with shorter sampling times WHAM analysis was prone to give false minima on the (partial) free energy surface, due to an error in the WHAM code used. This was resolved by locating these false minima and deleting the corresponding coordinate lines from the input files. Usually the false minima were due to only few coordinates, and in each case less than 1 % of data was removed. This problem can be overcome by utilizing a different analysis method or by fixing the WHAM code.

The complete efficient assay

The complete efficient assay follows these steps:

1. Prepare the starting structures for all studied acylenzymes either from crystal structures or based on analogous crystal structures (as described above). Solvate all proteins in a periodic box of TIP4P-Ew water, neutralize charges with counterions.
2. Minimize the structures briefly (100 of steepest descent followed by 900 steps of conjugate gradient).
3. Heat the systems from 50 K to 300 K in 50 ps using Langevin dynamics.
4. Equilibrate the systems in 300 K for 50 ps using unrestrained QM/MM MD (DFTB2/ff12SB), afterwards perform 300 ps of further QM/MM MD to generate starting structures for US.

5. Utilize QM/MM US for calculating deacylation barriers for all β-lactamases. Three different variations are used in the manuscript as described below:
    a. The original assay: Do US in every window for 20 ps, calculate the whole surface (374 windows).
    b. 20 ps along the standard MFEP: Do US in the 29 windows listed above starting from the reactant structure, use the restart file from the previous window as a starting point for the next one. Sample 20 ps in each window.
    c. 2 ps along the standard MFEP (the efficient assay): The same procedure as described in b), except the sampling time is shortened from 20 ps to 2 ps in each US window. Repeat a), b), or c) three times using different starting structures to test the convergence of calculated deacylation barriers.
6. Analyse the results of each individual run using WHAM. For the overall barrier, the three US calculations were combined into one WHAM run.

WHAM analysis of shorter sampling

To first inspect to possibility of reducing sampling time in each US window, US results for 20 ps sampling along the MFEP were inspected by including only the first 10/5/2/1/0.5 ps in the WHAM analysis. For all three snapshots, the desired amount of sampling was included for each US window, which was followed by the same WHAM analysis as described earlier (where the same US windows for three different snapshots were combined into one). Results for this analysis are presented in Table S2.

Table S2. $\Delta^{\ddagger}G_{calc}$ values calculated using WHAM, where results from three different calculations are combined into one WHAM analysis.

	$\Delta^{\ddagger}G_{calc}$ (20 ps)	$\Delta^{\ddagger}G_{calc}$ (10 ps)	$\Delta^{\ddagger}G_{calc}$ (5 ps)	$\Delta^{\ddagger}G_{calc}$ (2 ps)	$\Delta^{\ddagger}G_{calc}$ (1 ps)	$\Delta^{\ddagger}G_{calc}$ (0.5 ps)
KPC-2	8.5	8.9	8.9	9.8	10.2	10.5
SFC-1	10.9	11.0	10.3	10.8	11.3	12.8
SME-1	9.5	7.7	7.6	7.6	8.1	8.4
NMC-A	8.8	8.6	8.9	9.0	9.6	10.5
SHV-1	16.1	16.5	16.5	16.8	16.7	17.5
TEM-1	16.3	16.8	16.9	17.2	17.9	18.6
BlaC	15.5	17.0	17.0	17.9	17.9	18.0
CTX-M-16	16.8	17.1	17.2	17.6	17.9	17.9

Alternative proton transfer pathways

The two possible proton transfer pathways were inspected using the efficient protocol. Glu166 acting as the general base has two chemically inequivalent oxygens, which can both act as the proton acceptor. As the DW hydrogen bonds with Glu166:OE2 in MD simulations, it was used as the proton acceptor in all US calculations. However, technically the proton acceptor can also be Glu166: OE1. A comparison of activation barriers for the two different proton transfers are presented in Table S3. Using OE1 as the proton acceptor increases $\Delta^{\ddagger}G_{\text{calc}}$ values for all enzymes 2.0-9.7 kcal/mol: new $\Delta^{\ddagger}G_{\text{calc}}$ values for carbapenemases are 2.0 – 7.2 kcal/mol higher, and for non-carbapenemases 3.0-9.7 kcal/mol. This suggests that Glu166: OE2 should be used as the proton acceptor when modelling deacylation in class A β-lactamases, and that the hydrogen bonding interaction with Lys73 is important for efficient catalysis.

Table S3. $\Delta^{\ddagger}G_{calc}$ values for the two possible proton transfer pathways (with 2 ps sampling). All energies in kcal/mol, standard deviations in parenthesis.

	$\Delta^{\ddagger}G_{\text{calc}}$ (OE2)	$\Delta^{\ddagger}G_{\text{calc}}$ (OE1)	Difference
KPC-2	9.1 (1.1)	14.5 (2.2)	+5.4
SFC-1	9.9 (1.3)	17.1 (1.8)	+7.2
SME-1	9.5 (1.4)	15.2 (2.6)	+5.7
NMC-A	10.4 (0.7)	13.8 (2.1)	+3.4
SHV-1	19.5 (0.5)	29.2 (1.2)	+9.7
TEM-1	23.6 (1.4)	26.6 (1.6)	+3.0
BlaC	24.7 (1.1)	26.7 (2.6)	+2.0
CTX-M-16	17.2 (1.6)	21.1 (0.4)	+3.9

Chapter 4 - Antimicrobial resistance conferred by OXA-48 β-lactamases: towards a detailed mechanistic understanding

The work in this chapter comprises a minireview "Antimicrobial resistance conferred by OXA-48 β-lactamases: towards a detailed mechanistic understanding" published in Antimicrobial Agents and Chemotherapy.[205] The original draft of the review was written by myself, and my co-authors Marc van der Kamp and James Spencer provided comments, additional ideas, and text editing at later stages.

4.1 Abstract

OXA-48-type β-lactamases are now routinely encountered in bacterial infections caused by carbapenem-resistant *Enterobacterales.* These enzymes are of high and growing clinical significance due to the importance of carbapenems in treatment of healthcare-associated infections by Gram-negative bacteria, the wide and increasing dissemination of OXA-48 enzymes on plasmids, and the challenges posed by their detection. OXA-48 confers resistance to penicillin (which is efficiently hydrolyzed) and carbapenem antibiotics (more slowly broken down). In addition to the parent enzyme, a growing array of variants of OXA-48 is now emerging. The spectrum of activity of these variants varies, with some hydrolyzing expanded-spectrum oxyimino-cephalosporins. The growth in importance and diversity of the OXA-48 group has motivated increasing numbers of studies that aim to elucidate the relationship between structure and specificity and establish the mechanistic basis for β-lactam turnover in this enzyme family. In this review we collate recently published structural, kinetic, and mechanistic information on the interactions between clinically relevant β-lactam antibiotics and inhibitors with OXA-48 β-lactamases. Collectively, these studies are starting to form a detailed picture of the underlying bases for the differences in β-lactam specificity between OXA-48 variants, and the consequent differences in resistance phenotype. We focus specifically on aspects of carbapenemase and cephalosporinase activities of OXA-48 β-lactamases and discuss β-lactamase inhibitor development in this context. Throughout the review, we also outline key open research questions for future investigation.

4.2 Introduction

Antimicrobial resistance has been recognized globally as one of the most serious threats to modern medicine. According to the 2014 UK Review on Antimicrobial Resistance, antibiotic resistant bacterial infections are predicted to result in 10 million deaths annually by 2050 if no preventative measures are taken.[206] β-lactams are the single most prescribed antibiotic class, accounting for over half of all antibiotic prescriptions in human patients,[18] thus the consequences of widespread resistance to these agents are especially severe. Resistance against carbapenems is a particular concern, as these drugs are the most recently introduced and potent class of b-lactams; they are for example favored treatments for opportunistic infections of secondary care patients by Gram-negative bacteria resistant to other agents.[24] Furthermore, the continuing weakness of the antibacterial pipeline means that alternative treatments are limited.[207] This existing threat is highlighted by the Centers for Disease Control and Prevention, who classified carbapenem-resistant *Enterobacterales* as an urgent antibiotic resistance threat in the United States in 2019.[6]

Since the initial introduction of β-lactam antibiotics in the 1940s, bacteria have developed many different mechanisms to bypass their effect; these include changes in expression levels of porins and efflux pumps, target modification through gene acquisition or mutation, and enzymatic drug modification.[48] In Gram-negative bacteria, β-lactamase enzymes are the main resistance mechanism against β-lactam antibiotics. β-Lactamases modify the antibiotic by hydrolytic cleavage of the β-lactam amide bond;[49] as β-lactams work by binding to penicillin-binding proteins (PBPs) and disrupting bacterial cell wall biosynthesis,[50, 208] degrading the β-lactam pharmacophore renders these antibiotics inactive. Over 4500 β-lactamases have now been identified (see www.bldb.eu for details),[62] with the continuing explosion of genomic data driving further discovery of new enzymes from both environmental and clinical sources.

According to the Ambler classification, β-lactamases are divided into four groups: classes A, C, and D are serine β-lactamases (SBLs), which utilize an active site serine nucleophile to hydrolyze β-lactams via a covalent acylenzyme intermediate, while class B metallo-β-lactamases (MBLs) utilize zinc cofactors to activate a water molecule to undertake antibiotic inactivation.[49] Within SBLs, class D β-lactamases form a structurally diverse group of enzymes, which were first identified as having enhanced hydrolytic activity towards semisynthetic penicillins such as oxacillin, and reduced activity towards penicillin (rates

compared against class A β-lactamases).[75, 209] Subsequently, they were named as oxacillinases, or OXAs for short. OXA β-lactamases include five recognized subgroups of carbapenem-hydrolyzing enzymes: four of these, namely OXA-23-like, OXA-24/40-like, OXA-51-like, and OXA-58-like β-lactamases, are largely restricted to *Acinetobacter baumannii*, while OXA-48-like β-lactamases are most commonly encountered in the *Enterobacterales*.[32, 206, 210-216] Additionally, some OXA enzymes (OXA-2, OXA-10) classified as narrow-spectrum β-lactamases have demonstrated comparable rates of carbapenem hydrolysis to recognized carbapenem-hydrolyzing OXAs, which could imply that most OXAs can (to some extent) be considered carbapenemases.[217] OXA-48 β-lactamases are now among the most common carbapenemases[218] and are often co-produced with other β-lactamases (MBLs or ESBLs).[219] For an in-depth overview of the global epidemiology of β-lactamase, specifically OXA-48-type, producing pathogens we refer the reader to recent reviews by Bush and Bradford[220] and Pitout *et al.*[221]

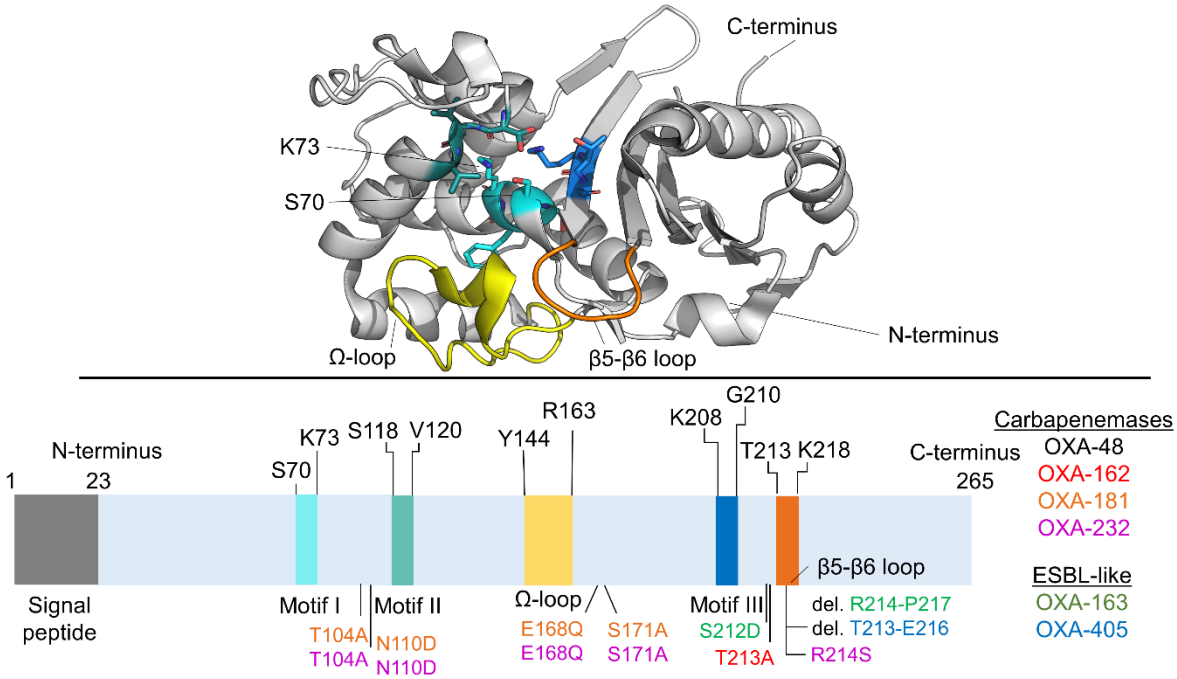

Figure 4.1 Structure of OXA-48. Cartoon shows unliganded OXA-48 (PDB ID 6P96)[71] with selected elements of the structure highlighted. The three conserved motifs within class D β-lactamases are shown in blue shades, the Ω-loop in yellow, and the β5-β6-loop in orange. Selected OXA-48 variants are listed according to their primary hydrolysis phenotype, and their amino acid substitutions or deletions highlighted in the corresponding color in the amino acid sequence. Carbapenemase = efficient imipenem hydrolysis, some activity towards other carbapenem substrates. ESBL-like = only weak activity against all carbapenems, activity against expanded-spectrum oxyimino cephalosporins.

Even though OXA-48 β-lactamases are not closely related in sequence to other class D β-lactamases (less than 50 % amino acid identity), their sequences include three active site motifs that are broadly conserved within class D enzymes.[222] Motif I (SxxK) includes the nucleophilic Ser70 and the catalytically important Lys73, which needs to be carboxylated for efficient hydrolysis to take place (Figure 4.1).[222, 223] Motifs II and III are in the vicinity of these key catalytic residues and include residues Ser118-Val119-Val120 and Lys208-Thr209-Gly210, respectively, in OXA-48-like enzymes. Additionally, the Ω-loop (residues 143-165) and β5-β6-loop (residues 213-218) bordering the active site seem to be important determinants of OXA-48 activity, as discussed below. According to the β-lactamase database, at least 15 plasmid-encoded OXA-48 β-lactamases have been identified and validated (with further variants chromosomally encoded mainly in different *Shewanella* species[224, 225]). These variants differ from wild-type OXA-48 by certain amino acid substitutions or deletions. Selected key family members along with their hydrolytic profiles are listed in Figure 4.1.

As mentioned above, OXA-48 enzymes degrade a variety of β-lactam antibiotics, including ampicillin and oxacillin (more efficiently than e.g. temocillin),[222, 226] and perhaps most notably the "last-resort antibiotics" carbapenems (Figure 4.2).[227] However, there are large phenotypic variations within the enzyme family. Compared to the parent OXA-48 enzyme, some variants have enhanced carbapenemase activity (like OXA-162[228] and OXA-181[229]), while others have expanded their hydrolysis profile to better accommodate expanded-spectrum oxyimino cephalosporins (such as OXA-163[230] and OXA-405[231]). OXA-48 carbapenemases tend to favour imipenem over other carbapenems and display only low-level meropenem and ertapenem hydrolysis (Table 4.1). Weak carbapenem hydrolysis can complicate diagnosis and treatment of bacterial infections involving OXA-48 producers, as their activity can be below the detection limit of clinical tests but still sufficient to confer resistance, especially in strains with reduced antibiotic permeability.[232] OXA-48 itself shows varying activity against cephalosporins; e.g. cefalotin and cefotaxime are inactivated readily, whereas minimal (or no) activity is measured against ceftazidime and cefepime.

Table 4.1. Kinetic parameters for OXA-48, OXA-163, OXA-181, and OXA-232 with different β-lactam antibiotics. Presented values taken from ref. [226], and more comprehensive data of enzyme kinetics is provided as part of the SI.

	OXA-48[a]		***OXA-163***		***OXA-181***		***OXA-232***	
	k_{cat} (s^{-1})	K_m (μM)	k_{cat} (s^{-1})	K_m (μM)	k_{cat} (s^{-1})	K_m (μM)	k_{cat} (s^{-1})	K_m (μM)
Imipenem	5	13	0.03	520	7.5	13	0.2	9
Meropenem	0.07	10	>0.1	>2000	0.1	70	0.03	100
Ertapenem	0.13	100	0.05	130	0.2	100	0.04	110
Doripenem	-[b]	-[b]	NH	NH	0.04	55	0.005	10
Ceftazidime	NH	NH	8	>1000	-	-	>0.6	>1000
Cefotaxime	>9	>900	10	45	>62	>1000	>6.5	>1000
Cefalotin	44	195	3	10	13	250	13	125
Benzylpenicillin	-[c]	-[c]	23	13	444	90	125	60
Ampicillin	955	400	23	315	218	170	132	220
Temocillin	0.3	45	NH	NH	0.3	60	0.03	60
Oxacillin	130	95	34	90	90	80	156	130

[a] Values for OXA-48 in ref. [226] are from ref. [222].

[b] Data from ref. [228] do not show doripenem hydrolysis by OXA-48, but kinetic data from ref. [217] indicate weak doripenem hydrolysis.

[c] Kinetic data from ref. [227] indicate that benzylpenicillin is hydrolysed by OXA-48.

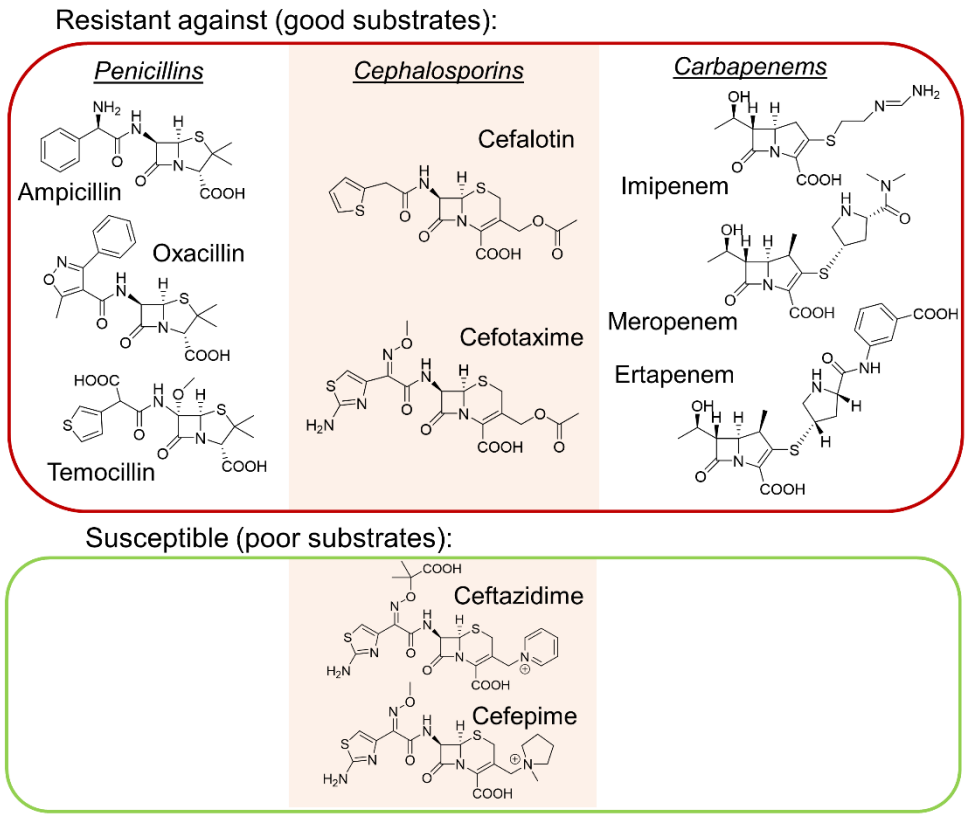

Figure 4.2. β-lactam antibiotics as substrates for OXA-48. Examples of penicillin, cephalosporin, and carbapenem antibiotics (left, middle, and right respectively), which are generally ineffective against OXA-48 producers (red box), and which can be used to treat OXA-48-producing infections (green box). Notably, activity profiles vary within the OXA-48 family, as e.g. the ESBL-like OXA-163 has acquired activity against expanded-spectrum oxyimino cephalosporins (ceftazidime).

4.3 General hydrolysis mechanism

In SBLs, the overall hydrolysis reaction consists of two parts, acylation followed by deacylation (Figure 4.3).[49] After initial formation of the non-covalent Michaelis complex, the β-lactamase is acylated by the antibiotic resulting in covalent bond formation between Ser70 and the carbonyl carbon of the β-lactam ring. This covalent acylenzyme structure is hydrolyzed in the deacylation step, where an active site water molecule (the so-called deacylating water) acts as the nucleophile to attack the acylenzyme carbonyl. Both acylation and deacylation involve formation of short-lived tetrahedral intermediate (TI) structures. For OXA-48-like β-lactamases, deacylation was shown to be rate-limiting for carbapenem breakdown.[233]

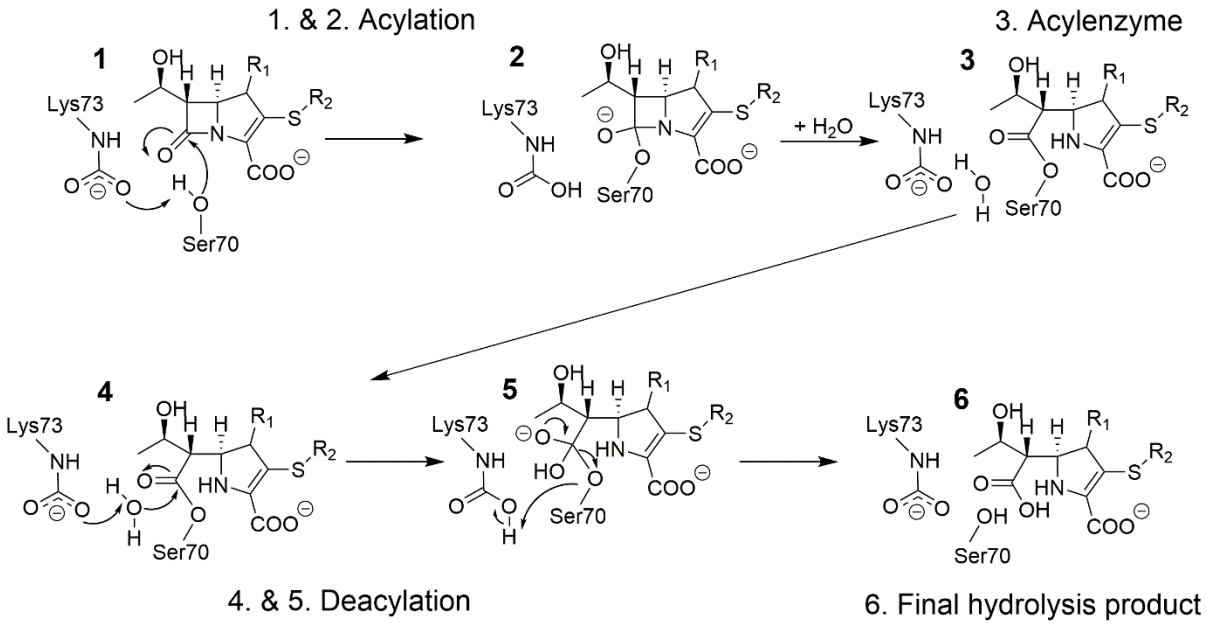

Figure 4.3. Hydrolysis mechanism of OXA-48 β-lactamases. Starting from the formation of a Michaelis complex for a general carbapenem substrate (1), the substrate is acylated (tetrahedral intermediate formation in 1 → 2), which yields a covalent acylenzyme structure (3). The bound antibiotic is subsequently deacylated (4 & tetrahedral deacylation intermediate 5) resulting in the final hydrolysis product (6).

As depicted in Figure 4.3, both acylation and deacylation involve a negatively charged general base. For class A β-lactamases, this residue is largely accepted to be Glu166,[89, 201] but for OXA enzymes, the general base is a carboxylated lysine (Lys73 in OXA-48 numbering).[222, 234] This post-translational carboxylation is needed for efficient hydrolysis to take place, as mutating Lys73 results in enzymes incapable of substrate turnover.[223] The degree of carboxylation increases with pH, and preparation of catalytically competent enzymes can be ensured by adding a suitable CO_2 source for carboxylation (bicarbonate), even though atmospheric CO_2 may also be enough.[235] This carboxylation is reversible, and it has been monitored with ^{19}F NMR spectroscopy in the presence of different inhibitors to understand how (de)carboxylation contributes to enzyme inhibition.[236] The results indicate that Lys73 is carboxylated to a lesser extent with some covalently-bound inhibitors (like avibactam), which may contribute to more efficient inhibition.

4.4 Carbapenemase activity

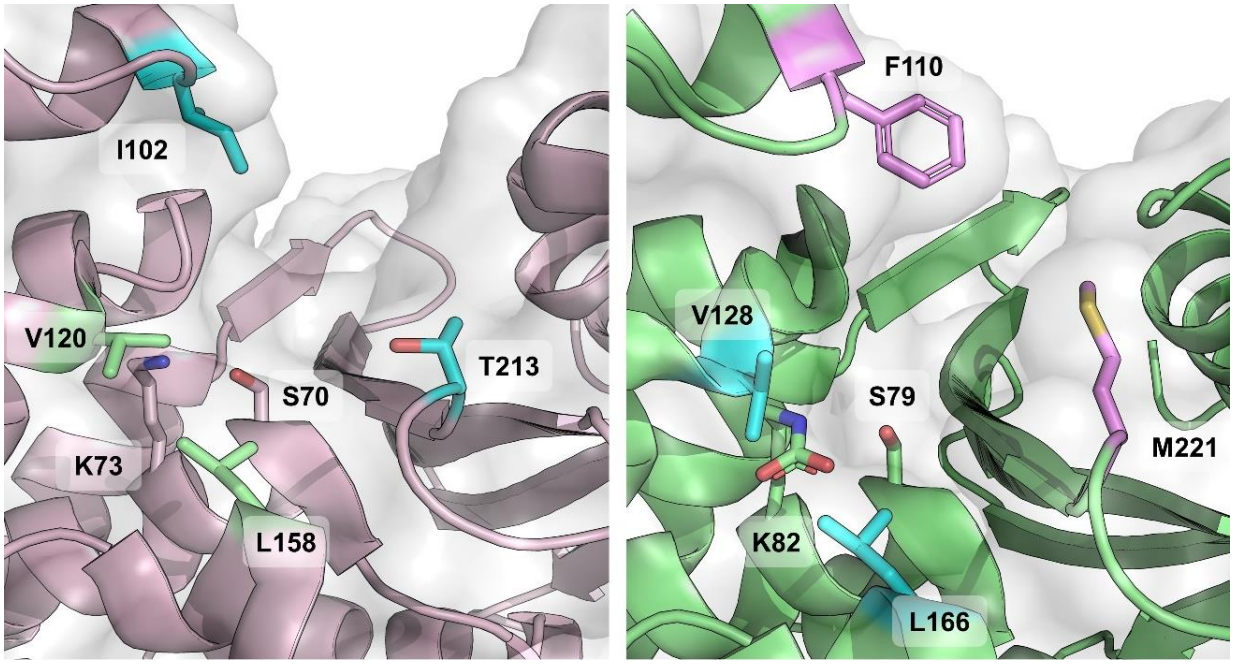

Figure 4.4. Divergent active sites of carbapenem-hydrolyzing OXA enzymes. Active sites of OXA-48 (PDB ID 6P96, left)[71] and OXA-23 (PDB ID 4K0X, right)[237] highlight the missing hydrophobic bridge in OXA-48 with respect to other class D carbapenemases. In OXA-23, the hydrophobic bridge is formed by residues Phe110 and Met221, while the corresponding residues in OXA-48 are Ile102 and Thr213, which leave the active site more open. Additionally, residues forming the so-called "deacylating water channel" are also highlighted in sticks (V120 and L158 for OXA-48, V128 and L166 for OXA-23).

OXA-48 enzymes are carbapenemases or, more specifically, imipenemases with weak turnover rates for other carbapenems such as meropenem and ertapenem (Table 4.1). Based on the structural information originally derived from other carbapenem-hydrolyzing OXAs,[238] carbapenemase activity in class D β-lactamases was hypothesized to originate from a hydrophobic bridge spanning the active site (Phe110 and Met221 for OXA-23, Tyr112 and Met223 for OXA-24). However, structural comparisons between OXA-48 and other OXA carbapenemases show OXA-48 to be lacking this hydrophobic bridge,[222] which implies that the OXA-48 group has evolutionally diverged from other class D β-lactamases and acquired carbapenemase activity by other means (Figure 4.4). Fortunately, within the last years a plethora of new crystal structures of OXA-48s complexed with carbapenems have been released, and new mechanistic knowledge has been derived from them.

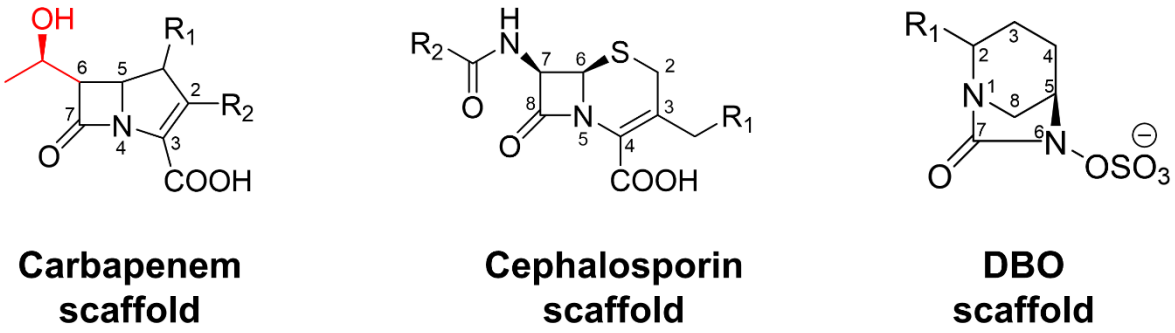

Figure 4.5. Carbapenem, cephalosporin, and diazabicyclooctanone (DBO) scaffolds with atom numbering. The 6α-hydroxyethyl group (C6 substituent) in the carbapenem scaffold is shown in red.

The first carbapenem acylenzyme structure of OXA-48 (with imipenem) was released in 2018 (PDB ID 5QB4) alongside multiple structures with small inhibitor fragments.[239] From 2019 onward, further acylenzyme structures have been deposited with imipenem (PDB IDs 6P97, 6PTU, and 7KH9),[71, 233, 240] meropenem (PDB IDs 6P98, 6PT1, and 7KHQ),[71, 233, 240] doripenem (PDB IDs 6P9C and 6PXX),[71, 241] ertapenem (PDB ID 6P99),[71] and faropenem (PDB ID 6PSG)[240]. Additionally, two acylenzyme structures of inactivated OXA-163 (K73A) with imipenem and meropenem are available (PDB IDs 7KHZ and 7KHY, respectively)[233]. Common features in these structures include a covalent bond between Ser70 and the substrate and hydrogen bonds between Thr209/Arg250 and the carbapenem C3 carboxylate (Figure 4.5). The carbonyl oxygen of the cleaved β-lactam ring is positioned in the oxyanion hole formed by the backbone amides of Ser70 and Tyr211, active site interactions in selected crystallized carbapenem acylenzyme complexes are presented in Figures 4.6 and 4.7. Carbapenem "tail" groups (C2 substituents) are not anchored by any strong interactions, which implies that they are dynamic and do not need to adopt any one specific orientation. This likely disorder was also inspected by Papp-Wallace *et al.*, who further refined previously deposited imipenem and doripenem complexes (PDB IDs 5QB4 and 6P9C, respectively).[241] Their analysis of the re-refined structures supports the presence of a covalent bond between Ser70 and the antibiotic, but observation of weak or absent density for the pyrroline ring and C2 tail groups indicates disorder (i.e. multiple conformations) for these regions. In addition to previously mentioned covalent complexes, a structure of OXA-48 with hydrolyzed imipenem has also been published (PDB ID 6PK0).[240] Non-covalently bonded hydrolyzed imipenem forms similar interactions with Thr209 and Arg250 to those observed in the acylenzyme, and the newly formed C7

carboxylate group is hydrogen bonded to Ser70, Lys73, and Tyr211 (Figure 4.6). Although the deacylating water is not present in any acylenzyme structure, the orientation of hydrolyzed imipenem (specifically coordination of the C7 carboxylate to Ser70 and Lys73) indicates the possible position of the deacylating water molecule prior to deacylation.

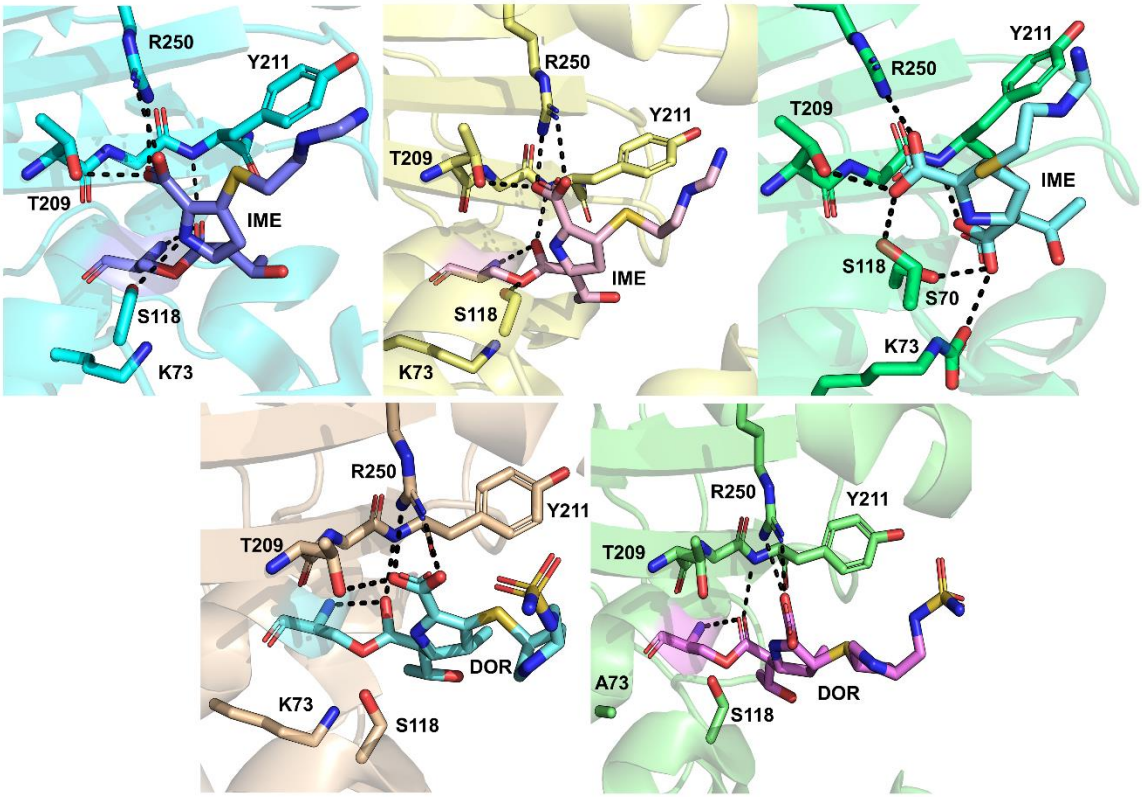

Figure 4.6. Carbapenem complexes of OXA-48. Top left: Imipenem acylenzyme (PDB ID 6P97)[71], interactions with active site residues highlighted. Imipenem pyrroline ring modelled as the Δ^2 tautomer. Top middle: Imipenem acylenzyme (PDB ID 6PTU)[240], with the pyrroline ring as the (R)-Δ^1 tautomer. Top right: Hydrolyzed imipenem (PDB ID 6PK0)[240], with the pyrroline ring as the (S)-Δ^1 tautomer. Bottom left: Doripenem acylenzyme (PDB ID 6P9C)[71], with the pyrroline ring as the Δ^2 tautomer. Bottom right: Doripenem acylenzyme (PDB ID 6PXX)[241], with the pyrroline ring as the (R)-Δ^1 tautomer.

In OXA-48 enzymes the basis for carbapenemase activity has been attributed to the presence of the β5-β6 loop bordering the active site, as for example engineering this loop from OXA-48 into the non-carbapenemase OXA-10 changes its phenotype to hydrolyze imipenem at higher rates than native OXA-48.[242] The specific role of Arg214 (in the β5-β6 loop) was studied by comparing hydrolysis kinetics and crystal structures of OXA-181 and OXA-232, the difference between these two variants being residue 214 (Arg in OXA-181, Ser in OXA-

232).[243] OXA-181 is a slightly better carbapenemase than OXA-48,[229] whilst OXA-232 has decreased carbapenem hydrolysis rates but has also acquired weak activity against ceftazidime (Table 4.1).[244] The authors suggest that the presence of Arg214 is crucial for carbapenem hydrolysis by OXA-48, as it aids in the formation of a productive binding pose for imipenem. Replacing this arginine with a negatively charged residue (Glu) results in poor affinity, which was reasoned to be due to unproductive binding pose of imipenem (both hypotheses based on molecular docking). Similar results were found by Dabos *et al.*, who substituted the β5-β6 loop of OXA-18 into OXA-48.[245] Steady-state kinetics of the OXA-48loop18 variant showed decreased ampicillin and imipenem hydrolysis and elevated ceftazidime hydrolysis. The importance of the β5-β6 loop for the hydrolysis profile indicated by these studies is further emphasized by the decrease in imipenem hydrolysis and increase in ceftazidime hydrolysis in OXA-163 (Table 4.1),[226, 230] in which the loop is partially deleted (Figure 4.1). Pre-steady state kinetics indicate that the loss of efficient imipenemase activity in OXA-163 is due to decreased deacylation rates.[233] However, even though the β5-β6 loop is evidently important for carbapenem hydrolysis, the specific origin of imipenemase activity in OXA-48 enzymes (e.g. over meropenem hydrolysis) remains to be investigated. The presence of the 1β-methyl group e.g. in meropenem and doripenem (instead of the 1β-proton in imipenem) has been suggested to impair hydrolysis, as this methyl group might prevent deacylation by disfavoring rotation of the carbapenem 6α-hydroxyethyl moiety (attached to C6, Figure 4.5), which would in turn prohibit the nucleophilic attack.[240] In all OXA-48/carbapenem crystal structures (excluding 5QB4), the 6α-hydroxyethyl sidechain adopts a similar orientation where its methyl group points towards Leu158 and Arg214 and values for the C7-C6-C-O dihedral angle are between 147°-192° (Figure 4.7). However, for hydrolyzed imipenem this orientation has changed, and the methyl group points out of the active site towards bulk solvent (with the same dihedral angle being between 275°-292° depending on the protein chain). As the 6α-hydroxyethyl group is likely able to rotate in the acylenzyme, verifying the extent of its influence on e.g. positioning and movement of the deacylating water remains as an important aspect for future mechanistic studies.

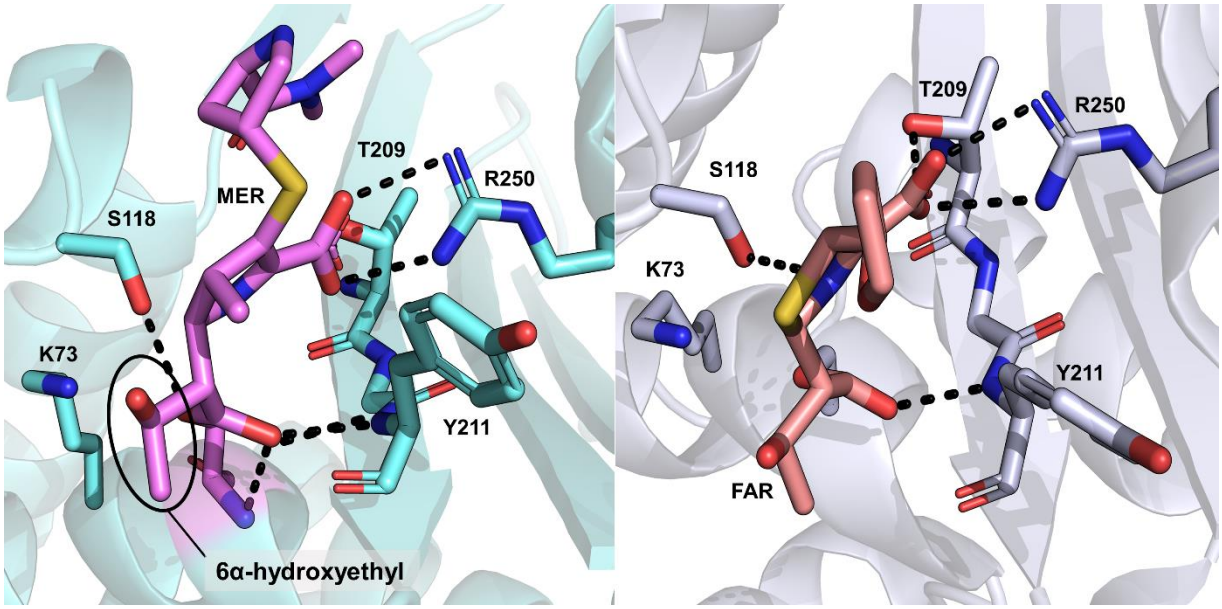

Figure 4.7. Further carbapenem complexes of OXA-48. Acylenzyme structures with meropenem (left, PDB ID 6P98)[71] and faropenem (right, PDB ID 6PSG)[240]. The pyrroline ring is present as the Δ^2 tautomer in both structures.

The pyrroline ring of carbapenem acylenzymes can exist as two different tautomers: Δ^2 or Δ^1, the latter of which also has two stereoisomers (*R*)-Δ^1 and (*S*)-Δ^1 (Figure 4.8). For class A β-lactamases, the Δ^2 tautomer has been proposed to be the catalytically competent form,[246, 247] and the Δ^1 to not deacylate efficiently (potentially due to displacement of the deacylating water from the active site[248] or loss of stabilizing interactions with the oxyanion hole[249]). The same has been suggested for class D enzymes when comparing the doripenem complex of carbapenem-hydrolyzing OXA-24 against carbapenem-inhibited OXA-1.[250] The tautomeric form can be identified in crystal structures with sufficiently strong electron density for the ligand, as the pyrroline ring C2 – sulphur bond present in all carbapenems is planar (sp^2 hybridized) in the case of the Δ^2, and sp^3 hybridized for the Δ^1 forms. For previous class D β-lactamases complexed with carbapenems, all three tautomers have been observed.[250, 251] In the case of OXA-48, the Δ^2 form was assigned in the first deposited imipenem complex,[239] and the same tautomer was subsequently observed for the meropenem, imipenem, doripenem, and ertapenem acylenzymes published by C. A. Smith *et al.* (structures prepared by soaking crystals of apo-OXA-48 with 50 mM carbapenem solution over time scales between 30 seconds and 10 minutes).[71] The same authors inspected the possibility of accommodating ligands in the active site in the Δ^1 form by superimposition of their structures onto OXA-23 with (*R*)-Δ^1 and (*S*)-Δ^1 ligands. They suggest that the formation of the (*S*)-Δ^1 tautomer of meropenem is feasible, while

the (*R*)-Δ^1 conformer would clash sterically with Tyr211. Shortly after the publication of these carbapenem acylenzymes, a new structure of deacylation-deficient OXA-48 (Lys73Ala) in complex with doripenem was released (also prepared using crystal soaking).[241] The doripenem acylenzyme was observed as both (*R*)-Δ^1 and (*S*)-Δ^1 tautomers (Figure 4.6), and only a partial salt bridge with Arg250 is formed, which most likely prevents any severe steric clashes between doripenem and Tyr211 for either tautomer. In further structures deposited by Akhtar *et al.*, different carbapenems have different tautomers present: the meropenem acylenzyme is in the Δ^2 form (as depicted for another crystal structure in Figure 4.7), imipenem and faropenem are found as (*R*)-Δ^1 (Figures 4.6 and 4.7), and the imipenem hydrolysis product as the (*S*)-Δ^1 tautomer (Figure 4.6, structures prepared by soaking OXA-48 crystal with a solution containing the ligand for 30 minutes, or for the OXA-48 imipenem product complex for 2 hours).[240] Characterization of the enzyme-hydrolyzed products by NMR spectroscopy implies that for OXA-48 (as well as all other tested SBLs and MBLs) the preferred hydrolysis product would be either in the Δ^2 or (*R*)-Δ^1 form, but deducing the exact enzyme-catalyzed reaction product was not feasible due to the ability of released products to undergo tautomerization in solution.[252]

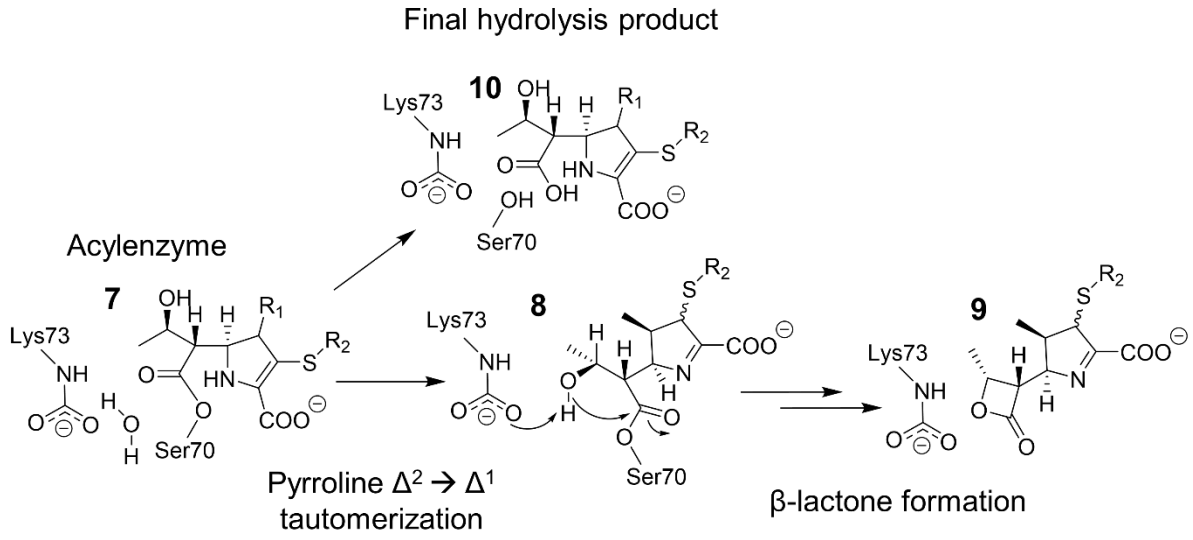

Figure 4.8. Mechanism for carbapenem side product formation by OXA-48. The pyrroline ring in carbapenem substrates can undergo $\Delta^2 \rightarrow \Delta^1$ tautomerization (7 → 8) post-acylation. In addition to the general hydrolysis mechanism (7 → 10), 1β-methyl carbapenems such as meropenem can form a 1β-lactone product (8 → 9), which has been suggested to be mainly in the Δ^1 form.[253]

In addition to the generic hydrolysis mechanism of serine β-lactamases, OXA-48 enzymes were shown to possess an additional mechanism for carbapenem breakdown that involves the formation of a β-lactone product, as illustrated in Figure 4.8.[253, 254] Starting from the acylenzyme, the β-lactone is suggested to form by intramolecular cyclization, where the hydroxyl group of the carbapenem 6α-hydroxyethyl sidechain donates a proton to the carboxylated lysine (Lys73) and attacks the same electrophilic C7 carbon as in deacylation. This results in formation of a four-membered lactone ring, which is structurally close to the original β-lactam ring and capable of reacting further to give (unidentified) reaction products. Interestingly, β-lactone formation by OXA-48 appears carbapenem-dependent, as it was observed only for 1β-methyl carbapenems (such as meropenem, doripenem, and ertapenem), but not for carbapenems with a 1β-hydrogen (imipenem and biapenem). The reason for this dependence on the presence of the 1β-substituent was studied by simulating the dynamics of OXA-1 (one 100ns simulation), and suggested to be due to more favorable conformational sampling of the 6α-hydroxyethyl sidechain: with a 1β-methyl group, bound carbapenems formed closer interactions with the carboxylated lysine, which would aid in proton transfer from the hydroxyl group to the lysine carboxylate oxygen.[253] More recently, however, lactone formation was shown to also depend upon the structure of the active site: OXA-519 (Val120Leu variant of OXA-48) demonstrated both an increase in the proportion of the lactone product as well as generated lactones from both of 1β-proton and 1β-methyl carbapenems.[254]

4.5 Cephalosporinase activity

While OXA-48 is considered of particular importance as a result of its carbapenemase activity, there are variations in hydrolytic phenotypes between different OXA-48 variants. OXA-48 itself does hydrolyze some cephalosporin antibiotics, such as cefalotin and cefotaxime, but shows no significant hydrolysis of the expanded-spectrum oxyimino cephalosporin ceftazidime or the fourth-generation cephalosporin cefepime.[226] However, variants such as OXA-163 and OXA-405 (that contain partial deletions in the β5-β6 loop) are capable of hydrolyzing ceftazidime, at the expense of efficient imipenem breakdown (Figure 4.1, Table 4.1).[230, 231] Interestingly, their hydrolysis rates for other carbapenems (such as meropenem) seem to be on the same low level as for OXA-48.

In 2019, the structure of an OXA-48 (Pro68Ala) ceftazidime acylenzyme was deposited (PDB ID 6Q5F, Figure 4.9);[255] this single point mutant was obtained by passage of a laboratory

OXA-48 producer strain against increasing concentrations of ceftazidime. Comparison of this OXA-48 structure with previously deposited OXA/ceftazidime complexes (OXA-225 and OXA-160, PDB IDs 4X55 and 4X56, respectively)[256] shows that ceftazidime exhibits a different binding pose in OXA-48 than observed in the OXA-23 or OXA-24/40 variants, the difference being in the orientation of the C7 substituents (carboxypropyl oxyimino and thiazole groups, Figure 4.5). Another distinct feature in the OXA-48/ceftazidime structure was the lack of interpretable electron density for the Ω-loop (including residues Leu158 and Asp159, Figure 4.1). The authors suggested ceftazidime binding to displace Arg214, which in turn results in a distorted (and thus flexible) Ω-loop; the Pro68Ala mutation might then contribute to Ω-loop distortion by increasing flexibility of the active site. Molecular dynamics simulations and QM/MM reaction modelling of ceftazidime deacylation by OXA-48, OXA-163, and OXA-181 suggest that in addition to the β5-β6 loop and Arg214, Leu158 could also play an important role in determining the efficiency of ceftazidime turnover.[257] The orientation of Leu158 was observed to correlate with active site hydration, and an increase in water molecules in the active site was observed to impair deacylation efficiency in OXA-48. Additionally, the study proposed that distorting the Ω-loop, as is implied by the absence of electron density for this region in the OXA-48 ceftazidime crystal structure, would fully open the active site to bulk water and diminish deacylation rates. Although some consideration has been given to the routes by which the water molecule necessary for deacylation may enter the active site,[71, 251] the importance of active site hydration to the activity of OXA-48 β-lactamases (or of SBLs in general) has to date not been extensively discussed in the literature.

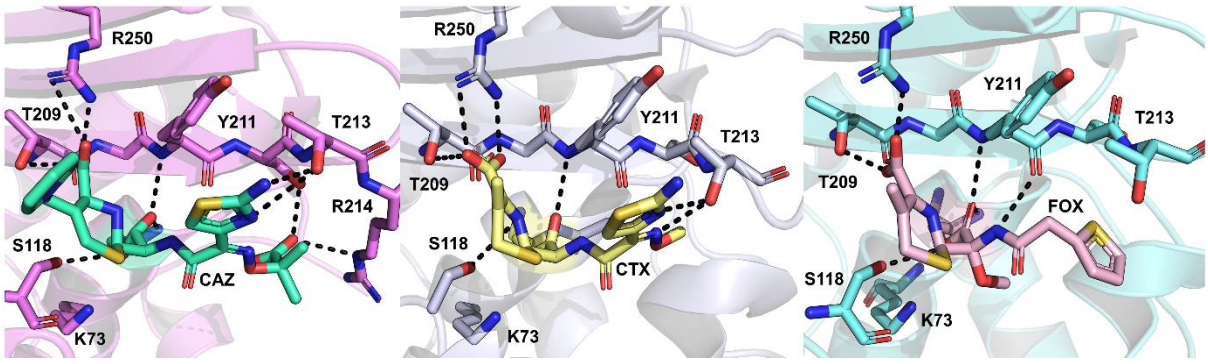

Figure 4.9. Cephalosporin acylenzyme complexes of OXA-48. Hydrogen bonds between the substrate and active site residues highlighted with dashed lines. Left: ceftazidime (CAZ, PDB ID 6Q5F)[255], middle: cefotaxime (CTX, PDB ID 6PQI)[240], right: cefoxitin (FOX, PDB ID 6PT5)[240].

In addition to ceftazidime, structures of OXA-48 acylenzyme complexes with cefotaxime and cefoxitin have also been determined (PDB IDs 6PT5 and 6PQI for cefoxitin and cefotaxime, respectively).[240] Cefotaxime has a similar binding pose to ceftazidime, where the thiazole ring orients to make stacking interactions with Tyr211 and the oxyimino group occupies a pocket between residues Leu158, Thr213, and Arg214 (Figure 4.9). Unlike the ceftazidime complexes, the Ω-loop remains ordered, as found in the apoenzyme, and the salt bridge between Asp159 and Arg214 is preserved. This is most likely due to the smaller size of the cefotaxime C7 methoxyimino group, compared to the equivalent carboxypropyl oxyimino group of ceftazidime. In the case of cefoxitin, the thiophene ring is rotated towards Leu158, breaking the Asp159-Arg214 salt bridge. Low cefotaxime hydrolysis rates are hypothesized to be due to limited access of potential deacylating water molecules to the active site, while cefoxitin hydrolysis ($k_{cat} > 0.05\ s^{-1}$ and $K_m > 200\ \mu M$, SI) is essentially hindered by the presence of its 7-α-methoxy group, which would sterically clash with any active site water molecules.[240] Additionally, carboxylation of Lys73 could lead to further steric clashes with the 7-α-methoxy group, which could increase preference for lysine decarboxylation in the presence of cefoxitin (Lys73 is decarboxylated in the crystal structure).

4.6 OXA-48 inhibitors

A common strategy for treating challenging, β-lactam resistant bacterial infections is to prescribe a β-lactam antibiotic together with a β-lactamase inhibitor.[27, 258] FDA approved antibiotic/inhibitor combinations include e.g. amoxicillin/clavulanate, piperacillin/tazobactam, ceftazidime/avibactam, and meropenem/vaborbactam.[25, 27, 33, 258] In general, OXA-48 β-lactamases are not susceptible to traditional β-lactamase inhibitors like sulbactam, tazobactam, and clavulanate (except for some exceptions like OXA-163).[259] Of the new generation β-lactamase inhibitors, avibactam[31, 32] shows efficacy against OXA-48.[34, 260] Avibactam belongs to the diazabicyclooctanone (DBO) class and exhibits broad-spectrum inhibition of SBLs. The ceftazidime/avibactam combination specifically shows promise as an effective therapy against OXA-48 producers in both *in vitro* testing and clinical practice.[219, 259, 261-263] When compared with other OXAs, it appears that DBOs such as avibactam inhibit OXA-48 better than enzymes with more hydrophobic active site residues.[36] Several crystal structures of OXA-48 with covalently-bound avibactam all show a very similar binding pose for the acylenzyme (PDB

IDs 6Q5B[255], 4WMC,[264] 4S2J[235], 4S2K[235], and 4S2N[235]), with the carbamate carbonyl positioned in the oxyanion hole (analogous to the position of the ester carbonyl carbon in β-lactam antibiotics), and the sulfonate group positioned towards motif II and Arg250 (Figure 4.10). The amide group of avibactam is positioned towards Leu158 on the Ω-loop. Based on the published OXA-48/avibactam structures, the presence of avibactam seems to favour Lys73 decarboxylation: for structures crystallized at pH 6.5 or 7.5 (PDB IDs 4S2J and 4S2K), no carboxylation was observed, and at pH 8.5 only partial occupancy of the carboxylate was seen in two out of four monomers in the asymmetric unit (PDB ID 4S2N).[235] Partial carboxylation of Lys73 was also observed in another study, where only two out of eight monomers displayed electron density for carboxylated Lys73 (PDB ID 4WMC).[264]

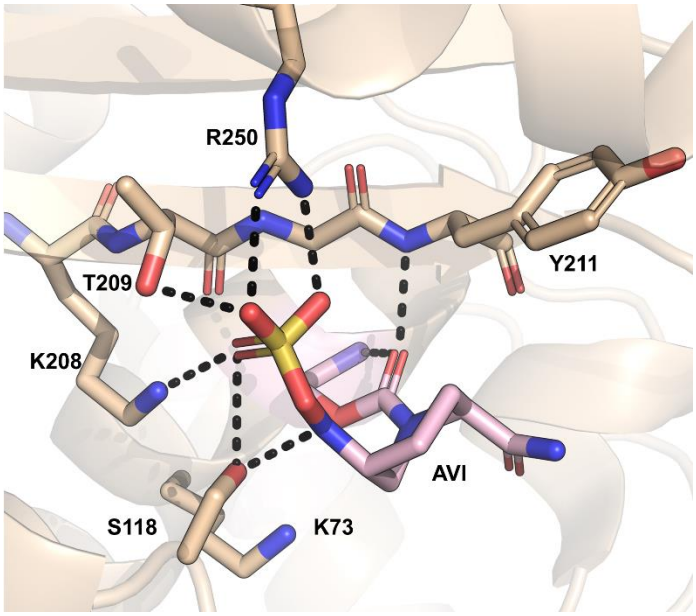

Figure 4.10. Crystal structure of the avibactam-OXA-48 acylenzyme at pH 7.5 (PDB ID 4S2K)[235].

Inhibition kinetics indicate that avibactam readily acylates OXA-48, but that its recyclization to release intact avibactam happens very slowly (whilst no analogue for the 'standard' β-lactam ring-opened hydrolysis product is observed).[264] In acylation, the C7-N6 bond in the five-membered ring structure is broken (as opposed to the C7-N1 bond, Figure 4.5), likely due to the N6-sulphate moiety being a better leaving group than N1-R group.[235] At least two different reaction mechanisms for avibactam with OXA-48 have been proposed in the literature (Figure 4.11). King *et al.* proposed a general mechanism for all SBLs, which involves a decarboxylated, neutral Lys73 acting as a general base in acylation; Lys73 would then

subsequently protonate the N6 ring nitrogen via Ser118.[235] Recyclization occurs as the reverse reaction (Figure 4.11, pathway 1). This mechanism was based on the preference for Lys73 to be decarboxylated in the presence of avibactam. Additionally, mutational studies of the class A ESBL CTXM-15 identified Lys73 to be the most likely general base in avibactam acylation.[235] Since decarboxylated Lys73 was observed to form a hydrogen bond with Ser118 (Figure 4.10), it is possible it has a similar role in class D and class A SBLs.

The second proposed mechanism for avibactam inhibition in Figure 4.11 (pathway 2) was suggested by Lahiri *et al.*; in this case, Lys73 is indicated to be carboxylated for the whole reaction cycle.[264] Carboxylated Lys73 acts as the general base in acylation, and Lys208 protonates N6 via Ser118. Recyclization takes place similarly but in reverse, where N6 first donates a proton back to Lys208 via Ser118, and Lys73 acts as a general acid protonating Ser70. As the authors also observed decarboxylation of Lys73 in the presence of avibactam, they attribute the slow avibactam recyclization rates to Lys73 decarboxylation, which hinders reactivity. In addition to these crystal structures, decarboxylation of Lys73 in the presence of covalently bound avibactam has also been measured using NMR spectroscopy.[236] The authors observed that Lys73 favors the decarboxylated form when OXA-48 is complexed with avibactam (or the related DBO inhibitors relebactam and zidebactam). The extent of Lys73 decarboxylation in reactions of OXA-48 with DBOs and its exact mechanistic role remain unclear.

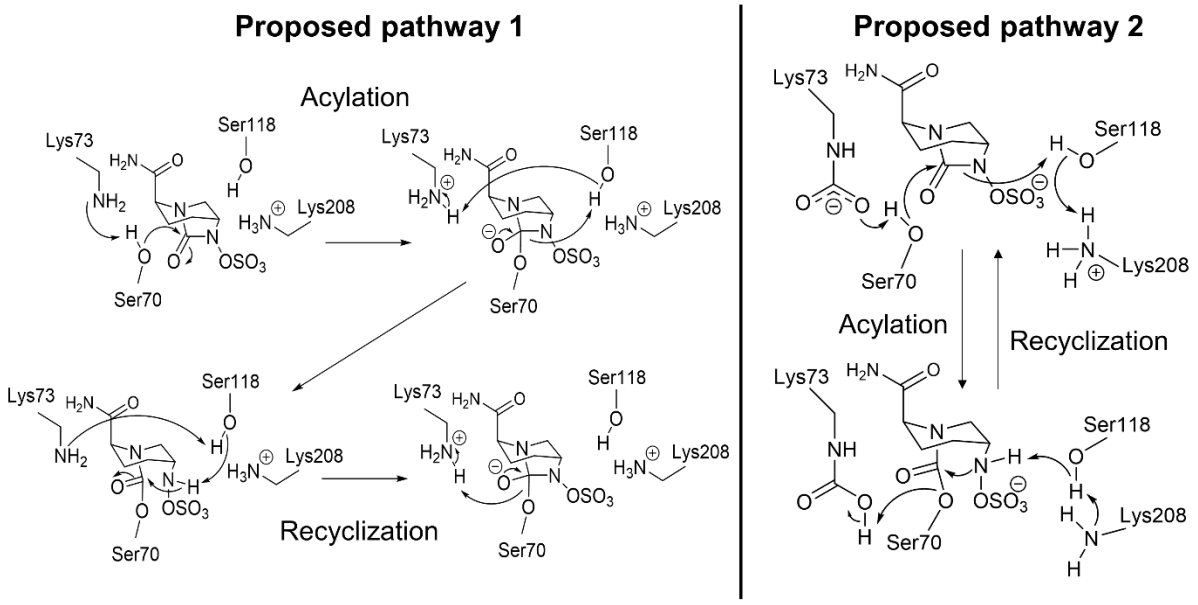

Figure 4.11. Two proposed reaction pathways for the avibactam inhibition mechanism with OXA-48. Left: Pathway 1, based on a "universal" avibactam reaction scheme for SBLs, adapted from ref. [235]. Neutral Lys73 is suggested to act as a general base in acylation and recyclization, whilst Ser118 (de)protonates the ring nitrogen. Right: Pathway 2, where carboxylated Lys73 is proposed to act as the general base in acylation, and as the general acid in recyclization, adapted from ref. [264]. Ser118 has the same role as in pathway 1, except it donates a proton to Lys208 instead of Lys73 during recyclization.

To study the possible emergence of resistance to avibactam, OXA-48 producers were passaged against a combination of ceftazidime and avibactam.[255] Resistance was observed to develop as a result of two amino acid substitutions: Pro68Ala (as discussed above in the section "Cephalosporinase activity"), and Tyr211Ser. The catalytic efficiency of ceftazidime turnover increased >10-fold and >20-fold for the single and double substituted variants, respectively. Inhibitory activity of avibactam stayed on the same level as for OXA-48 for the Pro68Ala variant, but for Pro68Ala/Tyr211Ser the activity of avibactam decreased >5-fold. Tyr211 is known to be a key residue in stabilizing tetrahedral intermediates in β-lactam hydrolysis through the formation of an oxyanion hole (together with the backbone amide of Ser70). Additionally, Tyr211 was suggested to possibly aid in the formation of a Michaelis complex. Notably, however, the observed evolutionary trajectory towards ceftazidime/avibactam resistance comes at a fitness cost, as the enzyme thermostability is reduced and the primary hydrolysis phenotype (carbapenemase/penicillinase) is compromised.[255]

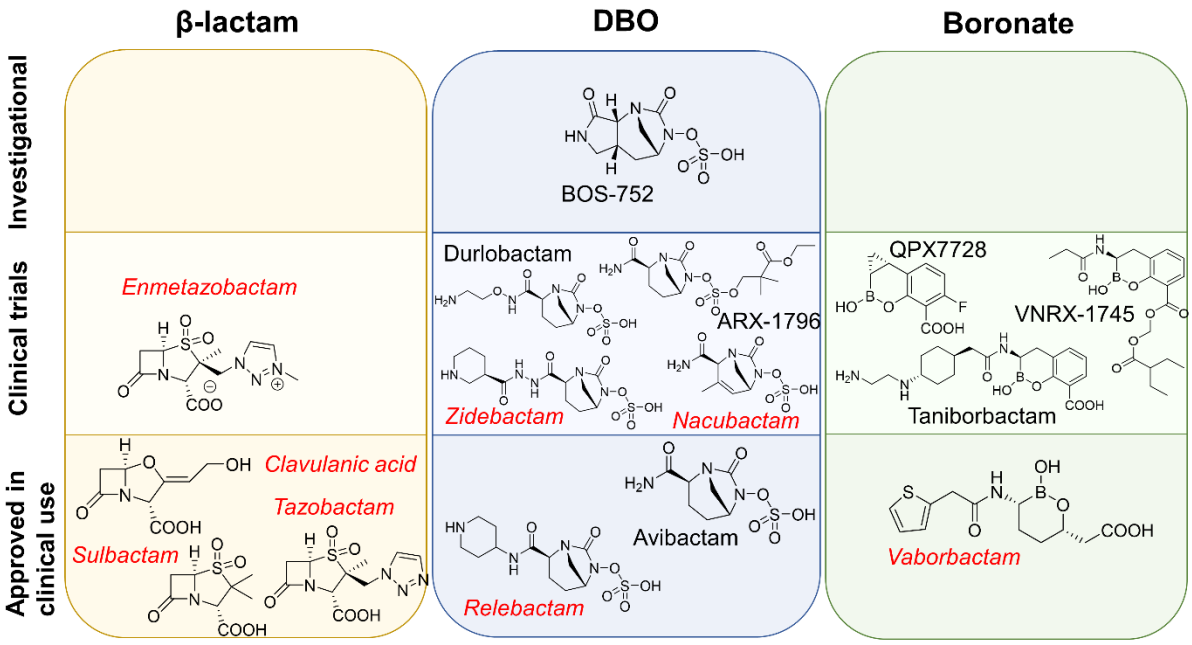

Figure 4.12. Examples of β-lactamase inhibitors in different inhibitor classes: β-lactam ring-based inhibitors, DBO = diazabicyclooctanones, and boronates, each block divided into investigational compounds (top), compounds in clinical trials (middle), and inhibitors approved in clinical use (bottom). Inhibitors in red and cursive do not effectively inhibit OXA-48, inhibitors in black show inhibitory activity.

Other β-lactamase inhibitors with a DBO scaffold include relebactam, nacubactam, zidebactam, durlobactam (previously ETX2514), ARX-1796 and the investigational compound BOS-752 (Figure 4.12). The relebactam/imipenem combination has been approved for clinical use, but this inhibitor does not effectively inhibit OXA-48; measured MICs for carbapenems do not change (or change only slightly) in the presence of relebactam.[265-267] Based on MICs, zidebactam combined with cefepime shows inhibitory activity against OXA-48.[268] This is due to OXA-48 inhibition by cefepime, as *in vitro* kinetics indicate that zidebactam on its own does not inhibit OXA-48.[37] Similarly, nacubactam inhibits class A and C SBLs, but *in vitro* data on its activity against OXA-48 are sparse. In MIC tests, bacterial isolates expressing OXA-48 were susceptible to aztreonam/nacubactam and cefepime/nacubactam, but the potentiation of antibiotic activity by nacubactam was concluded to be mainly due to inhibition of co-expressed ESBLs and AmpC β-lactamases.[269] Durlobactam was originally developed to combat infections involving OXA enzymes in *Acinetobacter baumannii*,[36] and this compound inhibits OXA-48 effectively irreversibly (as well as class A and C SBLs): in MIC tests, durlobactam

restored imipenem potency against OXA-48 better than avibactam.[35] Durlobactam is currently in Phase III clinical trials in combination with sulbactam.[4] New β-lactamase inhibitors utilizing the DBO scaffold have been synthesized by substituting the avibactam C2 carboxamide (Figure 4.5) with new functional groups.[37, 270] The size of the C2 substituent appears to correlate with β-lactamase inhibitory activity: new DBO compounds with larger C2 groups (with respect to avibactam) have approximately an order of magnitude slower on-rates and faster off-rates for OXA-48.[270] However, the studied derivatives with larger C2 substituents inhibit PBPs in bacterial cells. OXA-48 complexes with avibactam derivatives (PDB IDs 5FAQ, 5FAS, and 5FAT)[270] show essentially the same binding pose as observed for avibactam, the main differences being in the respective C2 substituents. Avibactam itself has poor oral bioavailability, but the avibactam prodrug ARX-1796 can be administered orally and subsequently metabolized in the body to produce avibactam.[271] ARX-1796 differs from avibactam through the addition of a neopentyl ester protecting group on the N6 sulfate moiety. Recent data show DBO inhibitory activity towards OXA-48 to be dependent upon the N6 substituent, as replacing the durlobactam N6 sulfate with fluoroacetate reduces potency but can form the basis for an orally available therapy.[39] Another investigational β-lactamase inhibitor in the DBO group is BOS-752, which has a third ring fused to the DBO scaffold (making it a dioxotriazatricyclohendecane).[38] BOS-752 does not possess antibacterial activity on its own, but combined with piperacillin it lowered measured MICs against SBLs including OXA-48.[38]

In addition to DBOs, other β-lactamase inhibitors currently in clinical development include mechanism-based β-lactam inhibitors and boronic acid compounds (Figure 4.12). An example of a β-lactam inhibitor is enmetazobactam, which is a penicillanic acid sulfone currently developed in combination with cefepime.[272, 273] This combination was found to be effective against OXA-48 producers, but the efficacy is most likely again attributed to the activity of cefepime and not to efficient inhibition by enmetazobactam, which is active primarily against ESBLs.[273, 274] On the other hand, boronates show promise as broad-spectrum β-lactamase inhibitors. In particular, cyclic boronates can act as analogues of the tetrahedral acylation transition state of SBLs,[41] and have potential for at least moderate activity against MBLs.[40, 275] The first boronic acid inhibitor approved in clinical use was vaborbactam (originally RPX7009),[42] which is currently administered in combination with meropenem.[43, 276] Vaborbactam is a monocyclic boronic acid compound showing inhibition mainly against class A and C SBLs, and it is not able to effectively inhibit OXA-48 based on both biochemical data and MIC measurements (potency of meropenem not restored).[265, 277] Further development

of boronic acid derivatives as β-lactamase inhibitors includes taniborbactam (VNRX-5133), which is a bicyclic boronate.[278] Based on both *in vitro* and whole cell assay data, taniborbactam exhibits pan-β-lactamase inhibition (i.e. is able to inhibit all four Ambler classes) including moderate inhibition of OXA-48 (with an IC_{50} value of approximately 0.54 μM).[44] Taniborbactam is currently in clinical development in combination with cefepime.[279] Another potent bicyclic boronate with ultrabroad-spectrum β-lactamase inhibition is the compound QPX7728, which can efficiently inhibit carbapenem-resistant *Enterobacterales* and restore the potency of meropenem against OXA-48.[45, 280] QPX7728 entered Phase I clinical trials in December 2020.[281, 282] VNRX-7145, which is orally bioavailable, also demonstrates OXA-48 inhibition and has entered Phase I clinical trials in 2020 combined with ceftibuten.[22, 283, 284] In addition to boronates, other cyclic compounds mimicking the tetrahedral intermediate (such as phosphonates, sulfonates, and sulfonamides), may also provide a source of future inhibitors, but these are yet to be explored in detail.[41] Growing appreciation of the clinical importance of OXA-48 has also motivated exploration of other routes to inhibitors, such as the use of DNA-encoded libraries, but these too remain at an early stage.[285]

4.7 Conclusions

Carbapenem-hydrolyzing *Enterobacterales* are classified as an urgent global threat to modern medicine, while OXA-48 β-lactamases are endemic in some regions (especially Turkey and the Mediterranean) and continue to disseminate. In general, OXA-48 enzymes convey penicillin and low-level carbapenem resistance; their weak carbapenem hydrolysis often complicates diagnosis and subsequent treatment of infections involving OXA-48 producers. Most variants within the OXA-48 family are imipenemases with slow turnover rates for other carbapenems, and resist established mechanism-based β-lactam inhibitors. However, certain variants (such as OXA-163 and OXA-405) have acquired a more ESBL-like hydrolysis profile with activity against expanded spectrum oxyimino-cephalosporins (such as ceftazidime) and significantly decreased imipenemase activity. The extent to which further evolution of the OXA-48 scaffold towards genuinely broad-spectrum activity is possible remains to be established.

Recent crystallographic efforts have yielded structures of acylenzyme complexes of OXA-48 not only with clinically relevant carbapenem and cephalosporin substrates, but also with new generation DBO inhibitors (avibactam). These supply much new information

regarding the interactions of substrates and inhibitors with the OXA-48 active site, including the importance of active site structure (specifically the Ω-loop), hydration and, with respect to carbapenems, rearrangements such as tautomerization and lactone formation that occur after β-lactam cleavage. The origin of preferential activity towards imipenem over other carbapenems, however, remains to be verified. Importantly, structural data for other OXA-48-like enzymes has started to emerge too, which is important to increase understanding of how substitutions affect specificity across the enzyme group. Combining knowledge from biochemical characterization, X-ray crystallography as well as atomistic computational modelling will likely lead to a detailed picture of the origin of activity and specificity in OXA-48 enzymes, ultimately benefitting design of inhibitors effective against this widespread and variable β-lactamase family.

Chapter 5 – Small changes in hydration determine cephalosporinase activity of OXA-48 β-lactamases

This chapter contains the article titled "Small changes in hydration determine cephalosporinase activity of OXA-48 β-lactamases" published in ACS Catalysis in 2020.[257] The aim of this article is to compare ceftazidime hydrolysis for selected OXA-48 β-lactamases, which are either known to be cephalosporin-inhibited or cephalosporinases, to illustrate any possible determinants behind efficient ceftazidime breakdown. A comparison of OXA-48 (inhibited) and OXA-163 (cephalosporinase) reveals active site hydration to be a key factor correlating with the calculated free energy barriers: increased hydration near the catalytic base (carboxylated Lys73) impairs catalysis by raising the energy barrier. I performed all the simulations and analysed the data together with my co-authors. I also wrote the original draft of the manuscript, and others provided comments and text editing at later stages. Section 5.6 comprises the Supporting Information data for this article.

5.1 Abstract

β-lactamase mediated antibiotic resistance threatens treatment of bacterial infections. OXA-48 enzymes are clinically important class D serine β-lactamases (SBLs) that confer resistance to most β-lactam antibiotics, including carbapenems. However, OXA-48 and related enzymes vary widely in their activity towards different substrates: OXA-48 primarily hydrolyzes carbapenems, whereas the OXA-163 variant is a cephalosporinase with minimal carbapenemase activity. The basis of cephalosporinase activity in OXA-163 remains elusive. Here we use QM/MM reaction simulations (umbrella sampling molecular dynamics) to study breakdown of the cephalosporin antibiotic ceftazidime, a key antibiotic for healthcare-associated infections, by selected OXA-48 variants. Calculated free energy barriers for ceftazidime deacylation correctly capture the differing catalytic efficiencies of the studied enzymes and identify the catalytically competent orientation for bound ceftazidime. Additionally, we show that high flexibility of the Ω-loop bordering the active site, a determinant of specificity in many SBLs, is not required for efficient deacylation. Based on our simulations, cephalosporin breakdown in OXA-163 is efficient due to subtle control of active site solvation, which requires a particular orientation of Leu158 in the Ω-loop. Our simulations

further predict that a single mutation in the OXA-48 β5 - β6 loop (Arg214Ser) will increase the efficiency of ceftazidime deacylation to that of OXA-163. The finding that the hydration of the general base in the active site determines deacylation efficiency is possibly important in other class D β-lactamases.

5.2 Introduction

Antimicrobial resistance is a complex phenomenon requiring urgent global action.[286, 287] For example, it is estimated that if no preventive measures are taken, antibiotic resistance will result in 10 million deaths annually by 2050.[206] From their initial clinical introduction in the 1940s, β-lactam antibiotics remain the most important drugs for treating bacterial infections.[18] They are the oldest and largest group of commercially available antibiotics, and have undergone continuous development, but their efficacy is threatened by growing resistance especially in Gram-negative bacteria, in which breakdown by β-lactamase enzymes are the major resistance mechanism.[49] β-lactamases hydrolyze β-lactams by opening the β-lactam amide, which inactivates the antibiotic as it prevents binding to its bacterial transpeptidase target.[208]

According to the Ambler classification, β-lactamases can be divided into four classes based on specific sequence motifs. Classes A, C and D are serine β-lactamases (SBLs), and class B zinc-dependent metallo-β-lactamases (MBLs).[63] Serine β-lactamases have an active site serine residue (part of the invariant S-X-X-K motif common to SBLs and transpeptidases) that acts as the essential reaction nucleophile, whilst class B enzymes have a different mechanism that employs zinc-activated water. OXA-48 β-lactamases are class D SBLs, and are now common on mobile genetic elements (plasmids) in Enterobacteriaceae responsible for healthcare-associated infections in Europe (especially Mediterranean countries) and worldwide.[216, 288, 289] This resistance to broad spectrum β-lactams in Enterobacteriaceae is now a major public health challenge.[290] OXA-48 confers resistance to carbapenems (especially imipenem),[222, 291, 292] but some variants have acquired cephalosporinase activity (especially against the oxyiminocephalosporin ceftazidime) through amino acid deletions and substitutions.[226] For example, OXA-163 has increased cephalosporinase and decreased carbapenemase activities; it differs from OXA-48 by four amino acid deletions and one substitution in the β5 - β6 loop that borders the active site (Figure 5.1).[230]

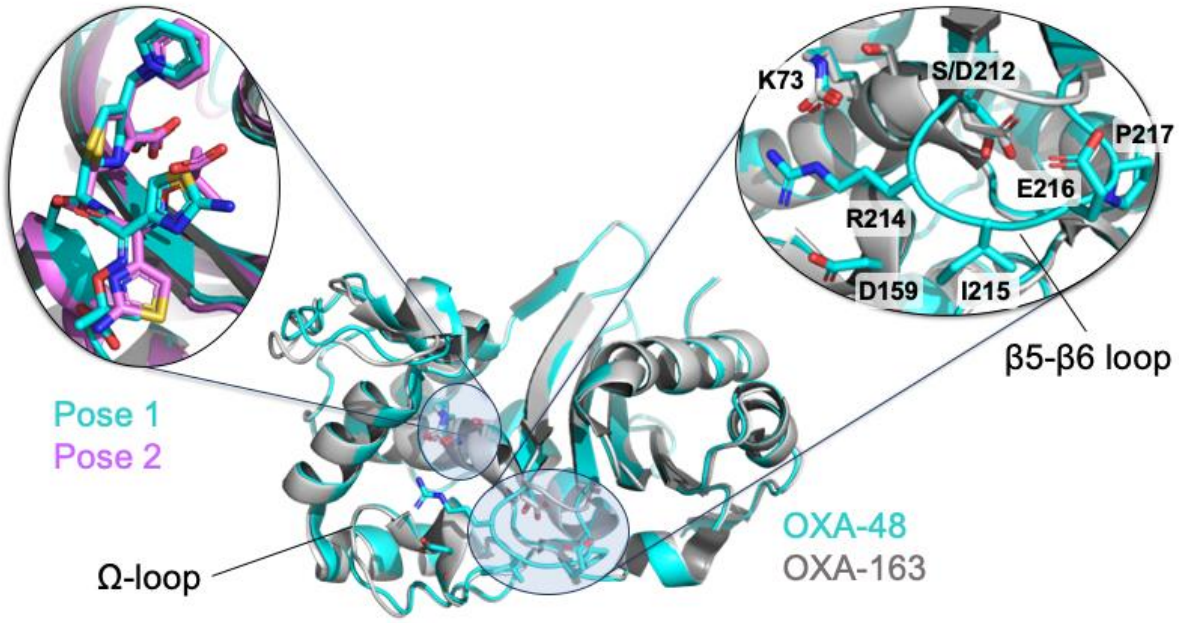

Figure 5.1 Comparison of class D β-lactamase structures. Left inset: Comparison of two OXA-ceftazidime acylenzyme crystal structures, where the ceftazidime binding pose differs. For OXA-48 (PDB: 6Q5F), the ceftazidime oxyimino group is between the β5 - β6 and Ω*-loops (binding pose 1 in turquoise),[255] whilst for OXA-225 (PDB: 4X55),[256] this space is occupied by the thiazole ring (binding pose 2 in purple). Right inset: Apoenzyme structures of OXA-48 (turquoise, PDB:4S2P) and OXA-163 (gray, PDB: 4S2L) showing the partly deleted β5 - β6 loop (R214-P217) and the S212D mutation in OXA-163 with respect to OXA-48.*

The hydrolysis mechanism of serine β-lactamases consists of acylation and subsequent deacylation;[49] between these two reactions the antibiotic is covalently bound to the enzyme via the active site Ser70. Both acylation and deacylation involve formation of a tetrahedral intermediate (TI) via attack of a nucleophile upon the carbonyl carbon of the scissile bond. In the acylation reaction the unstable tetrahedral intermediate (TI) collapses to form the covalent acylenzyme intermediate (AE); after TI formation in the deacylation reaction, turnover is completed when the hydrolyzed drug is cleaved from the enzyme (the complete hydrolysis reaction is illustrated in scheme S1 in Section 5.6). Often only the first step in deacylation needs to be modelled to distinguish β-lactamase activities, as this is frequently the rate-limiting step in hydrolysis.[190, 202] Furthermore, β-lactamases are inhibited when the AE intermediate persists, with high energetic barriers for deacylation. For class D enzymes, a carboxylated lysine (Lys73) acts as a general base in both acylation and deacylation;[234] in deacylation, the base abstracts a proton from an active site water molecule (deacylating water, DW), allowing

the DW to act as a nucleophile and attack the electrophilic carbonyl carbon (C8) of the AE (Scheme 5.1).

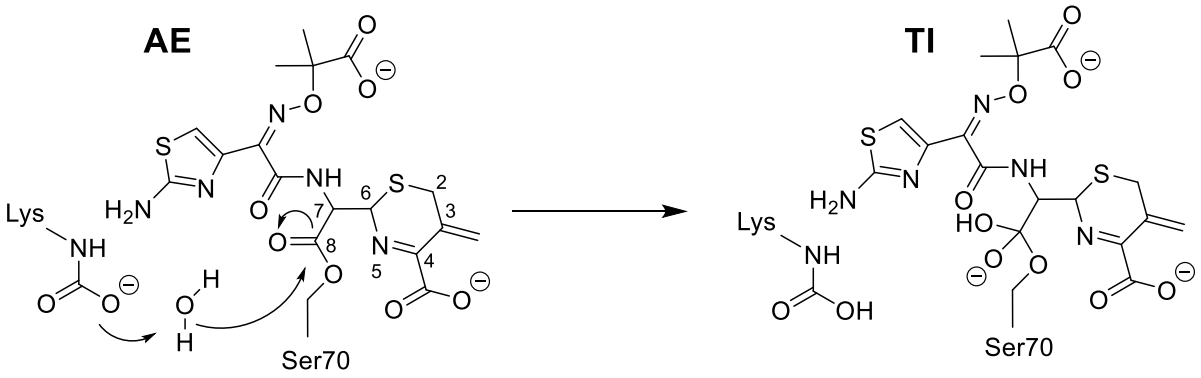

Scheme 5.1. Tetrahedral intermediate formation in ceftazidime deacylation. AE=acylenzyme, TI=tetrahedral intermediate.

The structural determinants of cephalosporinase activity in OXA-48 and its variants remain unclear. The β5 - β6 loop near the active site has been demonstrated to be important for carbapenem breakdown,[242] and most likely has some effect on cephalosporin hydrolysis e.g. by limiting available space in the active site. It has been suggested that the cephalosporinase phenotype of OXA-163 originates from increased enzyme flexibility due to the loss of two salt bridge interactions upon amino acid deletions.[293] Cephalosporin breakdown was also studied by Fröhlich *et al*., where serial passage of OXA-48 producers against ceftazidime resulted in a single amino acid mutation (Pro68Ala).[255] Based on crystal structures of the ceftazidime AE, the authors hypothesize that upon ceftazidime binding and hydrolysis in OXA-48, Arg214 (part of the β5 - β6 loop) is displaced, thus breaking the salt bridge between Arg214 and Asp159 (part of the Ω-loop that is a major determinant of substrate binding and specificity across multiple β -lactamase classes). The Pro68Ala substitution was in turn reasoned to facilitate ceftazidime binding, and subsequent loop displacement, by providing more flexibility in the active site. Notably, similar results have been observed with two other class D carbapenemases, OXA-23 and OXA-24/40. Two of their subfamily members, namely OXA-160 (a variant of OXA-24/40) and OXA-225 (a variant of OXA-23), have single proline to serine substitutions (Pro225Ser and Pro227Ser, respectively)[256] that enhance their hydrolytic activities against oxyimino cephalosporins e.g. ceftazidime and cefotaxime. Interestingly, however, comparison of the crystal structures shows two different binding poses for ceftazidime in OXA-48 and OXA-225. For OXA-48, the ceftazidime C7 substituent, including the oxyimino moiety, is

oriented towards the β5 - β6 and Ω-loops (referred to as binding pose 1), whilst for both OXA-160 and OXA-225 the thiazole ring occupies this area (binding pose 2, Figure 5.1).

Current hypotheses regarding the origin of cephalosporinase activity in OXA-163 ascribe increased hydrolysis to more favorable substrate binding made possible by residue deletions near the active site. Changes in substrate binding alone, however, may not explain why ceftazidime turnover by OXA-163 is greatly increased compared to OXA-48: reported ceftazidime k_{cat} values for OXA-48 range from unmeasurably low to 3 s^{-1},[226, 255] whilst those for OXA-163 range from 8 to 200 s^{-1}.[226, 230] Hence, to complement and extend existing experimental work, here we study ceftazidime breakdown by OXA-48 variants using combined quantum mechanical / molecular mechanical (QM/MM) reaction simulations. QM/MM simulations can provide a good approach to examine enzyme-catalyzed reaction mechanisms (including in β-lactamases[189, 190, 201, 247, 294]) and can identify e.g. determinants of activity and effects of mutation.[97] Starting from a covalent AE model, TI formation in deacylation (Scheme 5.1) is simulated using QM/MM umbrella sampling (US) molecular dynamics simulations, resulting in free energy barriers for this reaction for different AE complexes. Additionally, AE dynamics are simulated using classical MM molecular dynamics. Our simulations reveal that structural features of the OXA-163-ceftazidime complex impair the ability of extra water molecules to enter the active site, accelerating ceftazidime breakdown. In OXA-48, an increased number of water molecules near the carboxylated lysine decreases ceftazidime turnover. Simulations of the OXA-48 Arg214Ser point mutant identify deletion of Arg214 as the major contributor to increased ceftazidime turnover by OXA-163 as a result of desolvation of the catalytic base. Our findings suggest that reactivity of other serine β-lactamases with carboxylic acid general bases may also be modulated by changes in solvation.

5.3 Methods

Computational details and system set-up are described in detail in the Supporting Information (Section 5.6). We applied QM/MM and MD simulation protocols similar to those we have applied successfully previously to other serine β-lactamases.[189, 190, 202] In short, AE starting structures were built using the crystal structure of OXA-48 in complex with imipenem (PDB: 5QB4)[239] and replacing imipenem with ceftazidime as found in complexes with OXA-225 (PDB: 4X55)[256] or OXA-48 (PDB: 6Q5F)[255]. Starting models of the OXA-163 ceftazidime complex were built using the apoenzyme crystal structure (PDB: 4S2L)[295] and the same ceftazidime binding poses as above. A "disordered" Ω-loop model of OXA-48 was built into

the OXA-48 and ceftazidime crystal structure using MODELLER[296] as described in the Supporting Information, along with further details of system setup and non-standard residue parameter generation. All systems were initially minimized, followed by heating from 50 K to 300 K in 20 ps molecular dynamics (MD), followed by further MD for a total of 1 ns, to generate starting structures for QM/MM calculations. Four different starting structures for QM/MM umbrella sampling (US) calculations were taken from the last 500 ps of each 1 ns run (at least 50 ps apart). We used short equilibrations prior to the umbrella sampling to ensure that there are no significant changes away from the starting structures (e.g. a change in binding pose), and to test whether efficient computational 'assays' are feasible.[189] Extended MD simulations (5x 120ns) and additional QM/MM MD US simulations (one profile each) were performed for OXA-48, OXA-48 R214S and OXA-163 with the acylenzyme in binding mode 1 (see Supporting Information in Section 5.6, section "Extended MD Simulations: Stability, Loop Conformation, and Free Energy Barriers"). These simulations verified that (1) the systems remain conformationally stable over longer timescales (Figure S16, Section 5.6); (2) the R214S mutation does not cause a large shift in β5 - β6 loop conformation (Figure S17, Section 5.6); and (3) the free energy barriers obtained from QM/MM reaction simulations are not significantly affected by longer MM MD equilibration beforehand (Table S7, Section 5.6). Two-dimensional US was performed using two reaction coordinates (Figure S3, Section 5.6): one describing proton transfer between DW and the carboxylated lysine (Lys73) general base (defined as the difference in the carboxylate oxygen – proton distance and the water oxygen - proton distance), and one for the nucleophilic attack between DW and the electrophilic carbonyl carbon in the acylenzyme (oxygen-carbon distance). DFTB3[159] was used as the QM method for a QM region consisting of the reactive part of the ceftazidime acylenzyme, DW, and the carboxylated lysine (Figure S4 in Section 5.6). US was run initially for 2 ps on the whole surface, consisting of 525 US windows, and afterwards the restart files for this surface were used as starting structures for more extensive sampling. Further US was run for 20 ps in windows corresponding to an approximate minimum energy path on the surface, and for 2 ps in the rest of the windows. Calculations were done using the sander program as implemented in the AmberTools16 package.[203, 297] Results of US calculations were analysed using WHAM[186] with 21 and 25 bins for proton transfer and nucleophilic attack coordinates, respectively, and a convergence criterium of 10^{-13}. Minimum free energy paths on calculated surfaces were constructed using the MEPSA code.[298] Extended MM MD simulations of AE models were each run for 50 ns (at least five independent simulations per model, trajectory frames recorded every 40 ps) using pmemd.cuda as implemented in Amber.[299-301] Electrostatic

interaction strengths were calculated using BioSimSpace[302] with the Sire[303] biomolecular simulation program.

5.4 Results and discussion

We first set out to calculate (relative) free energy barriers for cephalosporin deacylation in OXA-48 enzymes using reaction simulations by comparing several different models of the acylenzyme complex (Table 5.1). Using QM/MM umbrella sampling molecular dynamics simulations along the two reaction coordinates (one for nucleophilic attack of the deacylating water DW and the acylenzyme and one for proton transfer from DW to the carboxylated lysine; see Methods and Figure S3 in Section 5.6), we calculated free energy surfaces and corresponding free energy barriers for the first step of the AE deacylation (i.e. TI formation, Figure 5.2). Altogether, three AE models were prepared for OXA-48 due to differences between existing crystal structures. The most recent crystal structure[255] suggests disorder in the Ω-loop, which was not observed in previous OXA-48 structures.[71, 222, 239] Additionally, prior to publication of the OXA-48:ceftazidime complex, previously available OXA:ceftazidime structures[256] indicate a different binding pose for the substrate from that observed in the crystallized OXA-48 complex. To establish both the effect of Ω-loop disorder on reactivity (as opposed to drug binding), and the extent of preference for a particular binding pose, three models were built: 1. OXA-48 complex with ceftazidime AE as found in the crystal structure complex (binding pose 1, enzyme modelled as found in the imipenem complex[239]), but with the Ω-loop as in the apoenzyme structure; 2. ceftazidime AE oriented as in the OXA-225 complex structure (binding pose 2) with the same apoenzyme Ω-loop as in model 1; and 3. 'disordered' Ω-loop constructed using MODELLER[296] and AE as in OXA-48 and ceftazidime complex (binding pose 1). Two models with the different ceftazidime binding poses 1 and 2 were also prepared for OXA-163, but no model with a disordered Ω-loop (as there is no evidence of Ω-loop distortion for this enzyme). Models for OXA-48 and OXA-163 are illustrated in Figure S1 in the Supporting Information (Section 5.6). Two models equivalent to those generated for OXA-163 were also prepared for OXA-181, which has a similar resistance phenotype to OXA-48.[229, 259]

5.4.1 Comparison of the binding poses

Comparison of $\Delta^{\ddagger}G_{calc}$ values for formation of the TI in ceftazidime deacylation shows that the orientation of the bulky ceftazidime C7 substituents has a large effect on overall hydrolysis. AE models constructed with ceftazidime oriented as in the OXA-225 co-crystal structure (binding pose 2, Figure 5.1), in which the thiazole ring is positioned between the Ω- and β5 - β6 loops, yield relatively high $\Delta^{\ddagger}G_{calc}$ values of 19.0 and 16.0 kcal/mol for OXA-48 and OXA-163, respectively. This is a large increase over $\Delta^{\ddagger}G_{calc}$ values for the binding pose observed in the OXA-48 structure (binding pose 1), with deacylation barriers for these models are 12.5 and 7.3 kcal/mol for OXA-48 and OXA-163, respectively. Deacylation barriers for OXA-181 are similar albeit slightly lower to OXA-48 (17.9 kcal/mol for binding pose 2, 11.1 kcal/mol for binding pose 1). We note that the absolute values of the barriers are underestimated when compared to rates of turnover, due to the approximate semi-empirical QM method used. Benchmarking calculations against DFT and *ab initio* methods (M06-2X & SCS-MP2; see Supporting Information, section "Benchmarking") indicate that the use of DFTB3 may lead to underestimation of (at least) 7 kcal/mol. The reaction mechanism is similarly concerted with DFTB3 or more accurate DFT treatment (indicated both by M06-2X and BLYP small model transition state optimizations and a M06-2X corrected DFTB3/MM potential energy profile; see Figures S5 and S6, Table S2 in Section 5.6). The relative differences in our semi-empirical free energy barriers, therefore, give a good indication of the reaction feasibility. The consistently and significantly higher barriers for binding pose 2 compared to binding pose 1 (at least 6.5 kcal/mol), indicate that for all three OXA-48 variants studied, binding pose 1 is more competent for deacylation. Further, it is highly likely that binding pose 1 is also the thermodynamic minimum for the acylenzyme conformation, as it is found in the X-ray structure of OXA-48 and it remains in this pose in extended MD simulations of the solvated enzyme (see Supporting Information in Section 5.6, "Extended MD Simulations: Stability, Loop Conformation and Free Energy Barriers"). Any correction for a difference in free energy between poses 1 and 2 should therefore be in favor of binding pose 1. The fact that the acylenzyme pose found in a homologous enzyme (binding pose 2, found in OXA-225, which has 41% sequence identity to OXA-48) is not likely to undergo deacylation highlights the importance of determining AE crystal structures for specific OXA families and family members as a prerequisite for analyzing and understanding catalytic turnover. An assumption that the ceftazidime conformation observed in the OXA-225 complex structure (binding pose

2) indicates the conformation found in OXA-48 would result in calculated barriers that are too high, and thus inconsistent with experimental assays.

5.4.2 Comparison of OXA-48 variants

For binding pose 1, a consistent difference of approximately 5 kcal/mol is seen between OXA-48 (with an ordered Ω-loop) and OXA-163 (Figure 5.2); the same trend as for OXA-48 is also observed for OXA-181. As OXA-163 has moderate cephalosporinase activity, whereas OXA-48 has essentially no activity against ceftazidime, this difference is consistent with experimental observations (Table 5.1).[226] Based on our previous work on class A β-lactamases, we would expect semiempirical DFTB methods to underestimate the magnitude of deacylation barriers, which would explain the deviation of calculated $\Delta^{\ddagger}G_{\text{calc}}$ values from deacylation barriers determined from the experimental k_{cat} values using transition state theory.[189] As illustrated in the Supporting Information (Table S1 in Section 5.6), differences in calculated barriers obtained by shorter sampling (only 2 ps sampling per umbrella sampling window, without equilibration) are minor (< 0.5 kcal/mol difference). This indicates that cephalosporinase activity of OXA-48-like enzymes could be assayed by efficient QM/MM protocols in a similar fashion to carbapenem turnover by class A carbapenemases.[189, 190]

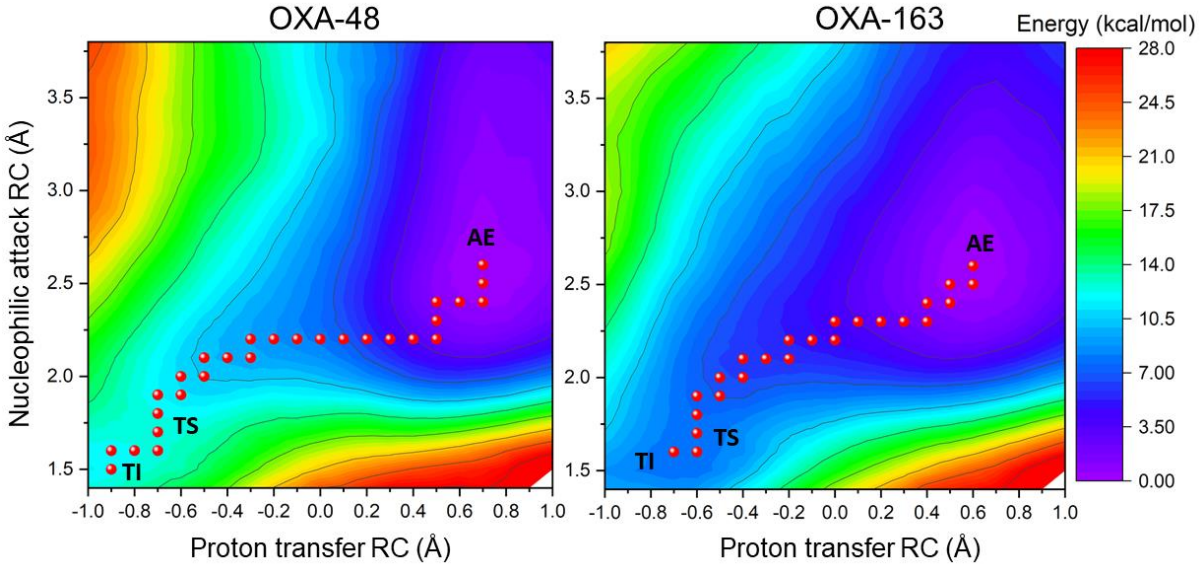

Figure 5.2 Calculated free energy surfaces for ceftazidime deacylation in binding pose 1 by OXA-48 (left) and OXA-163 (right). Red dots indicate the minimum free energy path on the surface. AE=acylenzyme, TS=approximate transition state, TI=tetrahedral intermediate.

Table 5.1 Calculated free energy barriers for deacylation for all acylenzyme models (standard deviations in parenthesis).

Enzyme	**Mutations wrt. OXA-48**	k_{cat} **(s^{-1})**[226]	$\Delta^{\ddagger}G_{calc}$ **(kcal/mol), wildtype**		
			Binding pose 1 [a]	Binding pose 2 [b]	New Ω-loop [c]
OXA-48	-	NH	12.5 (0.8)	19.0 (0.9)	>20[e]
OXA-48 R214S	R214S	-	6.9 (0.5)	14.5 (1.2)	>20[e]
OXA-163	S212D, del. R214-P217	8[d]	7.3 (0.3)	16.0 (1.8)	N/A
OXA-181	T104A, N110D, E175Q, S179A	ND	11.1 (1.3)	17.9 (0.7)	-
OXA-181 R214S	T104A, N110D, E175Q, S179A, R214S	-	6.6 (0.3)	-	-

NH = No hydrolysis detected. ND = Not determined. N/A = Not applicable (Ω-loop not present).

[a] Acylenzyme orientation as found in the crystal structure for OXA-48 with ceftazidime (see Figure 5.1).

[b] Acylenzyme as found in OXA-225 K82D structure with ceftazidime (see Figure 5.1).

[c] Ω-loop representative of a disordered loop, constructed using MODELLER as described in the Supporting Information (Section 5.6).

[d] Corresponds to $\Delta^{\ddagger}G_{exp}$ =16.3 kcal/mol, as estimated with transition state theory.

[e] Transition state could not be located on the free energy surface, with energy values rising to above 20 kcal/mol near the TI.

5.4.3 Role of the Ω-loop

Recently published crystal structures support the hypothesis that ceftazidime binding disrupts the Ω-loop in OXA-48-like enzymes.[255] We thus studied the effect of Ω-loop distortion by constructing a possible model for the "disordered" Ω-loop variant of OXA-48 *in silico*; MM MD simulations confirm that the selected starting conformation of the loop leads to high

flexibility, consistent with the lack of density for this region in structures obtained by X-ray crystallography (Supporting Information Figure S2). Notably, deacylation $\Delta^{\ddagger}G_{calc}$ values for the "disordered" Ω-loop variants show no hydrolysis for OXA-48, as free energy minima representing the deacylation TI could not be located on the calculated free energy surfaces, and therefore nor can transition states (surfaces show an increase in energy from AE to >20 kcal/mol when approaching the TI structure). This is perhaps not surprising as crystal structures tend to capture the thermodynamic minimum free energy structure, which may be catalytically deficient.[304, 305] Additionally, in the OXA-48-ceftazidime complex structure, triethylene glycol is co-crystallized in the space occupied by the Ω-loop in the apoenzyme, which might in turn contribute to the disorder and consequent lack of density for this loop in experimental crystal structures. Our simulations thus indicate that a more disordered Ω-loop conformation (different from the conformation found in the OXA-48 apoenzyme structure) is not necessary to increase the rate of deacylation and may indeed decrease it. It is possible, however, that Ω-loop disorder aids in the formation of the initial Michaelis complex and possibly acylation by expanding the active site to better accommodate ceftazidime. For example, Fröhlich *et al.* argued that ceftazidime binding is likely favoured in OXA-48 P68A due to increased Ω-loop flexibility; Ω-loop disorder was observed in the crystal structure of this variant.[17]

5.4.4. Comparison of acylenzyme dynamics

To further elucidate the reason for the difference in cephalosporinase activity in OXA-48-related enzymes, the ceftazidime AE complexes of OXA-48 and OXA-163 were studied by extended MM MD and QM/MM MD simulations. At least five independent 50 ns MD simulations of each AE model with binding pose 1 were run in order to inspect the dynamics and possible catalytically relevant interactions between ceftazidime and the protein. Additionally, 20 ps of QM/MM MD were run for selected US windows close to the calculated AE and TI minima. It is well known that interactions with an oxyanion hole,[73] in OXA-48 formed by the backbone amides of Ser70 and Tyr211,[222] stabilize TI formation in β-lactamases (similar to many other co-factor independent hydrolases). Thus, hydrogen bond distances between these residues and the ceftazidime AE were measured in both the extended MM MD and QM/MM MD simulations and are shown in the Supporting Information (S8-S11, Section 5.6). Additionally, electrostatic interactions between the quantum region (Figure S4, Section 5.6) used for QM/MM simulations and Tyr211 as part of the oxyanion hole were quantified by measuring the electrostatic interaction strength as described in the Methods section. However,

neither the distance nor the electrostatic analyses reveal any significant difference between OXA-48 (disordered/ordered Ω-loop), and OXA-163. Electrostatic interactions of each enzyme with the modelled TI show the measured stabilization to be similar in all systems tested (Figure 5.3). Hence, our simulations do not provide evidence that enhanced ceftazidime hydrolysis by OXA-163 is a result of stronger stabilizing interactions in the oxyanion hole than take place in OXA-48. The population of different ceftazidime conformers was also investigated using clustering analysis of the sampled AE orientations; this revealed that variation in ceftazidime orientations in the different enzymes is largely confined to the oxyimino group, which interacts mainly with bulk solvent (details of clustering can be found in Section 5.6, Figure S8). These data indicate that increased ceftazidime hydrolysis by OXA-163 is unlikely to be due to a more favorable orientation of the AE that results from partial deletion of the β5 - β6 loop.

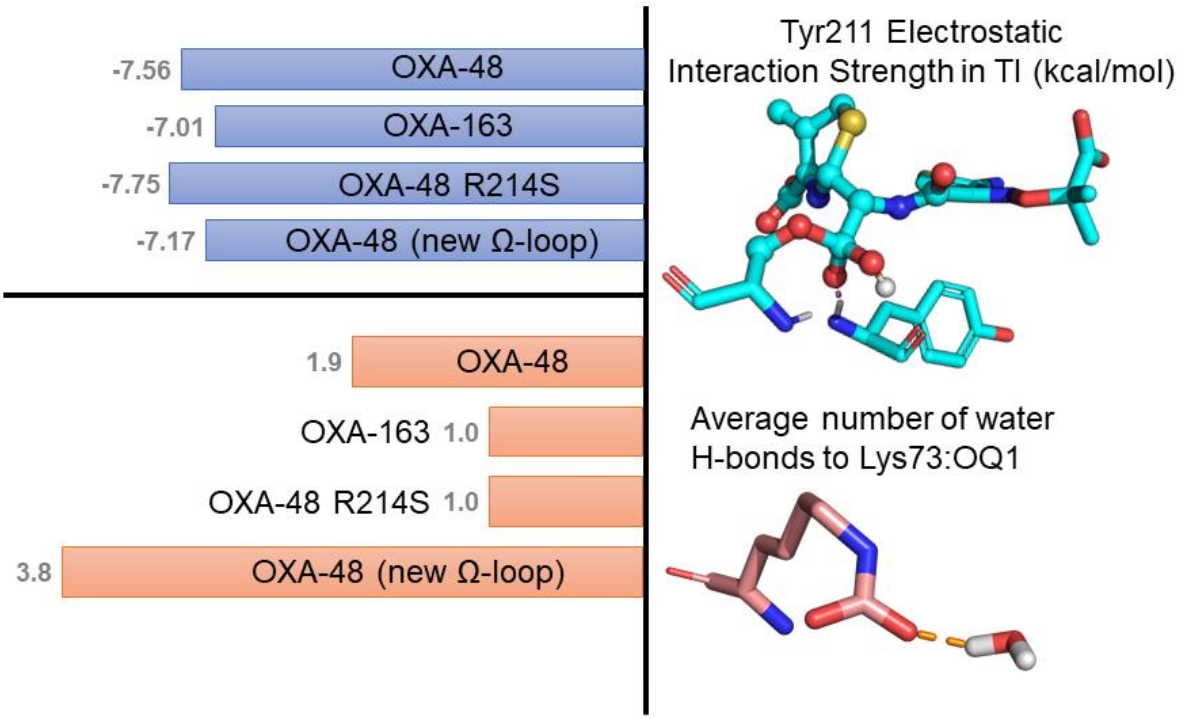

Figure 5.3 Top: Oxyanion hole interaction strength in the tetrahedral intermediate structure between the QM region and Tyr211 residue (the ceftazidime atoms part of the QM region are depicted with ball and sticks, and relevant MM atoms in licorice). Bottom: Average number of hydrogen bonds between the carboxylated lysine OQ1 oxygen and solvent water molecules measured from the acylenzyme structures in US reaction simulations.

5.4.5 Role of Leu158

One structural difference apparent from the OXA-48 and OXA-163 MD simulations is the rotation of Leu158 in the Ω-loop. The C-Cα-Cβ-Cγ (χ_1) dihedral angle for Leu158 in the starting models is approximately 170°, and in OXA-48 it rotates to around 50° (i.e. it changes from t to g+ according to the leucine rotamer naming convention; see Supporting Information Figures S14 and S15 in Section 5.6). This rotation happens both in the short 1 ns MD simulation used for generating starting structures for US, and in most of the 50 ns MD trajectories (for OXA-48, a total of seven 50 ns trajectories were run, Leu158 rotation was seen in five of these). For OXA-163, Leu158 rotation was not seen in the short 1 ns trajectory, but it was occasionally observed in the longer 50 ns simulations. However, OXA-48 samples this rotated Leu158 orientation (g+) more than OXA-163, as well as the orientation around 290° (g-)**.** In the distorted Ω-loop variant of OXA-48, Leu158 is part of the newly constructed loop and is thus free to move in the disordered structure. Another structural feature that distinguishes OXA-48 is formation of a salt bridge between Asp159 and Arg214, as Arg214 is one of the residues deleted in OXA-163. This salt bridge extends "over" the active site from the β5-β6 loop to the Ω-loop and is present in the apoenzyme crystal structures of OXA-48 as well as in some complexes with different substrates.[71, 222, 226] In starting structures for simulations of OXA-48, Arg214 is initially rotated towards bulk solvent (thus breaking the salt bridge) in order to avoid any possible steric clashes in the AE starting model, but it (re-)forms a salt bridge with Asp159 upon simulation either during or soon after the heating phase.

Importantly, in MM MD trajectories and in QM/MM US simulations, rotation of Leu158 correlates with the number of solvent molecules present around the carboxylated lysine (Lys73). Accordingly, we inspected possible differences in active site solvation by measuring the average number of hydrogen bonds formed between the carboxylated lysine oxygens (OQ1 as the proton acceptor in deacylation, and OQ2) and possible active site water molecules. In OXA-48 MM MD trajectories where Leu158 rotates (five out of seven 50 ns simulations), OQ1 forms on average 1.64 ± 0.17 hydrogen bonds (with standard deviation) with a solvent molecule. This is a large increase over the OXA-48 trajectories where Leu158 does not rotate (two 50 ns simulations), in which the average number of hydrogen bonds to OQ1 drops to 1.09 ± 0.12. In the simulations of OXA-163 (five 50 ns simulations), lysine OQ1 forms on average 1.20 ± 0.14 hydrogen bonds. This indicates that the hydrogen bonding environment around the general base differs between the ceftazidime AEs of OXA-48 and OXA-163. This difference is also observed in US simulations. For OXA-163, lysine OQ1 is hydrogen bonded only to the

DW during US, whereas for OXA-48, Lys73:OQ1 forms a hydrogen bond both to the DW and to an additional water molecule for the majority of the time (Figure 5.3 and 5.4). In the distorted Ω-loop of OXA-48, the active site is fully open for water molecules and on average 3.8 solvent hydrogen bonds are calculated (Figure 5.3). In contrast to class A β-lactamases, where both carboxylate oxygens of the general base (Glu166) form hydrogen bonds with other active site residues in a relatively organized manner,[189] the carboxylate moiety in Lys73 is hydrogen bonded only to Trp157 (Figure 5.4). Therefore, any additional water molecules hydrogen bonding to the general base can affect the reactivity of the enzyme.

5.4.6 Role of Arg214

Arg214 is one of the four residues present in the OXA-48 β5-β6 loop that is deleted in OXA-163. Its absence could play an important role in the increased cephalosporin hydrolysis in OXA-163, for example by affecting the number of hydrogen bonds between the catalytic base and water molecules. Therefore, we hypothesize that deletion of Arg214 could be an important determinant of increased ceftazidime turnover by OXA-163. However, it remains possible that the four-residue deletion in the OXA-163 β5-β6 loop is necessary to enhance initial substrate binding (i.e. Michaelis complex and subsequent acylenzyme formation). To investigate the importance of Arg214 to ceftazidime AE deacylation, we constructed an *in silico* Arg214Ser point mutant of OXA-48. Interestingly, $\Delta^{\ddagger}G_{calc}$ values for ceftazidime deacylation for this point mutant drop to the same level as those for OXA-163 (6.9 and 7.3 kcal/mol for OXA-48 R214S and OXA-163, respectively), a 5.6 kcal/mol decrease in comparison with wild-type OXA-48 (Table 5.1; this difference may be overestimated due to the simulation approach, see discussion in the next section). The calculated energetics imply that point substitution of OXA-48 Arg214 would result in an enzyme with deacylation rates comparable to those observed in OXA-163. Moreover, in OXA-48 Arg214Ser both the conformational dynamics of Leu158 and the population dynamics of active-site water molecules resemble those observed for OXA-163, rather than the wild-type enzyme (Figures S14 and S15 in Section 5.6). In the absence of the Asp159 - Arg214 salt bridge, Leu158 prefers to stay in its original orientation, as was observed for OXA-163. In the reaction simulations, again only the DW is hydrogen bonded to the reactive oxygen of the carboxylated lysine (Lys73, see Figure 5.4), with lysine OQ1 forming on average 1.08 ± 0.07 hydrogen bonds with water molecules during extended MM MD simulations of the AE (five 50 ns simulations). Mulliken charge analysis on the QM/MM reaction simulations of the different enzymes further

indicates that a difference in the environment, rather than a difference in QM region geometry, leads to a difference in electron distribution (with the DW more polarized when no additional hydrogen bonds between water and OQ1 are present, see Tables S2-S5 in Section 5.6). Therefore, we hypothesize that deletion of Arg214 is an important determinant of increased ceftazidime turnover by OXA-163, due to its effect on the Leu158 conformation which in turn changes the accessibility of water to the catalytic base.

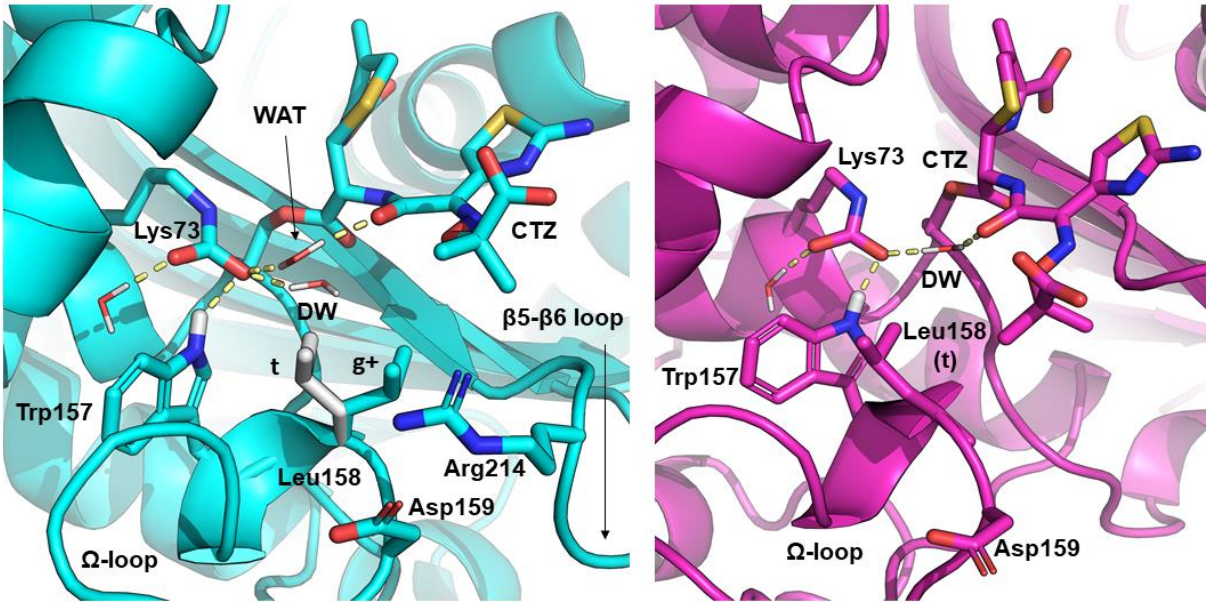

Figure 5.4 Examples of acylenzyme structures from US for OXA-48 (cyan, left) and OXA-163 (magenta, right). Water molecules within 4 Å of carboxylated lysine (Lys73) are illustrated. In OXA-48, the carboxylate oxygen participating in deacylation is hydrogen bonded with two water molecules, whereas in OXA-163 it is interacting only with the DW. Two different leucine orientations are highlighted for OXA-48: the orientation found in the apoenzyme (t), and the rotated orientation used in all reaction simulations (g+).

5.4.7 Relation between active site hydration and Leu158

To further investigate the role of active site water molecules in deacylation, and the role of Leu158, additional reaction simulations (2 ps per US window) were carried out for OXA-48 on starting structures taken from the two 50 ns MD trajectories where Leu158 does not rotate (Figure 5.3). In the chosen structures, each oxygen of the carboxylated lysine (Lys73) was hydrogen bonded to a single water molecule. The new deacylation $\Delta^{\ddagger}G_{\text{calc}}$ value was 6.5 kcal/mol for these simulations with no additional water in the active site (calculated from three

reaction simulations), a similar decrease as observed with the R214S mutation. Ergo, we hypothesize that rotation of Leu158 enables more water molecules to enter the active site, thus impairing ceftazidime deacylation by stabilizing the general base in the AE complex. Clearly, the reactivity of the carboxylated lysine is affected by the level of solvation. A reduction in hydration of key active site residues, such as the catalytic base involved in proton abstraction, also plays an important role in other enzymes. Several enzymes appear to have evolved such that water is excluded from the active site to aid in efficient catalysis of the chemical step.[306, 307] For example, in ketosteroid isomerase and triosephosphate isomerase, where proton transfer to a catalytic base is the rate-determining step, any increase in solvation of the catalytic base (e.g. due to partial opening of the active site) leads to a significant increase in barrier,[308, 309] so small changes in solvation (at the level of individual water molecules) have a significant effect on reactivity. In dihydrofolate reductase isoforms, higher catalytic rates due to enhanced dehydration appear directly related to evolution: more efficient, evolved enzymes have increased the substrate basicity (i.e. reactivity) by expelling water from the active site.[310] In the case of these other enzymes, significant loop motions are involved (e.g. triosephosphate isomerase, dihydrofolate reductase), or at least a closing of the substrate cleft (as in ketosteroid isomerase), whereas the effect found here in the OXA-48 type β-lactamases appears more subtle, primarily related to the rotational freedom of a single residue (Leu158). We note, however, that the energetic effect of an additional water molecule found here, around 6 kcal/mole, is likely to be overestimated due to the simulation approach. The additional water is modelled using TIP3P, i.e. a standard fix-point charge MM description. The lack of polarization, perhaps combined with a too short hydrogen bond, may cause this overestimation; a similar large effect was observed in potential energy profiles for ketosteroid isomerase with one additional water, treated MM, hydrogen bonding to the catalytic base.[309]

In our original US simulations for OXA-48, all the starting structures involved a rotated Leu158. Conversely, for OXA-163 all starting structures include Leu158 in the original rotamer. Interestingly, the role of water movement into the active site has recently been examined in carbapenem AE structures of OXA-48.[71] Based on these crystallized AE complexes, carbapenemase activity in OXA-48 is suggested to be largely dependent on an open "deacylating water channel", which allows water molecules to enter the active site. This water channel, consisting of Leu158 and Val120, is permanently "open" in OXA-48 and requires only slight shifts in residue positions upon carbapenem binding (unlike the case for other carbapenem-hydrolyzing Class D enzymes such as OXA-23,[251] where more substantial conformational changes are proposed to be necessary to open a water channel upon carbapenem

binding). However, our results indicate that, while water access to the active site is necessary for the deacylating water to participate in deacylation, the deacylation efficiency is also affected by the level of solvation of the carboxylated lysine. Specifically, ingress of additional solvent molecules able to readily hydrogen bond with the carboxylate moiety would reduce its basicity and thereby the deacylation reactivity.

5.5 Conclusions

Here, we have modeled ceftazidime hydrolysis by the OXA-48-family class D β-lactamase enzymes, using QM/MM reaction simulations. Our QM/MM protocol successfully distinguishes cephalosporinases (such as OXA-163) from non-cephalosporinases (such as OXA-48) by showing a consistent ~5 kcal/mol difference in calculated deacylation free energy barriers. It reveals the reactive ceftazidime AE conformation, and shows that the Ω-loop should not be disordered for efficient deacylation. This QM/MM protocol can be used for predictions of deacylation barriers (and, potentially, hydrolysis rates) for new and emerging OXA-48 mutants (as for OXA-48 Arg214Ser here). Analysis of our simulations reveals that the calculated cephalosporinase efficiency correlates with active site solvation. In OXA-48, more water molecules can hydrogen bond with the general base (carboxylated lysine), which likely stabilizes the AE intermediate and diminishes deacylation rates. Correspondingly, the absence of active site water molecules other than the deacylating water in simulations of OXA-163 and OXA-48 Arg214Ser aids deacylation. Active site solvation is influenced by the orientation of Leu158 (part of the Ω-loop), whilst the local dynamics of Leu158 and the rest of the Ω-loop are likely to be affected by the β5-β6-loop, the site of a four residue deletion in OXA-163. Our findings that active site solvation in the AE affects the reactivity may be also applicable to other OXA enzymes and potentially to other serine β-lactamases where the general base is not a part of an organized hydrogen bonding network in the active site. This study also highlights the importance of modeling enzyme dynamics to understand reactivity, as active site solvation is difficult to reliably assess from static crystal structures that rarely yield information on conformational and solvation dynamics. The combination of experimental structures with detailed computational simulation techniques employed here thus enables deeper understanding of the mechanistic details of β-lactamase-mediated resistance, as well as prediction of activities of new drug-resistant enzyme variants.[98] Ultimately, the availability of efficient and reliable reaction simulation techniques such as the QM/MM approach used here

will aid identification of new β-lactams that exploit the resulting mechanistic understanding to evade deacylation, as well as design of new mechanism-based β-lactamase inhibitors.

5.6 Computational details

This section comprises the Supporting Information for the publication presented in Chapter 5.

System Set-up and Parameterisation

OXA-48 with ceftazidime was originally set-up using OXA-48 acylenzyme structure with imipenem as the template (PDB:5QB4)[239], and by replacing imipenem with ceftazidime as found in OXA-225 K82D structure (PDB: 4X55)[256]. Upon the publication of OXA-48 P68A with ceftazidime crystal structure (PDB: 6Q5F),[255] further models were built based on the new binding pose of ceftazidime either by taking the new binding pose and combining it with the protein structure used with the first model (with the Ω-loop and β5-β6 loops as found in the apoenzyme), or by mutating the new crystal structure back to the wild-type enzyme and reconstructing the Ω-loop in a disordered state using Modeller (described below). For OXA-163 models, the apoenzyme crystal structure (PDB: 4S2L)[295] was used with both CTZ binding poses. For OXA-181, four residues were mutated with respect to the OXA-48 model, all mutations were performed using the mutagenesis wizard in PyMol (OXA-181 and OXA-48 Arg214Ser). DW was manually added to the active site for all models, and all crystallographic water molecules were kept excluding the ones clashing with the acylenzyme (closer than 2.5 Å from any acylenzyme atom). Carboxylated lysine (Lys73) was kept as found in the OXA-48 and imipenem structure, which is essentially the same as in the OXA-48 apoenzyme structure (PDB: 4S2P)[235]. To avoid any possible steric clashes between the acylenzyme and the rest of the protein, Arg214 was rotated towards bulk solvent in all starting structures. All starting structures are available to download from Supporting Information as a zip file. Ceftazidime in the acylenzyme was modelled without the pyridine ring, as its elimination has been observed experimentally.[311]

Protonation states of titratable residues were determined using propKa3.1.[167, 312] Based on the predicted pK_a values, all titratable residues were kept in their default state (all Glu/Asp

deprotonated, all Lys protonated). Histidine tautomers were predicted using reduce as implemented in the Amber program package (all histidines were singly protonated, are solvent exposed and distant from the active site). Hydrogen atoms were then added and all systems were solvated in a 10 Å box of TIP3P water using tLeap, with overall charge neutralized by replacing bulk water molecules with Na^+ ions. The ff14SB force field was used to describe the protein, and the TIP3P compatible parameters were used for the counterions.[100] Charge parametrization for non-standard residues (carboxylated lysine, KCX, and ceftazidime acylenzyme, CTZ – without the pyridine ring) was done using restrained electrostatic potential (RESP) fitting as implemented in the RED Server.[172] Missing force field parameters were taken from analogous GAFF parameters.[168] Parameter files for both fragments are available as part of the Supporting information zip file.

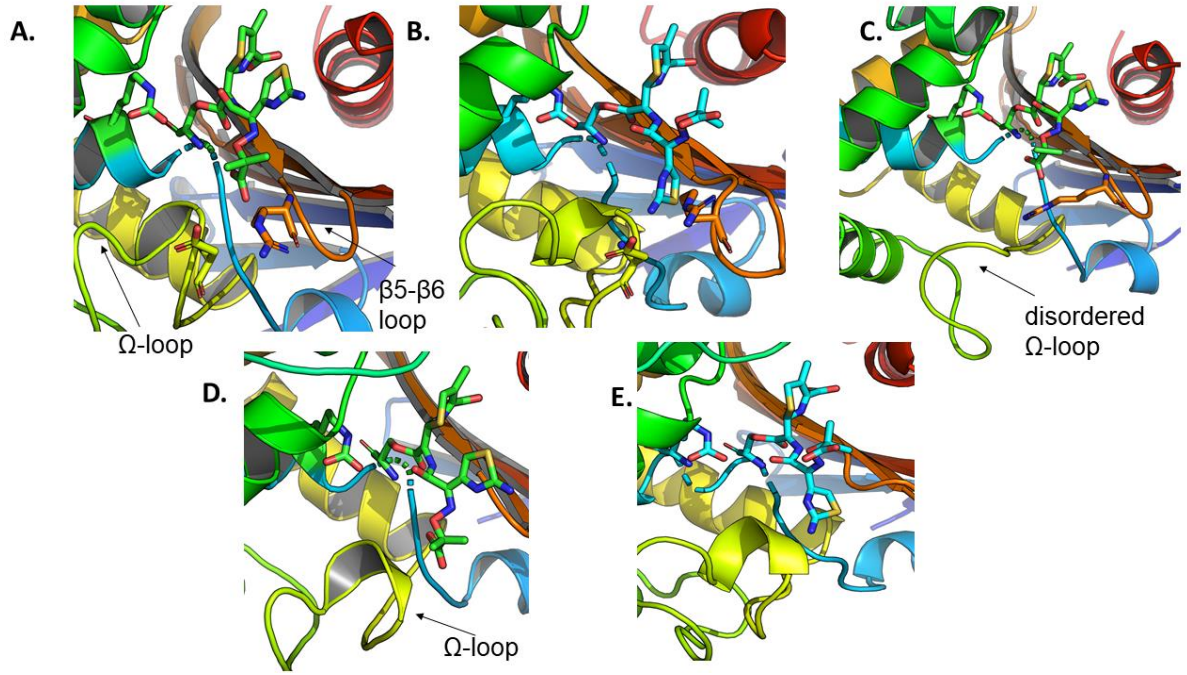

Figure S1. Different models built for OXA-48 and OXA-163 with ceftazidime. A. OXA-48 with Ω-loop as found in the apoenzyme and ceftazidime binding pose as in the OXA-48 and ceftazidime crystal structure (binding pose 1). B. OXA-48 with Ω-loop as found in the apoenzyme and ceftazidime binding pose as in the OXA-225 and ceftazidime complex (binding pose 2). C. OXA-48 with a disordered Ω-loop built using MODELLER and ceftazidime binding pose as in the OXA-48 and ceftazidime complex. D. OXA-163 and ceftazidime binding pose as in the OXA-48 and ceftazidime crystal structure (binding pose 1). E. OXA-163 and ceftazidime binding pose as in the OXA-225 and ceftazidime structure (binding pose 2).

Loop Generation

In the OXA-48 structure complexed with CTZ (PDB ID: 6Q5F),[255] electron density was not found for residues between Asp148 and Ile162 (ISGNVDSFWLDGGIR, 13 residue gap). 250 new models for the "disordered" Ω-loop were reconstructed using MODELLER[296] with slow loop refinement, whilst the rest of the atoms in the apoenzyme were kept fixed. (KCX was mutated back to lysine and CTZ removed for model generation to avoid parameter problems with non-standard residues.) Models were initially inspected using both the DOPE and molpdf scores, and 25 models were chosen for visual inspection (all models were in the top 50 for at least one scoring method, emphasis was given for DOPE scores to include more realistic loop conformations). The final loop model was chosen based on the following criteria: loop residues do not clash with bound ceftazidime in the active site, the new loop does not form interactions with Arg214, and loop reaches in the cavity near the active site (where the "ordered" loop is in the apoenzyme) rather than fully into bulk solvent. All crystallographic waters closer than 2.5 Å to the new loop were deleted to avoid possible clashes.

The "disordered" Ω-loop is not seen in the crystal structure of OXA-48 and ceftazidime (lacking electron density), and it is therefore predicted to be highly flexible compared to the surrounding structural elements. The chosen loop model was validated by measuring Cα-atom RMSF values for three 100 ns molecular dynamics simulations and by comparing the calculated fluctuations of the new Ω-loop against fluctuations in rest of the protein. The first 10 ns of each simulation were excluded from RMSF calculations to allow for system equilibration. RMSF values for each simulation are presented in Figure S2, and they indicate that the newly constructed loop region is the most flexible part of the protein. Loop flexibility is somewhat exaggerated in simulation 2, as it is observed to move into bulk solvent and then move back to the vicinity of the active site.

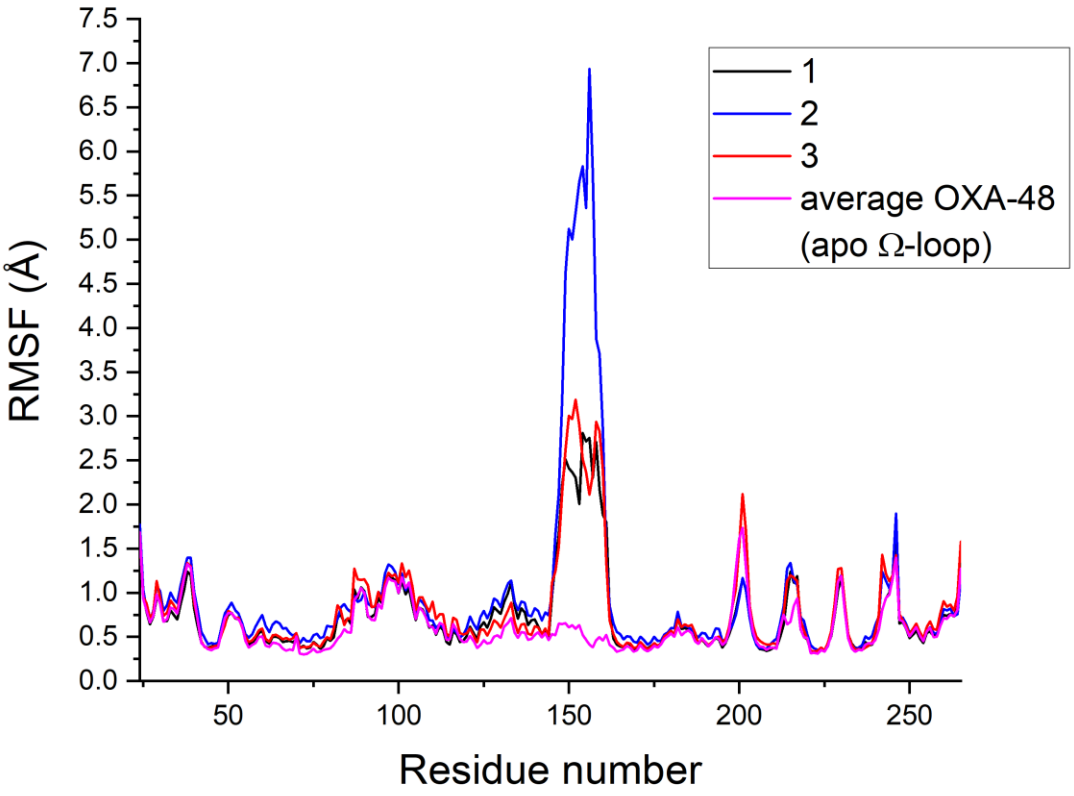

Figure S2. RMSF measurement for Cα-atoms for the distorted Ω-loop model of OXA-48. RMSF was measured from three 100 ns MD simulations and compared against the average RMSF for OXA-48 with the apo Ω-loop (magenta, average RMSF taken from five 100 ns MD simulations).

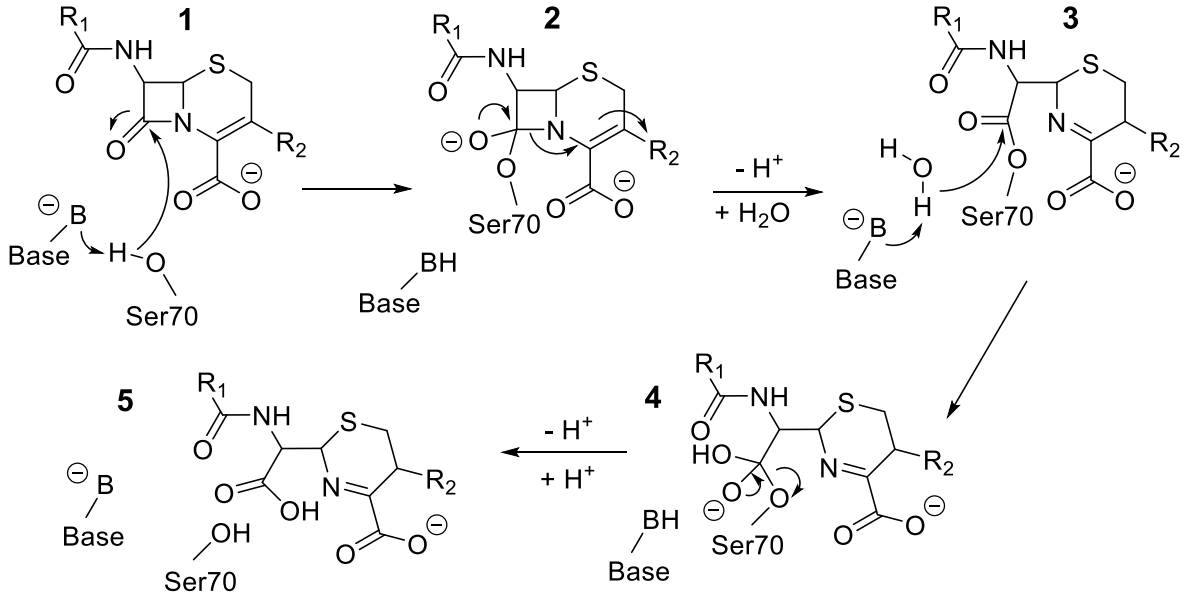

Scheme S1. Schematic illustration of the complete hydrolysis reaction in serine β-lactamases.[49] *After the initial Michaelis complex formation, the antibiotic is acylated (1) and a tetrahedral intermediate is formed (2), which collapses to give the acylenzyme structure (3). Subsequently, the acylenzyme is deacylated forming a second unstable tetrahedral intermediate (4), which collapses to the final hydrolysis product (5).*

Computational Methods

After initial preparation, all structures were briefly minimized (1000 and 1000 steps of steepest descent and conjugate gradient, respectively) and heated from 50 K to 300 K in 20 ps. After heating, 1 ns MM MD was run to generate starting structures for umbrella sampling (US) calculations. Classical MD simulations were run using Langevin dynamics with a 2 fs timestep constraining all bonds involving hydrogen atoms with the SHAKE algorithm. All starting structures were chosen from the last 500 ps of the 1 ns run to allow for system equilibration during the first half (starting structures at least 50 ps apart). (Tests were also performed using starting structures after at least 50 ns of MM MD, see section "*Extended MD Simulations: Stability, Loop Conformation and Free Energy Barriers*".) All MM MD simulations were performed using a 2 fs timestep, Langevin dynamics with a collision frequency of 0.2, and periodic boundary conditions. The SHAKE algorithm was applied for all bonds involving hydrogen atoms. QM/MM simulations were performed under the same conditions, but with a 1 fs timestep and SHAKE turned off for the QM region. The Amber program package was used for all calculations.[203]

QM/MM Free Energy Calculations

QM/MM US[185, 297] MD simulations were done using two analogous reaction coordinates as for class A enzymes: one for describing the proton transfer from DW to the general base, and one for describing the nucleophilic attack (Figure S3). The proton transfer reaction coordinate was sampled from 1.0 to −1.0 Å, and the nucleophilic attack coordinate from 3.8 to 1.4 Å, both in 0.1 Å increments with a 100 kcal mol^{-1} $Å^{-2}$ force constant. First, US was performed along an approximate (see below) minimum free energy path (MFEP) from AE to TI on the 2D free energy surface (FES) in 33 US windows, and afterwards sampling along the rest of the surface was performed using these windows as starting points (altogether 525 US windows). US was first done for in each window for 2 ps for equilibration, followed by a further 20 ps along the approximate MFEP and a further 2 ps in all other windows. This approach should ensure enough sampling near the true reaction path, whilst minimizing sampling in high energy regions on the FES. US was done for four different starting structures taken from a 1 ns MM/MD run. The QM region consists of the deacylating water (DW), KCX, and a part of the covalently bound drug (38 atoms, Figure S4), and DFTB3[159] was used as the QM method with a 1 fs timestep. Covalent bonds between the QM and MM regions were treated using the hydrogen link atom scheme implemented in sander (Amber). A one-sided restraint was added for the ester bond between Ser70 and the substrate to ensure it does not elongate above 1.6 A (Figure S4). All US results were analysed and FESs constructed using WHAM[186] with 21 and 25 bins for the proton transfer and nucleophilic attack coordinates respectively, with a convergence criterium set to $1x10^{-13}$. Calculations were done for four snapshots, and the overall energy barriers were obtained by combining all sampling from these four US calculations into one WHAM calculation. True MFEPs on the FESs were calculated using the Minimum Energy Pathway Analysis for energy landscapes (MEPSA) code.[298]

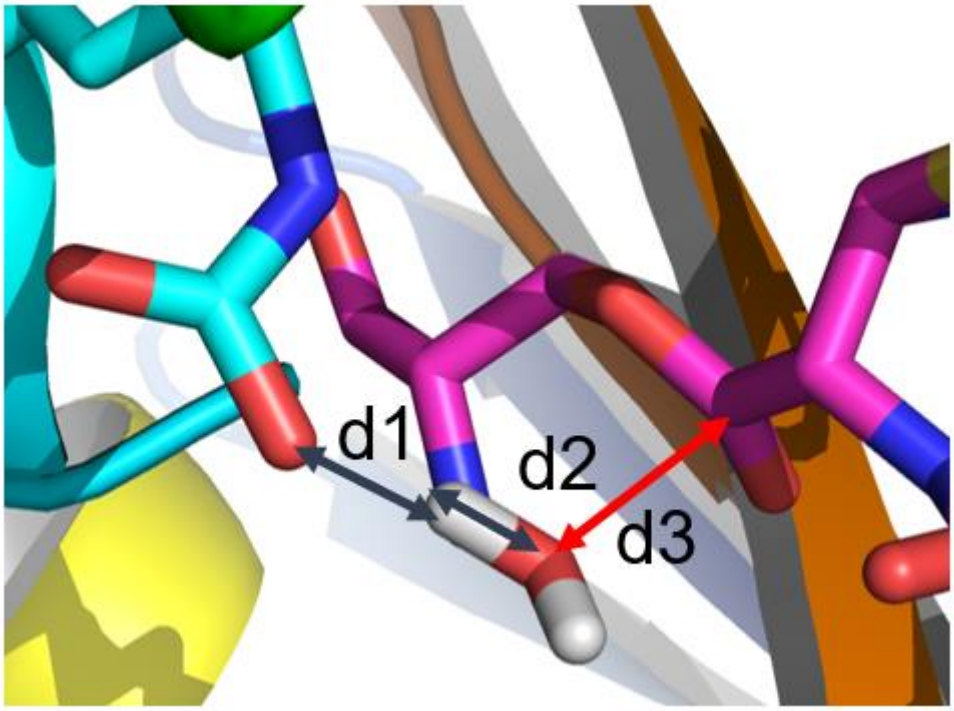

Figure S3. Illustration of the reaction coordinates used in umbrella sampling describing the changed in bonding during the tetrahedral intermediate formation. The proton transfer coordinate is defined with dark blue arrows as the difference d1-d2 (d[Lys73:O, DW:H] – d[DW:O, DW:H]). The nucleophilic attack coordinate is depicted as the red arrow, distance d3 (d[DW:O, CTZ:C]).

The approximate minimum energy path for OXA-48 variants was constructed based on calculated class A deacylation surfaces, and consists of 33 initial US windows (PT=proton transfer, NA=nucleophilic attack):

PT	1.0	0.9	0.8	0.8	0.8	0.8	0.8	0.8	0.8	0.8	0.8	0.8	0.8	0.7	0.6
NA	3.8	3.7	3.6	3.5	3.4	3.3	3.2	3.1	3.0	2.9	2.8	2.7	2.6	2.5	2.4

PT	0.5	0.4	0.3	0.2	0.1	0.0	-0.1	-0.2	-0.3	-0.4	-0.5	-0.6	-0.7
NA	2.3	2.2	2.2	2.1	2.1	2.0	1.9	1.8	1.7	1.7	1.6	1.6	1.5

PT	-0.8	-0.8	-0.9	-1.0
NA	1.5	1.4	1.4	1.4

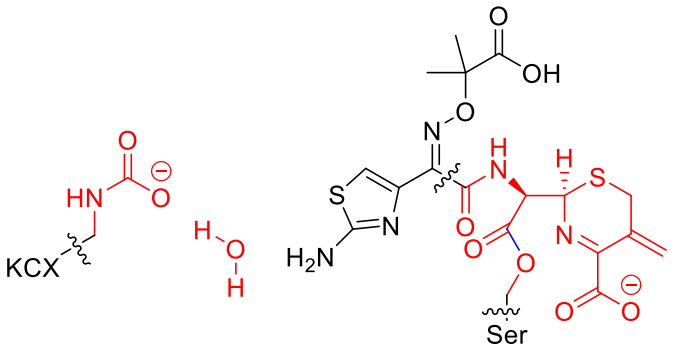

Figure S4. QM region used in US calculations; QM atoms in red, MM atoms in black; location of link atoms indicated with squiggly lines. The ester bond in blue was restrained to be less than (or equal to) 1.6 Å during US to avoid sampling the next step.

Free Energy Surfaces – short sampling

Free energy barriers for deacylation ($\Delta^{\ddagger}G_{calc}$ values) in Table 1 (main manuscript) were calculated by sampling 20 ps near the approximate minimum energy path and 2 ps elsewhere on the free energy surface (as described above, from now on referred to as 20 + 2 ps sampling). The 2 ps 'equilibration' sampling in each window (prior to the US used for the free energy analysis reported in Table 1) was also used directly for the calculation of free energy surfaces using WHAM (as detailed above). Notably, $\Delta^{\ddagger}G_{calc}$ values based on the 2 ps surfaces (without equilibration) do not largely differ from the 20 + 2 ps results (largest difference 0.5 kcal/mol; see Table S1), and show the same consistent difference in deacylation rates between different OXA-48 variants.

Table S1. Deacylation free energy barriers calculated from 2 ps sampling. All values in kcal/mol, standard deviations in parenthesis.

Enzyme	k_{cat} **(s^{-1})**[226]	$\Delta^{\ddagger}G_{calc}$ **(kcal/mol)**		
		Binding pose 1	Binding pose 2	New Ω-loop
OXA-48	NH	12.4 (0.8)	18.5 (1.0)	>20[a]
OXA-48 R214S	-	6.9 (0.5)	14.0 (1.4)	>20[a]
OXA-163	8	7.2 (0.3)	15.7 (1.4)	-
OXA-181	ND	11.0 (1.9)	17.7 (0.6)	-
OXA-181 R214S	-	6.4 (0.3)	-	-

NH = No hydrolysis detected. ND = Not determined.

[a] transition state could not be located on the free energy surface, with energy values rising to above 20 kcal/mol near the TI

Benchmarking

For the QM/MM MD umbrella sampling simulations, the semi-empirical DFTB3 method was used. The free energy surface indicates a concerted mechanism with a barrier lower than that expected from experiment. Here, we perform more accurate DFT calculations (and *ab initio* single-point energy calculations) using a small gas-phase system representing the quantum region used in our QM/MM simulations (Figure S5). Transition states (TS) were optimised on both the M06-2X/6-31+G(d)[134, 148] and BLYP/6-31G+(d)[130, 131] levels using the QST3 algorithm as implemented in Gaussian09[313]. UltraFine integration grid was used for all calculations.

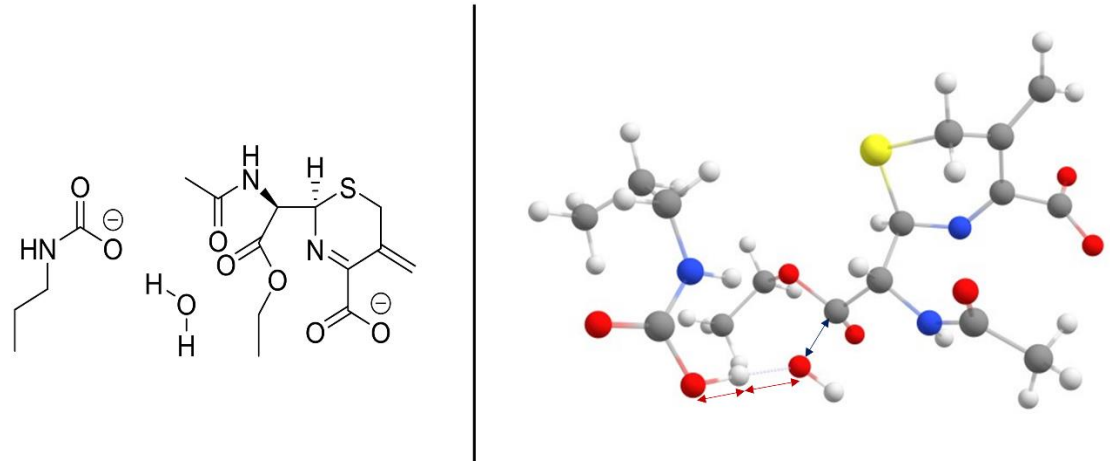

Figure S5. Left: Small molecule model representing the QM region used in benchmarking calculations. Right: M06-2X/6-31+G(d) optimized transition state of the small molecule model. Red arrows: proton transfer reaction coordinate, blue arrow: nucleophilic attack reaction coordinate.

TSs were characterized by frequency calculations, and the TS on the M06-2X level corresponded to one imaginary frequency (-293.2677), whilst TS optimized using the BLYP functional yielded two imaginary frequencies (-107.3119 corresponding to the reaction, and one at -1.8944, corresponding to an overall bend/twist motion). IRC calculations starting from the M06-2X TS structure were performed in both directions to obtain the reactant and product minima, and the end structures where further optimised on the M06-2X/6-31+G(d) level. Reactants and products were optimised also with BLYP (starting from the M06-2X optimised structures). The reaction coordinate values of the TSs indicate that the reaction proceeds through a concerted mechanism, similar to that predicted by the DFTB3/ff14SB free energy surface (Table S2). Calculated activation energies (Table S2) indicate that DFTB3 significantly underestimates this value. RI-SCS-MP2/aug-cc-pVTZ[314-316] single-point energies were calculated on the M06-2X optimized structures using Orca 4.2[317, 318] (using the RIJK approximation and aug-cc-pVTZ/C and aug-cc-pVQZ/JK auxiliary basis sets[319]). DFTB3 single-point energies were calculated for BLYP optimized structures using sqm as part of the Amber package.[297] Comparison of these RI-SCS-MP2/aug-cc-pVTZ and DFTB3 activation energies shows that, based on these potential energies only, DFTB3 underestimates the activation energy by 7 kcal/mol.

Table S2. Location of the transition state for M06-2X and BLYP optimized small QM model (Figure S5), and calculated activation energy barrier. NA RC = nucleophilic attack reaction coordinate, PT RC = proton transfer reaction coordinate.

Method	**NA RC (Å)**	**PT RC (Å)**	**$\Delta^{\ddagger}G_{calc}$ (kcal/mol)**
M06-2X/6-31+G(d)	1.97	-0.35	14.85
RI-SCS-MP2/aug-cc-pVTZ[a]	-	-	16.63
BLYP/6-31+G(d)	1.83	-0.51	15.53
DFTB3[b]	-	-	9.65
DFTB3/ff14SB FES (OXA-48)[c]	1.7	-0.5	

[a] Energy difference from single-point energies on M06-2X/6-31+G(d) optimized AE and TS structures.

[b] Energy difference from single-point energies on BLYP/6-31+G(d) optimised AE and TS structures; A transition state could not be optimized in the gas-phase with DFTB3 as no saddle point is indicated between the AE minimum and the tetrahedral intermediate.

[c] For reference, the approximate TS location obtained from the QM/MM free energy surface (see Figure 2) is indicated.

For the purpose of comparing the in-enzyme energy surface shape and energies, a QM/MM potential energy surface was obtained (Figure S6). Starting from a snapshot of one OXA-48 US simulation in the window corresponding to the (approximate) transition state, a potential energy surface (PES) was calculated for the deacylation reaction. The LBFGS method was used for minimization (with convergence criterium of 0.01 mol^{-1} $Å^{-1}$ for energy gradients). Residues further than 5 Å away from ceftazidime were restrained with a restraint weight of 50 kcal mol^{-1} $Å^{-2}$ (to avoid discontinuities). Single-point energy corrections were calculated by taking the difference in the QM region energies calculated at the M06-2X/def2-TZVP level (using the RIJK approximation with def2/JK auxiliary basis set) with Orca 4.2 and the DFTB3 level. (QM-MM interaction terms were thus calculated with DFTB3.)

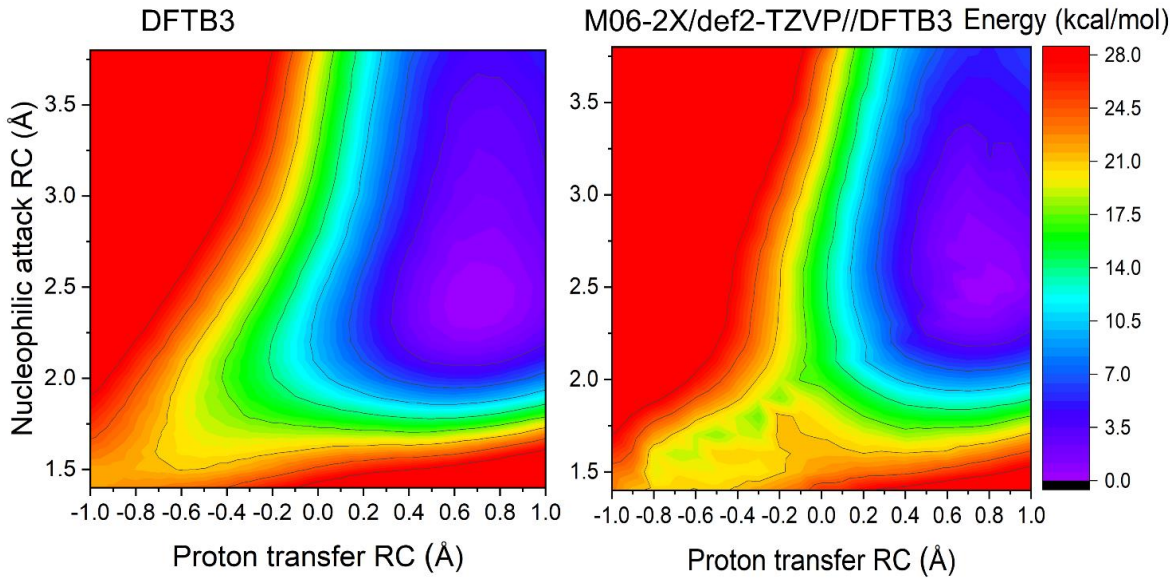

Figure S6. Left: Potential energy surface for ceftazidime deacylation calculated with DFTB3; energy at -0.5,1.6 (location of the free energy surface TS) is 13.4 kcal/mole. Right: DFTB3 potential energy surface with M06-2X/def2-TZVP energy corrections; approximate TS at -0.3,1.9 is 19.4 kcal/mole. The difference of 6 kcal/mole is in line with the small model calculations (Table S2).

Mulliken Charge Calculations

Mulliken charges for the QM region were calculated from extended US in both acylenzyme and tetrahedral intermediate minima from one individual US free energy surface. Charge values were calculated as an average from 1000 frames over 20 ps (i.e. snapshots recorded every 20 fs). Mulliken charges are presented for OXA-48 (both ordered and disordered Ω-loop), OXA-48 Arg214Ser, and OXA-163. All four models show the same trend, where largest charge variations are observed for the atoms that directly take part in deacylation or are near the reactive parts (Figure S7). Mulliken charges were recorded for the QM atoms in both the enzyme environment and in the gas-phase. For the gas-phase charge calculations, each frame of the QM/MM MD trajectory was extracted as a separate structure and pseudo-minimized (minimization with 0 steps) to obtain the QM region with link atoms. Subsequently, a single-point QM calculation was done for each QM region structure using sqm (as implemented in Amber) to obtain the Mulliken charges. The results on key atoms are reported in Tables S3-S5.

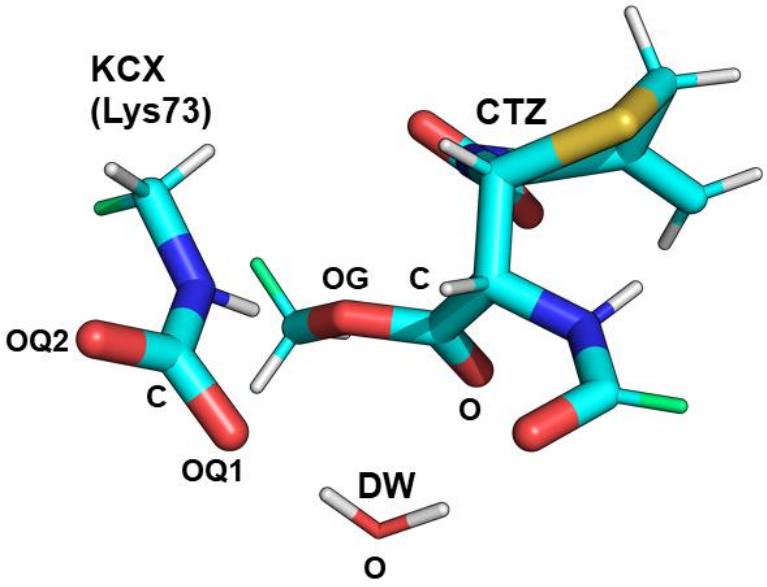

Figure S7. QM region with link atoms (in green). Atom names shown for selected heavy atoms, whose Mulliken charges were recorded during QM/MM MD.

Table S3. Mulliken charges for WT OXA-48 and ceftazidime.

QM atom	**Enzyme**			**QM region only**		
	Q^{AC}	Q^{TI}	ΔQ^{TI-AC}	Q^{AC}	Q^{TI}	ΔQ^{TI-AC}
KCX-OQ1	-1.01	-0.59	0.41	-0.93	-0.56	0.36
KCX-OQ2	-0.91	-0.80	0.11	-0.86	-0.74	0.12
KCX-C	0.98	0.83	-0.15	0.94	0.81	-0.13
DW-O	-0.85	-0.76	0.09	-0.84	-0.73	0.11
CTZ-O	-0.65	-1.0	-0.35	-0.56	-0.92	-0.37
CTZ-C	0.71	0.91	0.20	0.69	0.89	0.20
CTZ-OG	-0.34	-0.59	-0.26	-0.34	-0.6	-0.26

Table S4. Mulliken charges for WT OXA-48 with a 'disordered' Ω*-loop and ceftazidime.*

QM atom	**Enzyme**			**QM region only**		
	Q^{AC}	Q^{TI}	ΔQ^{TI-AC}	Q^{AC}	Q^{TI}	ΔQ^{TI-AC}
KCX-OQ1	-1.01	-0.59	0.41	-0.93	-0.56	0.36
KCX-OQ2	-0.91	-0.80	0.11	-0.86	-0.74	0.12
KCX-C	0.98	0.83	-0.15	0.94	0.81	-0.13
DW-O	-0.85	-0.76	0.09	-0.84	-0.73	0.11
CTZ-O	-0.65	-1.0	-0.35	-0.56	-0.92	-0.37
CTZ-C	0.71	0.91	0.20	0.69	0.89	0.20
CTZ-OG	-0.34	-0.59	-0.26	-0.34	-0.6	-0.26

Table S5. Mulliken charges for R214S OXA-48 and ceftazidime.

QM atom	**Enzyme**			**QM region only**		
	Q^{AC}	Q^{TI}	ΔQ^{TI-AC}	Q^{AC}	Q^{TI}	ΔQ^{TI-AC}
KCX-OQ1	-0.94	-0.59	0.35	-0.89	-0.56	0.33
KCX-OQ2	-0.89	-0.78	0.11	-0.86	-0.74	0.12
KCX-C	0.96	0.83	-0.14	0.94	0.81	-0.13
DW-O	-0.93	-0.79	0.14	-0.87	-0.76	0.11
CTZ-O	-0.69	-1.00	-0.31	-0.56	-0.88	-0.32
CTZ-C	0.73	0.93	0.20	0.70	0.91	0.21
CTZ-OG	-0.32	-0.60	-0.27	-0.34	-0.62	-0.28

Table S6. Mulliken charges for OXA-163 and ceftazidime.

QM atom	**Enzyme**			**QM region only**		
	Q^{AC}	Q^{TI}	ΔQ^{TI-AC}	Q^{AC}	Q^{TI}	ΔQ^{TI-AC}
KCX-OQ1	-0.94	-0.61	0.33	-0.90	-0.59	0.32
KCX-OQ2	-0.89	-0.79	0.10	-0.86	-0.75	0.11
KCX-C	0.97	0.84	-0.13	0.94	0.82	-0.12
DW-O	-0.92	-0.82	0.10	-0.88	-0.81	0.06
CTZ-O	-0.67	-1.00	-0.33	-0.57	-0.90	-0.33
CTZ-C	0.73	0.92	0.20	0.70	0.90	0.21
CTZ-OG	-0.32	-0.53	-0.21	-0.33	-0.54	-0.21

Acylenzyme Clustering

Clustering of the acylenzyme was done based on five 50 ns MD simulations (1250 frames/simulation) per acylenzyme model (OXA-48 with (dis)ordered Ω-loop, OXA-48 Arg214Ser, OXA-163). All MD simulations were combined into one clustering calculation by stripping all solvent molecules and parts of the protein that did not match between all enzymes (e.g β5 - β6 loop in OXA-48). Trajectories were aligned based on Cα-atoms of 12 residues near the active site (CTZ, Thr71-Pro75, Ser118, Lys208-Tyr211, Lys218), and the substrate orientations were clustered into four clusters (using a sieve of 20) based on the RMSD of CTZ heavy atoms. The clustering analysis does not show any significant differences between the different enzyme models near the formed ester bond and the electrophilic carbon, but larger deviations between enzymes are seen for the oxyimino and thiazole groups. As depicted in Figure S8, OXA-48 with a newly constructed Ω-loop is seen to sample one orientation not observed for other enzymes (green cluster), as it has more space in the active site for substrate movement due to loop distortion.

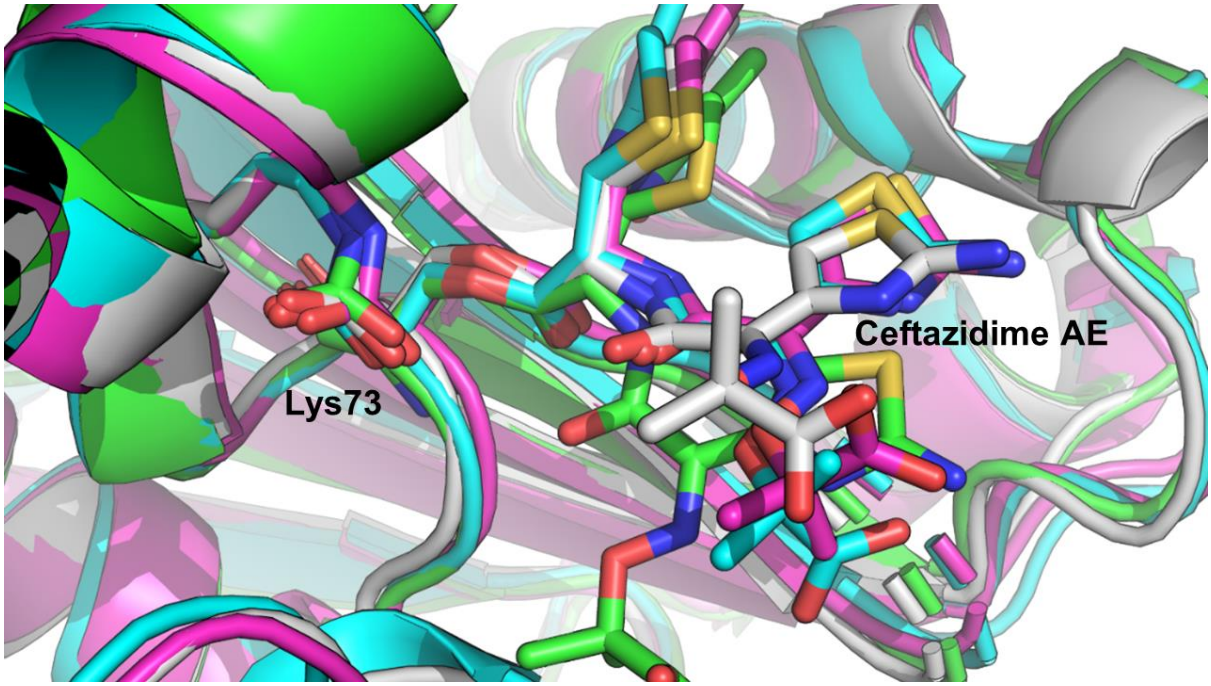

Figure S8. Acylenzyme orientations during extended MD from k-means clustering analysis. Representative structures (cluster centroids) are shown of the largest clusters (most sampled orientations) for OXA-48 (grey), OXA-163 (magenta), OXA-48 Arg214Ser (cyan), and OXA-48 with distorted Ω*-loop (cyan & green).*

Oxyanion Hole Hydrogen Bond Distances

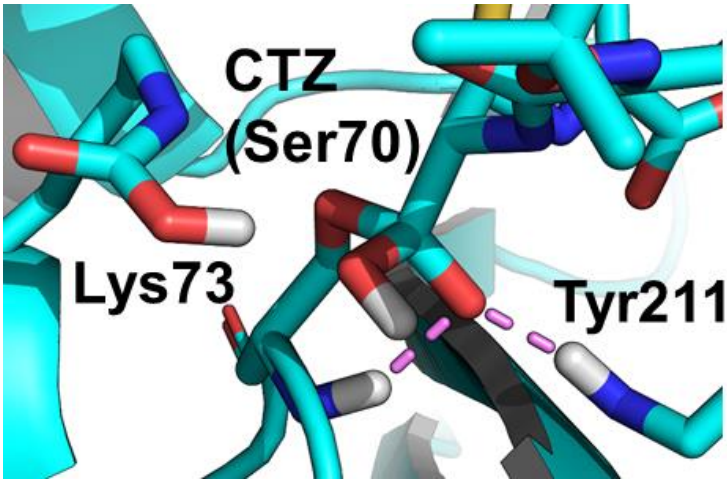

Figure S9. The oxyanion hole, formed by backbones of Ser70 (the AE) and Tyr211, stabilises the formation of a tetrahedral intermediate (hydrogen bonds highlighted in violet).

Because oxyanion hole interactions are known to stabilise the forming tetrahedral intermediate structure, distances of these hydrogen bonds (formed by the backbones of Ser70 in the ceftazidime acylenzyme and Tyr211, Figure S9) were measured both from five 50 ns

MM MD simulations per enzyme (for the acylenzyme), and from four 20 ps QM/MM MD simulations per enzyme (for the tetrahedral intermediate). Distance measurements are presented in Figures S10-S13. Overall, distances are very similar, and do not correlate with differences in the reaction barrier between the different enzyme models.

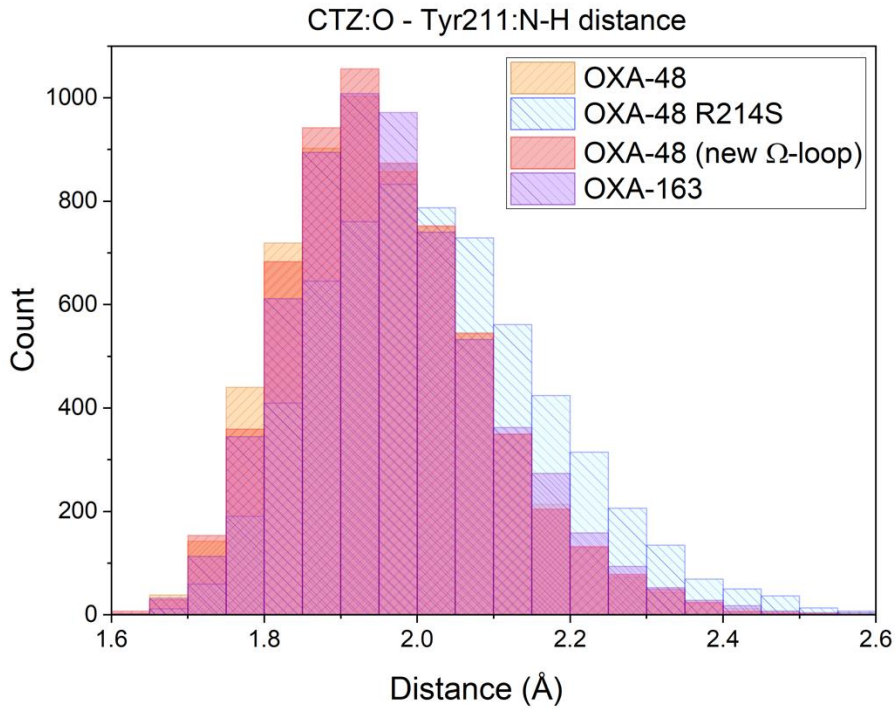

Figure S10. Hydrogen bond distances between the mainchain of Tyr211 and ceftazidime in the oxyanion hole from 50 ns MM/MD (measured from five MD simulations per acylenzyme model).

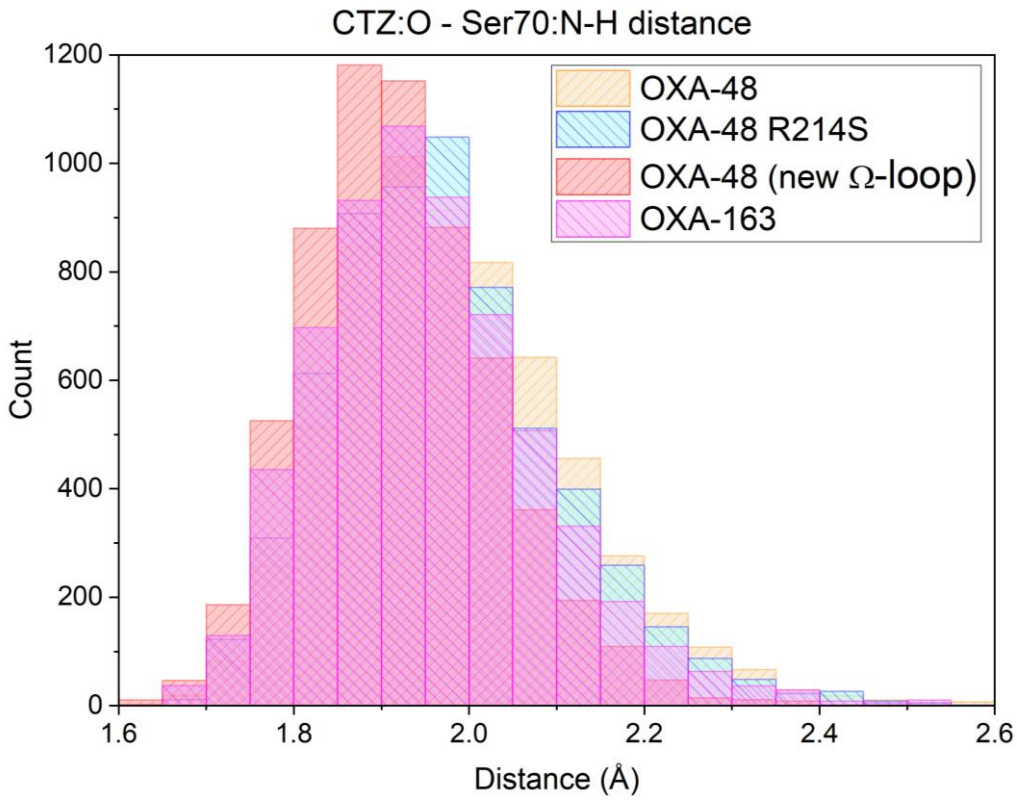

Figure S11. Hydrogen bond distances between the mainchain of Ser70 and ceftazidime in the oxyanion hole from 50 ns MM/MD (measured from five MD simulations per acylenzyme model).

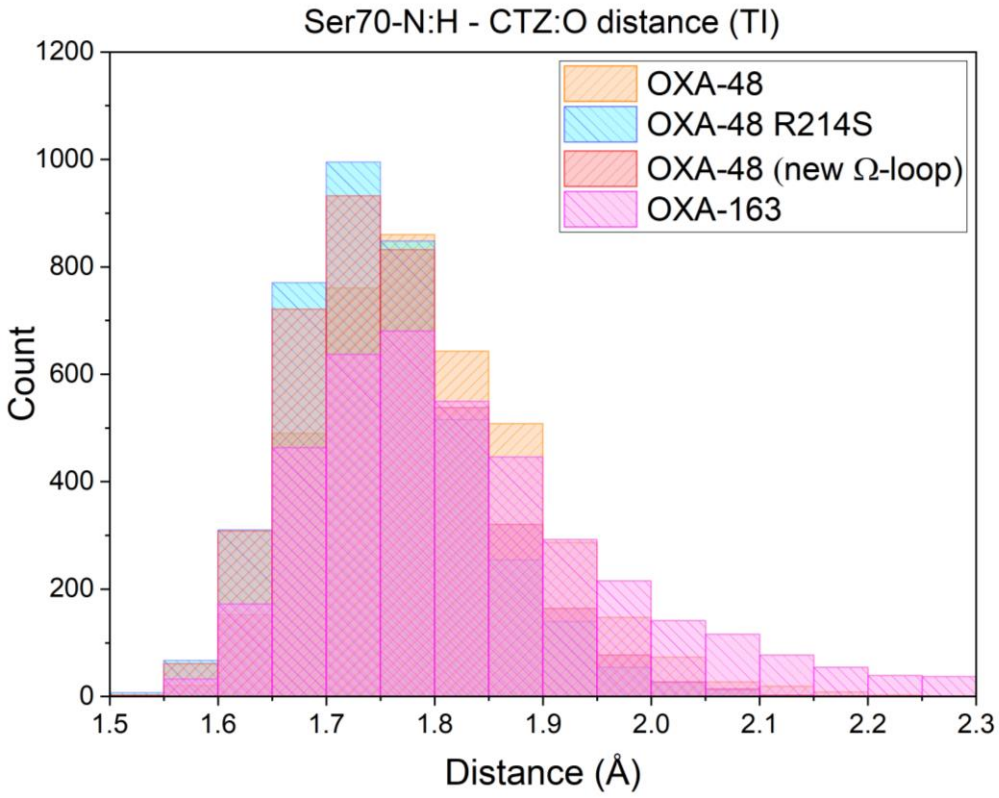

Figure S12. Oxyanion hole distances between Ser70 backbone and ceftazidime in the tetrahedral intermediate from 20 ps QM/MM MD.

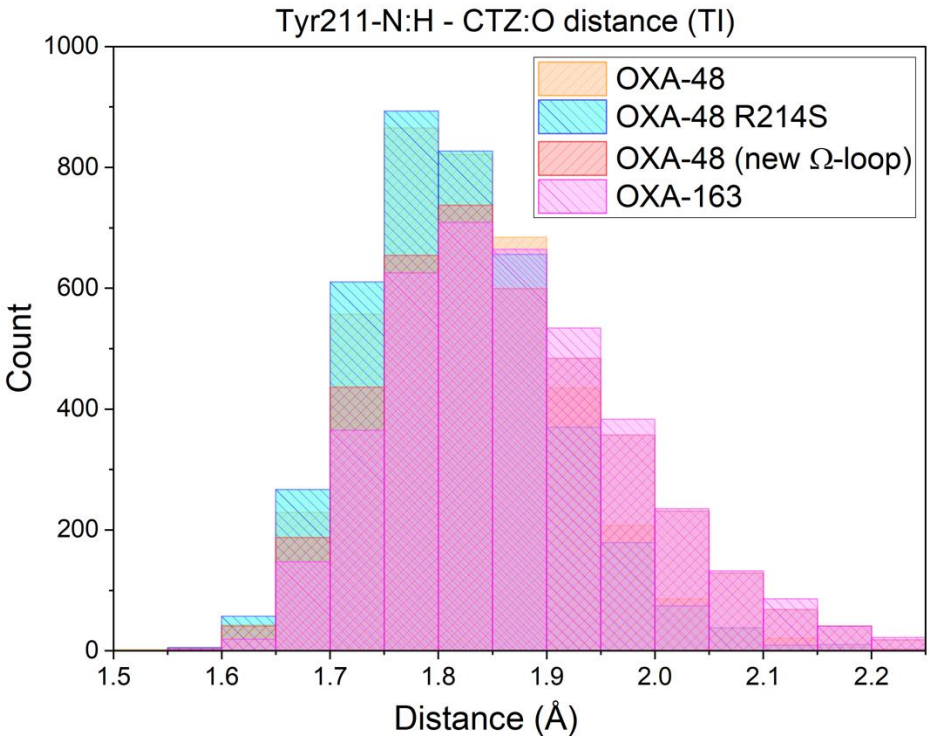

Figure S13. Oxyanion hole distances between Tyr211 backbone and ceftazidime in the tetrahedral intermediate from 20 ps QM/MM MD.

Leu158 Rotation

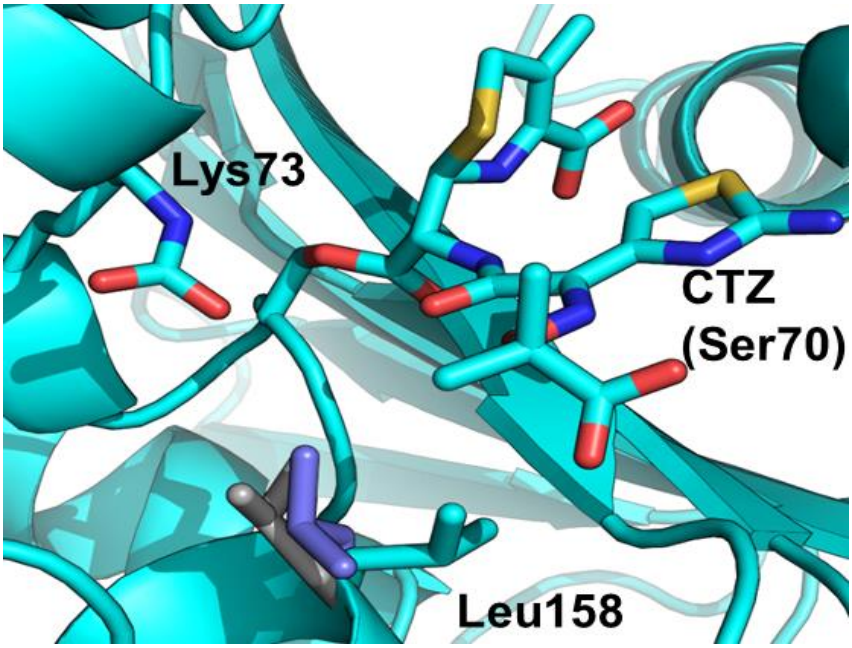

Figure S14. Three observed rotamers of Leu158. Representative structures are highlighted for structures where the C-Cα-Cβ-Cγ dihedral angle (χ_1) is approximately 50° (g+; cyan), 170° (t; grey), and 290° (g-; purple).

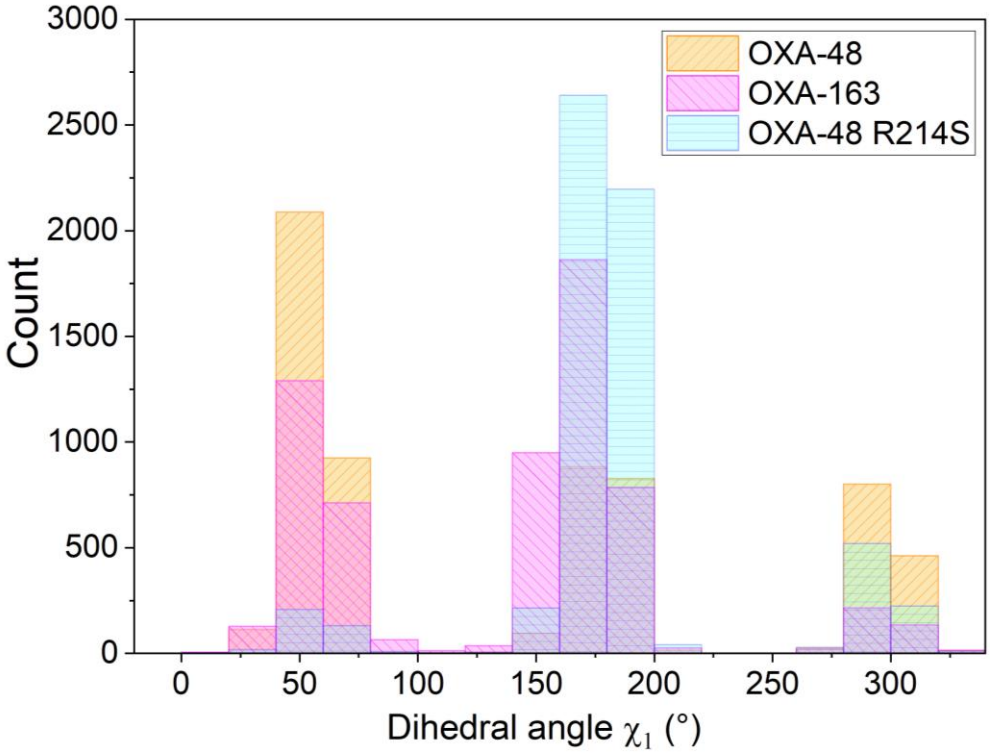

Figure S15. Leu158 C-Cα-Cβ-Cγ dihedral (χ_1) values measured from five 50 ns MD simulations for each enzyme. Three different rotamers are observed for each enzyme during MD simulations: around 50°, 170° and 290° (g+, t, and g-, respectively). The orientation found in the apoenzyme corresponds to the 170° orientation, and the two different orientations mainly occur for OXA-48.

Extended MD Simulations: Stability, Loop Conformation and Free Energy Barriers

To further inspect the stability of the simulation systems and check for possible of conformational changes in the studied OXA-48 variants, we ran five additional independent 120 ns MD simulations each for the acylenzymes of OXA-48, OXA-163 and OXA-48 R241S (in binding mode 1 and with the ordered Ω-loop). Measurement of the RMSD for Cα-atoms (excluding the first flexible five residues in the N terminus) indicates that all three systems are stable (Figure S16).

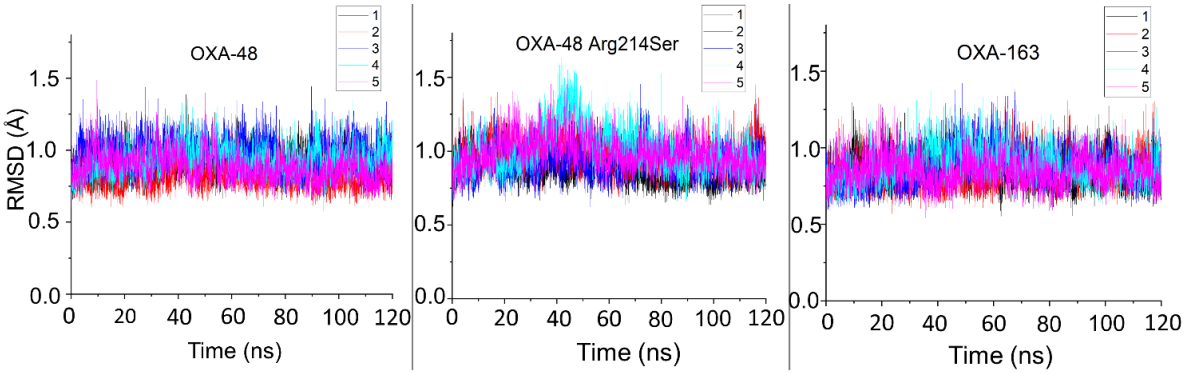

Figure S16. Cα-RMSD of five 120 ns MM MD simulations for OXA-48 (left), OXA-48 Arg214Ser (middle), and OXA-163 (right).

The β5 – β6 loop movement in OXA-48 and OXA-48 R214S was further inspected from the 120 ns MD simulations by clustering the sampled loop orientations based on Cα-RMSD. All five OXA-48 trajectories and five OXA-48 R214S trajectories were aligned on Cα-atoms of residues 29-211 & 219-265 (excluding five residues from the N-terminal end), and then divided in 5 clusters based on Cα-RMSD of the β5 – β6 loop (residues 212-218). Clustering was performed with the *k*-means algorithm as implemented in cpptraj with a sieve of 20. For the majority of simulation time, the β5 - β6 loop in OXA-48 and in OXA-48 R214S sample the same conformational space (70% and 76% in clusters 1-3 for OXA-48 and OXA-48 R214S, respectively, with populations ≥ 20% for each enzyme/cluster). Although the remainder of the time (30% and 23% for OXA-48 and OXA-48 R214S, respectively) the loop conformations are slightly different, it is clear that the mutation does not lead to a significant shift to a new conformational state (Figure S17).

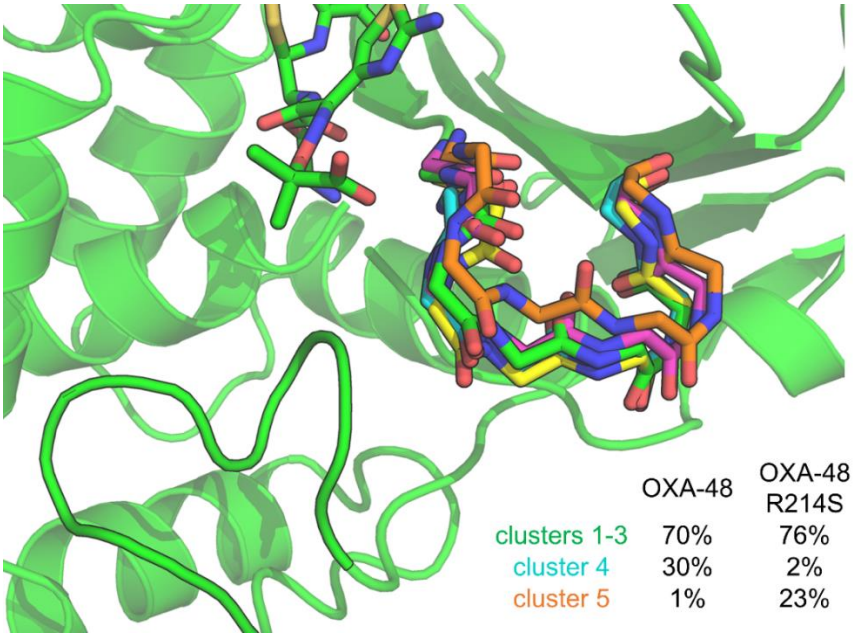

Figure S17. Clustering of the β5 - β6 loop (k-means clustering based on loop backbone RMSD after alignment on the rest of the protein, into 5 clusters) of 5x 120ns simulations of both OXA-48 and OXA-48 R214S. Loop carbons are coloured by cluster as follows: 1 green, 2 magenta, 3 yellow, 4 cyan and 5 orange. Ceftazidime acylenzyme and the Ω-loop are also shown, for reference.

Additionally, we performed one QM/MM (DFTB3/ff14SB) US simulation per enzyme variant by taking a starting structure from the 120 ns MD simulations. To make the calculated energetics comparable with the ones calculated for starting structures taken from 1 ns MD simulation, the structure for each variant was chosen so that Leu158 conformation and active site hydration replicate the ones observed in the original starting structures (i.e. Leu158 dihedral is 50° for OXA-48, and 170° for OXA-48 Arg214Ser and OXA-163). Results from 2 ps QM/MM US simulations, using the same procedure as applied previously, indicate similar free energies are obtained as with snapshots from the initial short 1 ns MD simulation (Table S7).

Table S7. Free energy barriers calculated with DFTB3/ff14SB umbrella sampling from extended MD snapshots.

Enzyme	**Time**	**$\Delta^{\ddagger}G_{calc}$ (kcal/mol)**
OXA-48	50 ns	12.42
OXA-48 R214S	120 ns	7.45
OXA-163	110 ns	7.93

Chapter 6 – Dissection of carbapenem hydrolysis by the OXA-48 β-lactamase reveals the origin of difference in efficiency

Chapter 6 comprises a draft manuscript titled "Dissection of carbapenem hydrolysis by the OXA-48 β-lactamase reveals the origin of difference in efficiency". The following version, i.e. the first draft, was written by myself with text editing from my supervisor Marc van der Kamp. Section 6.6 comprises the data intended as Supporting Information for the manuscript.

6.1 Abstract

OXA-48 β-lactamases are frequently encountered in bacterial infections caused by carbapenem-resistant Gram-negative bacteria. Due to the importance of carbapenems in treatment of healthcare-associated infections and the increasingly wide dissemination of OXA-48 enzymes on plasmids, these enzymes are of high clinical significance. Notably, OXA-48 hydrolyses imipenem more efficiently than other common carbapenems, such as meropenem. Here, we use extensive multi-scale simulations of imipenem and meropenem hydrolysis to dissect the differences in reactivity of possible conformational substates of the carbapenem acylenzymes. We highlight in detail which active site interactions lead to most efficient hydrolysis, including the orientation of the carbapenem 6α-hydroxyethyl group, and we correctly identify the experimentally observed difference in hydrolysis efficiency. In addition to increased insights into carbapenem breakdown by OXA β-lactamases, which may aid design of new antibiotics, our approach exemplifies the combined use of atomistic dynamics simulations and multi-scale reaction simulations to determine different possible enzyme-substrate substates and their influence on enzyme reaction kinetics.

6.2 Introduction

The World Health organization describes antibiotic resistance as "...one of the biggest threats to global health, food security, and development today."[320] Antibiotic resistance arises naturally,[321] but it is considerably accelerated by the current excessive use of antibacterial drugs.[61, 322] This evolving resistance does not only complicate the standard practice of

medicine, but has additionally expensive implications e.g. for global economy and food production.[206, 323, 324] Moreover, we are currently living in the so-called antibiotic discovery void: discovering new and safe antibacterials, especially against Gram-negative bacteria, is difficult, time-consuming, and often unprofitable for big pharmaceutical companies.[13, 325] β-Lactam antibiotics offer broad-spectrum antibacterial activity against Gram-negative bacteria and persist as the most prescribed drugs in clinical practice.[18] The significance of β-lactams in healthcare is highlighted by the World Health Organization, who has included multiple different β-lactam antibiotics in the Model List of Essential Medicine.[26] All these antibiotics contain a four-membered β-lactam ring, which ensures antibiotic binding to penicillin-binding proteins and consequently inhibition of bacterial cell wall biosynthesis.[50, 326] Clinically used β-lactam compounds can be divided into four different groups: penicillins, cephalosporins, carbapenems, and monobactams, of which especially carbapenems play a critical role as potent "last resort" antibiotics.[24]

Emerging resistance against β-lactams is evident, and currently β-lactamase enzymes are the main resistance mechanism against these drugs (especially in Gram-negative bacteria).[49] β-Lactamases prevent antibiotic action by hydrolysing the β-lactam ring, which prevents antibiotic binding to their ultimate target in cells. According to the Ambler classification, β-lactamases are divided into four major subgroups: serine-β-lactamases (SBLs) are classes A, C, and D, and metallo-β-lactamases (MBLs) class B.[63] The hydrolysis mechanism differs between SBLs and MBLs, as SBLs utilise a nucleophilic serine residue and MBLs employ zinc cofactors.[49] Class D SBLs are referred to as OXA enzymes, the name stemming from the term oxacillinase,[288] and they are currently of interest due to their wide spread globally as well as due to their ability to inactivate carbapenems. OXAs include five subgroups of recognised carbapenemases: OXA-23, OXA24/40, OXA-51, and OXA-58 β-lactamases are mainly found in *Acinetobacter baumannii*, while OXA-48-like β-lactamases are common in *Enterobacterales*.[221]

Focusing on *Enterobacterales,* OXA-48 β-lactamases are among the most commonly diagnosed carbapenemases in clinical samples.[218] Their activity is directed against imipenem, but other carbapenem substrates (such as meropenem and ertapenem) are also hydrolysed, albeit slowly.[226] The specific origin of this imipenemase activity is not well established, even though variations in measured hydrolysis rates between OXA-48 variants hint to structural moieties contributing to specific hydrolytic phenotypes. In OXA-163, a partial deletion of the β5-β6 loop (Arg214-Pro217) and one amino acid substitution (Ser212Asp) expands the hydrolysis profile to accommodate expanded-spectrum oxyimino cephalosporins (like

ceftazidime) at the expense of efficient imipenem breakdown.[230] Further studies show that the β5-β6 loop plays a role in acquired carbapenemase activity.[242, 243, 245] In recent years, structural studies have yielded a variety of OXA-48 crystal structures with carbapenems, which shed new light on the acylenzyme (AC) intermediate state.[71, 233, 239-241] Intriguingly, even when the β5-β6 loop is suggested to influence carbapenem activity, the only interaction between the substrate and loop residues (Thr213-Lys218) are hydrogen bonds to a bridging water molecule between imipenem 6α-hydroxyethyl hydroxyl and Thr213.[71, 233] Furthermore, carbapenem tail groups (C2 substituents) seem to be dynamic and able to adopt multiple conformations, which suggests they do not form strong interactions with the protein.[241]

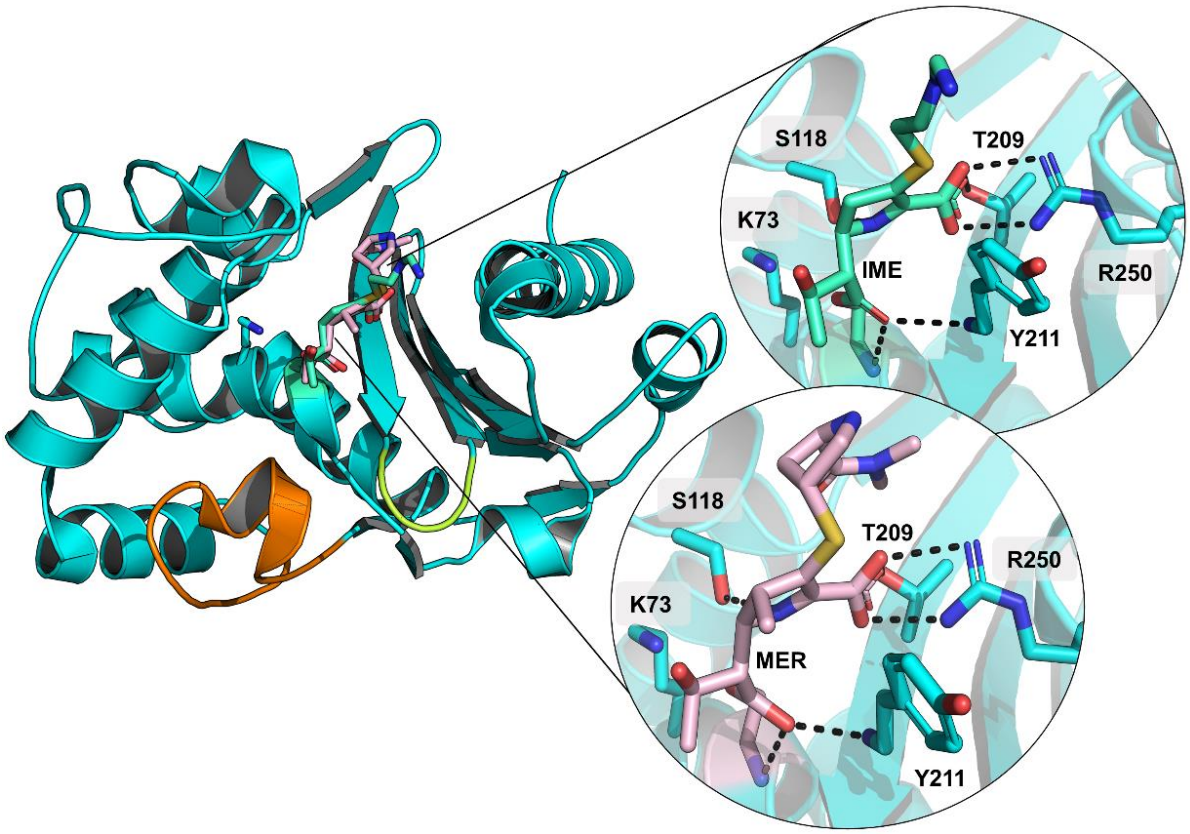

Figure 6.1. Crystal Structures of OXA-48 with Carbapenems. Acylenzyme structures of OXA-48 with imipenem (PDB ID 6P97, green sticks) and meropenem (PDB ID 6P98, light pink sticks) show a very similar binding pose for both substrates, where mainly the orientation of carbapenem tail group differs.[71] The Ω-loop is highlighted in orange, the β5-β6-loop in yellow, and relevant active site interactions with dashed black lines. The carbapenem pyrroline ring is found as the Δ2-tautomer for both carbapenems.

The standard hydrolysis mechanism of SBLs with β-lactams consists of acylation followed by deacylation.[49] Both acylation and deacylation include the formation of a shortly lived tetrahedral intermediate (TI) through a nucleophilic attack; the TI collapses to yield either a covalent AC structure (after acylation), or the final hydrolysed product (after deacylation). In both reactions, the nucleophile, which is Ser70 in acylation and a water molecule (deacylating water, DW) in deacylation, is activated via proton abstraction by a general base. For OXA enzymes, this general base is a carboxylated lysine residue (Lys73).[222, 223] Notably, Lys73 needs to be carboxylated for hydrolysis to take place, and its carboxylation is reversible and pH dependent, i.e. a carboxylation is observed to a higher degree at higher pH values.[223] Characteristic only for carbapenems, the pyrroline ring can undergo Δ2 → Δ1 tautomerization in the AC state, the Δ1 tautomer also having two stereoisomers (R or S). For class A SBLs, the Δ2 tautomer has been suggested to be the catalytically competent form, whereas Δ1 would essentially inhibit the enzyme.[247] For OXA-48s, all three tautomers have been observed in AC crystal structures,[71, 233, 240, 241] but based on NMR studies, the hydrolysis product is suggested to be either the Δ2 or R-Δ1 tautomer.[252]

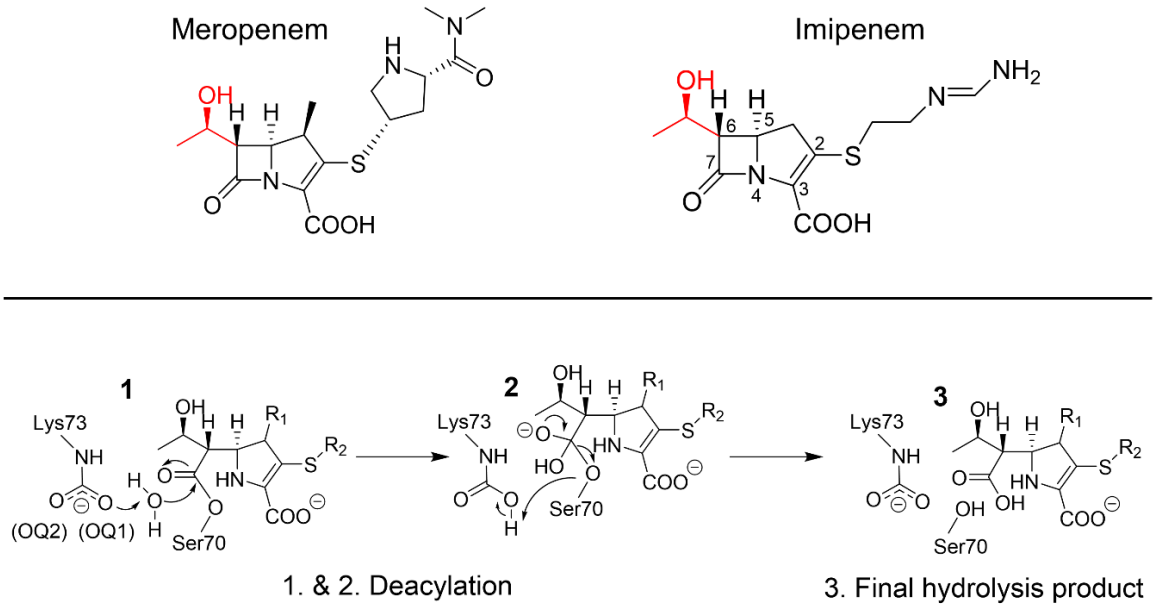

Scheme 6.1. Top: Structures of meropenem and imipenem with atom numbering, the 6α-hydroxyethyl group highlighted in red. Bottom: Deacylation mechanism in OXA-48 with a carbapenem substrate (Δ2 tautomer). Starting from the acylenzyme, the antibiotic is deacylated via tetrahedral intermediate formation (1 → 2), which collapses to yield the hydrolysed antibiotic.

Kinetics measurements suggest that for OXA-48-like β-lactamases, deacylation is the rate-limiting hydrolysis step in carbapenem breakdown.[233] The authors suggested that the impaired imipenemase activity in the ESBL-like OXA-163 is due to a larger active site, which would not constrain the substrate in deacylation-compatible conformations. Molecular dynamics simulations of the non-covalent complexes of OXA-48 and OXA-163 with both meropenem and imipenem were conducted (a single trajectory for each complex), which may indicate differences in stability. However, the measured K_m values for OXA-48 with imipenem and meropenem are highly similar (according to one assay, 11 and 13 μM, respectively)[226], which indicates that there is likely no significant difference in the initial Michaelis complex stability. The difference in the inactivation efficiency of imipenem compared to meropenem should thus be related to a difference in the deacylation step. To inspect differences in catalysis for carbapenems on an atomistic level, we simulate the TI formation in deacylation, i.e. the identified rate-limiting step, for both imipenem and meropenem with OXA-48 using combined quantum mechanics/molecular mechanics (QM/MM) simulations. Our simulations support the hypothesis of the dynamic nature of carbapenem substrates in the AC state. We identify which conformations of the 6α-hydroxyethyl group allow for efficient deacylation. Additionally, active site hydration around the carboxylated Lys73 is observed to affect the calculated free energy barriers, as has been noted previously for ceftazidime hydrolysis by OXA-48 enzymes.[257] Based on further analysis of the reaction simulations, efficient carbapenem breakdown results both from decreased hydration around carboxy-Lys73 and from subtle changes in the hydrogen bonds between the substrate and the catalytic water molecule.

6.3 Methods

Computational methods and details for system setup are described in detail in the SI. To summarise, models of OXA-48 with imipenem and meropenem were prepared based on corresponding acylenzyme (AC) crystal structures (PDB IDs 6P97[71] and 6P98[71] for imipenem and meropenem, respectively). The ff14SB parameter set was used for the protein,[100] parameters and partial charges for non-standard residues (acylated carbapenems and carboxylated lysine) were derived with the R.E.D. Server.[172] Both systems were briefly minimised, heated from 50 K to 300 K (in 20 ps), and then the dynamics in the AC state were simulated for 200 ns using Langevin dynamics (collision frequency 0.2 ps-1) with a 2 fs timestep. Five independent simulations for each AC system were run. All bonds involving

hydrogens were restrained using the SHAKE algorithm. Starting structures for QM/MM[185] were chosen from MD simulations based on visual inspection of the active site hydration and the 6α-hydroxyethyl orientation; the 6α-hydroxyethyl orientation was kept from changing during subsequent US by applying a mild dihedral restraint (except for orientation I). Free energy barriers for the first (rate-limiting) step of deacylation for different active site conformations were determined from three separate QM/MM US calculations.[297] Two reaction coordinates were employed in US, one for the nucleophilic attack and one for the proton transfer. Sampling time in each window was 2 ps, and DFTB2 (SCC-DFTB)[158, 327, 328] was used as the QM method for QM region consisting of 43 and 46 atoms for imipenem and meropenem, respectively (including link atoms, depicted in Figure S1, Section 6.6). Free energy surfaces were constructed from 399 individual US windows. The Weighted Histogram Analysis Method (WHAM)[186, 329] was used to construct the free energy surfaces, and the minimum energy paths were analysed using the Minimum Energy Path Surface Analysis (MEPSA) program[298]. All simulations and trajectory analysis were done using the Amber18 software package[166] (pmemd.cuda[299, 301] for MM MD, and sander for QM/MM calculations).

6.4 Results and discussion

6.4.1 Acylenzyme dynamics

AC dynamics for both imipenem and meropenem complexed with OXA-48 were explored by running five 200 ns MM MD simulations for each complex, the first 50 ns were excluded from trajectory analysis to allow time for system equilibration. For both carbapenems, the salt bridge between C3 carboxylate and Arg250 was preserved during simulations, and the C7 carbonyl stayed in the oxyanion hole formed by the backbone amides of Ser70 (part of the AC) and Tyr211. The carbapenem tail moieties sampled a range of conformations during the simulations, consistent with previous suggestions based on structural analysis.[241] Clustering of imipenem and meropenem poses based on their heavy atom RMSD yielded four distinct clusters, which differ slightly from the poses defined in the deposited crystal structure coordinates by 0.8-1.8 Å and 1.7-2.5 Å for imipenem and meropenem, respectively (Figure S2, Table S1 and SI section “Acylenzyme Clustering” in Section 6.6). The main deviations between cluster centroids and the crystal structure coordinates are due to the C2 tail group position, as the pyrroline ring and its substituents are anchored in place by the oxyanion hole hydrogen bonds and the salt bridge with Arg250. However, there is only limited electron

density beyond the sulfur atom for both imipenem and meropenem in crystal structures 6P97 and 6P98, so the deposited substrate coordinates may not completely reliably depict the actual binding poses.

During MM MD, the carbapenem 6α-hydroxyethyl group rotated to occupy three different orientations, which can be distinguished by the value of the C7-C6-C-O dihedral angle: around 50°, 180°, or 290°, and these are henceforth referred to as orientations I, II, and III, respectively (Figure 6.2). The 6α-hydroxyethyl orientation affects interactions in the active site, because its hydroxyl group can hydrogen bond either with the DW (I), Lys73 carboxylate (III), or stay close to the crystallographically observed pose, in which its methyl group is positioned next to the DW and points towards Leu158 (II, Figure 6.2). The starting orientation of the 6α-hydroxyethyl for both carbapenems is II, from the crystal structures used in model building. During MD, this sidechain is free to move and sample all three orientations. For meropenem, orientation I is sampled more than II, while III is sampled only minimally (Figure 6.2). Conversely, both orientations II and III are sampled more than I for imipenem. The free energy difference between the different orientations of the 6α-hydroxyethyl group was estimated by calculating the ratio of MD trajectory frames corresponding to each orientation (Z), and using $\Delta G = RT\ln(Z)$, where R is the molar gas constant and T the simulation temperature (300 K). For imipenem, the lowest free energy state is orientation II, with slightly higher relative energies of 0.6 and 0.2 kcal/mol for orientations I and III, respectively. For meropenem, orientation I has the lowest free energy, orientation II is slightly higher (0.6 kcal/mol) but orientation III is significantly higher (2.2 kcal/mol). The presence of a methyl group in the 1β-position in meropenem (instead of a 1β-proton in imipenem) may explain the relatively higher penalty for orientation III, as in this orientation the 1β-substituent is located directly next to the 6α-hydroxyethyl moiety.

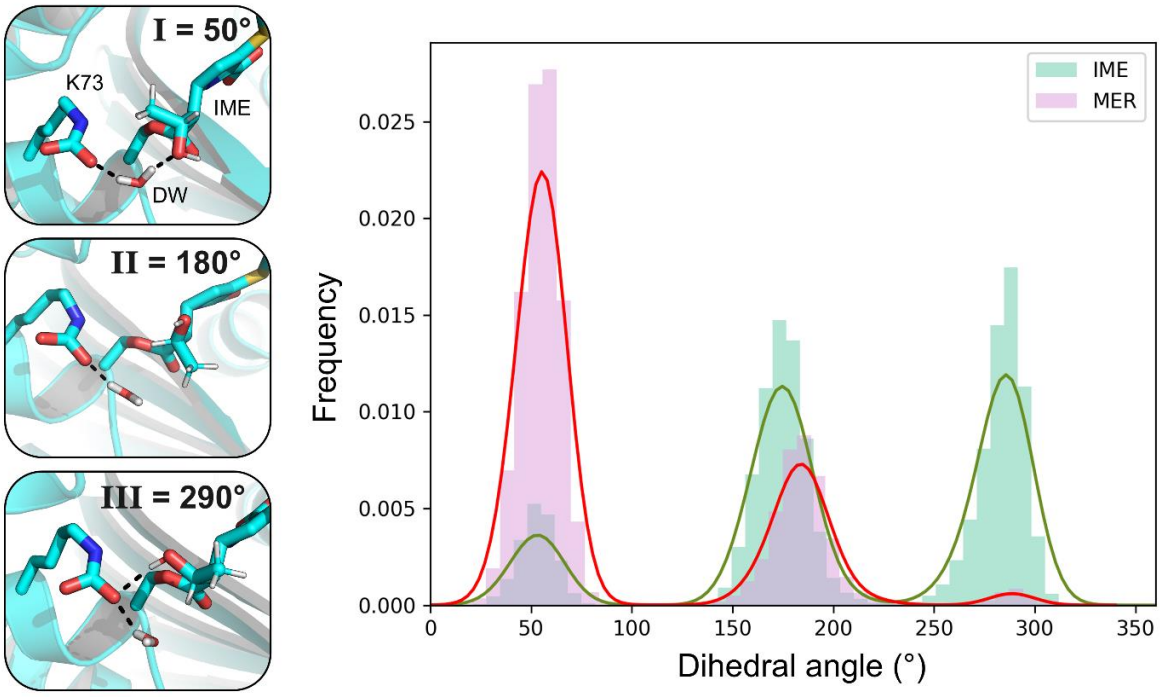

Figure 6.2. Sampling of the 6α-hydroxyethyl group of carbapenems. Left: The 6α-hydroxyethyl group can assume three different orientations, which can be distinguished by the C7-C6-C-O dihedral angle values. When the dihedral is around 50° (orientation I), the hydroxyl group is hydrogen bonded with the DW, and in the 180° orientation (II) the hydroxyl group can only interact with solvent. In 290° orientation (III), the hydroxyl group is donating a hydrogen bond to the carboxylated Lys73. Right: The distribution of sampled dihedral values during MM MD (5x150 ns per carbapenem).

Previously, our QM/MM simulations indicated that Leu158 may play an important role in modulating active site hydration in the deacylation of ceftazidime by OXA-48-like enzymes.[257] The orientation of Leu158 also differed initially between the two OXA-48/carbapenem systems, as the Cβ-Cγ bond has rotated by 180° in the meropenem structure. To study if Leu158 has a similar effect in carbapenem hydrolysis as observed for ceftazidime, its rotamers were recorded during MD by measuring the χ_1 dihedral (N-Cα-Cβ-Cγ). The distribution of sampled rotamers is presented in Figure S4 in Section 6.6. After the heating phase, Leu158 essentially always rotates away from the crystallographic *g-* orientation ($\chi_1 \approx$ 290°) to the *t* orientation ($\chi_1 \approx$ 180°) to allow space for the 6α-hydroxyethyl moiety, which in turn also permits two water molecules to form hydrogen bonds with K73:OQ1. As the cephalosporin scaffold lacks a moiety similar to the 6α-hydroxyethyl group in the carbapenem

scaffold, it is likely that Leu158 does not possess a similar role in carbapenem hydrolysis to that suggested for cephalosporins.

6.4.2 Deacylation efficiencies for the 6α-hydroxyethyl orientations

Because the interactions of the 6α-hydroxyethyl group in the active site have been suggested to play a role in modulating β-lactamase activity towards carbapenems,[222] deacylation free energy barriers were calculated separately for all three orientations observed in MD for both imipenem and meropenem. Starting structures for US were chosen from the 200 ns MM MD simulations following two criteria: a potential DW was at a suitable distance for nucleophilic attack, and the 6α-hydroxyethyl orientation was the desired one. For orientations II and III, the sidechain dihedral was restrained close to the reference values to avoid the substrate changing between orientations during the reaction (no restraints were needed for I, as no sidechain rotation during US was observed). Overall barriers were determined by combining sampling from three separate US calculations (with different starting structures), with standard deviations calculated between the free energy barriers for individual US simulations (Table S3 in Section 6.6). More details of the US setup and analysis are available in the SI in Section 6.6.

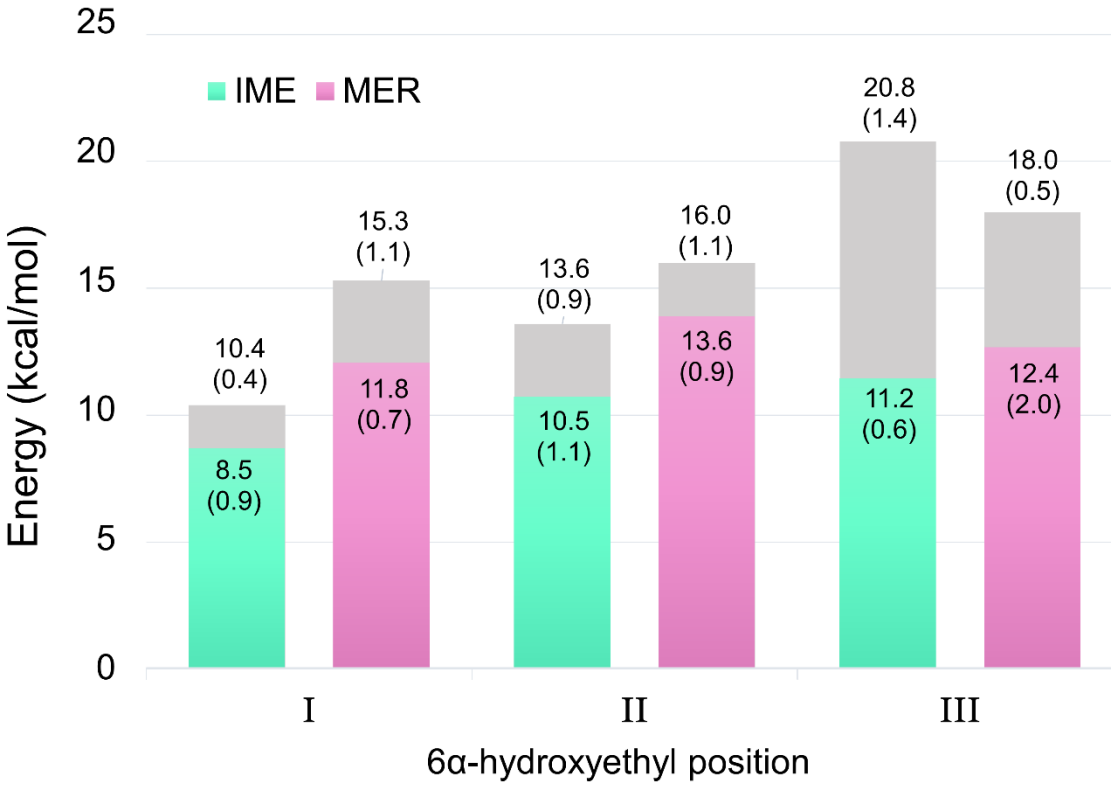

Figure 6.3. Free energy barriers for the three different 6α-hydroxyethyl orientations. Each bar includes the barrier obtained with a single water molecule hydrogen bonded to Lys73:OQ2 (lowest barrier, in colour; see Figure 6.4 for depiction of OQ2) and the barrier obtained with two water molecules hydrogen bonded to K73:OQ2 (highest barrier, in grey). Each barrier derived from three individual US simulations, standard deviations in parenthesis. Imipenem = green, meropenem = pink.

Figure 6.3 introduces the calculated deacylation free energy barriers for the three 6α-hydroxyethyl orientations. For all orientations, two barriers are presented, which correspond to two different hydration states around the general base. The lower barrier (in color) corresponds to a state with only one water hydrogen bonded to Lys73:OQ2 and one or two waters hydrogen bonded to Lys73:OQ1, while the higher barrier corresponds to a state with two water molecules hydrogen bonded to both carboxylate oxygens (Figure 6.4, carboxylate oxygens labelled in Scheme 6.1). For all hydration states, the calculated barriers follow the same trend of I < II < III, i.e. the lowest barriers are calculated for orientation I. Notably, the lowest barriers are consistently underestimated due to the QM method used (SCC-DFTB), as indicated by our benchmarking results (SI section "Benchmarking"). Converting the experimentally determined k_{cat} values from one assay to free energy barriers using the Eyring equation gives activation free energies of 16.6 and 19.2 kcal/mol for imipenem and meropenem, respectively.[226]

However, despite the difference in calculated barriers and those derived from experiment, we expect our protocol with semi-empirical QM methods to be a reliable indicator of energetic trends between different enzymes active site conformations, as we have demonstrated previously for studying β-lactam deacylation by class A and D SBLs.[189, 257]

As discussed above and in ref. [257], increased hydration around the proton-accepting Lys73:OQ1 is expected to impair deacylation in ceftazidime hydrolysis. A similar phenomenon was observed for carbapenems, with the addition that hydration around the second carboxylate oxygen affects reactivity as well. In orientation I, the average number of hydrogen bonds Lys73:OQ1 accepts during the reaction is 2.1-2.6 (calculated from the US minimum free energy path trajectories), which aligns with OQ1 being hydrogen bonded to two waters and partly to Trp157. The two subpopulations with different deacylation barriers arise from a change in hydration around Lys73:OQ2. For the lower barriers in Figure 6.3, the number of hydrogen bonds to OQ2 is 1.3-1.4, and for the higher barriers 2.1-2.3 for orientation I. The lowest calculated deacylation barrier, 8.5 kcal/mol, is for imipenem in orientation I with one water hydrogen bonded to OQ2 and two to OQ1 (Figure 6.4). The barrier increases by 1.9 kcal/mol when another solvent molecule donates a hydrogen bond to OQ2. For meropenem, the barrier is raised by 3.5 kcal/mol upon introducing an additional water near OQ2. The hydration effect around Lys73:OQ2 indicated here has a smaller effect on calculated barriers than hydration around Lys73:OQ1, since having an additional water hydrogen bonded to OQ1 raised the barrier by approximately 5 kcal/mol for ceftazidime deacylation.[257] As the electrons are delocalised in the carboxylate anion, it is plausible that changing the interactions around the non-reactive oxygen affects also the charge distribution, i.e. basicity, of the reactive OQ1.

Orientation II is observed in most OXA-48/carbapenem crystal structures (corresponding dihedral between 147°-192° depending on the structure and protein chain). In this orientation, no part of the 6α-hydroxyethyl moiety interacts with the DW or with Lys73, so the antibiotic may possibly not interfere with the reactive atoms. However, calculated deacylation barriers are increased by 2.0 for imipenem and by 1.8 kcal/mol for meropenem when comparing orientation II against I (with only one water hydrogen bonded to OQ2). Having two waters donating hydrogen bonds to both OQ1 and OQ2 further raises the barriers to 13.6 and 16.0 kcal/mol for imipenem and meropenem, respectively. Therefore, our simulations suggest that II is not the most deacylation-compatible AC orientation. Additionally, orientation II might hinder the presence of the DW in the active site in proximity to the electrophilic acyl carbon. For 93% and 87% of simulation time for imipenem and meropenem (respectively) in orientation II, the distance between the AC electrophilic carbon

and the closest water falls beyond 4 Å (an arbitrary threshold distance for a feasible nucleophilic attack; Figure S5 in Section 6.6). This is likely due to the 6α-hydroxyethyl methyl group partly occupying the space in the deacylating water pocket and thereby forcing water further away from the AC. This is reflected in deposited crystal structures, as a suitable DW positioned for nucleophilic attack is not observed in any OXA-48/carbapenem complex.[71, 233, 239-241] In a previous study, orientation II was observed to obstruct the positioning of the DW in the active site. The authors concluded that only slight re-positioning of the methyl group of the 6α-hydroxyethyl sidechain is needed to better accommodate a water molecule at a suitable distance for nucleophilic attack. However, these conclusions are based on one 10 ns MD simulation, which provides insufficient conformational sampling of all available substrate orientations. Based on our MM MD simulations as well as calculated free energy barriers, orientation II is less likely to contribute to efficient deacylation both due to an increase in required energy as well as due to the lack of suitable active site configurations to undergo nucleophilic attack.

The largest increase in energetics between the two hydration states is calculated for orientation III, where the barriers increase 9.6 and and 5.6 kcal/mol for imipenem and meropenem (respectively), when changing the hydration state. For the lower barriers, OQ1 and OQ2 form on average 1.9-2.1 and 1.4-1.5 hydrogen bonds, respectively, for imipenem and meropenem complexes, while for the higher barriers the same numbers are 2.7-2.9 and 1.8-2.3. For the lower barriers, Leu158 has not (yet) rotated from the *g*- to *t* rotamer (Figure S4, Section 6.6), as the starting structures were chosen almost directly after the heating phase. The g- rotamer of L158 allows space only for the DW near Lys73:OQ1, which was inserted to the active site in the starting model. Further, only one water is donating a hydrogen bond to OQ2. Upon MD equilibration, Leu158 rotates, allowing for active site hydration to change to two water molecules hydrogen bonding to both carboxylate oxygens. Subsequently, only the "high barrier" hydration state is sampled. This explains the large increase in activation free energy when comparing the two hydration substates for orientation III, as two water molecules are added near Lys73 as opposed to only one near Lys73:OQ2 (as for I and II). Therefore, our simulations indicate that III is the least deacylation-compatible AC orientation for the equilibrated system (where Leu158 has rotated). Experimentally, this AC orientation is seen in the crystal structure of OXA-48 with hydrolysed, non-covalently bound imipenem (PDB ID 6PK0)[240], where the hydroxyl part is donating a hydrogen bond to the newly-formed carboxylate group. As observed in our MM MD simulations of the AC, the exchange between 6-hydroxyethyl dihedral orientations is frequent (indicating a low energy barrier). This is likely

true also for the hydrolysed antibiotic, in which case the rotation of this moiety can occur post-deacylation.

Further analysis of the US trajectories reveals that hydration around Lys73:OQ2 correlates with the rotamer of Val120. Valine has three rotamers for the χ_1 dihedral (N-Cα-Cβ-Cγ1): *g*+ rotamer around 50°, *t* around 180°, and *g*- around 300° (Figure 6.4, Figure S6 in Section 6.6). In the starting structures for simulations, Val120 is in the *t* orientation for both carbapenems (for meropenem, partial occupancy for both *t* and *g*– rotamers were observed in the deposited structure, but the *t* rotamer was used in model building).[71] The rotameric state can switch to either *g*+ or *g*- during MD (Figure S6 in Section 6.6). For the *g*+ rotamer, one of the methyl groups points directly to Lys73, which only leaves space for one water molecule next to Lys73:OQ2; this water is positioned to accept a hydrogen bond from Gln124 and to donate one to Lys73. Conversely, the *t* rotamer allows for a second water to occupy the space between Lys73 and Val120, where the water molecule donates hydrogen bonds to both Lys73:OQ2 and the Val120 backbone carbonyl. Val120 is part of motif II, which is formed by residues Ser118-Val120 and conserved across class D β-lactamases.[222] Together with Leu158, it forms the so-called "deacylating water channel" in the vicinity of Lys73; this hydrophobic patch essentially partly shields the active site from bulk solvent.[71] For other OXAs, a similar water channel has been proposed to open upon substrate binding to allow for water ingress into the active site and ergo efficient deacylation.[251, 330] For OXA-48, previous comparison of apoenzyme and acylenzyme structures shows that substrate binding shifts the Val120 and Leu158 only slightly, and the water channel is permanently more open than e.g. in OXA-23.[71] Access of water into the catalytic position next to the substrate and Lys73 is necessary for antibiotic hydrolysis, but as we indicate above, any additional solvent in the active site will impair reactivity. In OXA-48, it appears that the rotamer of Val120 is an important gateway residue for bulk solvent to approach Lys73:OQ2, and our previous work (on ceftazidime hydrolysis in OXA-48-like enzymes) indicates that Leu158 can module hydration near Lys73:OQ1.[257] Interestingly, Val120 has been mutated to a leucine in OXA-519, a single point mutant of OXA-48. This mutation results in increased measured hydrolysis for some 1β-methyl carbapenems, like meropenem and ertapenem, but decreased imipenemase efficiency.[331] Further studies indicate that OXA-519 increases the portion of β-lactone reaction products with respect to standard hydrolysis products for meropenem.[254] Establishing the role of Val120 mutations to the hydrolysis efficiency as well as to β-lactone formation remains as a subject for future research efforts.

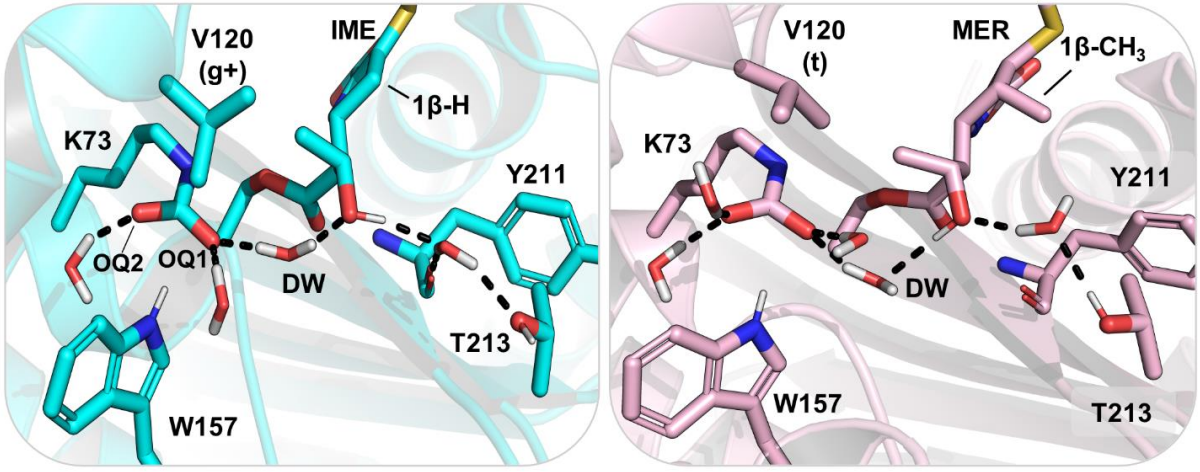

Figure 6.4. Alternative hydrogen bond configurations found with the 6α-hydroxyethyl in orientation I. Left: Active site of OXA-48 with imipenem in hydrogen bond configuration 1. Val120 adopts the g+ rotamer, and consequently only one water molecule is forming a hydrogen bond with Lys73:OQ2. The 6α-hydroxyethyl is in orientation I and donates a hydrogen bond to a water lodged between the Tyr211 backbone and Thr213. Right: Active site interactions of OXA-48 with meropenem in hydrogen bond configuration 2. Val120 is in its t rotameric state, which allows for two waters to hydrogen bond with both Lys73 carboxylate oxygens. The 6α-hydroxyethyl is in orientation I but donating a hydrogen bond to the DW.

6.4.3 Comparison of carbapenem deacylation in orientation I

As presented above, orientation I of the 6α-hydroxyethyl moiety is calculated to have the overall lowest deacylation free energy barriers for both carbapenems. The combined free energy surfaces for the hydration state with lower free energy barriers are presented in Figure S7 (Section 6.6) for all three substrate conformations. In this section, we focus further on orientation I and the 'reactive' active site configuration with only one water molecule hydrogen bonded to Lys73:OQ1, and two to Lys73:OQ2 (unless otherwise stated). For this AC conformation, two different hydrogen bond arrangements in the active site are possible: the DW can donate a hydrogen bond to the hydroxyl group (named configuration 1), or the hydroxyl group can donate a hydrogen bond to the DW (configuration 2), see Figure 6.4. In MM MD, configuration (1) is sampled for 87% and 86% of simulation time for imipenem and meropenem, respectively. In addition to donating a hydrogen bond to the DW, the hydroxyl group can also donate a hydrogen bond directly to Lys73:OQ1 if the DW is displaced. This 6α-hydroxyethyl orientation may be the relevant one for β-lactone formation, which has been

characterised as a side product for OXA-48 with 1β-methyl carbapenems (such as meropenem).[253, 254] The β-lactone product has been proposed to form via intramolecular cyclisation, where the hydroxyl group acts as a nucleophile and donates a proton to Lys73. If the reaction occurs without a bridging water molecule, i.e. by a direct proton transfer between -OH and Lys73, lactonisation is most likely lower in energy in orientation I than in III based on the trends observed for deacylation energetics.

For imipenem deacylation, both configurations (1) and (2) were observed in US sampling. The lowest free energy barrier of 8.5 kcal/mol was calculated for configuration (1), and the barrier was increased by 1.9 kcal/mol for configuration (2). In addition to raising the free energy barriers, changing from (1) to (2) shifts the location of the transition state on the FES. For (1), the TS is located approximately at values –0.1 Å and 1.7 Å for the proton transfer and nucleophilic attack reaction coordinates, respectively. However, for (2), the TS location on the FES shifts to around –0.5 Å and 2.0 Å. Free energy surfaces with corresponding TS structures for both active site configurations are presented in Figure 6.5 and Figure S8 (Section 6.6). With active site configuration (2), the proton transfer has progressed further at the TS, whereas the approach of the DW oxygen to the acyl carbon less advanced. This is potentially due to the additional hydrogen bond from the 6α-hydroxyethyl moiety hydroxyl decreasing the nucleophilicity of the DW, which requires the proton transfer reaction to have progressed further from the starting structure at the TS. Notably, a similar shift in the TS position on the FES is observed also in orientation III, where a water molecule is donating a hydrogen bond to the DW instead of the 6α-hydroxyethyl group (Figure S7 in Section 6.6). Mulliken charge analysis of the key QM atoms does not reveal many significant differences for the calculated charges along the reaction when comparing US calculations with either configuration (1) or (2) (Tables S5-S8 in Section 6.6). The main difference is calculated at the TS, where for

Lys73:OQ1, the charge is more positive and for DW:O the charge is more negative for configuration (2), as expected by the shift in the TS location towards the TI.

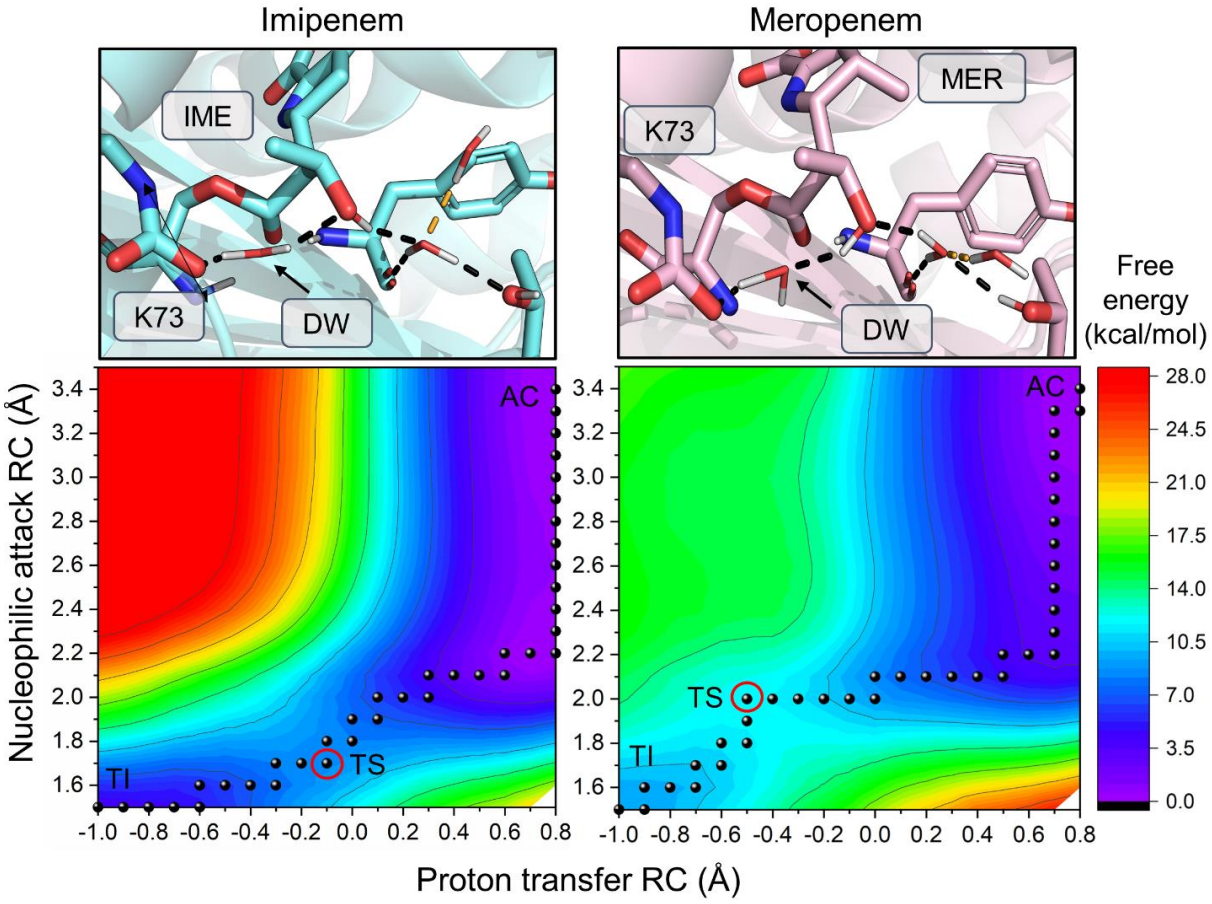

Figure 6.5. Free energy surfaces and transition state structures for alternative active site hydrogen bond configurations. Left: Free energy surface for imipenem deacylation for the lowest calculated barrier in orientation I. The DW is donating a hydrogen bond to the carbapenem hydroxyl group. Right: Free energy surface for meropenem deacylation with the lowest calculated barrier in orientation I. The carbapenem hydroxyl group donates a hydrogen bond to the DW. AC=acylenzyme, TS=transition state, TI=tetrahedral intermediate.

For meropenem, the lowest calculated deacylation barrier is 11.8 kcal/mol with an average of 2.3 and 1.3 hydrogen bonds accepted by K73:OQ1 and OQ2, respectively. This is 3.3 kcal/mol higher than the lowest calculated barrier for imipenem, or 2.7 kcal/mol higher if the free energy penalty derived from MM MD for imipenem to form orientation I is considered as well. In contrast to imipenem, the hydroxyl of the 6α-hydroxyethyl moiety in meropenem always rotates during unrestrained US sampling to hydrogen bond configuration (2), donating

a hydrogen bond to the DW. This rotation occurs before the TS is reached even when configuration (1) is present in the starting structure. Enforcing the DW to donate a hydrogen bond to the 6α-hydroxyethyl -OH, i.e. restraining the reaction simulations to configuration (1), affects the location of the TS in a similar manner to that observed with imipenem. TS locations for configurations (1) and (2) are at –0.2/1.8 Å and –0.5/2.0 Å (proton transfer/nucleophilic attack), respectively. However, changing the hydrogen bonding pattern between configurations has only a minimal effect on the energetics, as the barrier for (1) is 11.9 kcal/mol. Therefore, the decrease in activation energy for configuration (1) vs. (2) does not follow the same trend for meropenem as it does for imipenem. Possible reasons for this may include the presence of a 1β-methyl in meropenem, as this group may hinder the rotation of the 6α-hydroxyethyl group to better optimise further hydrogen bonds between active site residues and water molecules nearby. A water molecule lodged between Tyr211 and Thr213 accepts a hydrogen bond from the carbapenem -OH moiety in configuration (1) or donates a hydrogen bond to it in configuration (2) (Figure 6.5 and Figure S8 in Section 6.6). The 1β-methyl group occupies the space above this water and may therefore induce its displacement or the re-organization of the surrounding water molecules to optimise hydrogen bonds between them, which could subsequently lead to a change from configuration (1) to (2). Additionally, the initial nucleophilic approach of the DW (from 3.5 Å to 2.2 Å) with the 6α-hydroxyethyl moiety in orientation I and hydrogen bond configuration (1) is calculated to be slightly lower in energy for imipenem (Figure S9, Section 6.6). (Notably, the initial approach between the DW and the carbapenem is also slightly higher in energy in orientations II and III than in orientation I, which may contribute to their overall energetics being less favourable for deacylation). However, the reasons for the preference for the imipenem complex to adopt configuration (1), but not for the meropenem complex, are likely subtle and can result from small structural changes between the active site, substrate, and solvent molecules.

6.4.4 Comparison with experimental data

Most of the variants in the OXA-48 family are carbapenemases, with elevated imipenem hydrolysis rates when compared against other carbapenems.[205] For OXA-48, experimental measurement of k_{cat} values for imipenem hydrolysis vary between 1.5 and 22.5 s^{-1}, which can be converted to $\Delta^{\ddagger}G$=15.7-17.3 kcal/mol using the Eyring equation. For meropenem, the measured k_{cat} values range between 0.07-0.16 s^{-1}, which converts to $\Delta^{\ddagger}G$=18.7-

19.2 kcal/mol. Comparing these experimentally determined free energies of activation, there is a difference between imipenem and meropenem hydrolysis ($\Delta\Delta^{\ddagger}G$) of 1.4-3.5 kcal/mol, which is approximately the same magnitude as the strength of a single hydrogen bond (1-3 kcal/mol).[332] Hence, structural factors contributing to efficient imipenem breakdown over 1β-methyl carbapenems are most likely to be subtle. Our QM/MM simulations suggest that orientation I of the 6α-hydroxyethyl moiety is the most likely AC orientation to undergo deacylation, together with decreased hydration around Lys73:OQ2 (i.e., only one water molecule donating a hydrogen bond to this carboxylate oxygen). When comparing the lowest free energy barriers calculated in orientation I for imipenem and meropenem (Figure 6.3), the difference for the two substrates is $\Delta\Delta^{\ddagger}G$=3.3 kcal/mol; adding the free energy penalty for the imipenem 6α-hydroxyethyl moiety adopting orientation I (0.6 kcal/mol, as determined from our MM MD simulations), the obtained $\Delta\Delta^{\ddagger}G$ value drops to 2.7 kcal/mol. This is in excellent agreement with the experimentally determined range of $\Delta\Delta^{\ddagger}G$ values, which implies that the difference between imipenem and meropenem deacylation may indeed be caused by the subtle difference in the preferred hydrogen bonding patterns involving the DW and the 6α-hydroxyethyl sidechain reported here. In turn, the 1β-methyl group is likely involved in causing this difference.

6.5 Conclusions

We have modelled carbapenem hydrolysis by the OXA-48 β-lactamase using QM/MM reaction simulations. For two carbapenem substrates with differing hydrolysis efficiencies, imipenem and meropenem, deacylation reactions were compared to deduct the origin of the higher activity towards imipenem compared to other carbapenems. MM MD simulations of the acylenzyme complexes support that the carbapenem tail groups do not conform to any particular orientation but are able to adopt many different conformations. Furthermore, the 6α-hydroxyethyl group is able to rotate and to adopt three different orientations, where it either interacts with the DW (I), Lys73 (III), or is rotated so that the methyl end is oriented towards Leu158 (II). Subsequently, deacylation was modelled for all these three orientations to investigate their effect on deacylation efficiency. Our calculated free energy barriers indicate that the most deacylation-compatible orientation is I, where the hydroxyl group interacts with the DW, and that the orientation III has the highest free energy barriers.

Detailed comparison of the reaction simulations revealed two factors contributing to the calculated energetics: hydration around Lys73, and the hydrogen bonding pattern between

the DW and substrate. Hydration around the general base has been noted to affect predicted hydrolysis rates for other β-lactam substrates,[257] and here we extend this argument to include hydration around both Lys73 carboxylate oxygens (instead of only the oxygen participating in proton transfer). Increase in hydration around the second, non-reactive, oxygen (Lys73:OQ2) was observed to correlate with higher calculated barriers, and the rotation of Val120 in turn to correlate with the number of water molecules near this oxygen. Another aspect influencing the deacylation efficiency are the hydrogen bonds in the active site involving the DW and the 6α-hydroxyethyl sidechain. Imipenem shows a preference for the configuration where the DW donates hydrogen bonds to Lys73 and the 6α-hydroxyethyl hydroxyl group, with an increase in barrier when the hydroxyl group rotates to donate a hydrogen bond to the DW instead. This preference is not observed for meropenem, where the reaction simulations with both hydrogen bond configurations have comparable energy barriers, which are similar to that calculated for imipenem in the "less-favorable" orientation. Therefore, we hypothesise that the difference between hydrolysis activities for carbapenem substrates stems from subtle differences in the active site hydrogen bonding patterns, which affect the reactivity of the DW. Furthermore, our results indicate that active site hydration is an important determinant for catalysis in OXA-48 enzymes, as increasing the hydration around the general base is observed to impair carbapenem hydrolysis. Our study highlights the importance of detailed atomistic modelling in addition to experimental research to determine origins of activity, as simulation protocols such as ours enable studying specific active site interactions during catalysis.

6.6 Computational details

This section comprises the Supporting Information for Chapter 6.

System Setup

The OXA-48 with imipenem model was set-up starting from a corresponding acylenzyme (AC) crystal structure (PDB ID: 6P97)[71], as well as OXA-48 with meropenem (PDB ID: 6P98)[71]. In both structures, Lys73 is not carboxylated and was thus replaced by its carboxylated form as found in another OXA-48 + imipenem acylenzyme structure (PDB ID: 5QB4)[239]. The deacylating water (DW) was added manually to both models, and all crystallographic water molecules were kept in place. The pK_a values of titratable residues were

inspected using propKa 3.1,[167] and all residues were kept in their standard state (protonated Lys, deprotonated Glu and Asp residues). Histidine tautomers were assigned using the reduce program (in Amber): all histidines were singly protonated at the ε-nitrogen except for residues 38 and 140, which were singly protonated at the δ-nitrogen. Hydrogens were added to the structures using tLeap upon system preparation, and the enzyme was solvated in a 12 Å TIP3P water box. The systems were neutralized by randomly replacing bulk water molecules with Na^+ counter ions (using the default TIP3P compatible ion parameters in Amber). The ff14SB parameter set was used for the protein.[100]

Partial charges and force field parameters for the non-standard Ser70+carbapenem residues were derived using the restrained electrostatic potential (RESP) fitting as implemented in the R.E.D. Server.[172] Analogous gaff parameters were substituted for any missing parameters.[168] Parameter files for carboxylated lysine and carbapenem ACs are available as part of the Supporting Information.

Computational Methods

After system preparation, all models were initially briefly minimized for 2000 steps to avoid any steric clashes (1000 steps conjugate gradient and 1000 steps steepest descent). After minimization, the systems were heated from 50 K to 300 K in 20 ps, and subsequently simulated for 200 ns in the NPT ensemble. Langevin dynamics were used in all simulations with a collision frequency of 0.2 ps^{-1}. MD timestep was 2 fs, and all bonds involving hydrogen atoms were constrained using the SHAKE algorithm. Structures during MD were recorded every 20 ps (10k MD frames/trajectory). The Amber18 package with Ambertools19 was used for all calculations,[166] and specifically the pmemd.cuda MD engine for all extended MM MD simulations.[299, 301] All trajectory analysis was done using cpptraj[333] (as implemented in Ambertools19) excluding 50 ns from the start to allow time for system equilibration. Hydrogen bond analysis using cpptraj was done using the default criteria set in cpptraj (donor-acceptor distance less than 3.4 Å, the D-H-A angle between hydrogen bond donor and acceptor deviates less than 45° from a linear angle).

Starting structures for QM/MM umbrella sampling (US) were chosen from restart files saved during the 200 ns MM MD simulations based on visual inspection (starting structures taken at least 1 ns apart unless otherwise stated). All starting snapshots had the desired 6α-

hydroxyethyl orientation and a suitable DW in place, as to not introduce big distortions through restraints when starting US calculations. Three different starting structures were used per free energy barrier (unless otherwise stated). The DFTB2 (SCC-DFTB)[158, 162] method was used for describing the QM region consisting of either 43 or 46 atoms for imipenem and meropenem, respectively (Figure S1). The ester bond in the AC was restrained with a one-sided harmonic restraint to avoid elongation beyond 1.6 Å (force constant 100 kcal mol^{-1} $Å^{-2}$), and the 6α-hydroxyethyl group dihedral was restrained near its initial values during reaction simulations. In orientation II, the sidechain dihedral was restrained between values 150-200°, and in orientation III between 270-310°, the applied force constant was 50 kcal mol^{-1} $Å^{-2}$. No dihedral restraints were applied in orientation I, as switching from this orientation to another one was not observed during US. However, distance restraints between the meropenem 6α-hydroxyethyl hydroxyl group and an active site water molecule were applied to enforce the active site configuration where the DW donates a hydrogen bond the hydroxyl group. A one-sided harmonic restraint was added for this hydrogen bond to avoid elongation beyond 2.2 Å (force constant of 50 kcal mol^{-1} $Å^{-2}$).

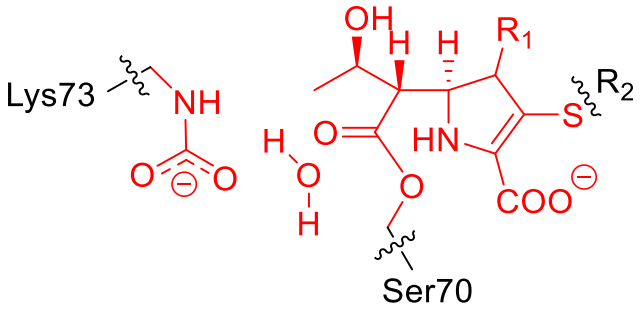

Figure S1. QM region in US simulations, QM atoms in red. Link atoms based along bonds indicated with wavy lines.

Full deacylation free energy surfaces (FESs) were calculated using two reaction coordinates to describe the proton transfer (PT) and nucleophilic attack (NA). Reaction coordinate values were decreased from 0.8 **Å** /3.5 **Å** (PT/NA) in the AC to -1.0 **Å** /1.5 **Å** in the TI by 0.1 Å. Force constants for both reaction coordinates were 100 kcal mol^{-1} $Å^{-2}$. Full deacylation free energy surfaces (FESs) were constructed by first performing US along an approximate diagonal on the FES (used as a proxy for the minimum free energy path), and then

calculating the rest of the US windows using these calculations as a starting point. Initial sampling along the diagonal included 36 windows with values:

PT	0.8	0.8	0.8	0.8	0.8	0.8	0.8	0.8	0.7	0.7	0.7	0.6	0.6	0.5	0.5	0.5	0.5
NA	3.5	3.4	3.3	3.2	3.1	3.0	2.9	2.8	2.7	2.6	2.5	2.5	2.4	2.4	2.3	2.2	2.2

PT	0.4	0.3	0.2	0.1	0.0	-0.1	-0.2	-0.3	-0.3	-0.4	-0.5	-0.6	-0.7	-0.7	-0.7
NA	2.2	2.2	2.1	2.1	2.1	2.1	2.1	2.1	2.0	2.0	1.9	1.9	1.9	1.9	1.8

PT	-0.7	-0.8	-0.8	-0.8	-0.9	-1.0
NA	1.7	1.7	1.6	1.5	1.5	1.5

The whole FESs consisted of a total of 399 US windows, and the sampling time was 2 ps/window with a 1 fs timestep. FESs were constructed using the weighted histogram analysis method (WHAM, Grossfield lab)[329] with 19 and 21 bins for the PT and NA coordinates, respectively. The convergence criterium was set to 10^{-13}. Minimum free energy paths on the FESs were analyzed using the Minimum Energy Path Surface Analysis (MEPSA) program.[298] All US calculations were performed using sander.MPI as implemented in Ambertools19.[166]

Acylenzyme clustering

Clustering of the AC orientations was done separately for imipenem and meropenem MM MD trajectories (excluding 50 ns from the start, five simulations per substrate with 7500 frames per simulation). Trajectories were aligned on Cα-atoms of residues 70-73, 118-120, 157, 158, and 209-211, and substrate orientations were clustered into four groups based on AC heavy atom RMSD. The kmeans algorithm (as implemented in cpptraj) was used for the clustering procedure with a sieve of 10. The representative structures for the four clusters are presented in Figure S2 along the corresponding AC orientation in the original crystal structure.

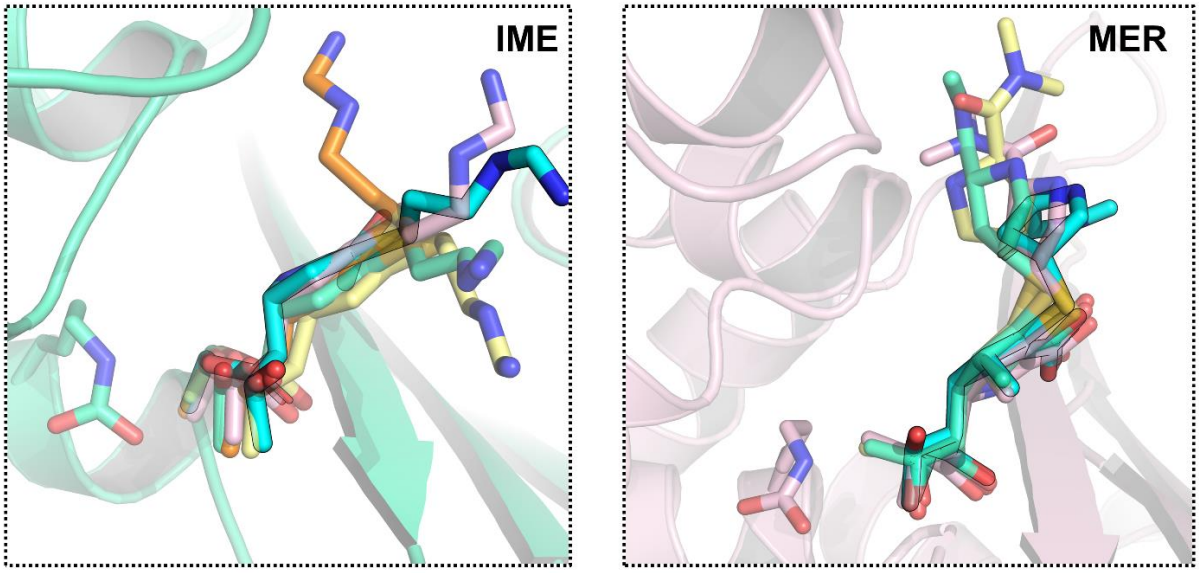

Figure S2. Representative structures from AC clustering for imipenem (left) and meropenem (right). Cluster 1, green; cluster 2, pink; cluster 3, yellow; cluster 4, orange, the crystallographic binding pose in cyan.

Table S1. Further clustering information for the substrate binding pose for imipenem (IME) and meropenem (MER). Fraction represents the fraction of simulation frames belonging to the clusters and colour the corresponding sticks representation color in Figure S2. RMSD measured between carbapenem heavy atoms in the representative cluster structure and in the crystal structure.

		IME		**MER**	
	Color	Fraction	RMSD (Å)	Fraction	RMSD (Å)
Cluster 1	Green	0.55	0.81	0.36	1.65
Cluster 2	Pink	0.21	0.82	0.34	1.75
Cluster 3	Yellow	0.13	1.09	0.25	2.16
Cluster 4	Orange	0.11	1.75	0.05	2.49

In addition to AC clustering, the active site conformations for both imipenem and meropenem simulations were compared by combining all trajectories and clustering the structures based on the common AC atoms (i.e. all atoms except C2 tail groups beyond sulphur and the 1β-group). Solvent molecules, counterions, and parts of the enzyme which were not identical between the two models were stripped before clustering. Trajectories were aligned on the mainchain heavy atoms of residues 70, 73, and 157, and clustering done based on RMSD

of the remaining carbapenem heavy atoms. The kmeans clustering algorithm was used to divide the structures in to four clusters with a sieve of 10 (as in cpptraj).

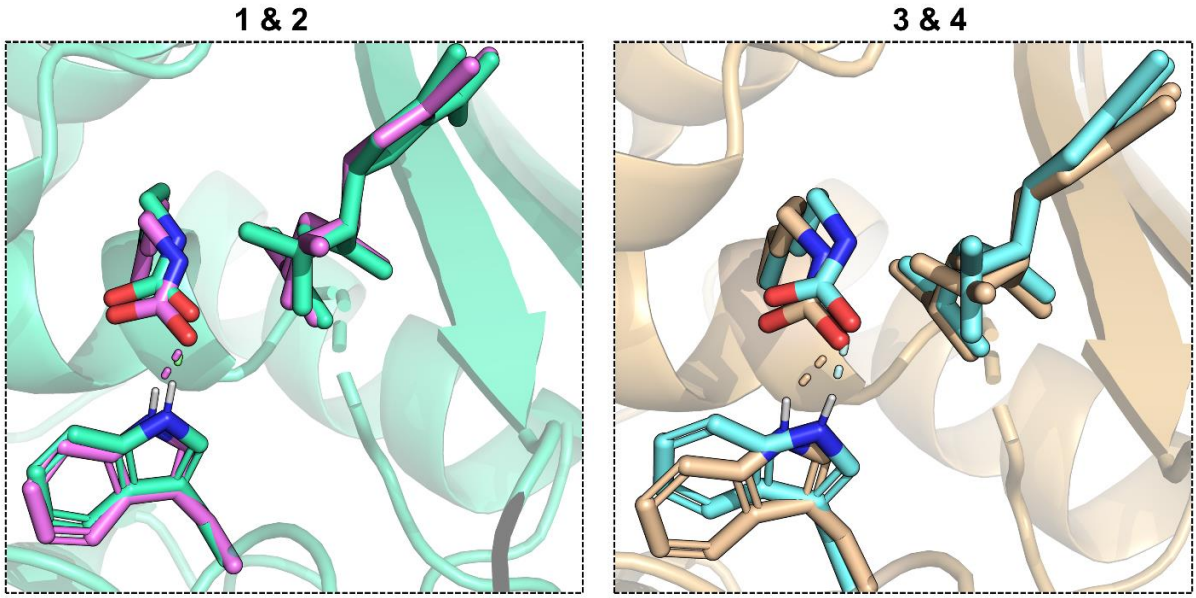

Figure S3. Representative cluster structures for the combined clustering of imipenem and meropenem trajectories. Left: Clusters 1 and 2 are sampled for most of the simulation time for meropenem (green) and imipenem (purple), respectively. Right: For the rest of time, cluster 3 (brown) is sampled for imipenem and cluster 4 (cyan) for meropenem.

Table S2. Combined cluster fractions in imipenem and meropenem trajectories.

	Color	Fraction (IME)	Fraction (MER)
Cluster 1	Green	0.00	0.71
Cluster 2	Purple	0.65	0.00
Cluster 3	Brown	0.35	0.00
Cluster 4	Cyan	0.00	0.29

Leu158 Dihedral Sampling

Leu158 has been proposed to modulate the access of bulk solvent near Lys73 in ceftazidime deacylation.[257] The orientations of Leu158 were analysed by measuring the sidechain χ_1 dihedral angle (N-Cα-Cβ-Cγ). In both crystal structures used for model building, Leu158 is in the *g-* orientation (in OXA-48/meropenem structure,[71] the residue has rotated 180° around the Cβ-Cγ bond). Upon MD equilibration, Leu158 essentially always adapts to the *t* state, as depicted by Figure S4.

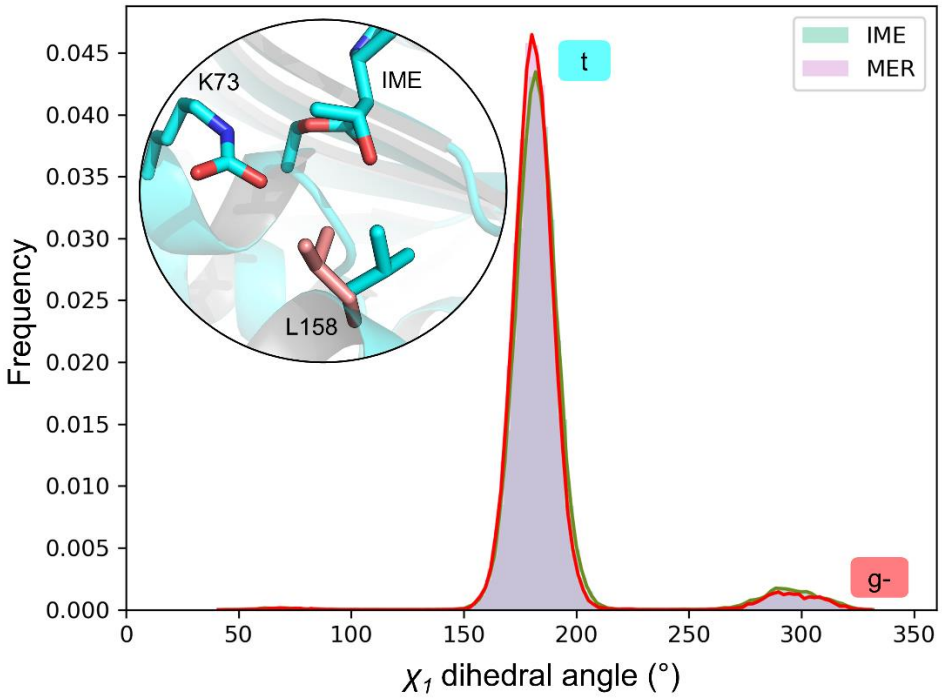

Figure S4. Sampling distribution for Leu158 rotamers in MM MD for imipenem (green) and meropenem (red). Leu158 rotates from the starting g- orientation (red sticks representation in the insert) to the t orientation (cyan) for the majority of the simulation time.

MM MD Analysis

To preliminarily study the effect a certain AC conformation has on the nucleophilic attack, the distance between the AC electrophilic carbon and the closest water molecule was measured. The corresponding scatter plots are presented in Figure S5, where a threshold of 4 Å is indicated with a dashed line; distances below this threshold are regarded suitable for a nucleophilic attack (although the choice of this threshold value is somewhat arbitrary). For both carbapenems, a water molecule is found at a suitable distance for the nucleophilic attack

in all three orientations, even when the majority of the active site configurations fall beyond 4 Å for orientations II (~180°) and III (290°).

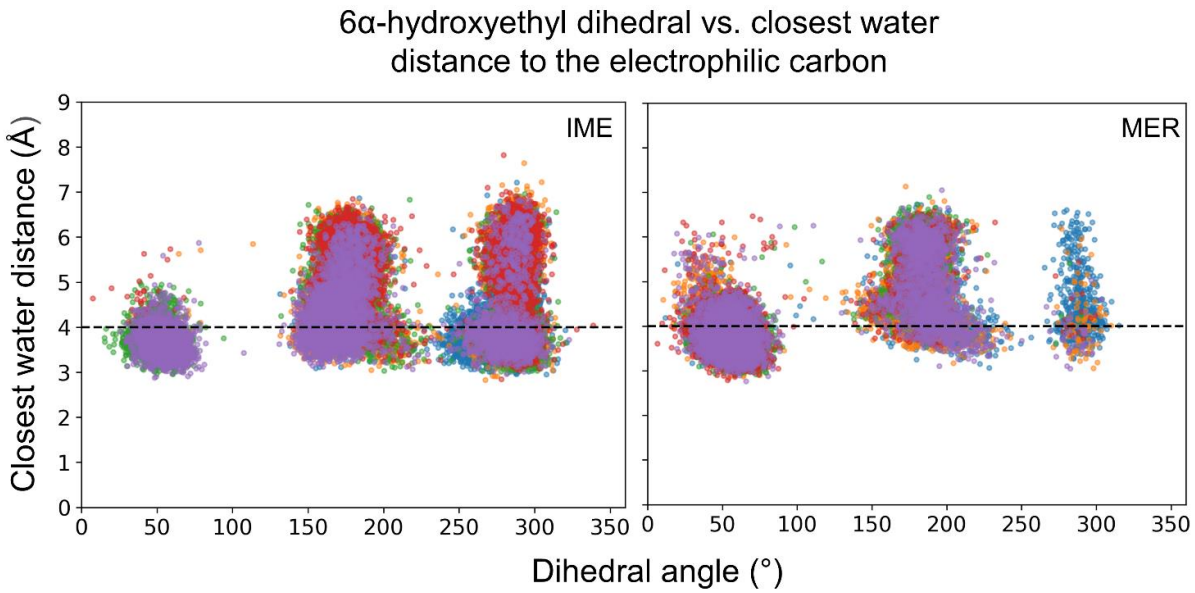

Figure S5. The distribution of distances from the AC electrophilic carbon to the closest water molecule in the active site. Distances measured for all five 150 ns simulations per system (50 ns were excluded from the start for each simulation, total simulation length 200 ns). Each scatter point represents a frame in a trajectory, different colours represent different trajectories. Dashed line at 4 Å is the used as an arbitrary threshold distance for determining the feasibility of nucleophilic attack, i.e. arrangements beyond 4 Å are not likely to undergo deacylation.

Val120 Dihedral Sampling

Val120 adopts three different orientations during MM MD, which can be differentiated by the χ_1 (N-Cα-Cβ-Cγ1) dihedral angle: *g*+ at around 60°, *t* at 180°, and *g*- at 290°. Val120 is situated in the vicinity of Lys73 and Trp157, and its rotamer influences the accessibility of water near Lys73 (especially near Lys73:OQ2). The distribution of sampled Val120 χ_1 dihedrals is presented in Figure S6. The *t* rotamer, which is observed in both crystal structures used as starting models, is the most sampled state for both imipenem and meropenem; this orientation allows for two water molecules to hydrogen bond with Lys73:OQ2. When the dihedral angle rotates to the *g*+ state, only one water has space to donate a hydrogen bond to

OQ2, as the γ2-carbon occupies the space available for water in the case of *t* rotamer. The *g*-rotamer was observed the least, and it was not present in any starting structure used for US.

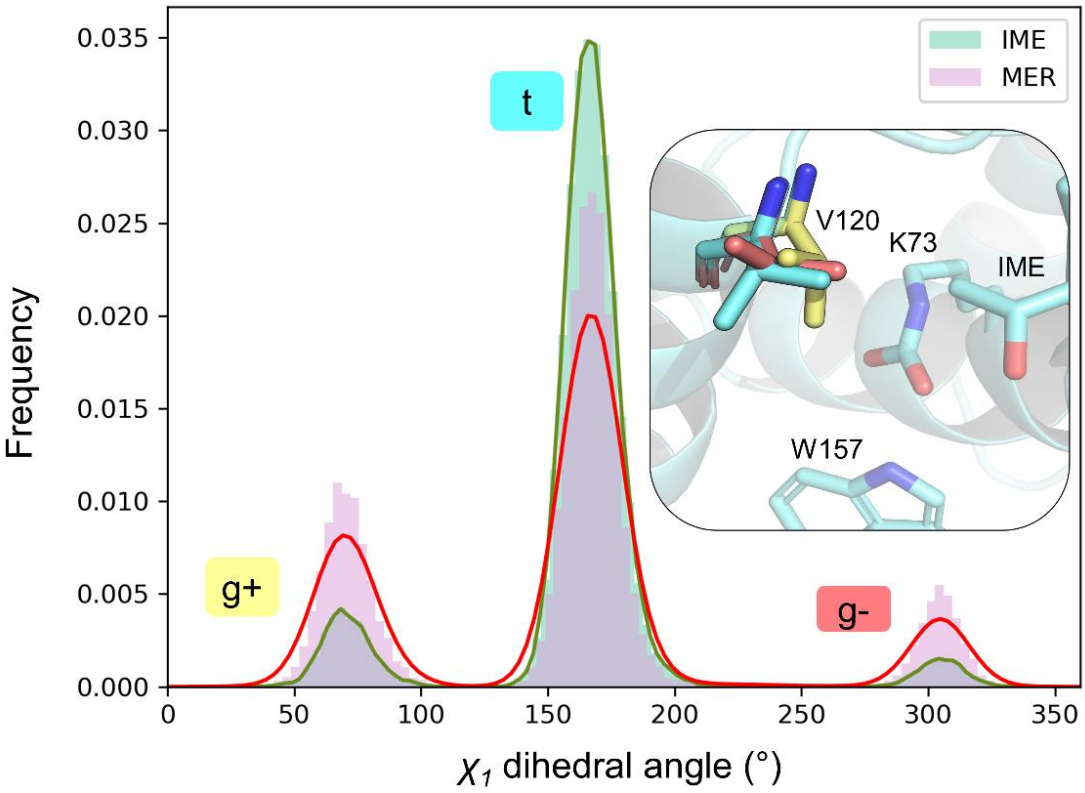

Figure S6. V120 rotamer distribution in MM MD for imipenem (green) and meropenem (red). Rotamer label coloring corresponds to the stick color representation of the rotamer structure in the inset. Histograms created using 100 bins, probability distributions (solid line) obtained using the kernel density estimation in the seaborn library (python) with default parameters.

Umbrella Sampling

Overall free energy barriers for different AC orientations with different hydration states are presented in Table S3. Barriers are calculated by combining sampling from three separate US calculations into one WHAM calculations (the overall sampling time being 2x3ps = 6ps/window, 2.4 ns for the full surface), standard deviations are between the individual snapshots.

Table S3. Free energy barriers for carbapenem deacylation from umbrella sampling. All energies in kcal/mol, standard deviations between barriers obtained for the three individual US calculations in parenthesis. Hydration state 1 = only one water donating a hydrogen bond to Lys73:OQ2, two waters donating a hydrogen bond to Lys73:OQ1 (except orientation III, where only one), hydration state 2 = two waters hydrogen bonded to both Lys73 carboxylate oxygens.

	Imipenem		**Meropenem**	
	Hydration state 1	Hydration state 2	Hydration state 1	Hydration state 2
Orientation I[1]	8.5 (0.9)	10.4 (0.4)	11.9 (0.7)	-
Orientation I[2]	10.4 (0.4)	13.5 (1.0)	11.8 (0.7)	15.3 (1.1)
Orientation II	10.5 (1.1)	13.6 (0.9)	13.6 (1.1)	16.0 (1.1)
Orientation III	11.2 (0.6)	20.8 (1.4)	12.4 (2.0)	18.0 (0.5)

[1] DW donates a hydrogen bond to the carbapenem hydroxyl group

[2] DW accepts a hydrogen bond from the carbapenem hydroxyl group

The FESs for both imipenem and meropenem for all three 6α-hydroxyethyl orientations are presented in Figure S7. The minimum free energy paths are illustrated with black dots. All surfaces are for the active site configuration, where only one water donates a hydrogen bond to Lys73:OQ2. In orientation I, the DW donates a hydrogen bond to imipenem 6α-hydroxyethyl hydroxyl group, whereas for meropenem, the DW accepts a hydrogen bond from the same hydroxyl.

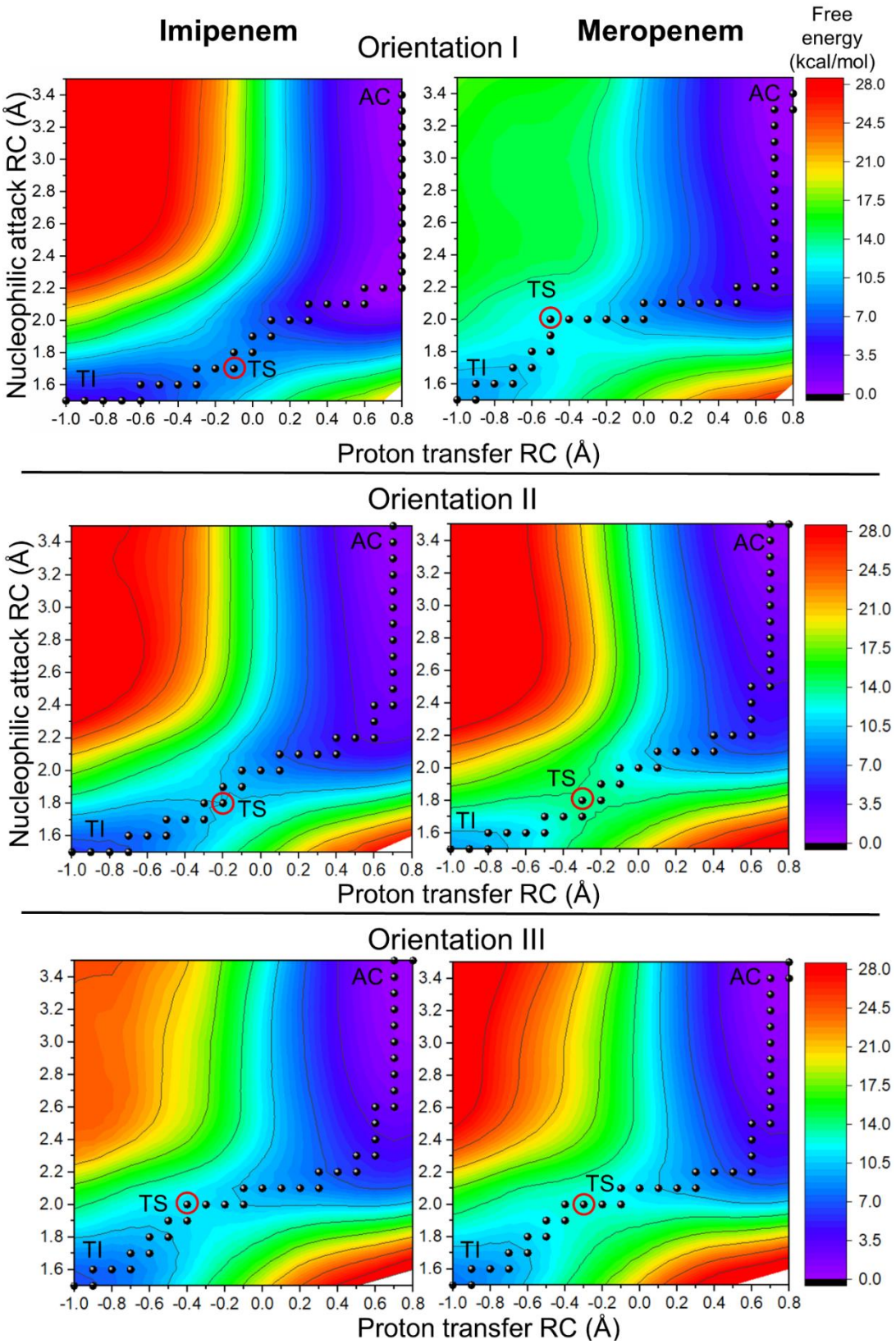

Figure S7. Calculated free energy surfaces for imipenem (left) and meropenem (right) deacylation in substrate orientations I (top), II (middle), and III (bottom. The minimum free energy paths marked with black dots. AC=acylenzyme, TS=transition state (circled), TI=tetrahedral intermediate.

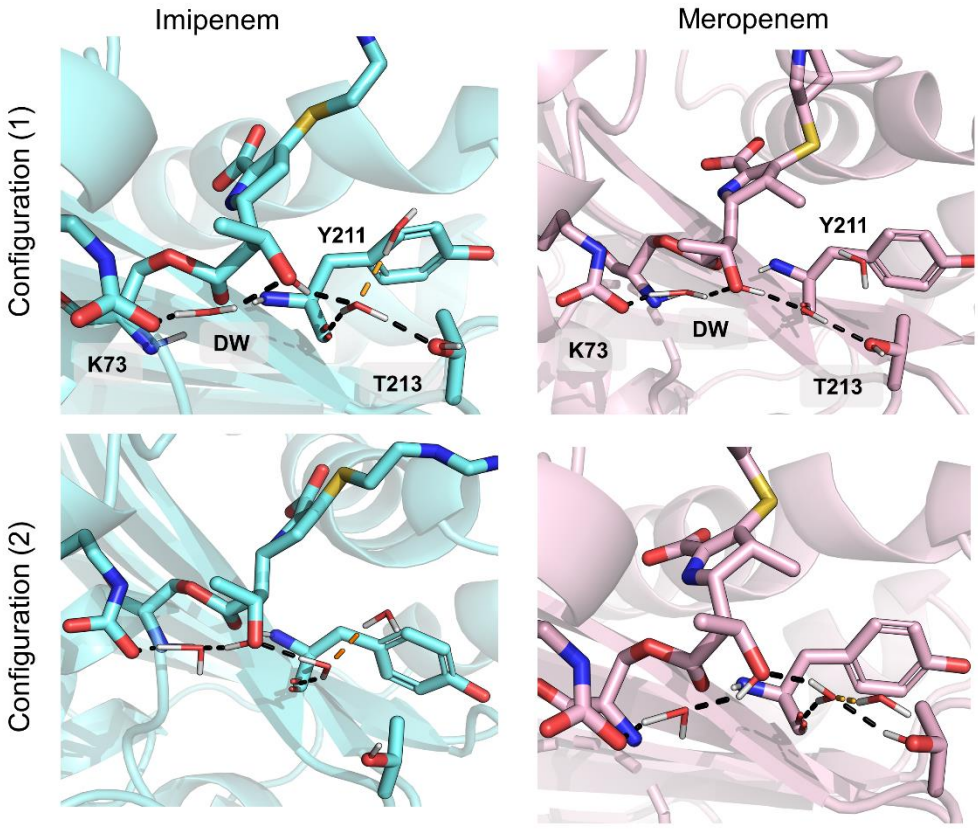

Figure S8. Transition state structures for imipenem and meropenem in orientation I. In configuration I (top row), the DW donates a hydrogen bond to the 6α-hydroxyethyl group, which in turn donates a hydrogen bond to a water molecule between Tyr211 and Thr213. For imipenem, this water can accept an additional hydrogen bond from another water molecule near the imipenem 1β-proton. For meropenem, this additional water is shifted due to the larger 1β-methyl group.

To further inspect possible differences causing the observed difference in efficiency between imipenem and meropenem, the initial approach of the DW to the substrate was inspected by US, where only the distance between the DW oxygen and the carbapenem carbon was used as a reaction coordinate. This was done for both imipenem and meropenem in active site configuration (1), where the DW donates a hydrogen bond to the 6α-hydroxyethyl group. Based on the calculated free energies, the energetic cost for the initial approach of the DW is lower for imipenem than for meropenem, which partly explains the lower calculated barriers in imipenem deacylation.

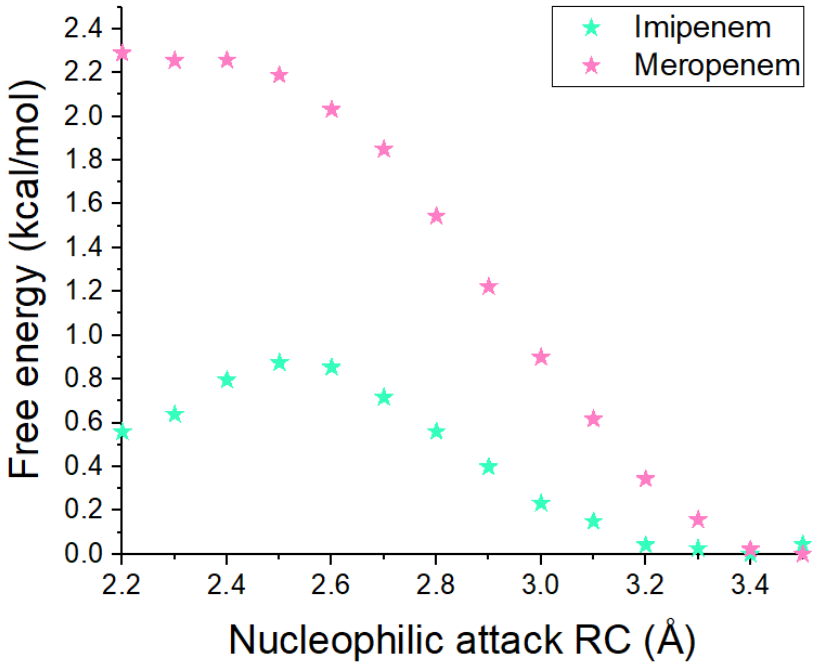

Figure S9. The calculated free energy profile for the initial approach of the deacylating water molecule to the carbapenem electrophilic carbon. Sampling was done for 20 ps/window for three snapshots starting from the structures on the full 2 ps free energy surface.

Benchmarking

DFTB2 (SCC-DFTB) was used as the QM method in all US simulations. Previously, this method has been shown to depict deacylation in serine β-lactamases well and to distinguish between carbapenemases and carbapenem-inhibited class A enzymes.[189] For OXA-48, the minimum free energy paths on DFTB2//ff14SB free energy surfaces indicate that the proton transfer and nucleophilic attack occur in a concerted fashion after the initial approach of the DW (from ~3.5 Å to 2.2 Å). The lowest calculated free energy barrier, which we expect to be a representative barrier for the most efficient deacylation reaction, was 8.5 kcal/mol, which is a significant underestimation from the experimental barrier of 16.6 kcal/mol (converted from a k_{cat} of 5 s^{-1} using the Eyring equation)[226]. To benchmark the performance of DFTB2, we performed transition state optimization for a representative small molecule model in the gas-phase as well as calculated a representative deacylation potential energy surface using a higher-level DFT method.

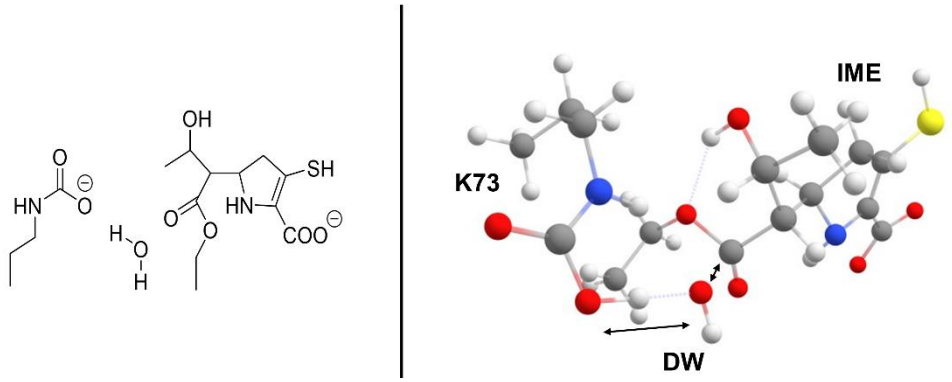

Figure S10. Small molecule model of the active site used in benchmarking calculations. The transition state corresponds to a concerted proton transfer between K73 carboxylate and C-O bond formation between the substrate and water (both indicated with arrows). Notably in the gas-phase, the 6α-hydroxyethyl group has been optimized to orientation III (with a 290° dihedral).

The small molecule model used in benchmarking is presented in Figure S10. The gas-phase model included methyl-capped Lys73 and imipenem acylenzyme with the DW taken from a representative full enzyme structure. TS corresponding to the tetrahedral intermediate (TI) formation in deacylation was first optimized using Gaussian16 on the M06-2X/6-31+G(d) level using looser criteria (with keywords Opt=(TS,calcfc,noeigentest)), and the final structure was optimized with tighter convergence criteria (Opt=(TS,VTight) SCF=Tight), ultrafine integration grid was used in all calculations (Int=UltraFine). TS was validated by visual inspection and normal mode calculation (one imaginary frequency at -296.63 corresponding to the reaction coordinates). The reactant (AC) and product (TI) structures were obtained with IRC calculations in both directions starting from the optimized TS, and the final IRC endpoints were further optimized on the same level as the final TS. TS optimisation and subsequent IRC calculations were done using Gaussian16.[334] Single-point energies were calculated on the higher SCS-MP2/aug-cc-pVTZ level[149, 316] (using the RIJK approximation with aug-cc-pVTZ/C and aug-cc-pVQZ/JK auxiliary basis sets), as well as using DFTB2. RI-SCS-MP2 calculations were done using orca 4.2.0,[317, 318] and semi-empirical calculations using sqm (part of the Amber18 and Ambertools19 package). Since the gas-phase model was optimized to the 290° orientation, the US barrier is shown for the lower 290° for imipenem.

Table S4. Benchmarking energies for the small molecule gas-phase system. The approximate TS location from US is shown for the 290° orientation (as opposed to 50°), as the gas-phase system was optimized to this orientation.

Method	**NA RC (Å)**	**PT RC (Å)**	**$\Delta^{\ddagger}G_{calc}$ (kcal/mol)**
M06-2X/6-31+G(d)	1.89	-0.37	19.9 kcal/mol
RI-SCS-MP2/aug-cc-pVTZ[a]	-	-	22.5 kcal/mol
DFTB2[a,b]	-	-	14.5 kcal/mol
DFTB2/ff14SB FES (OXA-48)[c]	2.0	-0.4	11.2 kcal/mol

[a] Energy difference from single-point energies on M06-2X/6-31+G(d) optimized AC and TS structures.

[b] TS could not be optimized in the gas-phase with DFTB2 as no saddle point is indicated between the AC minimum and the tetrahedral intermediate.

[c] The approximate TS location on the QM/MM free energy surface.

To study the performance of DFTB2 in the whole enzyme model, deacylation potential energy surfaces were calculated for imipenem in the 50° dihedral orientation using DFTB2 and M06-2X/def2-TZVP[134, 335] levels of theory (Figure S11). The LBFGS algorithm was used for energy minimization with a convergence criterium of 0.01 mol^{-1} $Å^{-1}$. Force constants for restraints used in US were increased to 5000 kcal mol^{-1} $Å^{-2}$, and residues further than 5 Å from the substrate were restrained (50 kcal mol^{-1} $Å^{-2}$ force constant). Energy correction using DFT was obtained by calculating single-point energies for the QM region on the M06-2X/def2-TZVP level (using Orca 4.2) and taking the difference between the M06-2X and DFTB2 energies (interactions terms between the QM and MM regions were thus calculated using DFTB2). The RIJCOSX approximation with the def2/J auxiliary basis set was used with M06-2X.

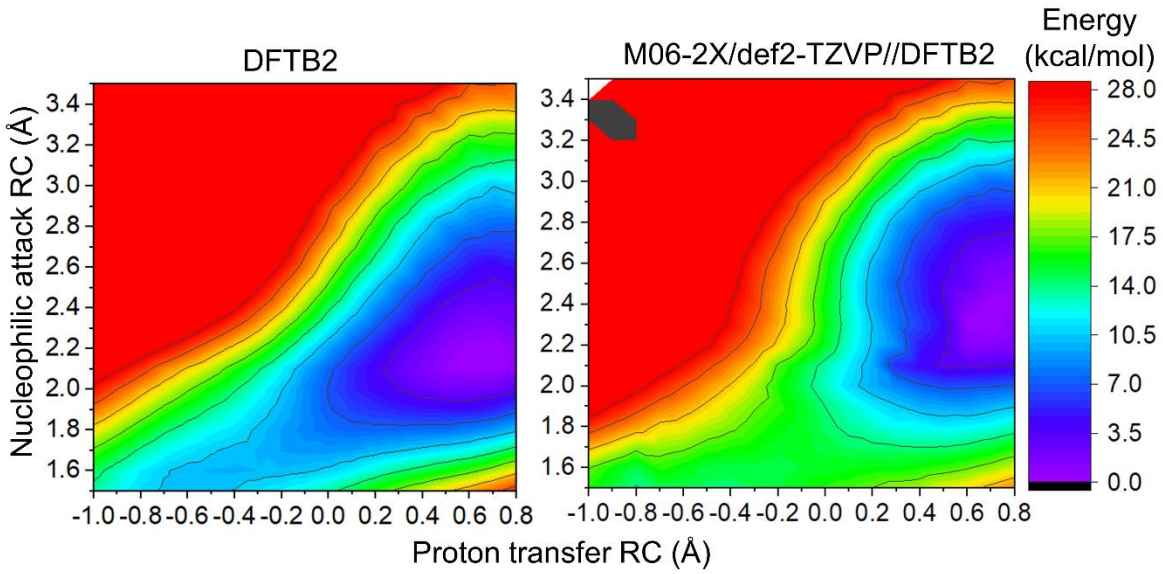

Figure S11. Potential energy surfaces for OXA-48/imipenem in orientation I calculated using DFTB2 (left) or M06-2X/def2-TZVP (right). Energy at the approximate TS position (-0.1/1.7 for PT and NA RCs, respectively) is 9.0 kcal/mol for DFTB2, and 15.3 kcal/mol for M06-2X. SCF did not converge satisfactorily for two structures in the high energy region and were hence left out from the M06-2X potential energy surface (black area).

Mulliken Charges

Mulliken charges for the key atoms in the QM region were calculated from extended US at the AC, TS, and TI minima, values determined from the minimum free energy path. Each state was sampled for 20 ps (starting from the last structure after the initial 2 ps sampling), and charges were calculated every 20 fs and averaged to obtain one value per atom. Key atoms with atom names are presented in Figure S12.

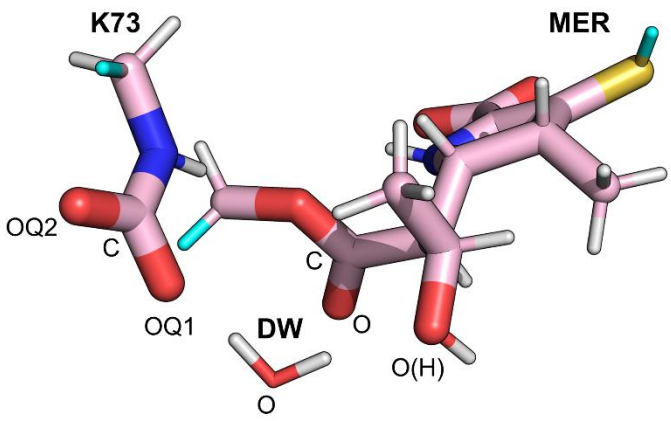

Figure S12. QM region atoms (for meropenem) with link atoms highlighted in cyan. Names shown for the key atoms, for which Mulliken charges were recorded along the reaction.

All Mulliken charges show the same trend, where during a reaction a positive charge emigrates to Lys73 carboxylate (proton acceptor), and the substrate carbonyl oxygen becomes more negative due to negatively-charged TI formation. The transition state location shifts slightly when the hydrogen bond pattern between the DW and the 6α-hydroxyethyl group changes, which results in different charges at the transition state. When the DW accepts a hydrogen bond from the carbapenem hydroxyl, the transition state location shifts to more negative values for the proton transfer reaction coordinate, i.e. closer to the TI structure. This results in more positive Lys73 carboxylate oxygen charges and more negative DW:O charges. No significant changes are seen between different active site conformations when comparing the change between endpoint charges (AC → TI).

Table S5. Mulliken charges for the key QM region atoms for imipenem in the 50° orientation. DW donates a hydrogen bond to the 6α-hydroxyethyl hydroxyl group. Locations for the minima and TS (proton transfer/nucleophilic attack values): AC 0.8/3.4, TS -0.1/1.7, TI -1.0/1.5.

QM atom	**Enzyme**				
	Q^{AC}	Q^{TS}	Q^{TI}	ΔQ^{TS-AC}	ΔQ^{TI-AC}
K73-OQ1	-0.84	-0.65	-0.51	0.19	0.33
K73-OQ2	-0.76	-0.73	-0.67	0.04	0.09
K73-C	0.74	0.72	0.71	-0.02	-0.03
DW-O	-0.69	-0.61	-0.59	0.08	0.10
IME-O	-0.60	-0.80	-0.87	-0.20	-0.26
IME-C	0.66	0.73	0.74	0.06	0.08
IME-O(H)	-0.51	-0.54	-0.54	-0.03	-0.03

Table S6. Mulliken charges for the key QM region atoms for imipenem in the 50° orientation. DW accepts a hydrogen bond from the 6α-hydroxyethyl hydroxyl group. Locations for the minima and TS: AC 0.7/3.4, TS -0.4/1.9, TI -1.0/1.5.

QM atom	**Enzyme**				
	Q^{AC}	Q^{TS}	Q^{TI}	ΔQ^{TS-AC}	ΔQ^{TI-AC}
K73-OQ1	-0.85	-0.59	-0.52	0.26	0.33
K73-OQ2	-0.76	-0.68	-0.67	0.08	0.09
K73-C	0.74	0.72	0.71	-0.02	-0.03
DW-O	-0.66	-0.74	-0.58	-0.08	0.08
IME-O	-0.60	-0.74	-0.87	-0.14	-0.27
IME-C	0.66	0.70	0.74	0.04	0.08
IME-O(H)	-0.58	-0.60	-0.57	-0.02	0.01

Table S7. Mulliken charges for the key QM region atoms for meropenem in the 50° orientation. DW accepts a hydrogen bond from the 6α-hydroxyethyl hydroxyl group. Locations for the minima and TS: AC 0.8/3.4, TS -0.5/1.9, TI -1.0/1.5.

QM atom	**Enzyme**				
	Q^{AC}	Q^{TS}	Q^{TI}	ΔQ^{TS-AC}	ΔQ^{TI-AC}
K73-OQ1	-0.85	-0.57	-0.52	0.28	0.33
K73-OQ2	-0.75	-0.69	-0.66	0.07	0.09
K73-C	0.74	0.71	0.71	-0.03	-0.03
DW-O	-0.67	-0.76	-0.59	-0.08	0.08
MER-O	-0.58	-0.72	-0.85	-0.14	-0.27
MER-C	0.66	0.70	0.74	0.04	0.08
MER-O(H)	-0.54	-0.59	-0.58	-0.05	-0.03

Table S8. Mulliken charges for the key QM region atoms for meropenem in the 50° orientation. DW donates a hydrogen bond to the 6α-hydroxyethyl hydroxyl group. Locations for the minima and TS: AC 0.8/3.4, TS -0.1/1.7, TI -1.0/1.5.

QM atom	**Enzyme**				
	Q^{AC}	Q^{TS}	Q^{TI}	ΔQ^{TS-AC}	ΔQ^{TI-AC}
K73-OQ1	-0.84	-0.67	-0.53	0.18	0.32
K73-OQ2	-0.76	-0.72	-0.68	0.03	0.07
K73-C	0.74	0.72	0.71	-0.02	-0.03
DW-O	-0.69	-0.62	-0.60	0.07	0.09
MER-O	-0.58	-0.78	-0.85	-0.20	-0.27
MER-C	0.66	0.72	0.74	0.06	0.08
MER-O(H)	-0.51	-0.53	-0.54	-0.02	-0.02

Chapter 7 - Acylation mechanism of the β-lactamase inhibitor avibactam by the OXA-48 β-lactamase

7.1 Introduction

As briefly discussed in Section 1.2, a common treatment option for severely resistant bacterial infections is combination therapy.[25] This means that an antibiotic is administered together with a β-lactamase inhibitor, which prevents β-lactamases from inactivating the drug prior to it binding to the target proteins. As combination therapy has proven to be useful in clinical practice,[261, 336-338] the field of β-lactamase inhibitor development is evolving fast.[283] Avibactam (depicted in Figure 1.1), a non-β-lactam β-lactamase inhibitor belonging to diazabicyclooctanones (DBOs), is a recent example of this.[31] Avibactam was approved for clinical use in 2015 in combination with ceftazidime (Figure 1.1), and the combination is sold under tradename Avycaz.[339] As shown in Figure 4.5, the β-lactam is replaced by cyclic urea in the DBO scaffold. Generally, avibactam exhibits broad-spectrum inhibition against SBLs, such as KPC-2 and OXA-48, but lacks inhibitory activity against MBLs.[34, 260, 340] Even though avibactam resembles β-lactams, its inhibition mechanism has been shown to be distinctly different. Avibactam is acylated in an analogous fashion to β-lactams to form a covalent acylenzyme (AC), but the AC is not deacylated using a water nucleophile like β-lactams. Instead, avibactam recyclizes to form an intact inhibitor molecule, which can react with further enzymes.[31] This is excluding KPC-2 β-lactamases, where an additional route involving avibactam fragmentation was observed.[34] Similar recyclization is not observed for any "traditional" mechanism-based inhibitors, and it is most likely enabled by decreased ring strain in the five-membered urea ring compared to the corresponding four-membered β-lactam ring.[31]

OXA-48 inhibition by avibactam is discussed in depth in Section 4.6. To summarise, *in vitro* kinetics indicate that avibactam is readily acylated by OXA-48, but that the recyclization occurs slowly. The measured acylation efficiency k_2/K_i is $1.4 \pm 0.1 \times 10^3\ M^{-1}\ s^{-1}$, whilst the recyclisation rate constant k_{off} is measured to be $1.2 \pm 0.4 \times 10^{-5}\ s^{-1}$ with a half-life of 1000 ± 300 minutes.[34] Multiple crystal structures of OXA-48 with covalently-bound avibactam (AC state) are deposited in the Protein Data Bank, and these structures yield information of the binding pose and interactions with active site residues (see Figure 4.10).[235, 255, 264] However, existing experimental studies have provided only hypotheses of the actual avibactam inhibition

mechanism. At least two different reaction pathways have been proposed, and these are presented in Figure 7.1. The first mechanism incorporates a neutral, non-carboxylated Lys73 as a general base, which acts as a proton acceptor activating the nucleophilic Ser70. Subsequently, avibactam ring opening and nitrogen protonation occur by shuffling a proton from Lys73 to avibactam via Ser118.[235] This mechanism is henceforth again referred to as pathway 1, and it is derived from a suggested "universal" reaction scheme for avibactam with SBLs. However, it is known that for β-lactam hydrolysis, Lys73 needs to be in its carboxylated form for efficient catalysis to take place.[223] Another proposed pathway employs a carboxy-Lys73 as the initial proton acceptor, and avibactam is subsequently protonated by Lys208 via Ser118.[264] This mechanism will be referred to as pathway 2. For pathway 2, slow recyclization rates are attributed to the preference of Lys73 being decarboxylated in the AC state, which would essentially hinder reactivity.[264] Pathways 1 and 2 are summarised again in Figure 7.1.

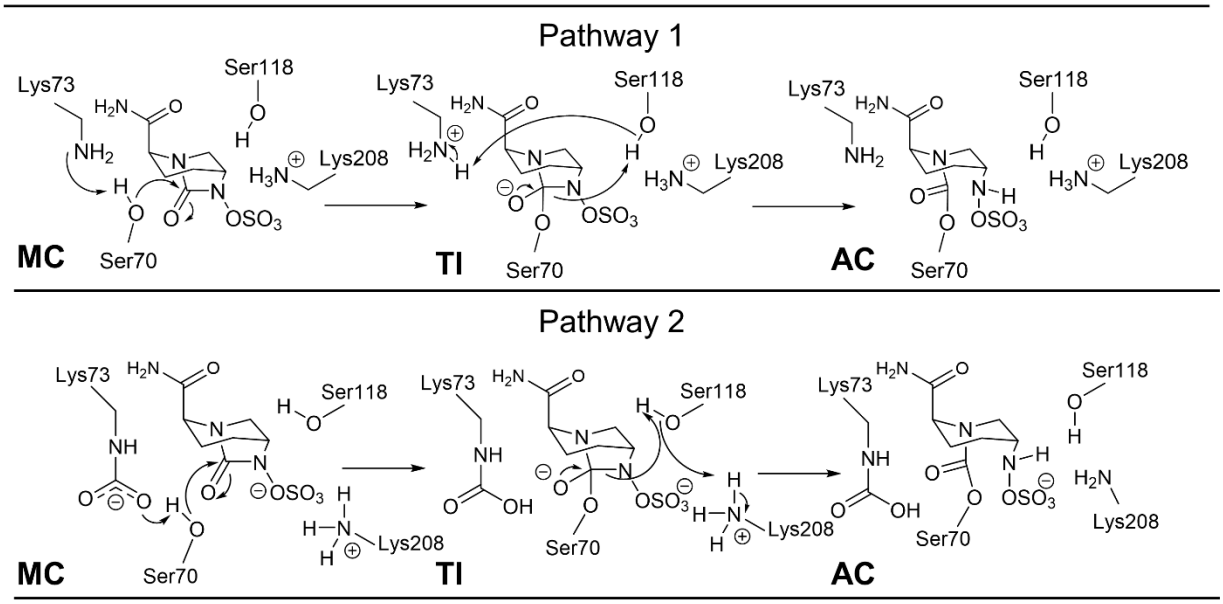

Figure 7.1 Three proposed mechanisms for avibactam acylation by OXA-48. Top: In pathway 1, the nucleophilic Ser70 is activated via proton transfer to a neutral Lys73 (in its standard amine form). After TI formation, the five-membered ring in avibactam opens and avibactam nitrogen is protonated by Lys73 via Ser118. Bottom: In pathway 2, a carboxylated Lys73 acts as the proton acceptor going from MC to TI. Subsequent avibactam protonation occurs by Lys208 via Ser118.

In this chapter, we utilise both MM MD and QM/MM methods to compare the presented reaction mechanisms for avibactam acylation. First, Michaelis complex (MC)

models for OXA-48 with either a decarboxylated and neutral Lys73 (for pathway 1) or a carboxylated Lys73 (for pathway 2) were constructed. The stabilities of the formed MCs were inspected by 10x50 ns MM MD simulations. Further, the presented reaction pathways were compared by calculating their corresponding potential energy profiles using QM/MM calculations with the nudged elastic band (NEB)[341] method. Both pathways were broken down into two separate NEB calculations, where the first calculation corresponds to the tetrahedral intermediate (TI) formation via a nucleophilic attack, and the second the subsequent avibactam ring opening and nitrogen protonation. Both the MM MD and QM/MM NEB calculations indicate that pathway 2, where a carboxylated Lys73 acts as a general base, is more feasible than pathway 1.

7.2 Computational methods

7.2.1 System set-up

Non-covalent Michaelis complexes of OXA-48 with avibactam were prepared using a crystal structure of covalently-bound avibactam as a template (PDB ID 4S2K).[235] Ser70-avibactam AC was replaced by an intact serine residue and non-covalently coordinated avibactam. Lys73 was either kept in its neutral form or replaced by a carboxylated lysine as found in analogous systems (e.g. in OXA-48/imipenem complex, PDB ID 5QB4).[239] Partial charges (RESP) and force field parameters for carboxy-Lys73 were derived using the constrained charge derivation as implemented in the R.E.D. Server,[172] any missing parameters were taken from analogous gaff[168] parameters. For avibactam, gaff parameters with AM1-BCC partial charges were derived using antechamber (part of Ambertools19).[170, 171] Any clashing water molecules (closer than 2.5 Å to any avibactam heavy atom) were removed, otherwise all crystallographic waters were retained. Both systems were solvated in a 10 Å box of TIP3P water, and existing charges were neutralised by replacing water molecules by counterions. The protonation states of ionisable residues were inspected using propKa3.1[167], and subsequently kept in their standard state based on the predicted pK_a values (Glu/Asp deprotonated, Lys protonated apart from Lys73). All histidine residues were singly protonated at the ε-nitrogen, except His140, which was singly protonated at the δ-nitrogen. Hydrogens were added using tLeap, and the ff14SB force field[100] (part of the Amber software suite) was used in all

calculations. Both prepared systems consisted of 32292 atoms. Active sites of both starting structures are illustrated in Figure 7.2.

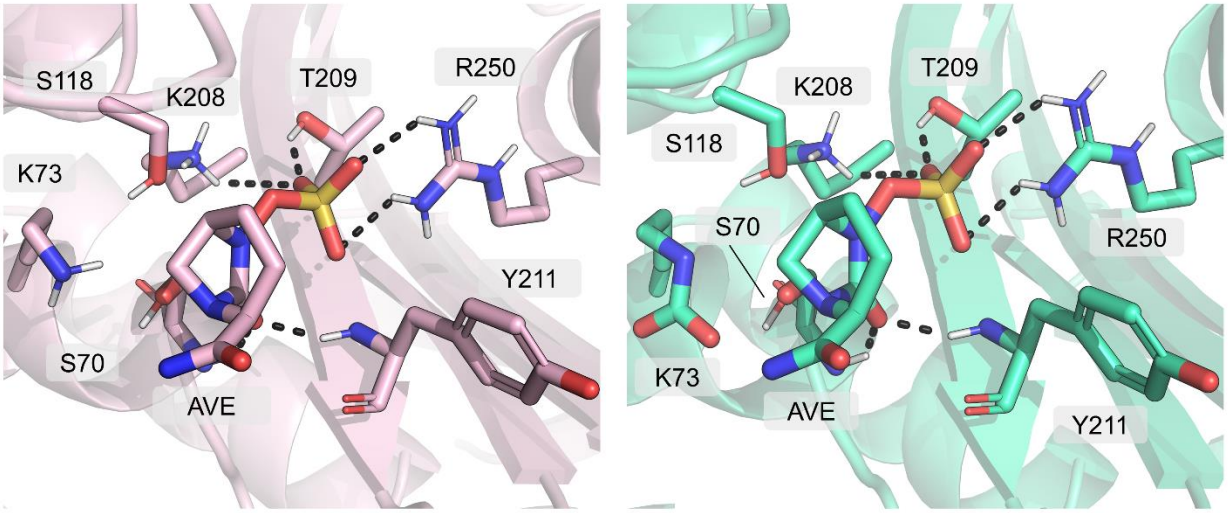

Figure 7.2 Starting MC models for the two studied OXA-48/avibactam systems. Left: Lys73 is kept in its neutral form. Right: Lys73 is carboxylated, Lys208 is protonated in both systems.

7.2.2 Molecular dynamics simulations

After initial preparation, the systems were minimised in three parts: i. only water molecules allowed to move, other parts restrained, ii. all atoms except Cα allowed to move, and finally iii. all atom positions minimized (restraint weights of 50 kcal/mol/Å^2 applied in i. and ii.). Each minimisation step consisted of 1000 steps using the steepest descent method followed by 1000 steps of the conjugate gradient method. After minimisation, systems were heated from 50 K to 300 K in 50 ps, and subsequently simulated for 50 ns in the NPT ensemble. All simulations were performed using Langevin dynamics with a 0.2 ps^{-1} collision frequency and a 2 fs timestep. Ten independent replicas were run for both systems to inspect the stability of the non-covalent MC model. In addition, a 10 ns MD run straight after heating using restraints was run to equilibrate the structure before QM/MM MD. To preserve the desired initial binding pose, restraints were applied for the Ser70-Lys73 hydrogen bond (<2.0 Å, 10 kcal/mol/Å^2), avibactam carbonyl oxygen and Tyr211 backbone amide (<2.5 Å, 10 kcal/mol/Å^2), and carbonyl carbon and sulphur to ensure positioning of the sulphate group (<3.5 Å, 10 kcal/mol/Å^2). Afterwards 100 ps of QM/MM MD using DFTB2[158] was performed

with the same restraints, but also enforcing the distance between Ser70 and avibactam electrophilic carbon staying below 4.0 Å (restraint weight 10 kcal/mol/Å^2) to ensure a suitable conformation for nucleophilic attack (only for the system with a neutral Lys73). The QM region consisted of avibactam and the sidechains of Ser70, Lys73, Ser118, and Lys208 as depicted in Figure 7.3. This resulted in a QM region consisting of 56 atoms for the system with a carboxylated Lys73, and 54 atoms for the system with a neutral Lys73 (including link atoms). All MM and QM/MM MD simulations were performed using the Amber18 software package with Ambertools19.[166]

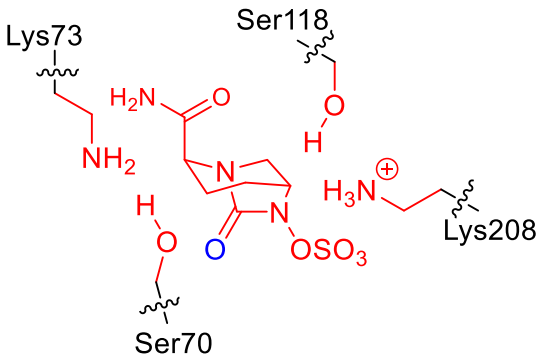

Figure 7.3 . QM region used in QM/MM MD and NEB calculations. Red and blue atoms included in the QM region, black atoms described using MM, link atoms placed along the bonds indicated with wavy lines. For a carboxylated Lys73, the terminal amine in Lys73 was replaced by -NCOO$^-$. The carbonyl oxygen used as a reference point when stripping atoms for QM/MM NEB calculations is shown in blue.

7.2.3 QM/MM potential energy calculations

The activation energies and minimum energy paths (MEPs) for the discussed reaction mechanisms were calculated using the nudged elastic band (NEB) method as implemented in orca 4.2.0[317, 318]. For NEB calculations, the systems were stripped of any residues with any atom further than 17 Å from the avibactam carbonyl oxygen (Figure 7.3). Atoms closer than 10 Å to the same oxygen were included in the active region, which was allowed to move during optimisation. Coordinates for the rest of the system were frozen. The stripped systems consisted of 1735 and 1723 atoms for the neutral Lys73 and carboxy-Lys73 systems, respectively. Reaction pathways were separated into two NEB calculations: TI formation from the MC (MC → TI), or AC formation from the TI (TI → AC). Starting structures for the TI and the AC were

initially created by doing a brief constrained minimisation to change the bonding arrangement, and the created structures were then subjected to a full minimisation using the L-BFGS optimiser and the GFN2-xTB[342] method (referred to as XTB2). The RMS gradient tolerance was set to be below $5x10^{-5}$ a.u. during this minimisation. The minimised structures were used as starting points for reaction path inspection using the climbing image NEB method (CI-NEB). The L-BFGS optimiser was used for constructing the NEB, and the images were re-distributed along the path every 50 iterations using linear interpolation. The default convergence criteria were kept for all images. MEPs were initially constructed using XTB2, and single-point energies (SPEs) were calculated on the ωB97XD/def2-TZVP and M06-2X/def2-TZVP levels.[134, 135, 150] Two MEPs for both MC→TI reactions were re-optimised using the ωB97XD/def2-SVP method for the QM region. The RIJCOSX approximation[343] with the default auxiliary def2/J basis set[344] was applied both during NEB optimisation and upon calculating single-point energies for all DFT calculations. All NEB and SPE calculations were done using orca 4.2.0.[317, 318]

7.3 Results and Discussion

7.3.1 Dynamics of the formed Michaelis complexes

After the initial minimisation and heating phases, the stability of the formed MCs was inspected by 50 ns MM MD simulations. Ten independent simulations were run for both systems. With a neutral Lys73, avibactam moved away from the initial "productive" pose in nine of the ten simulations (with the distance between avibactam carbonyl oxygen and Tyr211 backbone amide increasing beyond 3.5 Å). In the remaining simulation, avibactam stayed in the original pose for the whole 50 ns. Notably, in one trajectory avibactam re-bound to the initial pose after shifting away. Upon repositioning, avibactam does not completely diffuse out of the active site during the simulations. It changes its orientation so that the carbonyl group shifts out of the oxyanion hole, but so that the $-OSO_3^-$ group stays near Lys208, Thr209, and Arg250. Representative structures of avibactam in its original non-covalent binding pose and the shifted position are presented in Figure 7.4. In the eight trajectories where avibactam shifts away from its initial pose for the rest of the simulation, this repositioning occurs within the first 13 ns. In the trajectory where avibactam shifts away and then moves back to the oxyanion hole, this repositioning happens at 27 ns. In the single simulation, where avibactam stays in the

oxyanion hole, Ser70 is observed to donate a hydrogen bond to Lys73 throughout the simulation, but it does so whilst rotating further away from the avibactam electrophilic carbon. For the initial Ser70 rotamer, the distance between Ser70:O and avibactam carbon is below 3.3 Å, which is deemed feasible for a nucleophilic attack. Upon rotation, this distance increases to above 4 Å, which hinders the possibility of Ser70 hydroxyl forming a TI with avibactam. Ser70 would need to first rotate back to its initial rotameric state before the nucleophilic attack could occur (Ser70 rotamers also illustrated in Figure 7.4).

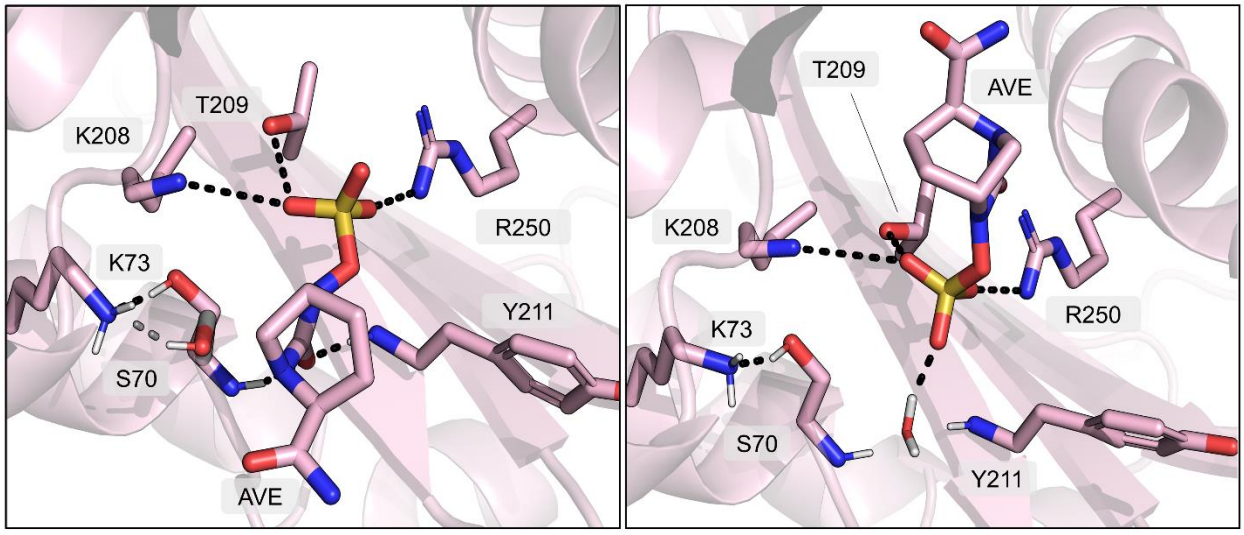

Figure 7.4 Representative structures of avibactam in MM MD simulations with a neutral Lys73. Important active site interactions highlighted with dashed black lines. Left: Avibactam orientation in the MM MD simulations, where it stays positioned in the oxyanion hole (formed by the backbone amides of Ser70 and Tyr211). The sulphate group is interacting with Lys208, Thr209, and Arg250. For the grey Ser70 rotamer, the distance to AVI:C is less than 3.3 Å, and for the pink rotamer, this distance is beyond 4 Å. Right: Avibactam position after shifting away from the oxyanion hole. The inhibitor is kept in the active site by electrostatic interactions and hydrogen bonds between the sulphate group and Lys208, Thr209, and Arg250.

For carboxy-Lys73, avibactam stays positioned in the oxyanion hole in five out of ten simulations, and shifts away in five simulations. In one trajectory, a similar shifting away and re-binding was observed as previously for the MC with a neutral Lys73. If avibactam shifts away from its initial pose, this shifting happens within 22 ns of the simulation start, except for the simulation with shifting and re-binding, where avibactam moves away at 35 ns. In the five

simulations, where avibactam stays close to its original position, Ser70 is observed to rotate between three different orientations. Two are the same ones as depicted for the system with a neutral Lys73, and the third one involves the Ser70 hydroxyl group donating a hydrogen bond to the avibactam sulphate moiety (Figure 7.5). In the five simulations where avibactam re-positions away from the oxyanion hole, it is still kept in the active site by electrostatic interactions and hydrogen bonds analogous to simulations with a neutral Lys73.

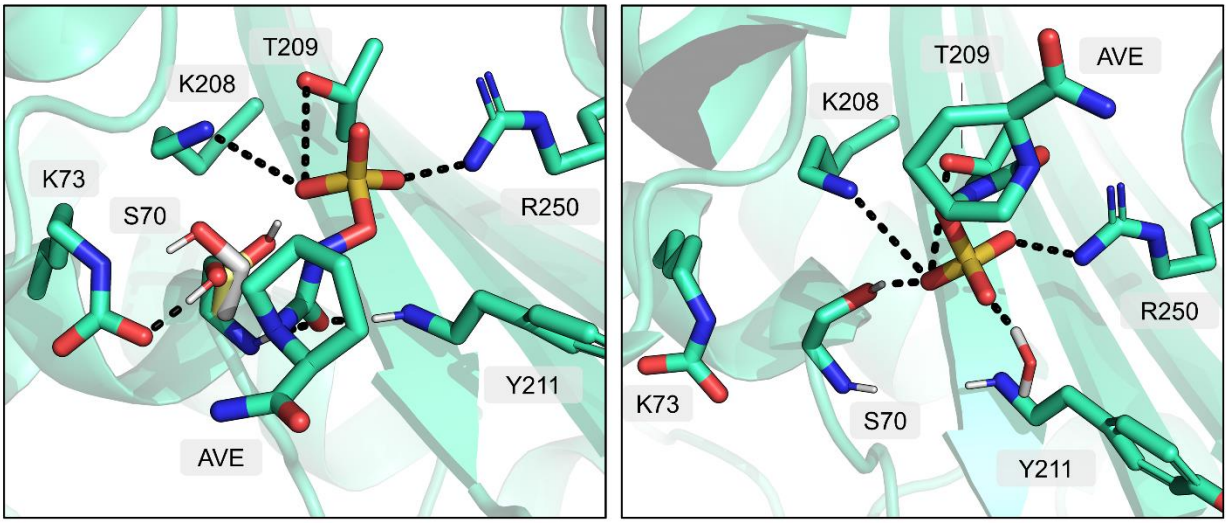

Figure 7.5 Representative structures of avibactam in MM MD simulations with a carboxy-Lys73. Important interactions between the inhibitor and active site residues indicated with dashed black lines. Left: Avibactam positioned in the oxyanion hole. The three possible orientations for Ser70 indicated with sticks representation. Right: After shifting away from the oxyanion hole, avibactam is kept in the active site by electrostatic and hydrogen bond interactions between the sulphate group and Ser70, Lys208, Thr209, and Arg250.

Further analysis of the MM MD data focuses on the subset of trajectories, where avibactam stays in the oxyanion hole (one trajectory for neutral Lys73, five for carboxy-Lys73). As briefly mentioned previously, Ser70 can adopt three different orientations, which can be distinguished by measuring the sidechain χ_1 (N-Cα-Cβ-OG) dihedral. The most acylation-compatible initial active site configuration is achieved, when i. Ser70 donates a hydrogen bond to Lys73, and ii. the distance between Ser70:OG and AVI:C is less than 3.5 Å. These criteria ensure both a feasible proton transfer and nucleophilic attack going from the MC to the TI. The hydroxyl oxygen in Ser70 and the avibactam carbon are closest, when χ_1 is

approximately 300° (*g*- rotamer), with the majority of the sampled distances between Ser70:OG and avibactam carbon falling mostly under 3.5 Å for this rotamer (Figure 7.6). When the dihedral is approximately 180° (*t*), Ser70 is still donating a hydrogen bond to neutral Lys73, or analogously to the amine nitrogen in carboxylated Lys73. However, the distance between Ser70:O-AVI:C increases to ~4 Å or beyond, and for bond formation between Ser70 and avibactam, rotation to the *g*− state would be required. For the third rotamer, where χ_1 is approximately 60°, Ser70 has rotated to donate a hydrogen bond to the sulphate group and is unable to transfer a proton to Lys73. Even though all three Ser70 orientation are observed in the simulations with the carboxylated Lys73, the *g*− rotamer is sampled the most. This, combined with the more stable non-covalent pose for avibactam, indicates that the carboxylated form of Lys73 is likely to participate in the acylation reaction.

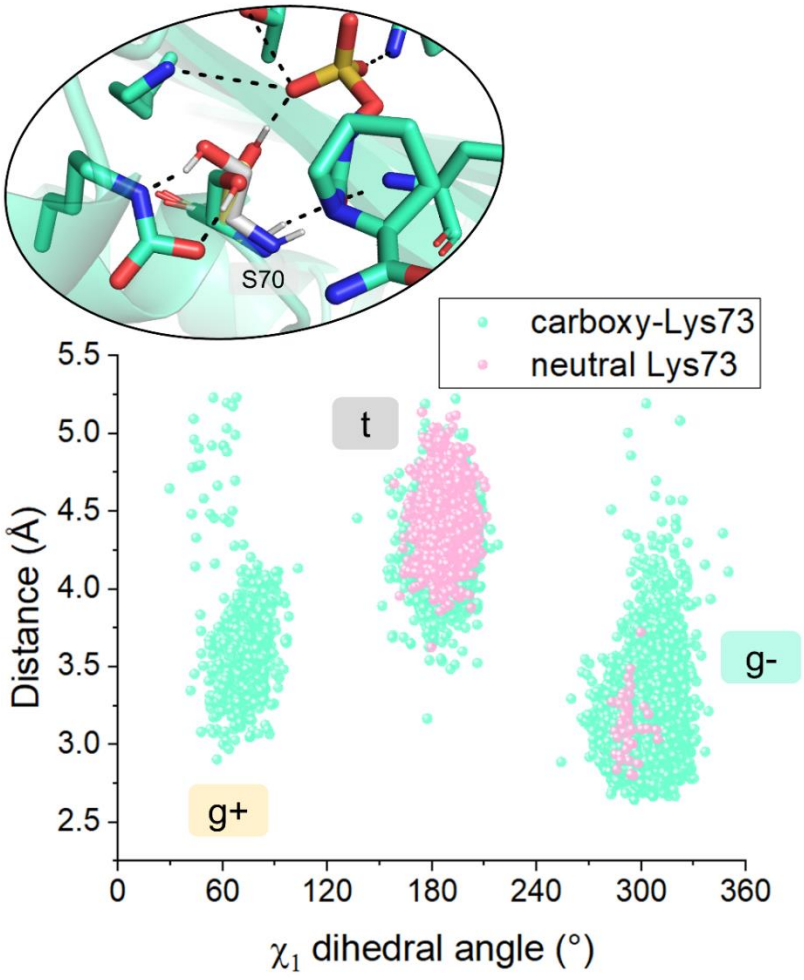

Figure 7.6 Distributions of the sampled Ser70 dihedrals and the corresponding distance between Ser70 oxygen and avibactam electrophilic carbon. The label colour for the different Ser70 rotamers matches the colour of the corresponding sticks representation in the inset.

7.3.2 Energetics of the proposed pathway 1

As discussed in section 7.1, at least two different pathways have been proposed for avibactam acylation. The compared reaction mechanisms are presented in Figure 7.1, and potential energy profiles for the approximate MEPs were calculated for models of the enzyme system (as described in Section 7.2.3). For pathway 1, the initial minimisation yielded only the MC and AC minima, as no stable minimum was found for the TI using the L-BFGS optimiser (the initial TI model changed back to the reactants during structure optimisation). Therefore, the MEP was first optimised from the MC all the way to the AC using 12 images, which helped to locate a better initial structure for the TI intermediate. This approximate TI structure was subsequently minimised prior to a new NEB optimisation in two parts going either from the MC to the TI, or from the TI to the AC. For the MC → TI calculation, the NEB consisted of 14 images including the endpoints, and for the TI → AC of 22 images including the endpoints. The XTB2/MM optimised MC/TI/AC structures are presented in Figure 7.7.

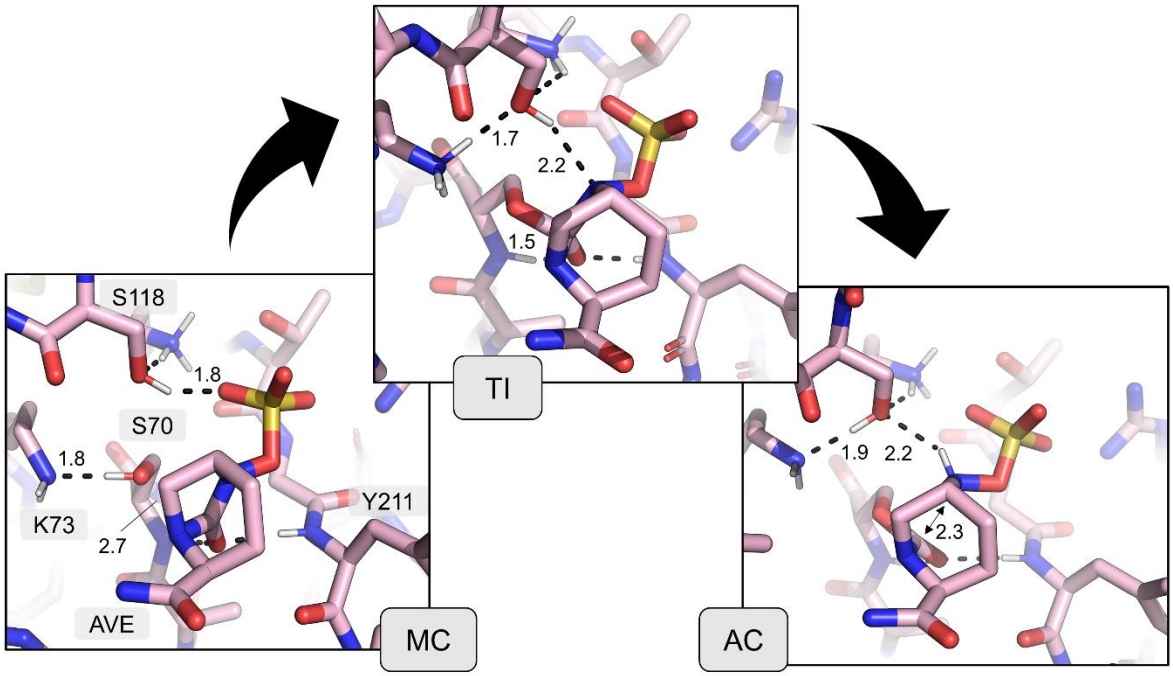

Figure 7.7 XTB2/ff14SB minimised structures for OXA-48 and avibactam with a neutral Lys73 (pathway 1).

All NEB calculations were done using the CI-NEB implementation in orca 4.2.0, where one of the images is converted into a so-called “climbing image” (CI). The CI converges to the

highest-energy saddle point along the MEP, which yields an approximate TS structure. This is not guaranteed for standard NEB, where the obtained images may not necessarily provide a good estimate of the TS as there may not be an image close to the saddle point. The obtained MEPs using XTB2/ff14SB for the NEB optimisation together with the DFT/MM single-point energy (SPE) values are presented in Figure 7.8 for both NEB calculations. Going from MC → TI, the activation energy obtained with XTB2 as the QM method is 13.6 kcal/mol, and the reaction energy 10.6 kcal/mol. Analogously, the activation and reaction energies for the TI → AC conversion are 16.0 and −10.6 kcal/mol, respectively. Notably, the calculated energetics for the MC → TI reaction are underestimated using XTB2 with respect to the SPEs using either M06-2X/def2-TZVP or ωB97X/def2-TZVP for the QM region. Using M06-2X, the activation barrier is 23.2 kcal/mol, which is 9.6 kcal/mol higher than the corresponding XTB2 energy. The difference is even higher with ωB97X, where the calculated barrier is 27.4 kcal/mol, a 13.8 kcal/mol increase with respect to XTB2. The opposite is observed for the second NEB calculation going from TI to the AC. Here, the XTB2 barrier is 16.0 kcal/mol, when M06-2X and ωB97X yield barrier heights of 6.0 and 9.8 kcal/mol, respectively. Even though the activation energies differ largely between XTB2 and the chosen functionals, XTB2 accurately predicts the forming TI to be high in energy with respect to the MC. The overall combined activation free energy barrier from the MC to the AC is 29.6 kcal/mol for XTB2, 29.2 kcal/mol for M06-2X, and 37.2 kcal/mol for ωB97X. The corresponding overall reaction energies are 0 kcal/mol for XTB2, −3.3 kcal/mol for M06-2X, and −0.4 kcal/mol for ωB97X.

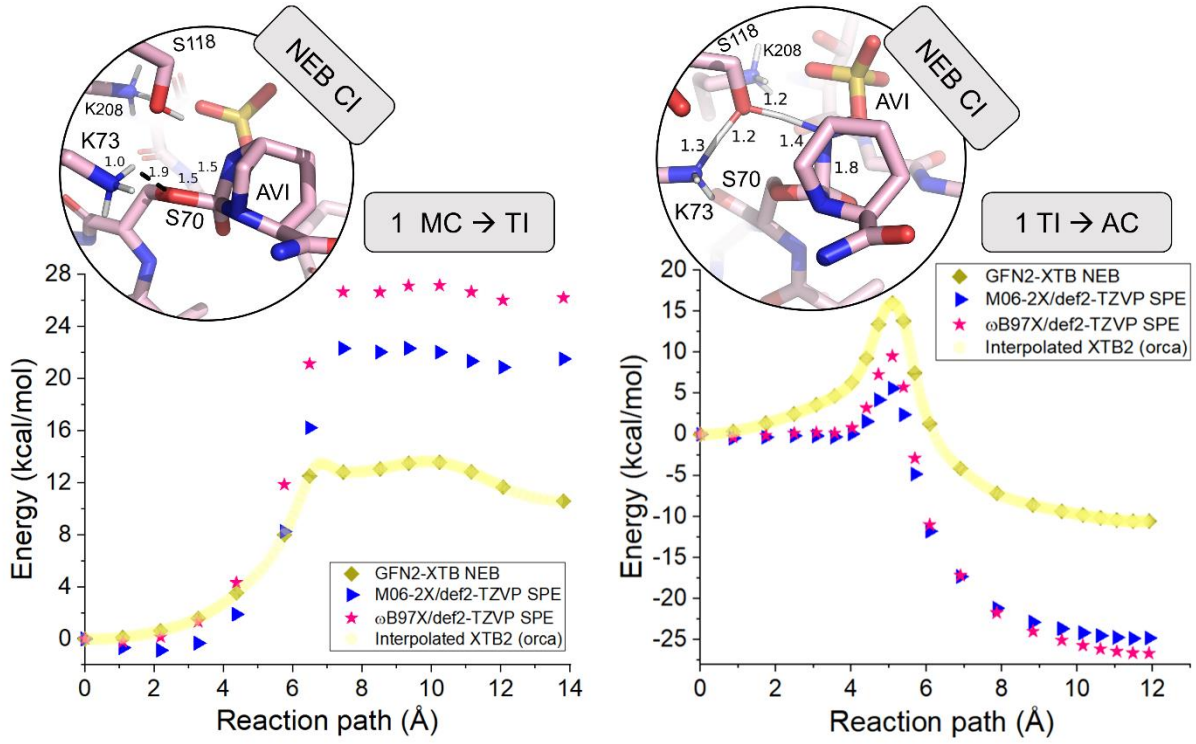

Figure 7.8 Potential energy along the MEP for the tetrahedral intermediate formation (MC → TI, left), and the subsequent avibactam ring opening and protonation (TI → AC, right) for pathway 1. QM/MM NEB calculations were performed using XTB2/ff14SB, and QM/MM SPEs were calculated using the ωB97X or M06-2X functional with the def2-TZVP basis set for the QM region. For both reactions, the structure of the climbing image, which corresponds to the highest energy saddle-point, is depicted (labelled NEB CI).

Key distances together with the full interpolated XTB2/MM energy profiles are presented in Figure 7.9. For the MC → TI transition, the distances between the transferred proton and both the donor and acceptor were recorded, as well as the nucleophilic attack distance between Ser70 and the avibactam carbon. The first steep rise in the energy curve corresponds both to the proton transfer and the nucleophilic attack, which happen in a concerted fashion. However, the calculated energy still increases slightly, as the protonated Lys73 moves closer to hydrogen bond with Ser118. This explains why the Ser70:O – Ser70:H distance increases even after the proton transfer has occurred. For the TI → AC reaction, the two proton transfers are concerted and happen simultaneously with the elongation of the avibactam C-N bond (in the five-membered ring).

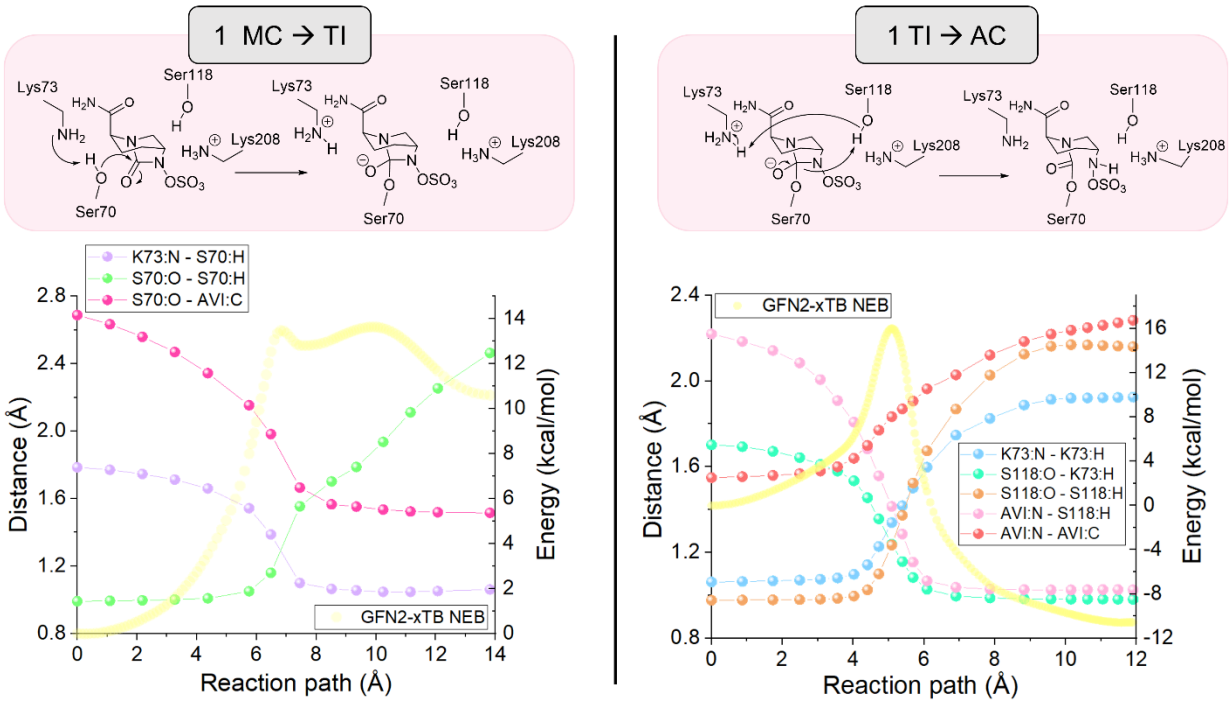

Figure 7.9 Key distances along the calculated MEP for the MC → TI (left) and TI → AC (right) reactions in pathway 1. Left y-axis: measured key distances along the MEP, depicted with dots connected by lines. Right y-axis: XTB2/ff14SB energy along the MEP, depicted by yellow circles.

7.3.3 Energetics of the proposed pathway 2

The procedures for calculating MEPs for pathway 2 are the same as discussed for pathway 1, with the exception that the QM/MM NEB calculations were done in two parts from the beginning, as the TI minimum was identified already during the initial minimisation. However, re-positioning of some active site solvent molecules was observed between the minimised MC and TI structures, and therefore the MC → TI MEP was optimised in two parts. As water movement in the active site occurred before any bonding changes in the initial MEP, a MC structure with newly positioned waters (closer to the arrangement in the TI structure) was subsequently minimised and used as a starting point for a new NEB calculation. This ensured that the calculated barrier excludes any re-organisation in the active site and mainly corresponds to the actual enzymatic reaction itself. The minimised structures used as NEB start and end points are presented in Figure 7.10.

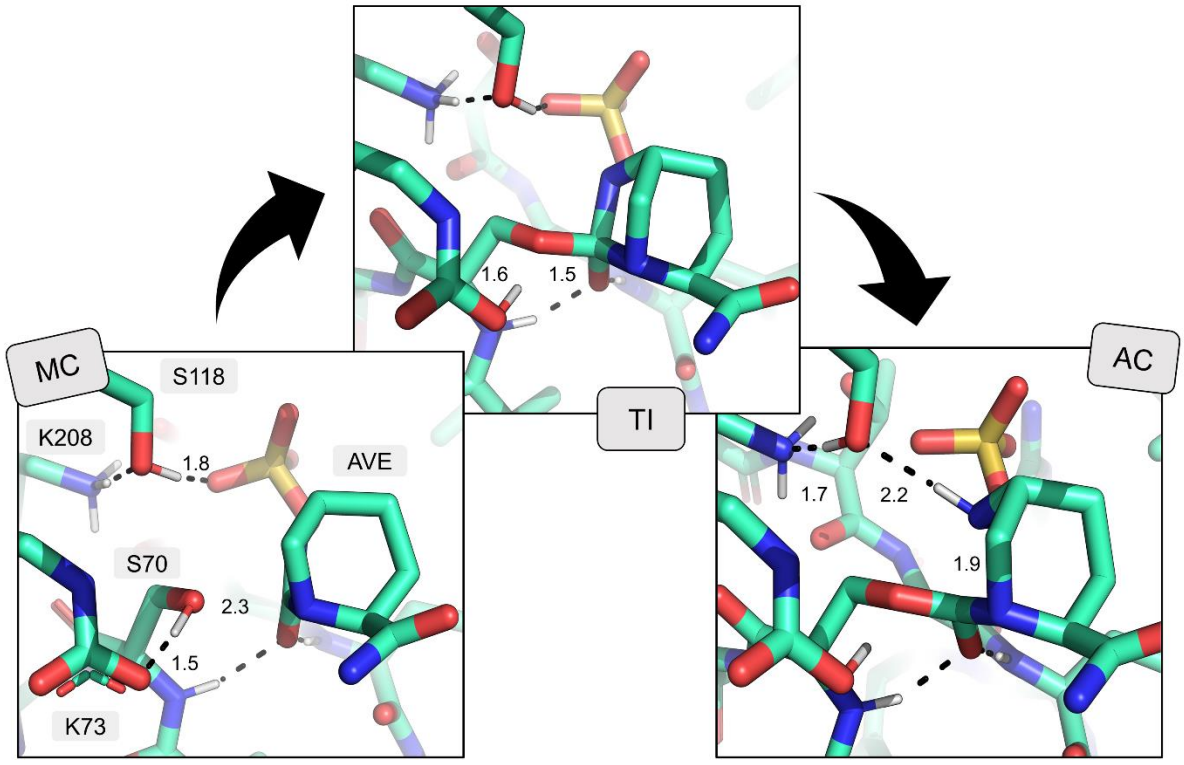

Figure 7.10 XTB2/ff14SB minimised structures for OXA-48/avibactam acylation with a carboxylated Lys73 (pathway 2).

The calculated potential energies along the MEP for both reactions in pathway 2 are presented in Figure 7.11. The MEPs consisted of 14 and 22 images for the MC → TI and the TI → AC reactions, respectively. Notably, the XTB2 method seems to vastly underestimate the barrier to forming a TI. Calculated energies using XTB2/ff14SB imply that the MC → TI reaction is essentially barrierless, as the required energy is only 0.6 kcal/mol, and that the TI is −9.5 kcal/mol lower in energy than the starting non-covalent MC. As the TI structure is expected to be higher in energy than the MC, XTB2 does not appear to give reliable energetics for the formation of this intermediate. However, this is partly overcome by obtaining SPEs using DFT for the QM region. The activation energy with M06-2X/def2-TZVP is 7.5 kcal/mol, and with ωB97X/def2-TZVP 11.3 kcal/mol. The reaction energies are also in better accordance with their expected values, as they are 0.7 and 5.4 kcal/mol for M06-2X and ωB97X, respectively. For the TI → AC reaction, XTB2/ff14SB yields an activation energy barrier of 23.8 kcal/mol. This is higher than the calculated QM/MM SPEs with DFT, as the M06-2X barrier is 12.5 kcal/mol and the ωB97X barrier 14.9 kcal/mol. Based on the energies, the TI minimum is also shifted to image 8 when using DFT as the QM method. The total activation energy barrier going from the MC to the AC for pathway 2 is 23.8 kcal/mol using XTB2, 20.0

kcal/mol using M06-2X, and 26.2 kcal/mol using ωB97X. However, just based on the XTB2/ff14SB energetics, the forming TI would be the stable intermediate structure. The total reaction energies for MC → TI are 4.3 kcal/mol for XTB2, −1.0 kcal/mol for M06-2X, and -0.8 kcal/mol for ωB97X.

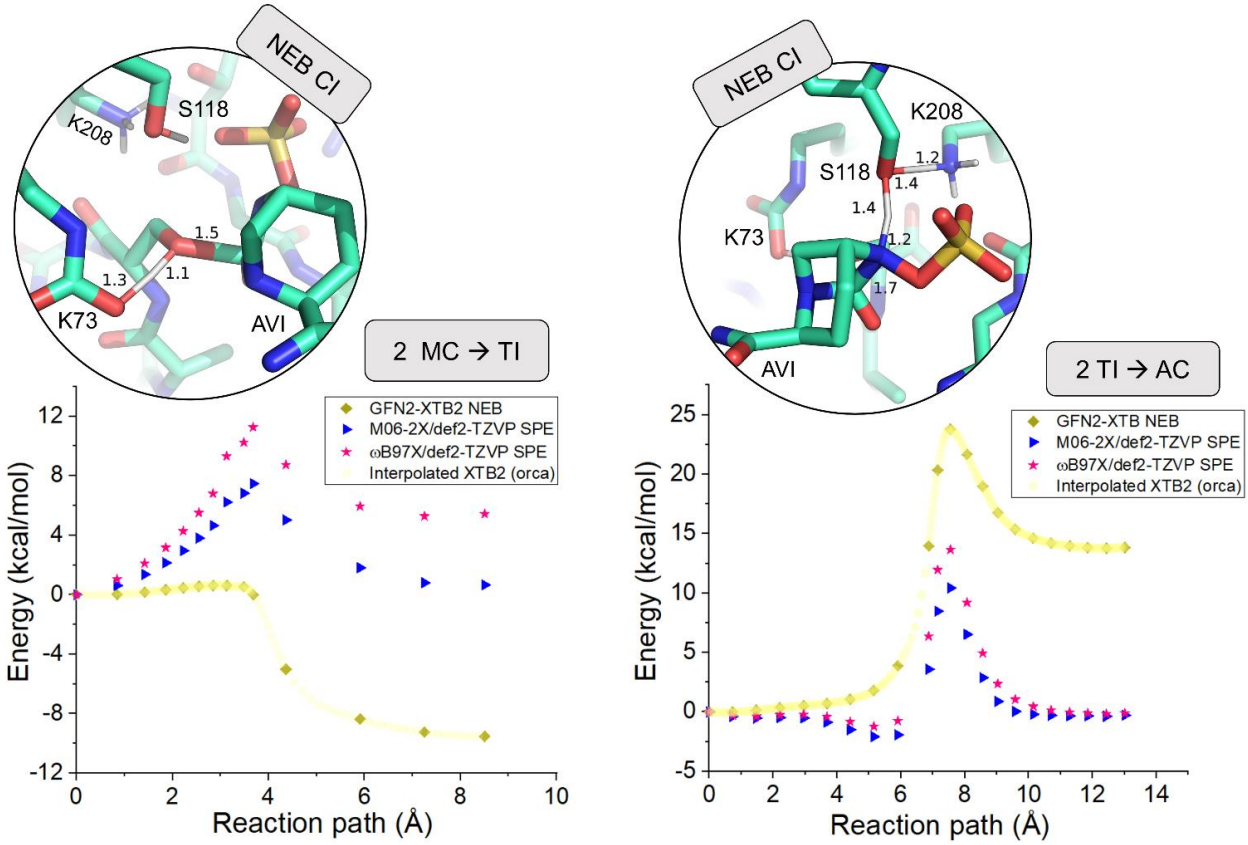

Figure 7.11 Potential energies for the tetrahedral intermediate formation (MC → TI, left), and the subsequent avibactam ring opening and protonation (TI → AC, right) for pathway 2. NEB calculations were performed using XTB2/ff14SB, QM/MM SPEs calculated using either ωB97X or M06-2X functionals with the def2-TZVP basis set for the QM region. The converged structure of the climbing image depicted for both reactions (labelled NEB CI).

Key distances for both reactions involved in pathway 2 are presented in Figure 7.12. They follow largely the same pattern observed for pathway 1, where the proton transfer and nucleophilic attack in the MC → TI reaction are concerted. This aligns with the slight increase in the calculated XTB2/ff14SB energy at the TS. For the TI → AC reaction, the proton transfers from Lys208 to Ser118 and from Ser118 to avibactam occur almost simultaneously, and coincide with the elongation of the avibactam C-N bond.

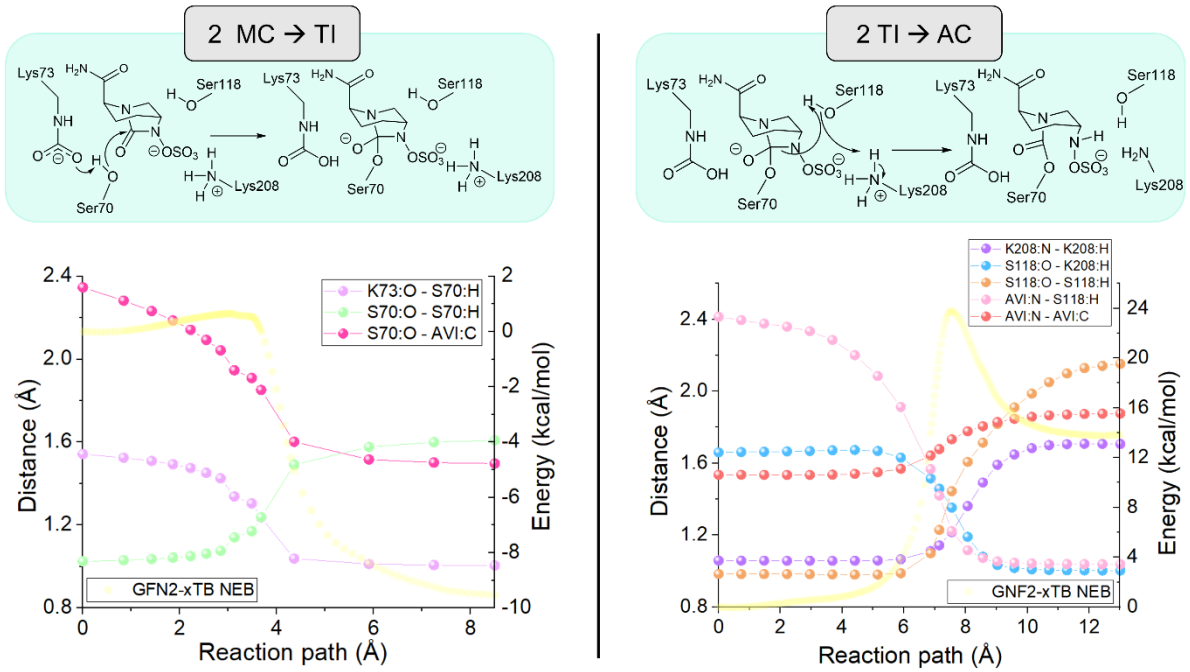

Figure 7.12 Key distances along the calculated MEP for the MC → TI (left) and TI → AC (right) reactions in pathway 2. Left y-axis: measured key distances along the MEP, depicted with dots connected by lines. Right y-axis: QM/MM energy with XTB2 as the QM method along the MEP, depicted by yellow circles.

7.3.4 Comparison of the pathways

The activation free energies calculated with all QM methods used are listed in Table 7.1. Energies are tabulated for the separate reactions as well combined to give the overall activation energy for the whole acylation reaction. Going all the way from MC to the AC, DFT/MM energies on the XTB2/MM optimised MEPs indicate that the overall barrier for pathway 2 is either 11.0 kcal/mol (ωB97X/def2-TZVP) or 9.2 kcal/mol (M06-2X/def2-TZVP) lower in energy than for pathway 1. Notably, the calculated energy barrier for the MC → TI reaction in pathway 1 is significantly higher than for pathway 2. In pathway 1, the TI formation requires either 16.1 kcal/mol (ωB97X) or 15.7 kcal/mol (M06-2X) more energy than the TI formation in pathway 2. Comparison of the calculated activation energy barriers implies that of the studied mechanisms, pathway 2 is the most likely mechanism for avibactam acylation. The activation energy barrier for the MC → TI conversion in pathway 2 was re-calculated using ωB97X/def2-SVP for the QM region during NEB optimisation, and calculating SPEs using either ωB97X/def2-TZVP or M06-2X/def2-TZVP. The obtained barriers of 10.2 kcal/mol

(ωB97X) and 6.6 kcal/mol (M06-2X) are in good agreement with the previously obtained corresponding energetics on the XTB2 optimised structures. Comparison of the CI and TI structures reveals the proton transfer between Ser70 and Lys73 to have progressed further when optimising the structured using ωB97X/def2-SVP//MM. The distances between Lys73:O – Ser70:H and Ser70:O – Ser70:H are 1.1 and 1.3 Å in the ωB97X/MM optimised TS, and conversely 1.3 and 1.1 Å in the TS optimised using XTB2/MM (respectively). The ωB97X/MM reaction energy is 4.2 kcal/mol, and the M06-2X/MM reaction energy is -0.7 kcal/mol. The TI structures are virtually identical when optimised either using XTB2/MM or ωB97X/MM, implying that whilst XTB2 does not give reliable energetics for the forming TI, the structures can be used for obtaining better energetics using a higher-level method for the QM region. Further, the barrier for the MC → TI conversion in pathway 1 using the same DFT methods for the QM region in NEB optimisation and subsequent SPEs yields barriers of 27.2 and 23.0 kcal/mol for ωB97X and M06-2X, respectively. This further support the hypothesis of a proton transfer from Ser70 to a neutral Lys73 being energetically unfeasible in comparison to a proton transfer to a carboxylated Lys73.

Table 7.1 QM/MM activation energy barriers ($\Delta^{\ddagger}E$) for pathways 1 and 2 with all QM methods used. All energies in kcal/mol. The combined barrier is obtained by summing together the individual barriers for MC → TI and TI → AC.

	GFN2-XTB/MM optimised structures		
$\Delta^{\ddagger}E$ (kcal/mol)	GFN2-XTB	ωB97X/def2-TZVP	M06-2X/def2-TZVP
1 MC → TI	13.6	27.4	23.2
1 TI → AC	16.0	9.8	6.0
1 MC → AC Combined	29.6	37.2	29.2
2 MC → TI	0.6	11.3	7.5
2 TI → AC	23.8	14.9	12.5
2 MC → AC Combined	23.8	26.2	20.0

A k_{cat} value for avibactam acylation by OXA-48 has not been measured, as only the combined k_2/K_i = 1.4 ± 0.1 x 10^3 M^{-1} s^{-1} is available in existing literature.[34] However, a separate rate

constant for recyclization is measured to be k_{off} = 1.2 ± 0.4 x 10^{-5} s^{-1} with a half-life of 1000 ± 300 minutes. This deacylation rate constant corresponds to a free energy barrier of approximately 24.3 kcal/mol (converted using the Eyring equation). As the free energy barrier for acylation is lower than for deacylation, it is likely that the calculated combined potential energy barriers of 23.8/26.2/20.0 kcal/mol (with XTB2/ωB97X/M06-2X as the QM method, respectively) for pathway 2 overestimate the actual acylation barrier. If recyclization occurs via the same reaction "backwards", the activation energy for the AC → TI reaction is 10 kcal/mol for XTB2, 15.0 kcal/mol for ωB97X, and 12.8 kcal/mol for M06-2X. Correspondingly, the TI → MC conversion to give intact avibactam requires 10.1 kcal/mol using XTB2, 10.6 kcal/mol using ωB97X, and 6.8 kcal/mol using M06-2X. The combined barriers for the whole AC → MC recyclization reaction are 10.1 kcal/mol with XTB2 as the QM method, 25.6 kcal/mol with ωB97X, and 19.6 kcal/mol with M06-2X. These are all lower than the corresponding overall barriers calculated for the whole MC → AC conversion in acylation. Therefore, avibactam inhibition most likely relies on Lys73 being preferentially in its decarboxylated form in the AC state, and thus unable to act as a general acid in recyclization. This hypothesis is further supported by experimental data from enzyme kinetics, crystallography, and NMR spectroscopy. Based on the crystallised OXA-48/avibactam complexes, Lys73 is preferentially decarboxylated when covalently-bound avibactam is present. For example, in structures obtained at pH values 6.5 and 7.5, none of the OXA-48 monomers displayed Lys73 carboxylation, and at 8.5 only partial carboxylation was observed.[235] This is expected, as increasing the pH of the solution favours Lys73 carboxylation. Further, ^{19}F NMR measurements suggest that Lys73 is decarboxylated in the OXA-48/avibactam AC complex.[236] Enzyme kinetics measurements indicate that avibactam recyclization is slower for class D β-lactamases than for classes A and C.[34] A distinct difference between class D and class A/C enzymes is that for the former, a reversibly carboxylated Lys73 acts as an acid/base in the reaction instead of a "standard", unmodified amino acid residue. "Inactivation" of this Lys73 through decarboxylation could explain the relative slow rates of class D SBLs.

7.4 Conclusions

In this chapter, the possible mechanisms of OXA-48 inhibition by the DBO inhibitor avibactam were studied using MM MD simulations and QM/MM potential energy calculations.

Two main reaction mechanisms were inspected. In pathway 1, a neutral Lys73 acts as the initial proton acceptor, but subsequently also donates a proton to Ser118, which further protonates avibactam. In pathway 2, a carboxy-Lys73 is the initial proton acceptor, and avibactam protonation occurs by Lys208 via Ser118. Accordingly, non-covalent MC models for OXA-48 with either a standard, neutral Lys73 or with a carboxylated Lys73 were constructed. The stabilities of these complexes were inspected by ten independent 50 ns MM MD simulations. With a neutral Lys73, avibactam shifted away from its initial acylation-compatible pose in nine out of ten simulations. With a carboxylated Lys73, the same avibactam re-positioning was observed in five simulations. Comparison of the reaction energetics for acylation was done by constructing MEPs for both pathways using the CI-NEB method. Energetics along the calculated MEPs indicate that the initial proton transfer and nucleophilic attack are more feasible for OXA-48 with a carboxylated Lys73; the activation energy barriers are 13.0-16.1 kcal/mol lower for the MC → TI reaction in pathway 2 (with a carboxy-Lys73) than in pathway 1 (neutral Lys73). Based on the combination of MM MD and QM/MM NEB calculations presented here, we suggest that avibactam acylation happens analogous to β-lactam hydrolysis, where a carboxy-Lys73 acts as the general base. The efficient inhibition of OXA-48 (and other class D β-lactamases) with avibactam is enabled by slow recyclization rates, which are likely due to post-acylation decarboxylation of Lys73 at the AC state.

8. Conclusions and outlook

In this thesis, I have outlined my research on selected serine β-lactamases, which have been identified among the most common enzymes in resistant bacterial infections globally. In Chapter 3, carbapenem hydrolysis by eight class A β-lactamases is compared using different types of computational assays. These computational assays are essentially simplified simulation protocols, which still distinguish between different hydrolytic phenotypes (i.e. correctly differentiate between carbapenemases and carbapenem-inhibited enzymes). Chapters 5 to 7 present simulations of class D β-lactamases, specifically the OXA-48 family. Cephalosporinase inactivation by selected OXA-48 enzymes is compared in Chapter 5, and the differences in carbapenem breakdown between imipenem and meropenem for OXA-48 in Chapter 6. Finally, Chapter 7 discusses the inhibition mechanism of OXA-48 by avibactam, a DBO-based β-lactamase inhibitor. In this last section, I will briefly outline the main conclusions of these chapters, consider their potential impact, and discuss possible future work in the corresponding research areas.

8.1 Class A β-lactamases

In Chapter 3, meropenem breakdown was simulated for four carbapenemases (KPC-2, NMC-A, SFC-1, and SME-1) and for four carbapenem-inhibited enzymes (TEM-1, SHV-1, BlaC, and CTX-M-16), all belonging to class A serine β-lactamases. A previous study, where QM/MM umbrella sampling (with DFTB2) was used to calculate full free energy surfaces for all enzymes, was used as a starting point for constructing more simplified simulation protocols.[190] The aim here was to limit both the sampling time in each umbrella sampling window, and the conformational sampling along the free energy surface. The sampling time was shortened from 20 ps/window to 2 ps/window, and the number of umbrella sampling windows was decreased from 374 to 28. The 28 windows correspond to structures near the approximate minimum free energy path, which was largely similar across all eight enzymes. This new simulation protocol used less than 99% of the computational resources required for the initial QM/MM computational assay, whilst still correctly differentiating between the two groups.

This study highlights, how simulations can be used as computational assays to compare enzyme activities. In addition to correctly distinguishing between known hydrolytic phenotypes, i.e. carbapenemases and non-carbapenemases, these type of *in silico* assays could be applied to study the phenotypes of new, emerging variants e.g. from sequence data. In addition to assaying new β-lactamase variants, newly designed β-lactam antibiotics or β-lactamase inhibitors could be inspected in a similar fashion e.g. prior to synthesising them. This underlines the paradigm shift in computational chemistry, where the role of simulations is moving from mainly rationalising experimental data to being fully predictive and guiding decision making. Further automation of these protocols could provide rough estimates of enzyme activities within hours with relatively modest computational resources. Establishing how much these computational assays could still be simplified and shortened remains as future work. Some possible ideas could include moving from periodic box simulations to a more simplified system descriptions (with fewer atoms), and using GPU accelerated QM programs or new, more efficient methods for the QM region (e.g. utilising machine learning potentials).

8.2 OXA-48 β-lactamases

8.2.1 Cephalosporinase activity

Generally, OXA-48 β-lactamases are either carbapenemases exhibiting low level carbapenem hydrolysis with a specific preference towards imipenem, or they are more ESBL-like, i.e. they have acquired activity against oxyimino cephalosporins like ceftazidime (usually at the expense of efficient imipenem breakdown). In Chapter 5, the cephalosporinase activities of carbapenemases OXA-48 and OXA-181 are compared against OXA-163, which has an ESBL-like hydrolytic phenotype. Comparison of the expected rate-limiting step (deacylation) in ceftazidime hydrolysis revealed that for cephalosporinases, the active site tends to be less hydrated. Hydration around the general base (carboxy-Lys73) correlated with the calculated free energy barriers: the fewer water molecules were hydrogen bonding to the proton accepting carboxylate oxygen, the lower the barriers were. Additionally, two further hypotheses were tested using our simulation protocols. Firstly, the effect of a single mutation (Arg214Ser) on the calculated deacylation barriers was analysed, as deletion of Arg214 was hypothesised to be the main determinant in the acquired activity in OXA-163. Secondly, the effect of the Ω-loop distortion was studied by constructing a model of OXA-48 with a flexible Ω-loop.

In this study, we demonstrated the power of our simplified simulation protocols presented in Chapter 3. All reaction simulations were performed using short simulation times (2 ps per US window) with semi-empirical QM methods. Whilst replicating the experimentally measured k_{cat} values within chemical accuracy was not possible with this approach, it is sufficient to discriminate between inhibited and active enzymes. Additionally, this modelling approach was used to indicate the ceftazidime orientation most compatible with deacylation. We were also able to complement existing experimental research by analysing the effect of Ω-loop distortion on the calculated rates. No visible electron density was observed for the Ω-loop region in a crystal structure of OXA-48 with ceftazidime (in the AC state), and hence Ω-loop distortion was hypothesised to be important for ceftazidime hydrolysis. However, our simulations show that this distortion is likely to lead to diminished catalytic rates, as the active site is fully exposed to solvent molecules. Therefore, the observed Ω-loop distortion most likely relates to the initial binding of ceftazidime, a relatively bulky cephalosporin substrate, instead of offering any rate enhancement beyond aiding in the formation of the initial non-covalent complex. In addition to rationalising experimental findings, we predicted the activity of an *in silico* Arg214Ser point mutant. This is an example of computational assays being used to study activities of new enzyme variants, as discussed in Section 8.1. Finally, this was the first work to highlight the effect active site hydration has on the catalytic efficiency of serine β-lactamases, aside the obvious need for a deacylating water to reach a position suitable for nucleophilic attack. We illustrated that whilst the argument concerning deacylating water movement is accurate, there is a more careful balance between the active site being accessible and additional hydration around the reactive residues impairing catalysis.

Our simulations focus on modelling the rate-limiting enzymatic reaction starting from the covalent AC intermediate. For this, we assume the initial non-covalent MC to have been formed and undergone acylation. However, experimental kinetics indicate that in addition to the actual rate constant, also ceftazidime binding differs for OXA-48 and OXA-163. Studying the role of the Ω-loop (and its possible distortion) in binding remains for future studies. Another interesting prospect is developing more broad-spectrum cephalosporin antibiotics against serine β-lactamases. E.g. the ceftazidime/avibactam combination is one of the recommended treatment options for OXA-48 infections,[259] as OXA-48 remains susceptible for both ceftazidime and avibactam. In addition to ceftazidime, another treatment option against OXA-48 is cefiderocol, another cephalosporin antibiotic. As OXA-48 spares these antibiotics, it is

likely that the cephalosporin scaffold could be improved to yield even more broad-spectrum antibacterial drugs.

8.2.2 Carbapenemase activity

As mentioned in the previous section, the OXA-48 β-lactamase exhibits a preference for imipenem over other carbapenem substrates. The origin of this imipenemase activity remains unclear, although the β5-β6 loop has been demonstrated to be integral for acquired carbapenemase activity in general.[242, 245] In Chapter 6, the rate-limiting step in carbapenem breakdown (deacylation, as for ceftazidime) is compared for imipenem and meropenem by MM MD and QM/MM reaction simulations. To briefly summarise, we observed carbapenem substrates to be able to accommodate three different conformations, which differ by the position of the 6α-hydroxyethyl group. The effect of changing the orientation of the 6α-hydroxyethyl group on the deacylation reaction was calculated by restraining this sidechain during QM/MM US simulations. For both carbapenems, the lowest free energy barriers were obtained, when the 6α-hydroxyethyl group is rotated near the oxyanion hole and either donates or accepts a hydrogen bond from the deacylating water. For imipenem, the lowest free energy barriers were calculated in this orientation upon the 6α-hydroxyethyl accepting a hydrogen bond from the deacylating water, and the barrier is increased if hydrogen bonds change so that the 6α-hydroxyethyl hydroxyl group donates a hydrogen bond to the water nucleophile. The same effect was not calculated for meropenem, where both hydrogen bond patterns had very similar barriers. Further, we were able to extend our argument concerning hydration around the general base, as increased hydration around both carboxylate oxygens was calculated to affect the barriers (not just around the proton accepting one).

Many arguments about the source of carbapenemase activity have been presented in existing literature, and whilst some have been related to the orientation of the discussed 6α-hydroxyethyl group,[222, 254] our simulations illustrate the precise effect a certain substrate conformation has on the deacylation efficiency. We are also able to pinpoint the exact orientation that is most likely to contribute to efficient deacylation. Additionally, we can deduct a very subtle difference between the preferred hydrogen bond networks in the active site, which in turn most likely leads to the observed difference between imipenem and meropenem hydrolysis efficiency. Finally, we further extended our findings of active site hydration (discussed in Section 8.2.1 for ceftazidime) impairing catalysis, indicating that it applies to

both Lys73 carboxylate oxygens. The free energy barriers were calculated to increase even when hydration around the second carboxylate oxygen, which does not participate in the reaction, increased as well.

Even though carbapenem hydrolysis by the OXA-48 β-lactamase was dissected rather exhaustively, the exact reason for the calculated lower energy barriers for imipenem in the most deacylation-compatible substrate orientation remains elusive. This is expected to relate to the 1β-methyl group in meropenem, which is replaced by a 1β-proton in imipenem. The larger methyl group might favour re-orienting water molecules near the substrate or the substrate itself, but establishing the validity of this hypothesis remains for future studies. Additionally, comparing carbapenem hydrolysis between the wildtype OXA-48 and its variants with enhanced carbapenemase activity could further indicate if similar patterns with respect to active site hydrogen bonds are observed. Another interesting aspect for future research would be inspecting a common side reaction for carbapenems, as in addition to standard hydrolysis, OXA-48 has been shown to degrade carbapenems additionally by β-lactone formation.[253, 254] Originally lactone formation was observed for the wildtype OXA-48 only with 1β-methyl carbapenems,[253] but later some OXA-48 variants were shown to lactonise 1β-proton carbapenems as well.[254] Comparison of deacylation vs. lactone formation for different carbapenem substrates, as well as establishing the role of amino acid mutations enhancing or diminishing lactone formation, would be an intriguing (albeit most likely challenging) subject for computational modelling.

8.2.3 Avibactam inhibition mechanism

To combat the growing resistance against β-lactam antibiotics, new β-lactamase inhibitors are in active development. Avibactam is one of these newer non-β-lactam β-lactamase inhibitors, which efficiently inhibits OXA-48.[34] Experimental studies indicate that avibactam is acylated in an analogous way to β-lactam substrates, but instead of being inactivated via deacylation, it undergoes recyclization to re-form the intact inhibitor.[34] However, the exact mechanisms for avibactam acylation and recyclization are not known, but two main hypotheses have been presented in existing literature. In the first proposed pathway, avibactam is acylated using a neutral, non-carboxylated Lys73 as the general base, which subsequently also protonates avibactam via Ser118.[235] In the second proposal, a carboxylated Lys73 acts the general base, whilst avibactam protonation occurs by Lys208 via Ser118.[264] We

compared these two pathways by calculating their potential energy profiles using QM/MM nudged elastic band calculations, and concluded the pathway incorporating a carboxylated Lys73 to be more likely than the alternative mechanism with a neutral Lys73 as the proton acceptor.

Even though it is known that Lys73 needs to be in its carboxylated form for β-lactam hydrolysis, this has so far not been verified for DBOs like avibactam. The hypothesis of a neutral Lys73 acting as a proton acceptor is mainly based on crystal structures, where Lys73 is observed to favour its standard, non-carboxylated form in the presence of a covalently-bound avibactam.[235] Here, we show that a proton transfer to a neutral Lys73 is energetically not feasible, in contrast to proton transfer to a carboxy-Lys73. Therefore, avibactam most likely utilises a similar mechanism for the initial proton transfer and nucleophilic attack as is known for β-lactam antibiotics. The inhibition power of avibactam is likely to come from post-acylation decarboxylation of Lys73, which traps the covalently-bound inhibitor in the acylenzyme state. This suggested mechanism aligns well with other experimental observations, such as class D β-lactamases exhibiting slower recyclization rates than class A or C β-lactamases.[34]

Even though we provide a mechanistic suggestion for avibactam acylation, different possible pathways for recyclization are not inspected in detail. Rather, recyclization is expected to happen via the same mechanism in the reverse direction; verifying if this expectation is true remains for future studies. Additionally, calculating free energy profiles (as opposed to potential energy) for the fully solvated enzyme system using e.g. the adaptive string method[345], will possibly provide more accurate energetics for the whole acylation reaction. Finally, studying the origin of Lys73 decarboxylation post-acylation can guide the design of new types of inhibitors, which essentially inhibit class D β-lactamases by enforcing Lys73 decarboxylation at the acylenzyme state.

8.3 Broad impact

Atomistic simulations of enzyme/substrate complexes complement experimental research, e.g. x-ray crystallography, by offering a more complete picture of the dynamic nature of these macromolecules. As illustrated in Sections 8.2.1-8.2.3., biomolecular simulations are useful for elucidating hypotheses concerning enzyme mechanisms and determinants of activity,

which are originally derived from experimental data. Simulations also provide a cost-effective and straight-forward way of testing new hypotheses or screening through large data libraries. As an example, serine β-lactamases can acquire activity against β-lactam antibiotics or β-lactamase inhibitors through point mutations. As new enzyme variants emerge e.g. from environmental or clinical samples, their phenotypes could be characterised *in silico* directly from sequence data. Simulations can also be used to elucidate the molecular level interactions, which lead to increased hydrolysis against certain antibiotics for enzyme variants emerging from experimental research.[346] Further, identified mutational sites in new variants could be screened for any alternative amino acid replacements, therefore identifying possible new variants before they have been detected. This would help to understand the evolution of broad-spectrum β-lactamase resistance on a more fundamental level. Combining further automation of simulation protocols with modest required computational resources enables using a standard laptop as a diagnostic tool for predicting enzymatic activities against a certain antibiotic. This in turn can be used to guide antibiotic prescriptions in a clinical setting. This kind of evidence-based antibiotic prescription is an integral part of antibiotic stewardship, as it reduces selection pressure for bacteria and slows down evolving resistance.

The subtle effects of solvation, highlighted by the studies of carbapenem and cephalosporin breakdown by OXA-48 enzymes, aid in gaining a better understanding of features contributing to antibiotic hydrolysis. Serine β-lactamases seem to enhance their activity by expulsing water away from the active site, especially away from the general base. Changes in active site hydration are especially important in class D β-lactamases, where the general base is not a part of a highly organised hydrogen bond network. A comparison of active site hydration between different enzyme variants could already be used as a relatively simple indicator of enzyme activity. Further, the findings concerning hydration have implications for future antibiotic and inhibitor design purposes. An ideal β-lactamase inhibitor is acylated efficiently and forms a very long-lived covalent acylenzyme structure post-acylation. One way to achieve this is to design ligands, which modulate the access of water molecules to the active site: as lack of catalytic water molecules essentially traps the ligand in the acylenzyme state. The use of reliable and efficient QM/MM protocols may also aid in designing new mechanism-based inhibitors as well as elucidating inhibition mechanisms for inhibitors with a new mode of action (as evidenced for avibactam).

References

1. Fact Sheet on Antimicrobial Resistance. https://www.who.int/news-room/fact-sheets/detail/antimicrobial-resistance (accessed 2021/03/29).
2. Kang, C. I.; Song, J. H., Antimicrobial resistance in Asia: current epidemiology and clinical implications. *Infect. Chemother.* 2013, *45* (1), 22-31.
3. Jean, S. S.; Hsueh, P. R., High burden of antimicrobial resistance in Asia. *Int. J. Antimicrob. Agents* 2011, *37* (4), 291-295.
4. Essack, S. Y.; Desta, A. T.; Abotsi, R. E.; Agoba, E. E., Antimicrobial resistance in the WHO African region: current status and roadmap for action. *J. Public Health (Oxf.)* 2017, *39* (1), 8-13.
5. Bernabé, K. J.; Langendorf, C.; Ford, N.; Ronat, J.-B.; Murphy, R. A., Antimicrobial resistance in West Africa: a systematic review and meta-analysis. *Int. J. Antimicrob. Agents* 2017, *50* (5), 629-639.
6. *Antibiotic Resistance Threats in the United States*; U.S. Department of Health and Human Services, CDC: Atlanta, GA, 2019.
7. *English Surveillance Programme for Antimicrobial Utilisation and Resistance (ESPAUR). Report 2019 to 2020*; Public Health England: London, 2020.
8. *Global Action Plan on Antimicrobial Resistance*; World Health Organization: Geneva, 2015.
9. World Antimicrobial Awareness Week. https://www.who.int/campaigns/world-antimicrobial-awareness-week (accessed 2021/03/29).
10. *Global antimicrobial resistance surveillance system (GLASS) report: early implementation 2020*; World Health Organization: Geneva, 2020.
11. *Tackling antimicrobial resistance 2019–2024. The UK's five-year national action plan*; HM Government: 2019.
12. Aly, A. H.; Debbab, A.; Proksch, P., Fifty years of drug discovery from fungi. *Fungal Divers.* 2011, *50* (1), 3-19.
13. Lewis, K., The Science of Antibiotic Discovery. *Cell* 2020, *181* (1), 29-45.
14. Hutchings, M. I.; Truman, A. W.; Wilkinson, B., Antibiotics: past, present and future. *Curr. Opin. Microbiol.* 2019, *51*, 72-80.
15. Lewis, K., Platforms for antibiotic discovery. *Nat. Rev. Drug Discov.* 2013, *12* (5), 371-387.
16. Plackett, B., No money for new drugs. *Nature* 2020, *586*, S50-S52.
17. Fleming, A., On the Antibacterial Action of Cultures of a Penicillium, with Special Reference to their Use in the Isolation of B. influenzæ. *Br. J. Exp. Pathol.* 1929, *10* (3), 226-236.
18. Klein, E. Y.; Van Boeckel, T. P.; Martinez, E. M.; Pant, S.; Gandra, S.; Levin, S. A.; Goossens, H.; Laxminarayan, R., Global Increase and Geographic Convergence in Antibiotic Consumption Between 2000 and 2015. *Proc. Natl. Acad. Sci. U S A* 2018, *115* (15), E3463-E3470.
19. Miller, E. L., The Penicillins: a review and update. *J. Midwifery Women's Health* 2002, *47* (6), 426-434.

20. Garaul, J.; Wilson, W.; Wood, M.; Carlet, J., Fourth-generation cephalosporins: a review of in vitro activity, pharmacokinetics, pharmacodynamics and clinical utility. *Clin. Microbiol. Infect.* 1997, *3* (S87-S101).
21. Barbour, A.; Schmidt, S.; Rand, K. H.; Derendorf, H., Ceftobiprole: a novel cephalosporin with activity against Gram-positive and Gram-negative pathogens, including methicillin-resistant Staphylococcus aureus (MRSA). *Int. J. Antimicrob. Agents* 2009, *34* (1), 1-7.
22. George G. Zhanel; Grace Sniezek; Frank Schweizer; Sheryl Zelenitsky; Philippe R.S. Lagace-Wiens; Ethan Rubinstein; Alfred S. Gin; Daryl J. Hoban; Karlowsky, J. A., Ceftaroline - A Novel Broad-Spectrum Cephalosporin with Activity against Meticillin-Resistant Staphylococcus aureus. *Drugs* 2009, *69* (7), 809-831.
23. Sykes, R. B.; Bonner, D. P., Aztreonam: The First Monobactam. *Am. J. Med.* 1985, *78*, 2-10.
24. Papp-Wallace, K. M.; Endimiani, A.; Taracila, M. A.; Bonomo, R. A., Carbapenems: Past, Present, and Future. *Antimicrob. Agents Chemother.* 2011, *55* (11), 4943-4960.
25. Tehrani, K.; Martin, N. I., β-Lactam/β-Lactamase Inhibitor Combinations: an Update. *Med. Chem. Commun.* 2018, *9* (9), 1439-1456.
26. *World Health Organization Model List of Essential Medicines, 21st List, 2019*; World Health Organization: Geneva, 2019.
27. Drawz, S. M.; Bonomo, R. A., Three Decades of β-Lactamase Inhibitors. *Clin. Microbiol. Rev.* 2010, *23*, 160-201.
28. Todd, P. A.; Benfield, P., Amoxicillin/Clavulanic Acid. *Drugs* 1990, *39*, 264-307.
29. Petros I. Rafailidis; Eleni N. Ioannidou; Falagas, M. E., Ampicillin/Sulbactam - Current Status in Severe Bacterial Infections. *Drugs* 2007, *67* (13), 1829-1849.
30. Harriet M. Bryson; Brogden, R. N., Piperacillin/Tazobactam - A Review of its Antibacterial Activity, Pharmacokinetic Properties and Therapeutic Potential. *Drugs* 1994, *47* (3), 506-535.
31. Ehmann, D. E.; Jahic, H.; Ross, P. L.; Gu, R. F.; Hu, J.; Kern, G.; Walkup, G. K.; Fisher, S. L., Avibactam Is a Covalent, Reversible, Non-β-lactam β-lactamase Inhibitor. *Proc. Natl. Acad. Sci. U S A* 2012, *109* (29), 11663-11668.
32. Wang, S.; Zhao, S. Y.; Xiao, S. Z.; Gu, F. F.; Liu, Q. Z.; Tang, J.; Guo, X. K.; Ni, Y. X.; Han, L. Z., Antimicrobial Resistance and Molecular Epidemiology of Escherichia coli Causing Bloodstream Infections in Three Hospitals in Shanghai, China. *PLoS One* 2016, *11* (1), e0147740.
33. Zhanel, G. G.; Lawson, C. D.; Adam, H.; Schweizer, F.; Zelenitsky, S.; Lagace-Wiens, P. R.; Denisuik, A.; Rubinstein, E.; Gin, A. S.; Hoban, D. J.; Lynch, J. P., 3rd; Karlowsky, J. A., Ceftazidime-Avibactam: a Novel Cephalosporin/β-Lactamase Inhibitor Combination. *Drugs* 2013, *73* (2), 159-177.
34. Ehmann, D. E.; Jahic, H.; Ross, P. L.; Gu, R. F.; Hu, J.; Durand-Reville, T. F.; Lahiri, S.; Thresher, J.; Livchak, S.; Gao, N.; Palmer, T.; Walkup, G. K.; Fisher, S. L., Kinetics of Avibactam Inhibition Against Class A, C, and D β-lactamases. *J. Biol. Chem.* 2013, *288* (39), 27960-27971.

35. Shapiro, A. B.; Gao, N.; Jahic, H.; Carter, N. M.; Chen, A.; Miller, A. A., Reversibility of Covalent, Broad-Spectrum Serine β-Lactamase Inhibition by the Diazabicyclooctenone ETX2514. *ACS Infect. Dis.* 2017, *3* (11), 833-844.
36. Durand-Reville, T. F.; Guler, S.; Comita-Prevoir, J.; Chen, B.; Bifulco, N.; Huynh, H.; Lahiri, S.; Shapiro, A. B.; McLeod, S. M.; Carter, N. M.; Moussa, S. H.; Velez-Vega, C.; Olivier, N. B.; McLaughlin, R.; Gao, N.; Thresher, J.; Palmer, T.; Andrews, B.; Giacobbe, R. A.; Newman, J. V.; Ehmann, D. E.; de Jonge, B.; O'Donnell, J.; Mueller, J. P.; Tommasi, R. A.; Miller, A. A., ETX2514 Is a Broad-Spectrum β-Lactamase Inhibitor for the Treatment of Drug-Resistant Gram-Negative Bacteria Including Acinetobacter baumannii. *Nat. Microbiol.* 2017, *2*, 17104.
37. Papp-Wallace, K. M.; Nguyen, N. Q.; Jacobs, M. R.; Bethel, C. R.; Barnes, M. D.; Kumar, V.; Bajaksouzian, S.; Rudin, S. D.; Rather, P. N.; Bhavsar, S.; Ravikumar, T.; Deshpande, P. K.; Patil, V.; Yeole, R.; Bhagwat, S. S.; Patel, M. V.; van den Akker, F.; Bonomo, R. A., Strategic Approaches to Overcome Resistance against Gram-Negative Pathogens Using β-Lactamase Inhibitors and β-Lactam Enhancers: Activity of Three Novel Diazabicyclooctanes WCK 5153, Zidebactam (WCK 5107), and WCK 4234. *J. Med. Chem.* 2018, *61* (9), 4067-4086.
38. Reck, F.; Bermingham, A.; Blais, J.; Casarez, A.; Colvin, R.; Dean, C. R.; Furegati, M.; Gamboa, L.; Growcott, E.; Li, C.; Lopez, S.; Metzger, L.; Nocito, S.; Ossola, F.; Phizackerley, K.; Rasper, D.; Shaul, J.; Shen, X.; Simmons, R. L.; Tang, D.; Tashiro, K.; Yue, Q., IID572: A New Potentially Best-In-Class β-Lactamase Inhibitor. *ACS Infect. Dis.* 2019, *5* (7), 1045-1051.
39. Durand-Réville, T. F.; Comita-Prevoir, J.; Zhang, J.; Wu, X.; May-Dracka, T. L.; Romero, J. A. C.; Wu, F.; Chen, A.; Shapiro, A. B.; Carter, N. M.; McLeod, S. M.; Giacobbe, R. A.; Verheijen, J. C.; Lahiri, S. D.; Sacco, M. D.; Chen, Y.; O'Donnell, J. P.; Miller, A. A.; Mueller, J. P.; Tommasi, R. A., Discovery of an Orally Available Diazabicyclooctane Inhibitor (ETX0282) of Class A, C, and D Serine β-Lactamases. *J. Med. Chem.* 2020, *63* (21), 12511-12525.
40. Brem, J.; Cain, R.; Cahill, S.; McDonough, M. A.; Clifton, I. J.; Jimenez-Castellanos, J. C.; Avison, M. B.; Spencer, J.; Fishwick, C. W.; Schofield, C. J., Structural Basis of Metallo-β-Lactamase, Serine-β-Lactamase and Penicillin-Binding Protein Inhibition by Cyclic Boronates. *Nat. Commun.* 2016, *7*, 12406.
41. Cahill, S. T.; Cain, R.; Wang, D. Y.; Lohans, C. T.; Wareham, D. W.; Oswin, H. P.; Mohammed, J.; Spencer, J.; Fishwick, C. W.; McDonough, M. A.; Schofield, C. J.; Brem, J., Cyclic Boronates Inhibit All Classes of β-Lactamases. *Antimicrob. Agents Chemother.* 2017, *61* (4), e02260-16.
42. Hecker, S. J.; Reddy, K. R.; Totrov, M.; Hirst, G. C.; Lomovskaya, O.; Griffith, D. C.; King, P.; Tsivkovski, R.; Sun, D.; Sabet, M.; Tarazi, Z.; Clifton, M. C.; Atkins, K.; Raymond, A.; Potts, K. T.; Abendroth, J.; Boyer, S. H.; Loutit, J. S.; Morgan, E. E.; Durso, S.; Dudley, M. N., Discovery of a Cyclic Boronic Acid β-Lactamase Inhibitor (RPX7009) with Utility vs Class A Serine Carbapenemases. *J. Med. Chem.* 2015, *58* (9), 3682-92.

43. Cho, J. C.; Zmarlicka, M. T.; Shaeer, K. M.; Pardo, J., Meropenem/Vaborbactam, the First Carbapenem/β-Lactamase Inhibitor Combination. *Ann. Pharmacother.* 2018, *52* (8), 769-779.
44. Krajnc, A.; Brem, J.; Hinchliffe, P.; Calvopina, K.; Panduwawala, T. D.; Lang, P. A.; Kamps, J.; Tyrrell, J. M.; Widlake, E.; Saward, B. G.; Walsh, T. R.; Spencer, J.; Schofield, C. J., Bicyclic Boronate VNRX-5133 Inhibits Metallo- and Serine-β-Lactamases. *J. Med. Chem.* 2019, *62* (18), 8544-8556.
45. Tsivkovski, R.; Totrov, M.; Lomovskay, O., Biochemical Characterization of QPX7728, a New Ultrabroad-Spectrum β-Lactamase Inhibitor of Serine and Metallo-β-Lactamases. *Antimicrob. Agents Chemother.* 2020, *64* (6), e00130-20.
46. *β-Lactam and β-Lactamase Inhibitors Market by Drug Class, Disease and Route of Administration: Global Opportunity Analysis and Industry Forecast, 2019-2028*; Allied Market Research: 2019.
47. About Antibiotic Resistance. https://www.cdc.gov/drugresistance/about.html (accessed 2021/03/30).
48. Alekshun, M. N.; Levy, S. B., Molecular Mechanisms of Antibacterial Multidrug Resistance. *Cell* 2007, *128* (6), 1037-1050.
49. Tooke, C. L.; Hinchliffe, P.; Bragginton, E. C.; Colenso, C. K.; Hirvonen, V. H. A.; Takebayashi, Y.; Spencer, J., β-Lactamases and β-Lactamase Inhibitors in the 21st Century. *J. Mol. Biol.* 2019, *431* (18), 3472-3500.
50. Sauvage, E.; Kerff, F.; Terrak, M.; Ayala, J. A.; Charlier, P., The penicillin-binding proteins: structure and role in peptidoglycan biosynthesis. *FEMS Microbiol. Rev.* 2008, *32* (2), 234-258.
51. Yocum, R. R.; Waxman, D. J.; Rasmussen, J. R.; Strominger, J. L., Mechanism of penicillin action: Penicillin and substrate bind covalently to the same active site serine in two bacterial D-alanine carboxypeptidases. *Proc. Natl. Acad. Sci. USA* 1979, *76* (6), 2730-2734.
52. Medeiros, A. A.; Hedges, R. W.; Jacoby, G. A., Spread of a "Pseudomonas-Specific" β-Lactamase to Plasmids of Enterobacteria. *J. Bacteriol.* 1982, *149* (2), 700-707.
53. Heffron, F.; Sublett, R.; Hedges, R. W.; Jacob, A.; Falkow, S., Origin of the TEM β-Lactamase Gene Found on Plasmids. *J. Bacteriol.* 1975, *122* (1), 250-256.
54. Matthew, M.; Hedges, R. W.; Smith, J. T., Types of β-Lactamase Determined by Plasmids in Gram-Negative Bacteria. *J. Bacteriol.* 1979, *138* (3), 657-662.
55. Hideo Ito; Yoshichika Arakawa; Shinji Ohsuka; Rochaporn Wacharotayankun; Nobuo Kato; Ohta, M., Plasmid-Mediated Dissemination of the Metallo-β-Lactamase Gene blaIMP among Clinically Isolated Strains of Serratia marcescens. *Antimicrob. Agents Chemother.* 1995, *39* (4), 824–829.
56. Elwell, L. P.; Roberts, M.; Mayer, L. W.; Falkow, S., Plasmid-Mediated β-Lactamase Production in Neisseria gonorrhoeae. *Antimicrob. Agents Chemother.* 1977, *11* (3), 528-533.
57. Arakawa, O.; Ohta, M.; Kido, N.; Mori, M.; Ito, H.; Komatsu, T.; Fujii, Y.; Kato, N., Chromosomal β-Lactamase of Klebsiella oxytoca, a New Class A Enzyme That

Hydrolyzes Broad-Spectrum β-Lactam Antibiotics. *Antimicrob. Agents Chemother.* 1989, *33* (1), 63-70.
58. Bret, L.; Chanal-Claris, C.; Sirot, D.; Chaibi, E. B.; Labia, R.; Sirot, J., Chromosomally Encoded AmpC-Type β-Lactamase in a Clinical Isolate of Proteus mirabilis. *Antimicrob. Agents Chemother.* 1998, *42* (5), 1110–1114.
59. Chaves, J.; Ladona, M. G.; Segura, C.; Coira, A.; Reig, R.; Ampurdanes, C., SHV-1 β-lactamase is mainly a chromosomally encoded species-specific enzyme in Klebsiella pneumoniae. *Antimicrob. Agents Chemother.* 2001, *45* (10), 2856-2861.
60. Decousser, J. W.; Poirel, L.; Nordmann, P., Characterization of a Chromosomally Encoded Extended-Spectrum Class A β-Lactamase from Kluyvera cryocrescens. *Antimicrob. Agents Chemother.* 2001, *45* (12), 3595-3598.
61. Davies, J.; Davies, D., Origins and Evolution of Antibiotic Resistance. *Microbiol. Mol. Biol. Rev.* 2010, *74* (3), 417-433.
62. Naas, T.; Oueslati, S.; Bonnin, R. A.; Dabos, M. L.; Zavala, A.; Dortet, L.; Retailleau, P.; Iorga, B. I., β-Lactamase Database (BLDB) - Structure and Function. *J. Enzyme Inhib. Med. Chem.* 2017, *32* (1), 917-919.
63. Ambler, R. P., The Structure of β-Lactamases. *Phil. Trans. R. Soc. Lond. B* 1980, *289*, 321-331.
64. Hall, B. G.; Barlow, M., Evolution of the serine β-lactamases: past, present and future. *Drug. Resist. Updat.* 2004, *7* (2), 111-123.
65. Medeiros, A. A., Evolution and Dissemination of β-Lactamases Accelerated by Generations of β-Lactam Antibiotics. *Clin. Infect. Dis.* 1997, *24*, S19-S45.
66. Goessens, W. H.; van der Bij, A. K.; van Boxtel, R.; Pitout, J. D.; van Ulsen, P.; Melles, D. C.; Tommassen, J., Antibiotic trapping by plasmid-encoded CMY-2 β-lactamase combined with reduced outer membrane permeability as a mechanism of carbapenem resistance in Escherichia coli. *Antimicrob. Agents Chemother.* 2013, *57* (8), 3941-3949.
67. Rolain, J. M.; Parola, P.; Cornaglia, G., New Delhi metallo-β-lactamase (NDM-1): towards a new pandemia? *Clin. Microbiol. Infect.* 2010, *16* (12), 1699-1701.
68. Crowder, M. W.; Spencer, J.; Vila, A. J., Metallo-β-lactamases: Novel Weaponry for Antibiotic Resistance in Bacteria. *Acc. Chem. Res.* 2006, *39*, 721-728.
69. Ke, W.; Bethel, C. R.; Thomson, J. M.; Bonomo, R. A.; van den Akker, F., Crystal Structure of KPC-2: Insights into Carbapenemase Activity in Class A β-Lactamases. *Biochemistry* 2007, *46* (19), 5732-5740.
70. Usher, K. C.; Blaszczak, L. C.; Weston, G. S.; Shoichet, B. K.; Remington, S. J., Three-Dimensional Structure of AmpC β-Lactamase from Escherichia coli Bound to a Transition-State Analogue: Possible Implications for the Oxyanion Hypothesis and for Inhibitor Design. *Biochemistry* 1998, *37* (46), 16082-16092.
71. Smith, C. A.; Stewart, N. K.; Toth, M.; Vakulenko, S. B., Structural Insights into the Mechanism of Carbapenemase Activity of the OXA-48 β-Lactamase. *Antimicrob. Agents Chemother.* 2019, *63* (10), e01202-19.

72. Kraut, J., Serine Proteases: Structure and Mechanism of Catalysis. *Ann. Rev. Biochem.* 1977, *46*, 331-358.
73. Warshel, A.; Naray-Szabo, G.; Sussman, F.; Hwang, J.-K., How Do Serine Proteases Really Work? *Biochemistry* 1989, *28*, 3629-3637.
74. Gherman, B. F.; Goldberg, S. D.; Cornish, V. W.; Friesner, R. A., Mixed Quantum Mechanical/Molecular Mechanical (QM/MM) Study of the Deacylation Reaction in a Penicillin Binding Protein (PBP) versus in a Class C β-lactamases *J. Am. Chem. Soc.* 2004, *126*, 7652-7664.
75. Datta, N.; Kontomichalou, P., Penicillinase Synthesis Controlled by Infectious R Factors in Enterobacteriaceae. *Nature* 1965, *208*, 239-241.
76. A. Bauemfeind; H. Grimm; Schweighart, S., A New Plasmidic Cefotaximase in a Clinical Isolate of Escherichia coil. *Infection* 1990, *18*, 294-298.
77. Yigit, H.; Queenan, A. M.; Anderson, G. J.; Domenech-Sanchez, A.; Biddle, J. W.; Steward, C. D.; Alberti, S.; Bush, K.; Tenover, F. C., Novel carbapenem-hydrolyzing β-lactamase, KPC-1, from a carbapenem-resistant strain of Klebsiella pneumoniae. *Antimicrob. Agents Chemother.* 2001, *45* (4), 1151-1161.
78. Palzkill, T., Structural and Mechanistic Basis for Extended-Spectrum Drug-Resistance Mutations in Altering the Specificity of TEM, CTX-M, and KPC β-lactamases. *Front. Mol. Biosci.* 2018, *5*, 16.
79. Rupp, M. E.; Fey, P. D., Extended Spectrum β-Lactamase (ESBL)-Producing Enterobacteriaceae. *Drugs* 2003, *63* (4), 353-365.
80. Walther-Rasmussen, J.; Hoiby, N., Class A carbapenemases. *J. Antimicrob. Chemother.* 2007, *60* (3), 470-482.
81. Naas, T.; Vandel, L.; Sougakoff, W.; Livermore, D. M.; Nordmann, P., Cloning and Sequence Analysis of the Gene for a Carbapenem-Hydrolyzing Class A β-Lactamase, Sme-1, from Serratia marcescens S6. *Antimicrob. Agents Chemother.* 1994, *38* (6), 1262-1270.
82. Nordmann, P.; Mariotte, S.; Naas, T.; Labia, R.; Nicolas, M.-H., Biochemical Properties of a Carbapenem-Hydrolyzing β-Lactamase from Enterobacter cloacae and Cloning of the Gene into Escherichia coli. *Antimicrob. Agents Chemother.* 1993, *37* (5), 939-946.
83. Henriques, I.; Moura, A.; Alves, A.; Saavedra, M. J.; Correia, A., Molecular characterization of a carbapenem-hydrolyzing class A β-lactamase, SFC-1, from Serratia fonticola UTAD54. *Antimicrob. Agents Chemother.* 2004, *48* (6), 2321-2324.
84. Levitt, P. S.; Papp-Wallace, K. M.; Taracila, M. A.; Hujer, A. M.; Winkler, M. L.; Smith, K. M.; Xu, Y.; Harris, M. E.; Bonomo, R. A., Exploring the role of a conserved class A residue in the Ω-Loop of KPC-2 β-lactamase: a mechanism for ceftazidime hydrolysis. *J. Biol. Chem.* 2012, *287* (38), 31783-31793.
85. Papp-Wallace, K. M.; Winkler, M. L.; Taracila, M. A.; Bonomo, R. A., Variants of β-lactamase KPC-2 that are resistant to inhibition by avibactam. *Antimicrob. Agents Chemother.* 2015, *59* (7), 3710-3717.

86. Hobson, C. A.; Bonacorsi, S.; Jacquier, H.; Choudhury, A.; Magnan, M.; Cointe, A.; Bercot, B.; Tenaillon, O.; Birgy, A., KPC β-Lactamases Are Permissive to Insertions and Deletions Conferring Substrate Spectrum Modifications and Resistance to Ceftazidime-Avibactam. *Antimicrob. Agents Chemother.* 2020, *64* (12), e01175-20.
87. Yu Chen; Richard Bonnet; Shoichet, B. K., The Acylation Mechanism of CTX-M β-Lactamase at 0.88 Å Resolution. *J. Am. Chem. Soc.* 2007, *129*, 5378-5380.
88. Tomanicek, S. J.; Wang, K. K.; Weiss, K. L.; Blakeley, M. P.; Cooper, J.; Chen, Y.; Coates, L., The active site protonation states of perdeuterated Toho-1 β-lactamase determined by neutron diffraction support a role for Glu166 as the general base in acylation. *FEBS Lett.* 2011, *585* (2), 364-368.
89. Hermann, J. C.; Ridder, L.; Mulholland, A. J.; Höltje, H.-D., Identification of Glu166 as the General Base in the Acylation Reaction of Class A β-Lactamases through QM/MM Modeling. *J. Am. Chem. Soc.* 2003, *125*, 9590-9591.
90. Adachi, H.; Ohta, T.; Matsuzawa, H., Site-directed mutants, at position 166, of RTEM-1 β-lactamase that form a stable acyl-enzyme intermediate with penicillin. *J. Biol. Chem.* 1991, *266* (5), 3186-3191.
91. Pan, X.; He, Y.; Lei, J.; Huang, X.; Zhao, Y., Crystallographic Snapshots of Class A β-Lactamase Catalysis Reveal Structural Changes That Facilitate β-Lactam Hydrolysis. *J. Biol. Chem.* 2017, *292* (10), 4022-4033.
92. Samy O. Meroueh; Jed F. Fisher; H. Bernhard Schlegel; Mobashery, S., Ab Initio QM/MM Study of Class A β-Lactamase Acylation: Dual Participation of Glu166 and Lys73 in a Concerted Base Promotion of Ser70. *J. Am. Chem. Soc.* 2005, *127*, 15397-15407.
93. Langan, P. S.; Vandavasi, V. G.; Cooper, S. J.; Weiss, K. L.; Ginell, S. L.; Parks, J. M.; Coates, L., Substrate Binding Induces Conformational Changes in a Class A β-lactamase That Prime It for Catalysis. *ACS Catal.* 2018, *8* (3), 2428-2437.
94. Hafner, J.; Wolverton, C.; Ceder, G., Toward Computational Materials Design: The Impact of Density Functional Theory on Materials Research. *MRS Bull.* 2011, *31* (9), 659-668.
95. Poree, C.; Schoenebeck, F., A Holy Grail in Chemistry: Computational Catalyst Design: Feasible or Fiction? *Acc. Chem. Res.* 2017, *50* (3), 605-608.
96. Durand, D. J.; Fey, N., Computational Ligand Descriptors for Catalyst Design. *Chem. Rev.* 2019, *119* (11), 6561-6594.
97. van der Kamp, M. W.; Mulholland, A. J., Combined quantum mechanics/molecular mechanics (QM/MM) methods in computational enzymology. *Biochemistry* 2013, *52* (16), 2708-2728.
98. Huggins, D. J.; Biggin, P. C.; Dämgen, M. A.; Essex, J. W.; Harris, S. A.; Henchman, R. H.; Khalid, S.; Kuzmanic, A.; Laughton, C. A.; Michel, J.; Mulholland, A. J.; Rosta, E.; Sansom, M. S. P.; van der Kamp, M. W., Biomolecular simulations: From dynamics and mechanisms to computational assays of biological activity. *Wiley Interdiscip. Rev. Comput. Mol. Sci.* 2019, *9* (3).

99. Rappe, A. K.; Casewit, C. J., *Molecular Mechanics across Chemistry*. University Science Books: Sausalito, California, 1997.
100. Maier, J. A.; Martinez, C.; Kasavajhala, K.; Wickstrom, L.; Hauser, K. E.; Simmerling, C., ff14SB: Improving the Accuracy of Protein Side Chain and Backbone Parameters from ff99SB. *J. Chem. Theory Comput.* 2015, *11*, 3696-3713.
101. Schrödinger, E., An Undulatory Theory of the Mechanics of Atoms and Molecules. *Phys. Rev.* 1926, *28* (6), 1049-1070.
102. Born, M.; Oppenheimer, R., Zur Quantentheorie der Molekeln. *Ann. Phys.* 1927, *389* (20), 457-484.
103. Pauli, W., Über den Zusammenhang des Abschlusses der Elektronengruppen im Atom mit der Komplexstruktur der Spektren. *Z. Phys.* 1925, *31*, 765-783.
104. Lewars, E. G., *Computational Chemistry - Introduction to the Theory and Applications of Molecular and Quantum Mechanics*. 3 ed.; Springer International Publishing: 2016; p 728.
105. Szabo, A.; Ostlund, N. S., *Modern Quantum Chemistry: Introduction to Advanced Electronic Structure Theory*. Dover Publications: Mineola, N.Y, 1996.
106. Roothaan, C. C. J., New Developments in Molecular Orbital Theory. *Rev. Mod. Phys.* 1951, *23* (2), 69-89.
107. Hall, G. G., The molecular orbital theory of chemical valency VIII. A method of calculating ionization potentials. *Proc. Math. Phys. Eng. Sci.* 1951, *205* (1083), 541-552.
108. DeFrees, D. J.; Levi, B. A.; Pollack, S. K.; Fiebre, W. J.; Binkley, J. S.; Pople, J. A., Effect of Electron Correlation on Theoretical Equilibrium Geometries. *J. Am. Chem. Soc.* 1979, *101* (15), 4085-4089.
109. Hout Jr., R. F.; Levi, B. A.; Hehre, W. J., Effect of Electron Correlation on Theoretical Vibrational Frequencies. *J. Comput. Chem.* 1981, *3* (2), 234-250.
110. Russo, T. V.; Martin, R. L.; Hay, P. J., Density functional calculations on first row transition metals. *J. Chem. Phys.* 1994, *101* (9), 7729-7737.
111. Raghavachari, K.; Anderson, J. B., Electron Correlation Effects in Molecules. *J. Phys. Chem.* 1996, *100* (31), 12960-12973.
112. Moller, C.; Plesset, M. S., Note on an Approximation Treatment for Many-Electron Systems. *Phys. Rev.* 1934, *46* (7), 618-622.
113. Cremer, D., Møller-Plesset perturbation theory: from small molecule methods to methods for thousands of atoms. *Wiley Interdiscip. Rev. Comput. Mol. Sci.* 2011, *1* (4), 509-530.
114. Feyereisen, M.; Fitzgerald, G., Use of approximate integrals in ab initio theory. An application in MP2 energy calculations. *Chem. Phys. Lett.* 1993, *208* (5,6), 359-363.
115. Grimme, S.; Goerigk, L.; Fink, R. F., Spin-component-scaled electron correlation methods. *Wiley Interdiscip. Rev. Comput. Mol. Sci.* 2012, *2* (6), 886-906.

116. Shavitt, I., *The Method of Configuration Interaction. In: Methods of Electronic Structure Theory. Modern Theoretical Chemistry*. Springer: Boston, MA, 1977; Vol. 3.
117. Bartlett, R. J.; Musiał, M., Coupled-cluster theory in quantum chemistry. *Rev. Mod. Phys.* 2007, *79* (1), 291-352.
118. Raghavachari, K.; Trucks, G. W.; Pople, J. A.; Head-Gordon, M., A fifth-order perturbation comparison of electron correlation theories. *Chem. Phys. Lett.* 1989, *157* (6), 479-483.
119. Christoph Riplinger; Barbara Sandhoefer; Andreas Hansen; Neese, F., Natural triple excitations in local coupled cluster calculations with pair natural orbitals. *J. Chem. Phys.* 2013, *139* (1), 134101.
120. Riplinger, C.; Pinski, P.; Becker, U.; Valeev, E. F.; Neese, F., Sparse maps - A systematic infrastructure for reduced-scaling electronic structure methods. II. Linear scaling domain based pair natural orbital coupled cluster theory. *J. Chem. Phys.* 2016, *144* (2), 024109.
121. Hohenberg, P.; Kohn, W., Inhomogeneous Electron Gas. *Phys. Rev.* 1964, *136* (3B), B864-B871.
122. Kohn, W.; Sham, L. J., Self-Consistent Equations Including Exchange and Correlation Effects. *Phys. Rev.* 1965, *140* (4A), A1133-A1138.
123. Perdew, J. P.; Schmidt, K., Jacob's Ladder of Density Functional Approximations for the Exchange-Correlation Energy. *AIP Conf. Proc.* 2001, *577*, 1-20.
124. Langreth, D. C.; Perdew, J. P., Theory of nonuniform electronic systems. I. Analysis of the gradient approximation and a generalization that works. *Phys. Rev. B* 1980, *21* (12), 5469-5493.
125. Langreth, D. C.; Mehl, M. J., Beyond the local-density approximation in calculations of ground-state electronic properties. *Phys. Rev. B* 1983, *28* (4), 1809-1834.
126. Perdew, J. P., Accurate density functional for the energy: Real-space cutoff of the gradient expansion for the exchange hole. *Phys. Rev. Lett.* 1985, *55* (16), 1665-1668.
127. Tao, J.; Perdew, J. P.; Staroverov, V. N.; Scuseria, G. E., Climbing the density functional ladder: nonempirical meta-generalized gradient approximation designed for molecules and solids. *Phys. Rev. Lett.* 2003, *91* (14), 146401.
128. Zhao, Y.; Truhlar, D. G., A new local density functional for main-group thermochemistry, transition metal bonding, thermochemical kinetics, and noncovalent interactions. *J. Chem. Phys.* 2006, *125* (19), 194101.
129. Becke, A. D., A new mixing of Hartree–Fock and local density-functional theories. *J. Chem. Phys.* 1993, *98* (2), 1372-1377.
130. Becke, A. D., Density-functional exchange-energy approximation with correct asymptotic behavior. *Phys. Rev. A* 1988, *38* (6), 3098-3100.
131. Lee, C.; Yang, W.; Parr, R. G., Development of the Colle-Salvetti correlation-energy formula into a functional of the electron density. *Phys. Rev. B* 1988, *37* (2), 785-789.

132. Vosko, S. H.; Wilk, L.; Nusair, M., Accurate spin-dependent electron liquid correlation energies for local spin density calculations: a critical analysis. *Can. J. Phys* 1980, *58*, 1200-1211.
133. Stephens, P. J.; Devlin, F. J.; Chabalowski, C. F.; Frisch, M. J., Ab Initio Calculation of Vibrational Absorption and Circular Dichroism Spectra Using Density Functional Force Fields. *J. Phys. Chem.* 1994, *98* (45), 11623-11627.
134. Zhao, Y.; Truhlar, D. G., The M06 suite of density functionals for main group thermochemistry, thermochemical kinetics, noncovalent interactions, excited states, and transition elements: two new functionals and systematic testing of four M06-class functionals and 12 other functionals. *Theor. Chem. Acc.* 2007, *120* (1-3), 215-241.
135. Chai, J. D.; Head-Gordon, M., Systematic optimization of long-range corrected hybrid density functionals. *J. Chem. Phys.* 2008, *128* (8), 084106.
136. Chai, J. D.; Head-Gordon, M., Long-range corrected hybrid density functionals with damped atom-atom dispersion corrections. *Phys. Chem. Chem. Phys.* 2008, *10* (44), 6615-6620.
137. Grimme, S., Semiempirical hybrid density functional with perturbative second-order correlation. *J. Chem. Phys.* 2006, *124* (3).
138. Chai, J. D.; Head-Gordon, M., Long-range corrected double-hybrid density functionals. *J. Chem. Phys.* 2009, *131* (17), 174105.
139. Kristyan, S.; Pulay, P., Can (semi)local density functional theory account for the London dispersion forces? *Chem. Phys. Lett.* 1994, *229*, 175-180.
140. Perez-Jorda, J. M.; Becke, A. D., A density-functional study of van der Waals forces: rare gas diatomics. *Chem. Phys. Lett.* 1995, *233*, 134-137.
141. Ruzsinszky, A.; Perdew, J. P.; Csonka, G. I., Binding Energy Curves from Nonempirical Density Functionals II. van der Waals Bonds in Rare-Gas and Alkaline-Earth Diatomics. *J. Phys. Chem. A* 2005, *109*, 11015-11021.
142. Marom, N.; Tkatchenko, A.; Rossi, M.; Gobre, V. V.; Hod, O.; Scheffler, M.; Kronik, L., Dispersion Interactions with Density-Functional Theory: Benchmarking Semiempirical and Interatomic Pairwise Corrected Density Functionals. *J. Chem. Theory Comput.* 2011, *7* (12), 3944-3951.
143. Grimme, S., Density functional theory with London dispersion corrections. *WIRES Comput. Mol. Sci.* 2011, *1* (2), 211-228.
144. Dion, M.; Rydberg, H.; Schroder, E.; Langreth, D. C.; Lundqvist, B. I., Van der Waals Density Functional for General Geometries. *Phys. Rev. Lett.* 2004, *92* (24), 246401.
145. Grimme, S.; Antony, J.; Ehrlich, S.; Krieg, H., A consistent and accurate ab initio parametrization of density functional dispersion correction (DFT-D) for the 94 elements H-Pu. *J. Chem. Phys.* 2010, *132* (15), 154104.
146. Korth, M.; Grimme, S., "Mindless" DFT Benchmarking. *J. Chem. Theory Comput.* 2009, *5*, 993-1003.

147. Hohenstein, E. G.; Chill, S. T.; Sherrill, C. D., Assessment of the Performance of the M05-2X and M06-2X Exchange-Correlation Functionals for Noncovalent Interactions in Biomolecules. *J. Chem. Theory Comput.* 2008, *4*, 1996-2000.
148. Ditchfield, R.; Hehre, W. J.; Pople, J. A., Self-Consistent Molecular-Orbital Methods. IX. An Extended Gaussian-Type Basis for Molecular-Orbital Studies of Organic Molecules. *J. Chem. Phys.* 1971, *54* (2), 724-728.
149. Dunning, T. H., Gaussian basis sets for use in correlated molecular calculations. I. The atoms boron through neon and hydrogen. *J. Chem. Phys.* 1989, *90* (2), 1007-1023.
150. Weigend, F.; Ahlrichs, R., Balanced basis sets of split valence, triple zeta valence and quadruple zeta valence quality for H to Rn: Design and assessment of accuracy. *Phys. Chem. Chem. Phys.* 2005, *7* (18), 3297-3305.
151. Pople, J. A.; Santry, D. P.; Segal, G. A., Approximate Self-Consistent Molecular Orbital Theory. I. Invariant Procedures. *J. Chem. Phys.* 1965, *43* (10), S129-S135.
152. Dewar, M. J. S.; Thiel, W., Ground States of Molecules. 38. The MNDO Method. Approximations and Parameters. *J. Am. Chem. Soc.* 1977, *99*, 4899-4907.
153. Dewar, M. J. S.; Zoebisch, E. G.; Healy, E. F.; Stewart, J. J. P., AM1: a new general purpose quantum mechanical molecular model. *J. Am. Chem. Soc.* 1985, *107* (13), 3902-3909.
154. Stewart, J. J. P., Optimization of Parameters for Semiempirical Methods I. Method. *J. Comput. Chem.* 1989, *10* (2), 209-220.
155. Stewart, J. J. P., Optimization of parameters for semiempirical methods V: modification of NDDO approximations and application to 70 elements. *J. Mol. Model.* 2007, *13* (12), 1173-1213.
156. Stewart, J. J. P., Optimization of parameters for semiempirical methods VI: more modifications to the NDDO approximations and re-optimization of parameters. *J. Mol. Model.* 2013, *19* (1), 1-32.
157. Dral, P. O.; Wu, X.; Sporkel, L.; Koslowski, A.; Weber, W.; Steiger, R.; Scholten, M.; Thiel, W., Semiempirical Quantum-Chemical Orthogonalization-Corrected Methods: Theory, Implementation, and Parameters. *J. Chem. Theory Comput.* 2016, *12* (3), 1082-1096.
158. Elstner, M.; Porezag, D.; Jungnickel, G.; Elsner, M.; Haugk, M.; Frauenheim, T. H.; Suhai, S.; Seifert, G., Self-Consistent-Charge Density-Functional Tight-Binding Method for Simulations of Complex Materials Properties. *Phys. Rev. B* 1998, *58* (11), 7260-7268.
159. Gaus, M.; Cui, Q.; Elstner, M., DFTB3: Extension of the self-consistent-charge density-functional tight-binding method (SCC-DFTB). *J. Chem. Theory Comput.* 2012, *7* (4), 931-948.
160. Porezag, D.; Frauenheim, T.; Kohler, T.; Seifert, G.; Kaschner, R., Construction of tight-binding-like potentials on the basis of density-functional theory: Application to carbon. *Phys. Rev. B* 1995, *51* (19), 12947-12957.

161. Gaus, M.; Cui, Q.; Elstner, M., Density functional tight binding: application to organic and biological molecules. *Wiley Interdiscip. Rev. Comput. Mol. Sci.* 2014, *4* (1), 49-61.
162. Elstner, M.; Frauenheim, T. H.; Kaxiras, E.; Seifert, G.; Suhai, S., A Self-Consistent Charge Density-Functional Based Tight-Binding Scheme for Large Biomolecules. *Phys. Status Solidi* 2000, *217*, 357-376.
163. Cui, Q.; Elstner, M., Density functional tight binding: values of semi-empirical methods in an ab initio era. *Phys. Chem. Chem. Phys.* 2014, *16* (28), 14368-14377.
164. Warshel, A.; Levitt, M., Theoretical studies of enzymic reactions: Dielectric, electrostatic and steric stabilization of the carbonium ion in the reaction of lysozyme. *J. Mol. Biol.* 1976, *103* (2), 227-249.
165. Senn, H. M.; Thiel, W., QM/MM methods for biomolecular systems. *Angew. Chem. Int. Ed.* 2009, *48* (7), 1198-1229.
166. Case, D. A.; Ben-Shalom, I. Y.; Brozell, S. R.; Cerutti, D. S.; Cheatham, T. E. I.; Cruzeiro, V. W. D.; Darden, T. A.; Duke, R. E.; Ghoreishi, D.; Giambasu, G.; Giese, T. J.; Gilson, H.; Gohlke, H.; Goetz, A. W.; Greene, D.; Harris, R.; Homeyer, N.; Huang, Y.; Izadi, S.; Kovalenko, A.; Krasny, R.; Kurtzman , T.; Lee, T. S.; LeGrand, S.; Li, P.; Lin, C.; Liu, J.; Luchko, T.; Luo, R.; Man, V.; Mermelstein, D.; Merz, K. M.; Miao, Y.; Monard, G.; Nguyen, C.; Nguyen, H.; Onufriev, A.; Pan, F.; Qi, R.; Roe, D. R.; Roitberg, A.; Sagui, C.; Schott-Verdugo, S.; Shen, J.; Simmerling, C. L.; Smith, J.; Swails, J.; Walker, R. C.; Wang, J.; Wei, H.; Wilson, L.; Wolf, R. M.; Wu, X.; Xiao, L.; Xiong, Y.; M., Y. D.; P.A., K. *AMBER 2019*, University of California: San Francisco, 2019.
167. Sondergaard, C. R.; Olsson, M. H.; Rostkowski, M.; Jensen, J. H., Improved Treatment of Ligands and Coupling Effects in Empirical Calculation and Rationalization of pKa Values. *J. Chem. Theory Comput.* 2011, *7* (7), 2284-2295.
168. Wang, J.; Wolf, R. M.; Caldwell, J. W.; Kollman, P. A.; Case, D. A., Development and Testing of a General Amber Force Field. *J. Comput. Chem.* 2004, *25* (9), 1157-1174.
169. Bayly, C. I.; Cieplak, P.; Cornell, W. D.; Kollman, P. A., A Well-Behaved Electrostatic Potential Based Method Using Charge Restraints for Deriving Atomic Charges: The RESP Model. *J. Phys. Chem.* 1993, *97* (40), 10269-10280.
170. Jakalian, A.; Bush, B. L.; Jack, D. B.; Bayly, C. I., Fast, Efficient Generation of High-Quality Atomic Charges. AM1-BCC Model: I. Method. *J. Comput. Chem.* 2000, *21* (2), 132–146.
171. Jakalian, A.; Jack, D. B.; Bayly, C. I., Fast, efficient generation of high-quality atomic charges. AM1-BCC model: II. Parameterization and validation. *J. Comput. Chem.* 2002, *23* (16), 1623-1641.
172. Vanquelef, E.; Simon, S.; Marquant, G.; Garcia, E.; Klimerak, G.; Delepine, J. C.; Cieplak, P.; Dupradeau, F. Y., R.E.D. Server: a Web Service for Deriving RESP and ESP Charges and Building Force Field Libraries for New Molecules and Molecular Fragments. *Nucleic Acids Res.* 2011, *39*, W511-7.

173. Jorgensen, W. L.; Chandrasekhar, J.; Madura, J. D.; Impey, R. W.; Klein, M. L., Comparison of simple potential functions for simulating liquid water. *J. Chem. Phys.* 1983, *79* (2), 926-935.
174. Berendsen, H. J. C.; Postma, J. P. M.; van Gunsteren, W. F.; Hermans, J., *Interaction Models for Water in Relation to Protein Hydration. In: Pullman B. (eds) Intermolecular Forces. The Jerusalem Symposia on Quantum Chemistry and Biochemistry*. Springer: Dordrecht, 1981; Vol. 14.
175. Berendsen, H. J. C.; Grigera, J. R.; Straatsma, T. P., The Missing Term in Effective Pair Potentials. *J. Phys. Chem.* 1987, *91* (24), 6269-6271.
176. Izadi, S.; Anandakrishnan, R.; Onufriev, A. V., Building Water Models: A Different Approach. *J. Phys. Chem. Lett.* 2014, *5* (21), 3863-3871.
177. Bernal, J. D.; Fowler, R. H., A Theory of Water and Ionic Solution, with Particular Reference to Hydrogen and Hydroxyl Ions. *J. Chem. Phys.* 1933, *1* (8), 515-548.
178. Mahoney, M. W.; Jorgensen, W. L., A five-site model for liquid water and the reproduction of the density anomaly by rigid, nonpolarizable potential functions. *J. Chem. Phys.* 2000, *112* (20), 8910-8922.
179. Stillinger, F. H.; Rahman, A., Improved simulation of liquid water by molecular dynamics. *J. Chem. Phys.* 1974, *60* (4), 1545-1557.
180. Mackay, D. H. J.; Cross, A. J.; Hagler, A. T., *The Role of Energy Minimization in Simulation Strategies of Biomolecular Systems. In: Fasman G.D. (eds) Prediction of Protein Structure and the Principles of Protein Conformation.* Springer: Boston, MA, 1989.
181. Verlet, L., Computer "Experiments" on Classical Fluids. I. Thermodynamical Properties of Lennard-Jones Molecules. *Phys. Rev.* 1967, *159* (1), 98-103.
182. Swope, W. C.; Andersen, H. C.; Berens, P. H.; Wilson, K. R., A computer simulation method for the calculation of equilibrium constants for the formation of physical clusters of molecules: Application to small water clusters. *J. Chem. Phys.* 1982, *76* (1), 637-649.
183. Frenkel, D.; Smit, B., *Understanding molecular simulation - From algorithms to applications*. Academic Press: San Diego, USA, 2001.
184. Berendsen, H. J. C.; Postma, J. P. M.; van Gunsteren, W. F.; DiNola, A.; Haak, J. R., Molecular dynamics with coupling to an external bath. *J. Chem. Phys.* 1984, *81* (8), 3684-3690.
185. Kästner, J., Umbrella Sampling. *WIREs Comput. Mol. Sci.* 2011, *1*, 932-942.
186. Kumar, S.; Bouzida, D.; Swendsen, R. H.; Kollman, P. A.; Rosenberg, J. M., The Weighted Histogram Analysis Method for Free-Energy Calculations on Biomolecules. I. The Method. *J. Comput. Chem.* 1992, *13*, 1011-1021.
187. Rosta, E.; Hummer, G., Free energies from dynamic weighted histogram analysis using unbiased Markov state model. *J. Chem. Theory Comput.* 2015, *11* (1), 276-285.
188. Kastner, J.; Thiel, W., Analysis of the statistical error in umbrella sampling simulations by umbrella integration. *J. Chem. Phys.* 2006, *124* (23), 234106.

189. Hirvonen, V. H. A.; Hammond, K.; Chudyk, E. I.; Limb, M. A. L.; Spencer, J.; Mulholland, A. J.; van der Kamp, M. W., An Efficient Computational Assay for β-Lactam Antibiotic Breakdown by Class A β-Lactamases. *J. Chem. Inf. Model.* 2019, *59* (8), 3365-3369.
190. Chudyk, E. I.; Limb, M. A.; Jones, C.; Spencer, J.; van der Kamp, M. W.; Mulholland, A. J., QM/MM simulations as an assay for carbapenemase activity in class A β-lactamases. *Chem. Commun.* 2014, *50* (94), 14736-14739.
191. Zaman, S. B.; Hussain, M. A.; Nye, R.; Mehta, V.; Mamun, K. T.; Hossain, N., A Review on Antibiotic Resistance: Alarm Bells are Ringing. *Cureus* 2017, *9* (6), 1403.
192. Fair, R. J.; Tor, Y., Antibiotics and bacterial resistance in the 21st century. *Perspect. Medicin. Chem.* 2014, *6*, 25-64.
193. Worthington, R. J.; Melander, C., Overcoming resistance to β-lactam antibiotics. *J. Org. Chem.* 2013, *78* (9), 4207-4213.
194. Bush, K., Alarming β-lactamase-mediated resistance in multidrug-resistant Enterobacteriaceae. *Curr. Opin. Microbiol.* 2010, *13* (5), 558-564.
195. Munita, J. M.; Arias, C. A., Mechanisms of Antibiotic Resistance. *Microbiol. Spectr.* 2016, *4* (2).
196. Queenan, A. M.; Bush, K., Carbapenemases: the versatile β-lactamases. *Clin. Microbiol. Rev.* 2007, *20* (3), 440-458.
197. Pfeifer, Y.; Cullik, A.; Witte, W., Resistance to cephalosporins and carbapenems in Gram-negative bacterial pathogens. *Int. J. Med. Microbiol.* 2010, *300* (6), 371-379.
198. *Antibiotic Resistance Threats in the United States, 2013*; Centers for Disease Control: Atlanta, GA, 2013.
199. Hermann, J. C.; Pradon, J.; Harvey, J. N.; Mulholland, A. J., High Level QM/MM Modeling of the Formation of the Tetrahedral Intermediate in the Acylation of Wild Type and K73A Mutant TEM-1 Class A β-Lactamase. *J. Phys. Chem. A* 2009, *113*, 11984-11994.
200. Minasov, G.; Wang, X.; Shoichet, B. K., An Ultrahigh Resolution Structure of TEM-1 β-lactamase Suggests a Role for Glu166 as the General Base in Acylation. *J. Am. Chem. Soc.* 2002, *124*, 5333-5340.
201. Hermann, J. C.; Ridder, L.; Holtje, H. D.; Mulholland, A. J., Molecular Mechanisms of Antibiotic Resistance: QM/MM Modelling of Deacylation in a Class A β-lactamase. *Org. Biomol. Chem.* 2006, *4* (2), 206-10.
202. Fritz, R. A.; Alzate-Morales, J. H.; Spencer, J.; Mulholland, A. J.; van der Kamp, M. W., Multiscale Simulations of Clavulanate Inhibition Identify the Reactive Complex in Class A β-Lactamases and Predict the Efficiency of Inhibition. *Biochemistry* 2018, *57* (26), 3560-3563.
203. Case, D. A.; Cerutti, D. S.; Cheatham, T. E. I.; Darden, T. A.; Duke, R. E.; Giese, T. J.; Gohlke, H.; Goetz, A. W.; Greene, D.; Homeyer, N.; Izadi, S.; Kovalenko, A.; Lee, T. S.; LeGrand, S.; Li, P.; Lin, C.; Liu, J.; Luchko, T.; Luo, R.; Mermelstein, D.; Merz, K. M.; Monard, G.; Nguyen, H.; Omelyan, I.; Onufriev, A.; Pan, F.;

Qi, R.; Roe, D. R.; Roitberg, A.; Sagui, C.; Simmerling, C. L.; Botello-Smith, W. M.; Swails, J.; Walker, R. C.; Wang, J.; Wolf, R. M.; Wu, X.; Xiao, L.; D.M., Y.; P.A., K. *AMBER 2017*, University of California: San Francisco, 2017.

204. Masgrau, L.; Ranaghan, K. E.; Scrutton, N. S.; Mulholland, A. J.; Sutcliffe, M. J., Tunneling and Classical Paths for Proton Transfer in an Enzyme Reaction Dominated by Tunneling: Oxidation of Tryptamine by Aromatic Amine Dehydrogenase. *J. Phys. Chem. B* 2007, *111*, 3032-3047.
205. Hirvonen, V. H. A.; Spencer, J.; van der Kamp, M. W., Antimicrobial Resistance Conferred by OXA-48 β-Lactamases: Towards a Detailed Mechanistic Understanding. *Antimicrob. Agents Chemother.* 2021, *65* (6), e00184-21.
206. Liapis, E.; Pantel, A.; Robert, J.; Nicolas-Chanoine, M.-H.; Cavalie, L.; van der Mee-Marquet, N.; de Champs, C.; Aissa, N.; Eloy, C.; Blanc, V.; Guyeux, C.; Hocquet, D.; Lavigne, J.-P.; Bertrand, X., Molecular Epidemiology of OXA-48 Producing Klebsiella pneumoniae in France. *Clin. Microbiol. Infect.* 2014, *20*, O1121–O1123.
207. Peri, A. M.; Doi, Y.; Potoski, B. A.; Harris, P. N. A.; Paterson, D. L.; Righi, E., Antimicrobial Treatment Challenges in the Era of Carbapenem Resistance. *Diagn. Microbiol. Infect. Dis.* 2019, *94* (4), 413-425.
208. Zapun, A.; Contreras-Martel, C.; Vernet, T., Penicillin-Binding Proteins and β-Lactam Resistance. *FEMS Microbiol. Rev.* 2008, *32*, 361-385.
209. Hedges, R. W.; Datta, N.; Kontomichalou, P.; Smith, J. T., Molecular Specificities of R Factor-Determined β-Lactamases: Correlation with Plasmid Compatibility. *J. Bacteriol.* 1974, *117* (1), 56-62.
210. Lascols, C.; Peirano, G.; Hackel, M.; Laupland, K. B.; Pitout, J. D., Surveillance and Molecular Epidemiology of Klebsiella pneumoniae Isolates that Produce Carbapenemases: First Report of OXA-48-like Enzymes in North America. *Antimicrob. Agents Chemother.* 2013, *57* (1), 130-136.
211. Palacios-Baena, Z. R.; Oteo, J.; Conejo, C.; Larrosa, M. N.; Bou, G.; Fernandez-Martinez, M.; Gonzalez-Lopez, J. J.; Pintado, V.; Martinez-Martinez, L.; Merino, M.; Pomar, V.; Mora-Rillo, M.; Rivera, M. A.; Oliver, A.; Ruiz-Carrascoso, G.; Ruiz-Garbajosa, P.; Zamorano, L.; Bautista, V.; Ortega, A.; Morales, I.; Pascual, A.; Campos, J.; Rodriguez-Bano, J.; Geih, G., Comprehensive Clinical and Epidemiological Assessment of Colonisation and Infection Due to Carbapenemase-producing Enterobacteriaceae in Spain. *J. Infect.* 2016, *72* (2), 152-160.
212. Dortet, L.; Poirel, L.; Al Yaqoubi, F.; Nordmann, P., NDM-1, OXA-48 and OXA-181 Carbapenemase-producing Enterobacteriaceae in Sultanate of Oman. *Clin. Microbiol. Infect.* 2012, *18* (5), E144-148.
213. Bouguenoun, W.; Bakour, S.; Bentorki, A. A.; Al Bayssari, C.; Merad, T.; Rolain, J. M., Molecular Epidemiology of Environmental and Clinical Carbapenemase-producing Gram-negative bacilli from Hospitals in Guelma, Algeria: Multiple Genetic Lineages and First Report of OXA-48 in Enterobacter cloacae. *J. Glob. Antimicrob. Resist.* 2016, *7*, 135-140.

214. Zowawi, H. M.; Sartor, A. L.; Balkhy, H. H.; Walsh, T. R.; Al Johani, S. M.; AlJindan, R. Y.; Alfaresi, M.; Ibrahim, E.; Al-Jardani, A.; Al-Abri, S.; Al Salman, J.; Dashti, A. A.; Kutbi, A. H.; Schlebusch, S.; Sidjabat, H. E.; Paterson, D. L., Molecular Characterization of Carbapenemase-producing Escherichia coli and Klebsiella pneumoniae in the Countries of the Gulf Cooperation Council: Dominance of OXA-48 and NDM Producers. *Antimicrob. Agents Chemother.* 2014, *58* (6), 3085-3090.
215. Lee, C. R.; Lee, J. H.; Park, K. S.; Kim, Y. B.; Jeong, B. C.; Lee, S. H., Global Dissemination of Carbapenemase-Producing Klebsiella pneumoniae: Epidemiology, Genetic Context, Treatment Options, and Detection Methods. *Front. Microbiol.* 2016, *7*, 895.
216. van Duin, D.; Doi, Y., The Global Epidemiology of Carbapenemase-producing Enterobacteriaceae. *Virulence* 2017, *8* (4), 460-469.
217. Antunes, N. T.; Lamoureaux, T. L.; Toth, M.; Stewart, N. K.; Frase, H.; Vakulenko, S. B., Class D β-lactamases: Are They All Carbapenemases? *Antimicrob. Agents Chemother.* 2014, *58* (4), 2119-2125.
218. Karlowsky, J. A.; Lob, S. H.; Kazmierczak, K. M.; Badal, R. E.; Young, K.; Motyl, M. R.; Sahm, D. F., In Vitro Activity of Imipenem against Carbapenemase-Positive Enterobacteriaceae Isolates Collected by the SMART Global Surveillance Program from 2008 to 2014. *J. Clin. Microbiol.* 2017, *55* (6), 1608-1611.
219. de Jonge, B. L.; Karlowsky, J. A.; Kazmierczak, K. M.; Biedenbach, D. J.; Sahm, D. F.; Nichols, W. W., In Vitro Susceptibility to Ceftazidime-Avibactam of Carbapenem-Nonsusceptible Enterobacteriaceae Isolates Collected during the INFORM Global Surveillance Study (2012 to 2014). *Antimicrob. Agents Chemother.* 2016, *60* (5), 3163-3169.
220. Bush, K.; Bradford, P. A., Epidemiology of β-Lactamase-Producing Pathogens. *Clin. Microbiol. Rev.* 2020, *33* (2), e00047-19.
221. Pitout, J. D. D.; Peirano, G.; Kock, M. M.; Strydom, K. A.; Matsumura, Y., The Global Ascendency of OXA-48-Type Carbapenemases. *Clin. Microbiol. Rev.* 2019, *33* (1), e00102-19.
222. Docquier, J. D.; Calderone, V.; De Luca, F.; Benvenuti, M.; Giuliani, F.; Bellucci, L.; Tafi, A.; Nordmann, P.; Botta, M.; Rossolini, G. M.; Mangani, S., Crystal Structure of the OXA-48 β-lactamase Reveals Mechanistic Diversity Among Class D Carbapenemases. *Chem. Biol.* 2009, *16*, 540-547.
223. Golemi, D.; Maveyraud, L.; Vakulenko, S.; Samama, J.-P.; Mobashery, S., Critical Involvement of a Carbamylated Lysine in Catalytic Function of Class D β-lactamases. *Proc. Natl. Acad. Sci. U S A* 2001, *98* (25), 14281-14285.
224. Zong, Z., Discovery of bla(OXA-199), a Chromosome-based bla(OXA-48)-like Variant, in Shewanella xiamenensis. *PLoS One* 2012, *7* (10), e48280.
225. Dabos, L.; Jousset, A. B.; Bonnin, R. A.; Fortineau, N.; Zavala, A.; Retailleau, P.; Iorga, B. I.; Naas, T., Genetic and Biochemical Characterization of OXA-535, a Distantly Related OXA-48-Like β-Lactamase. *Antimicrob. Agents Chemother.* 2018, *62* (10), e01198-18.

226. Oueslati, S.; Nordmann, P.; Poirel, L., Heterogeneous Hydrolytic Features for OXA-48-like β-lactamases. *J. Antimicrob. Chemother.* 2015, *70* (4), 1059-1063.
227. Poirel, L.; Heritier, C.; Tolun, V.; Nordmann, P., Emergence of Oxacillinase-mediated Resistance to Imipenem in Klebsiella pneumoniae. *Antimicrob. Agents Chemother.* 2004, *48* (1), 15-22.
228. Kasap, M.; Torol, S.; Kolayli, F.; Dundar, D.; Vahaboglu, H., OXA-162, a Novel Variant of OXA-48 Displays Extended Hydrolytic Activity Towards Imipenem, Meropenem and Doripenem. *J. Enzyme Inhib. Med. Chem.* 2013, *28* (5), 990-996.
229. Potron, A.; Nordmann, P.; Lafeuille, E.; Al Maskari, Z.; Al Rashdi, F.; Poirel, L., Characterization of OXA-181, a Carbapenem-hydrolyzing Class D β-lactamase from Klebsiella pneumoniae. *Antimicrob. Agents Chemother.* 2011, *55* (10), 4896-4899.
230. Poirel, L.; Castanheira, M.; Carrer, A.; Rodriguez, C. P.; Jones, R. N.; Smayevsky, J.; Nordmann, P., OXA-163, an OXA-48-related Class D β-lactamase with Extended Activity Toward Expanded-spectrum Cephalosporins. *Antimicrob. Agents Chemother.* 2011, *55* (6), 2546-2551.
231. Dortet, L.; Oueslati, S.; Jeannot, K.; Tande, D.; Naas, T.; Nordmann, P., Genetic and Biochemical Characterization of OXA-405, an OXA-48-type Extended-spectrum β-lactamase Without Significant Carbapenemase Activity. *Antimicrob. Agents. Chemother.* 2015, *59* (7), 3823-3828.
232. Hrabak, J.; Chudackova, E.; Papagiannitsis, C. C., Detection of Carbapenemases in Enterobacteriaceae: a Challenge for Diagnostic Microbiological Laboratories. *Clin. Microbiol. Infect.* 2014, *20* (9), 839-853.
233. Stojanoski, V.; Hu, L.; Sankaran, B.; Wang, F.; Tao, P.; Prasad, B. V. V.; Palzkill, T., Mechanistic Basis of OXA-48-like β-Lactamases' Hydrolysis of Carbapenems. *ACS Infect. Dis.* 2021, *7* (2), 445-460.
234. Maveyraud, L.; Golemi-Kotra, D.; Ishiwata, A.; Meroueh, O.; Mobashery, S.; Samama, J.-P., High-Resolution X-ray Structure of an Acyl-Enzyme Species for the Class D OXA-10 β-Lactamase. *J. Am. Chem. Soc.* 2002, *124* (11), 2461-2465.
235. King, D. T.; King, A. M.; Lal, S. M.; Wright, G. D.; Strynadka, N. C., Molecular Mechanism of Avibactam-Mediated β-Lactamase Inhibition. *ACS Infect. Dis.* 2015, *1* (4), 175-184.
236. van Groesen, E.; Lohans, C. T.; Brem, J.; Aertker, K. M. J.; Claridge, T. D. W.; Schofield, C. J., 19F NMR Monitoring of Reversible Protein Post-Translational Modifications: Class D β-Lactamase Carbamylation and Inhibition. *Chem. Eur. J.* 2019, *25* (51), 11837-11841.
237. Kaitany, K. C.; Klinger, N. V.; June, C. M.; Ramey, M. E.; Bonomo, R. A.; Powers, R. A.; Leonard, D. A., Structures of the Class D Carbapenemases OXA-23 and OXA-146: Mechanistic Basis of Activity Against Carbapenems, Extended-Spectrum Cephalosporins, and Aztreonam. *Antimicrob. Agents Chemother.* 2013, *57* (10), 4848-4855.

238. Santillana, E.; A., B.; Bou, G.; Romero, A., Crystal Structure of the Carbapenemase OXA-24 Reveals Insights Into the Mechanism of Carbapenem Hydrolysis. *Proc. Natl. Acad. Sci. U S A* 2007, *104* (13), 5354-5359.
239. Akhter, S.; Lund, B. A.; Ismael, A.; Langer, M.; Isaksson, J.; Christopeit, T.; Leiros, H. S.; Bayer, A., A Focused Fragment Library Targeting the Antibiotic Resistance Enzyme - Oxacillinase-48: Synthesis, Structural Evaluation and Inhibitor Design. *Eur. J. Med. Chem.* 2018, *145*, 634-648.
240. Akhtar, A.; Pemberton, O. A.; Chen, Y., Structural Basis for Substrate Specificity and Carbapenemase Activity of OXA-48 Class D β-Lactamase. *ACS Infect. Dis.* 2020, *6* (2), 261-271.
241. Papp-Wallace, K. M.; Kumar, V.; Zeiser, E. T.; Becka, S. A.; van den Akker, F., Structural Analysis of The OXA-48 Carbapenemase Bound to A "Poor" Carbapenem Substrate, Doripenem. *Antibiotics (Basel)* 2019, *8* (3), 145.
242. De Luca, F.; Benvenuti, M.; Carboni, F.; Pozzi, C.; Rossolini, G. M.; Mangani, S.; Docquier, J. D., Evolution to Carbapenem-hydrolyzing Activity in Noncarbapenemase Class D β-lactamase OXA-10 by Rational Protein Design. *Proc. Natl. Acad. Sci. U S A* 2011, *108* (45), 18424-18429.
243. Oueslati, S.; Retailleau, P.; Marchini, L.; Berthault, C.; Dortet, L.; Bonnin, R. A.; Iorga, B. I.; Naas, T., Role of the Arginine 214 in the Substrate Specificity of OXA-48. *Antimicrob. Agents Chemother.* 2020, *64* (5), e02329-19.
244. Potron, A.; Rondinaud, E.; Poirel, L.; Belmonte, O.; Boyer, S.; Camiade, S.; Nordmann, P., Genetic and Biochemical Characterisation of OXA-232, a Carbapenem-hydrolysing Class D β-lactamase from Enterobacteriaceae. *Int. J. Antimicrob. Agents* 2013, *41* (4), 325-329.
245. Dabos, L.; Zavala, A.; Bonnin, R. A.; Beckstein, O.; Retailleau, P.; Iorga, B. I.; Naas, T., Substrate Specificity of OXA-48 after β5-β6 Loop Replacement. *ACS Infect. Dis.* 2020, *6* (5), 1032–1043.
246. Taibi, P.; Mobashery, S., Mechanism of Turnover of Imipenem by the TEM β-Lactamase Revisited. *J. Am. Chem. Soc.* 1995, *117*, 7600-7605.
247. Fonseca, F.; Chudyk, E. I.; van der Kamp, M. W.; Correia, A.; Mulholland, A. J.; Spencer, J., The Basis for Carbapenem Hydrolysis by Class A β-lactamases: a Combined Investigation Using Crystallography and Simulations. *J. Am. Chem. Soc.* 2012, *134*, 18275-18285.
248. Tremblay, L. W.; Fan, F.; Blanchard, J. S., Biochemical and Structural Characterization of Mycobacterium tuberculosis β-lactamase with the Carbapenems Ertapenem and Doripenem. *Biochemistry* 2010, *49* (17), 3766-3773.
249. Kalp, M.; Carey, P. R., Carbapenems and SHV-1 β-Lactamase Form Different Acyl-Enzyme Populations in Crystals and Solution. *Biochemistry* 2008, *47*, 11830-11837.
250. Schneider, K. D.; Ortega, C. J.; Renck, N. A.; Bonomo, R. A.; Powers, R. A.; Leonard, D. A., Structures of the Class D Carbapenemase OXA-24 from

Acinetobacter baumannii in Complex with Doripenem. *J. Mol. Biol.* 2011, *406* (4), 583-594.
251. Smith, C. A.; Antunes, N. T.; Stewart, N. K.; Toth, M.; Kumarasiri, M.; Chang, M.; Mobashery, S.; Vakulenko, S. B., Structural Basis for Carbapenemase Activity of the OXA-23 β-lactamase from Acinetobacter baumannii. *Chem. Biol.* 2013, *20*, 1107-1115.
252. Lohans, C. T.; Freeman, E. I.; Groesen, E. V.; Tooke, C. L.; Hinchliffe, P.; Spencer, J.; Brem, J.; Schofield, C. J., Mechanistic Insights into β-Lactamase-Catalysed Carbapenem Degradation Through Product Characterisation. *Sci. Rep.* 2019, *9* (1), 13608.
253. Lohans, C. T.; van Groesen, E.; Kumar, K.; Tooke, C. L.; Spencer, J.; Paton, R. S.; Brem, J.; Schofield, C. J., A New Mechanism for β-Lactamases: Class D Enzymes Degrade 1β-Methyl Carbapenems through Lactone Formation. *Angew. Chem. Int. Ed.* 2018, *57* (5), 1282-1285.
254. Aertker, K. M. J.; Chan, H. T. H.; Lohans, C. T.; Schofield, C. J., Analysis of β-lactone Formation by Clinically Observed Carbapenemases Informs on a Novel Antibiotic Resistance Mechanism. *J. Biol. Chem.* 2020, *295* (49), 16604-16613.
255. Fröhlich, C.; Sorum, V.; Thomassen, A. M.; Johnsen, P. J.; Leiros, H. S.; Samuelsen, O., OXA-48-Mediated Ceftazidime-Avibactam Resistance Is Associated with Evolutionary Trade-Offs. *mSphere* 2019, *4* (2), e00024-19.
256. Mitchell, J. M.; Clasman, J. R.; June, C. M.; Kaitany, K. C.; LaFleur, J. R.; Taracila, M. A.; Klinger, N. V.; Bonomo, R. A.; Wymore, T.; Szarecka, A.; Powers, R. A.; Leonard, D. A., Structural Basis of Activity Against Aztreonam and Extended Spectrum Cephalosporins for Two Carbapenem-Hydrolyzing Class D β-lactamases from Acinetobacter baumannii. *Biochemistry* 2015, *54* (10), 1976-1987.
257. Hirvonen, V. H. A.; Mulholland, A. J.; Spencer, J.; van der Kamp, M. W., Small Changes in Hydration Determine Cephalosporinase Activity of OXA-48 β-Lactamases. *ACS Catal.* 2020, *10* (11), 6188-6196.
258. Toussaint, K. A.; Gallagher, J. C., β-lactam/β-lactamase Inhibitor Combinations: From Then to Now. *Ann. Pharmacother.* 2015, *49* (1), 86-98.
259. Stewart, A.; Harris, P.; Henderson, A.; Paterson, D., Treatment of Infections by OXA-48-Producing Enterobacteriaceae. *Antimicrob Agents Chemother* 2018, *62* (11), e01195-18.
260. Aktas, Z.; Kayacan, C.; Oncul, O., In vitro Activity of Avibactam (NXL104) in Combination with β-lactams Against Gram-negative Bacteria, Including OXA-48 β-lactamase-producing Klebsiella pneumoniae. *Int. J. Antimicrob. Agents* 2012, *39* (1), 86-89.
261. Sousa, A.; Perez-Rodriguez, M. T.; Soto, A.; Rodriguez, L.; Perez-Landeiro, A.; Martinez-Lamas, L.; Nodar, A.; Crespo, M., Effectiveness of ceftazidime/avibactam as salvage therapy for treatment of infections due to OXA-48 carbapenemase-producing Enterobacteriaceae. *J. Antimicrob. Chemother.* 2018, *73* (11), 3170-3175.

262. Kazmierczak, K. M.; Bradford, P. A.; Stone, G. G.; de Jonge, B. L. M.; Sahm, D. F., In Vitro Activity of Ceftazidime-Avibactam and Aztreonam-Avibactam against OXA-48-Carrying Enterobacteriaceae Isolated as Part of the International Network for Optimal Resistance Monitoring (INFORM) Global Surveillance Program from 2012 to 2015. *Antimicrob. Agents Chemother.* 2018, *62* (12), e00592-18.
263. Vasoo, S.; Cunningham, S. A.; Cole, N. C.; Kohner, P. C.; Menon, S. R.; Krause, K. M.; Harris, K. A.; De, P. P.; Koh, T. H.; Patel, R., In Vitro Activities of Ceftazidime-Avibactam, Aztreonam-Avibactam, and a Panel of Older and Contemporary Antimicrobial Agents against Carbapenemase-Producing Gram-Negative Bacilli. *Antimicrob. Agents Chemother.* 2015, *59* (12), 7842-7846.
264. Lahiri, S. D.; Mangani, S.; Jahic, H.; Benvenuti, M.; Durand-Reville, T. F.; De Luca, F.; Ehmann, D. E.; Rossolini, G. M.; Alm, R. A.; Docquier, J. D., Molecular Basis of Selective Inhibition and Slow Reversibility of Avibactam Against Class D Carbapenemases: a Structure-Guided Study of OXA-24 and OXA-48. *ACS Chem. Biol.* 2015, *10* (2), 591-600.
265. Lomovskaya, O.; Sun, D.; Rubio-Aparicio, D.; Nelson, K.; Tsivkovski, R.; Griffith, D. C.; Dudley, M. N., Vaborbactam: Spectrum of β-Lactamase Inhibition and Impact of Resistance Mechanisms on Activity in Enterobacteriaceae. *Antimicrob. Agents. Chemother.* 2017, *61* (11), e01443-17.
266. Schmidt-Malan, S. M. S.; Mishra, A. J.; Mushtaq, A.; Brinkman, C. L.; Patel, R., In Vitro Activity of Imipenem-Relebactam and Ceftolozane-Tazobactam against Resistant Gram-Negative Bacilli. *Antimicrob. Agents Chemother.* 2018, *62* (8), e00533-18.
267. Tselepis, L.; Langley, G. W.; Aboklaish, A. F.; Widlake, E.; Jackson, D. E.; Walsh, T. R.; Schofield, C. J.; Brem, J.; Tyrrell, J. M., In Vitro Efficacy of Imipenem-Relebactam and Cefepime-AAI101 Against a Global Collection of ESBL-positive and Carbapenemase-Producing Enterobacteriaceae. *Int. J. Antimicrob. Agents* 2020, *56* (1), 105925.
268. Livermore, D. M.; Mushtaq, S.; Warner, M.; Vickers, A.; Woodford, N., In Vitro Activity of Cefepime/Zidebactam (WCK 5222) Against Gram-Negative Bacteria. *J. Antimicrob. Chemother.* 2017, *72* (5), 1373-1385.
269. Livermore, D. M.; Mushtaq, S.; Warner, M.; Woodford, N., Activity of OP0595/β-Lactam Combinations Against Gram-negative Bacteria with Extended-Spectrum, AmpC and Carbapenem-Hydrolysing β-Lactamases. *J. Antimicrob. Chemother.* 2015, *70* (11), 3032-3041.
270. King, A. M.; King, D. T.; French, S.; Brouillette, E.; Asli, A.; Alexander, J. A.; Vuckovic, M.; Maiti, S. N.; Parr, T. R., Jr.; Brown, E. D.; Malouin, F.; Strynadka, N. C.; Wright, G. D., Structural and Kinetic Characterization of Diazabicyclooctanes as Dual Inhibitors of Both Serine-β-Lactamases and Penicillin-Binding Proteins. *ACS Chem. Biol.* 2016, *11* (4), 864-868.

271. Gordon, E. M.; Duncton, M. A. J.; Gallop, M. A., Orally Absorbed Derivatives of the β-Lactamase Inhibitor Avibactam. Design of Novel Prodrugs of Sulfate Containing Drugs. *J. Med. Chem.* 2018, *61* (22), 10340-10344.
272. Papp-Wallace, K. M.; Bajaksouzian, S.; Bonomo, R. A.; R. Bethel, C.; Caillon, J.; Rutter, J. D.; Reghal, A.; Jacqueline, C., Beyond Piperacillin-Tazobactam: Cefepime and AAI101 as a Potent β-Lactam-β-Lactamase Inhibitor Combination. *Antimicrob. Agents Chemother.* 2019, *63* (5), e00105-19.
273. Bernhard, F.; Odedra, R.; Sordello, S.; Cardin, R.; Franzoni, S.; Charrier, C.; Belley, A.; Warn, P.; Machacek, M.; Knechtle, P., Pharmacokinetics-Pharmacodynamics of Enmetazobactam Combined with Cefepime in a Neutropenic Murine Thigh Infection Model. *Antimicrob. Agents Chemother.* 2020, *64* (6), e00078-20.
274. Bush, K.; Bradford, P. A., Interplay Between β-Lactamases and New β-Lactamase Inhibitors. *Nat. Rev. Microbiol.* 2019, *17* (5), 295-306.
275. Langley, G. W.; Cain, R.; Tyrrell, J. M.; Hinchliffe, P.; Calvopina, K.; Tooke, C. L.; Widlake, E.; Dowson, C. G.; Spencer, J.; Walsh, T. R.; Schofield, C. J.; Brem, J., Profiling Interactions of Vaborbactam with Metallo-β-Lactamases. *Bioorg. Med. Chem. Lett.* 2019, *29* (15), 1981-1984.
276. Lee, Y.; Kim, J.; Trinh, S., Meropenem–Vaborbactam (Vabomere): Another Option for Carbapenem-Resistant Enterobacteriaceae. *Pharm. Ther.* 2019, *44* (3), 110-113.
277. Tsivkovski, R.; Lomovskaya, O., Biochemical Activity of Vaborbactam. *Antimicrob. Agents Chemother.* 2020, *64* (2), e01935-19.
278. Liu, B.; Trout, R. E. L.; Chu, G. H.; McGarry, D.; Jackson, R. W.; Hamrick, J. C.; Daigle, D. M.; Cusick, S. M.; Pozzi, C.; De Luca, F.; Benvenuti, M.; Mangani, S.; Docquier, J. D.; Weiss, W. J.; Pevear, D. C.; Xerri, L.; Burns, C. J., Discovery of Taniborbactam (VNRX-5133): A Broad-Spectrum Serine- and Metallo-β-lactamase Inhibitor for Carbapenem-Resistant Bacterial Infections. *J. Med. Chem.* 2020, *63* (6), 2789-2801.
279. Safety and Efficacy Study of Cefepime/VNRX-5133 in Patients With Complicated Urinary Tract Infections. https://clinicaltrials.gov/ct2/show/NCT03840148 (accessed 07/07/2020).
280. Nelson, K.; Rubio-Aparicio, D.; Sun, D.; Dudley, M.; Lomovskaya, O., In Vitro Activity of the Ultra-Broad-Spectrum β-Lactamase Inhibitor QPX7728 against Carbapenem-Resistant Enterobacterales (CRE) With Varying Intrinsic and Acquired Resistance Mechanisms. *Antimicrob. Agents Chemother.* 2020, *64* (8), e00757-20.
281. P1 Single and Multiple Ascending Dose (SAD/MAD) Study of IV QPX7728 Alone and Combined With QPX2014 in NHV. https://clinicaltrials.gov/ct2/show/NCT04380207 (accessed 07/07/2020).
282. Qpex Biopharma Initiates Phase 1 Clinical Trial of QPX7728 for Drug-Resistant Bacterial Infections. https://www.businesswire.com/news/home/20201203005300/en/Qpex-

Biopharma-Initiates-Phase-1-Clinical-Trial-of-QPX7728-for-Drug-Resistant-Bacterial-Infections (accessed 02/02/2021).
283. Papp-Wallace, K. M., The Latest Advances in β-Lactam/β-Lactamase Inhibitor Combinations for the Treatment of Gram-negative Bacterial Infections. *Expert Opin. Pharmacother.* 2019, *20* (17), 2169-2184.
284. VNRX-7145 SAD/MAD Safety and PK in Healthy Adult Volunteers. https://clinicaltrials.gov/ct2/show/NCT04243863 (accessed 02/25/2021).
285. Taylor, D. M.; Anglin, J.; Park, S.; Ucisik, M. N.; Faver, J. C.; Simmons, N.; Jin, Z.; Palaniappan, M.; Nyshadham, P.; Li, F.; Campbell, J.; Hu, L.; Sankaran, B.; Prasad, B. V. V.; Huang, H.; Matzuk, M. M.; Palzkill, T., Identifying Oxacillinase-48 Carbapenemase Inhibitors Using DNA-Encoded Chemical Libraries. *ACS Infect. Dis.* 2020, *6* (5), 1214-1227.
286. Levy, S. B.; Marshall, B., Antibacterial Resistance Worldwide: Causes, Challenges and Responses. *Nat. Med.* 2004, *10*, S122-129.
287. Laxminarayan, R.; Duse, A.; Wattal, C.; Zaidi, A. K. M.; Wertheim, H. F. L.; Sumpradit, N.; Vlieghe, E.; Hara, G. L.; Gould, I. M.; Goossens, H.; Greko, C.; So, A. D.; Bigdeli, M.; Tomson, G.; Woodhouse, W.; Ombaka, E.; Peralta, A. Q.; Qamar, F. N.; Mir, F.; Kariuki, S.; Bhutta, Z. A.; Coates, A.; Bergstrom, R.; Wright, G. D.; Brown, E. D.; Cars, O., Antibiotic Resistance—the Need for Global Solutions. *The Lancet Infectious Diseases* 2013, *13* (12), 1057-1098.
288. Evans, B. A.; Amyes, S. G., OXA β-lactamases. *Clin. Microbiol. Rev.* 2014, *27*, 241-63.
289. Logan, L. K.; Weinstein, R. A., The Epidemiology of Carbapenem-Resistant Enterobacteriaceae: The Impact and Evolution of a Global Menace. *J. Infect. Dis.* 2017, *215*, S28-S36.
290. Centers for Disease Control and Prevention Biggest Threats and Data. https://www.cdc.gov/drugresistance/biggest-threats.html#carp (accessed 23/12/2019).
291. Walsh, T. R., Emerging Carbapenemases: a Global Perspective. *Int. J. Antimicrob. Agents* 2010, *36(Suppl. 3)*, S8-S14.
292. Poirel, L.; Heritier, C.; Tolun, V.; Nordmann, P., Emergence of Oxacillinase-Mediated Resistance to Imipenem in Klebsiella pneumoniae. *Antimicrob. Agents Chemother.* 2004, *48*, 15-22.
293. Lund, B. A.; Thomassen, A. M.; Carlsen, T. J. O.; Leiros, H. K. S., Structure, Activity and Thermostability Investigations of OXA-163, OXA-181 and OXA-245 Using Biochemical Analysis, Crystal Structures and Differential Scanning Calorimetry Analysis. *Acta Crystallogr. F Struct. Biol. Commun.* 2017, *73*, 579-587.
294. Hermann, J. C.; Hensen, C.; Ridder, L.; Mulholland, A. J.; Höltje, H.-D., Mechanisms of Antibiotic Resistance: QM/MM Modeling of the Acylation Reaction of a Class A β-Lactamase with Benzylpenicillin. *J. Am. Chem. Soc.* 2005, *127*, 4454-4465.
295. Stojanoski, V.; Chow, D. C.; Fryszczyn, B.; Hu, L.; Nordmann, P.; Poirel, L.; Sankaran, B.; Prasad, B. V.; Palzkill, T., Structural Basis for Different Substrate

Profiles of Two Closely Related Class D β-Lactamases and Their Inhibition by Halogens. *Biochemistry* 2015, *54*, 3370-80.
296. Webb, B.; Sali, A., Comparative Protein Structure Modeling Using MODELLER. *Curr. Protoc. Bioinformatics* 2016, *54*, 5.6.1-5.6.37.
297. Walker, R. C.; Crowley, M. F.; Case, D. A., The Implementation of a Fast and Accurate QM/MM Potential Method in Amber. *J. Comput. Chem.* 2008, *29*, 1019-1031.
298. Marcos-Alcalde, I.; Setoain, J.; Mendieta-Moreno, J. I.; Mendieta, J.; Gomez-Puertas, P., MEPSA: Minimum Energy Pathway Analysis for Energy Landscapes. *Bioinformatics* 2015, *31*, 3853-3855.
299. Le Grand, S.; Götz, A. W.; Walker, R. C., SPFP: Speed Without Compromise—A Mixed Precision Model for GPU Accelerated Molecular Dynamics Simulations. *Comput. Phys. Commun.* 2013, *184*, 374-380.
300. Gotz, A. W.; Williamson, M. J.; Xu, D.; Poole, D.; Le Grand, S.; Walker, R. C., Routine Microsecond Molecular Dynamics Simulations with AMBER on GPUs. 1. Generalized Born. *J. Chem. Theory Comput.* 2012, *8*, 1542-1555.
301. Salomon-Ferrer, R.; Gotz, A. W.; Poole, D.; Le Grand, S.; Walker, R. C., Routine Microsecond Molecular Dynamics Simulations with AMBER on GPUs. 2. Explicit Solvent Particle Mesh Ewald. *J. Chem. Theory Comput.* 2013, *9*, 3878-3888.
302. Hedges, L.; Mey, A.; Laughton, C.; Gervasio, F.; Mulholland, A.; Woods, C.; Michel, J., BioSimSpace: An Interoperable Python Framework for Biomolecular Simulation. *Journal of Open Source Software* 2019, *4*.
303. Woods, C. Sire: An advanced, multiscale, molecular simulation framework. https://siremol.org/ (accessed 11/01/2019).
304. Srivastava, A.; Nagai, T.; Srivastava, A.; Miyashita, O.; Tama, F., Role of Computational Methods in Going beyond X-ray Crystallography to Explore Protein Structure and Dynamics. *Int. J. Mol. Sci.* 2018, *19*, 3401.
305. Chruszcz, M.; Wlodawer, A.; Minor, W., Determination of Protein Structures--a Series of Fortunate Events. *Biophys. J.* 2008, *95*, 1-9.
306. Richard, J. P.; Amyes, T. L.; Goryanova, B.; Zhai, X., Enzyme Architecture: on the Importance of Being in a Protein Cage. *Curr. Opin. Chem. Biol.* 2014, *21*, 1-10.
307. Malabanan, M. M.; Amyes, T. L.; Richard, J. P., A Role for Flexible Loops in Enzyme Catalysis. *Curr. Opin. Struct. Biol.* 2010, *20*, 702-710.
308. Liao, Q.; Kulkarni, Y.; Sengupta, U.; Petrovic, D.; Mulholland, A. J.; van der Kamp, M. W.; Strodel, B.; Kamerlin, S. C. L., Loop Motion in Triosephosphate Isomerase Is Not a Simple Open and Shut Case. *J. Am. Chem. Soc.* 2018, *140*, 15889-15903.
309. van der Kamp, M. W.; Chaudret, R.; Mulholland, A. J., QM/MM Modelling of Ketosteroid Isomerase Reactivity Indicates that Active Site Closure is Integral to Catalysis. *FEBS J.* 2013, *280*, 3120-3131.
310. Mhashal, A. R.; Pshetitsky, Y.; Cheatum, C. M.; Kohen, A.; Major, D. T., Evolutionary Effects on Bound Substrate pKa in Dihydrofolate Reductase. *J. Am. Chem. Soc.* 2018, *140*, 16650-16660.

311. Vakulenko, S. B.; Taibi-Tronche, P.; Toth, M.; Massova, I.; Lerner, S. A.; Mobashery, S., Effects on Substrate Profile by Mutational Substitutions at Positions 164 and 179 of the Class A TEMpUC19 β-Lactamase from Escherichia coli. *J. Biol. Chem.* 1999, *274*, 23052–23060.
312. Olsson, M. H. M.; Søndergaard, C. R.; Rostkowski, M.; Jensen, J. H., PROPKA3: Consistent Treatment of Internal and Surface Residues in Empirical pKa Predictions. *J. Chem. Theory Comput.* 2011, *7*, 525-537.
313. Frisch, M. J.; Trucks, G. W.; Schlegel, H. B.; Scuseria, G. E.; Robb, M. A.; Cheeseman, J. R.; Scalmani, G.; Barone, V.; Petersson, G. A.; Nakatsuji, H.; Li, X.; Caricato, M.; Marenich, A.; Bloino, J.; Janesko, B. G.; Gomperts, R.; Mennucci, B.; Hratchian, H. P.; Ortiz, J. V.; Izmaylov, A. F.; Sonnenberg, J. L.; Williams-Young, D.; Ding, F.; Lipparini, F.; Egidi, F.; Goings, J.; Peng, B.; Petrone, A.; Henderson, T.; Ranasinghe, D.; Zakrzewski, V. G.; Gao, J.; Rega, N.; Zheng, G.; Liang, W.; Hada, M.; Ehara, M.; Toyota, K.; Fukuda, R.; Hasegawa, J.; Ishida, M.; Nakajima, T.; Honda, Y.; Kitao, O.; Nakai, H.; Vreven, T.; Throssell, K.; Montgomery, J., J. A. ; Peralta, J. E.; Ogliaro, F.; Bearpark, M.; Heyd, J. J.; Brothers, E.; Kudin, K. N.; Staroverov, V. N.; Keith, T.; Kobayashi, R.; Normand, J.; Raghavachari, K.; Rendell, A.; Burant, J. C.; Iyengar, S. S.; Tomasi, J.; Cossi, M.; Millam, J. M.; Klene, M.; Adamo, C.; Cammi, R.; Ochterski, J. W.; Martin, R. L.; Morokuma, K.; Farkas, O.; Foresman, J. B.; Fox, D. J. *Gaussian 09, Revision D.01*, Gaussian, Inc.: Wallingford CT, 2016.
314. Kendall, R. A.; Dunning, T. H.; Harrison, R. J., Electron Affinities of the First-row Atoms Revisited. Systematic Basis Sets and Wave Functions. *J. Chem. Phys.* 1992, *96*, 6796-6806.
315. Woon, D. E.; Dunning, T. H. J., Gaussian Basis Sets for Use in Correlated Molecular Calculations. III. The Atoms Aluminum Through Argon. *J. Chem. Phys.* 1993, *98*, 1358-1371.
316. Gerenkamp, M.; Grimme, S., Spin-component Scaled Second-Order Møller–Plesset Perturbation Theory for the Calculation of Molecular Geometries and Harmonic Vibrational Frequencies. *Chem. Phys. Lett.* 2004, *392*, 229-235.
317. Neese, F., The ORCA program system. *Wiley Interdiscip. Rev. Comput. Mol. Sci.* 2012, *2* (1), 73-78.
318. Neese, F., Software update: the ORCA program system, version 4.0. *Wiley Interdiscip. Rev. Comput. Mol. Sci.* 2017, *8* (1), e1327.
319. Weigend, F.; Köhn, A.; Hättig, C., Efficient Use of the Correlation Consistent Basis Sets in Resolution of the Identity MP2 Calculations. *J. Chem. Phys.* 2002, *116*, 3175-3183.
320. WHO Antibiotic Resistance. https://www.who.int/news-room/fact-sheets/detail/antibiotic-resistance (accessed 01/19/2021).
321. D'Costa, V. M.; King, C. E.; Kalan, L.; Morar, M.; Sung, W. W. L.; Schwarz, C.; Froese, D.; Zazula, G.; Calmels, F.; Debruyne, R.; Golding, G. B.; Poinar, H. N.; Wright, G. D., Antibiotic Resistance is Ancient. *Nature* 2011, *477* (7365), 457-461.

322. Wang, J.; Wang, P.; Wang, X.; Zheng, Y.; Xiao, Y., Use and Prescription of Antibiotics in Primary Health Care Settings in China. *JAMA Intern. Med.* 2014, *174* (12).
323. Lammie, S. L.; Hughes, J. M., Antimicrobial Resistance, Food Safety, and One Health: The Need for Convergence. *Annu. Rev. Food Sci. Technol.* 2016, *7*, 287-312.
324. Ahmed, S. A.; Barış, E.; Go, D. S.; Lofgren, H.; Osorio-Rodarte, I.; Thierfelder, K., Assessing the Global Poverty Effects of Antimicrobial Resistance. *World Dev.* 2018, *111*, 148-160.
325. Harbarth, S.; Theuretzbacher, U.; Hackett, J., Antibiotic Research and Development: Business as Usual? *J. Antimicrob. Chemother.* 2015, *70* (6), 1604-1607.
326. Tipper, D. J.; Strominger, J. L., Mechanism of Action of Penicillins: a Proposal Based on Their Structural Similarity to AcyL-D-Alanyl-D-Alanine. *Proc. Natl. Acad. Sci. U S A* 1965, *54*, 1133-1141.
327. Seabra, G. d. M.; Walker, R. C.; Elstner, M.; Case, D. A.; Roitberg, A. E., Implementation of the SCC-DFTB Method for Hybrid QM/MM Simulations within the Amber Molecular Dynamics Package. *J. Phys. Chem. A* 2007, *111* (26), 5655-5664.
328. Niehaus, T. A.; Elstner, M.; Frauenheim, T. H.; Suhai, S., Application of an Approximate Density-Functional Method to Sulfur Containing Compounds. *J. Mol. Struct. THEOCHEM* 2001, *541*, 185-194.
329. Grossfield, A. *WHAM: an Implementation of the Weighted Histogram Analysis Method*, version 2.0.9; http://membrane.urmc.rochester.edu/content/wham/.
330. Toth, M.; Smith, C. A.; Antunes, N. T.; Stewart, N. K.; Maltz, L.; Vakulenko, S. B., The Role of Conserved Surface Hydrophobic Residues in the Carbapenemase Activity of the Class D β-lactamases. *Acta Crystallogr. C73* (8), 692-701.
331. Dabos, L.; Bogaerts, P.; Bonnin, R. A.; Zavala, A.; Sacre, P.; Iorga, B. I.; Huang, D. T.; Glupczynski, Y.; Naas, T., Genetic and Biochemical Characterization of OXA-519, a Novel OXA-48-Like β-Lactamase. *Antimicrob. Agents Chemother.* 2018, *62* (8), e00469-18.
332. Berg, J. M.; Tymoczko, J. L.; Stryer, L., *Biochemistry. 5th edition.* W. H. Freeman: New York, 2002.
333. Roe, D. R.; Cheatham, T. E., PTRAJ and CPPTRAJ: Software for Processing and Analysis of Molecular Dynamics Trajectory Data. *J. Chem. Theory Comput.* 2013, *9* (7), 3084-3095.
334. Frisch, M. J.; Trucks, G. W.; Schlegel, H. B.; Scuseria, G. E.; Robb, M. A.; Cheeseman, J. R.; Scalmani, G.; Barone, V.; Petersson, G. A.; Nakatsuji, H.; Li, X.; Caricato, M.; Marenich, A. V.; Bloino, J.; Janesko, B. G.; Gomperts, R.; Mennucci, B.; Hratchian, H. P.; Ortiz, J. V.; Izmaylov, A. F.; Sonnenberg, J. L.; Williams-Young, D.; Ding, F.; Lipparini, F.; Egidi, F.; Goings, J.; Peng, B.; Petrone, A.; Henderson, T.; Ranasinghe, D.; Zakrzewski, V. G.; Gao, J.; Rega, N.; Zheng, G.; Liang, W.; Hada, M.; Ehara, M.; Toyota, K.; Fukuda, R.;

Hasegawa, J.; Ishida, M.; Nakajima, T.; Honda, Y.; Kitao, O.; Nakai, H.; Vreven, T.; Throssell, K.; Montgomery, J. A. J.; Peralta, J. E.; Ogliaro, F.; Bearpark, M. J.; Heyd, J. J.; Brothers, E. N.; Kudin, K. N.; Staroverov, V. N.; Keith, T. A.; Kobayashi, R.; Normand, J.; Raghavachari, K.; Rendell, A. P.; Burant, J. C.; Iyengar, S. S.; Tomasi, J.; Cossi, M.; Millam, J. M.; Klene, M.; Adamo, C.; Cammi, R.; Ochterski, J. W.; Martin, R. L.; Morokuma, K.; Farkas, O.; Foresman, J. B.; Fox, D. J. *Gaussian 16, Revision A.03*, Gaussian Inc.: Wallingford CT, 2016.

335. Weigend, F.; Furche, F.; Ahlrichs, R., Gaussian Basis Sets of Quadruple Zeta Valence Quality for Atoms H–Kr. *J. Chem. Phys.* 2003, *119*, 12753-12762.
336. Vena, A.; Giacobbe, D. R.; Castaldo, N.; Cattelan, A.; Mussini, C.; Luzzati, R.; Rosa, F. G.; Del Puente, F.; Mastroianni, C. M.; Cascio, A.; Carbonara, S.; Capone, A.; Boni, S.; Sepulcri, C.; Meschiari, M.; Raumer, F.; Oliva, A.; Corcione, S.; Bassetti, M., Clinical Experience with Ceftazidime-Avibactam for the Treatment of Infections due to Multidrug-Resistant Gram-Negative Bacteria Other than Carbapenem-Resistant Enterobacterales. *Antibiotics (Basel)* 2020, *9* (2), 71.
337. Wunderink, R. G.; Giamarellos-Bourboulis, E. J.; Rahav, G.; Mathers, A. J.; Bassetti, M.; Vazquez, J.; Cornely, O. A.; Solomkin, J.; Bhowmick, T.; Bishara, J.; Daikos, G. L.; Felton, T.; Furst, M. J. L.; Kwak, E. J.; Menichetti, F.; Oren, I.; Alexander, E. L.; Griffith, D.; Lomovskaya, O.; Loutit, J.; Zhang, S.; Dudley, M. N.; Kaye, K. S., Effect and Safety of Meropenem-Vaborbactam versus Best-Available Therapy in Patients with Carbapenem-Resistant Enterobacteriaceae Infections: The TANGO II Randomized Clinical Trial. *Infect. Dis. Ther.* 2018, *7* (4), 439-455.
338. Wilson, G. M.; Fitzpatrick, M.; Walding, K.; Gonzalez, B.; Schweizer, M. L.; Suda, K. J.; Evans, C. T., Meta-analysis of Clinical Outcomes Using Ceftazidime/Avibactam, Ceftolozane/Tazobactam, and Meropenem/Vaborbactam for the Treatment of Multidrug-Resistant Gram-Negative Infections. *Open Forum Infect. Dis.* 2021, *8* (2), 1-9.
339. Mosley, J. F. I.; Smith, L. L.; Parke, C. K.; Brown, J. A.; Wilson, A. L.; Gibbs, L. V., Ceftazidime-Avibactam (Avycaz) - For the Treatment of Complicated Intra-Abdominal and Urinary Tract Infections. *Drug Forecast* 2016, *41* (8), 479-483.
340. Lohans, C. T.; Brem, J.; Schofield, C. J., New Delhi Metallo-β-Lactamase 1 Catalyzes Avibactam and Aztreonam Hydrolysis. *Antimicrob. Agents Chemother.* 2017, *61* (12), e01224-17.
341. Jonsson, H.; Mills, G.; Jacobsen, K. W., Nudged elastic band method for finding minimum energy paths of transitions. In *Classical and Quantum Dynamics in Condensed Phase Simulations*, World Scientific: 1998; pp 385-404.
342. Bannwarth, C.; Ehlert, S.; Grimme, S., GFN2-xTB-An Accurate and Broadly Parametrized Self-Consistent Tight-Binding Quantum Chemical Method with Multipole Electrostatics and Density-Dependent Dispersion Contributions. *J. Chem. Theory Comput.* 2019, *15* (3), 1652-1671.

343. Neese, F.; Wennmohs, F.; Hansen, A.; Becker, U., Efficient, approximate and parallel Hartree–Fock and hybrid DFT calculations. A 'chain-of-spheres' algorithm for the Hartree–Fock exchange. *Chem. Phys.* 2009, *356* (1-3), 98-109.
344. Weigend, F., Accurate Coulomb-fitting basis sets for H to Rn. *Phys. Chem. Chem. Phys.* 2006, *8* (9), 1057–1065.
345. Zinovjev, K.; Tuñón, I., Adaptive Finite Temperature String Method in Collective Variables. *J. Chem. Phys. A* 2017, *121* (51), 9764-9772.
346. Frohlich, C.; Gama, J. A.; Harms, K.; Hirvonen, V. H. A.; Lund, B. A.; van der Kamp, M. W.; Johnsen, P. J.; Samuelsen, O.; Leiros, H. S., Cryptic β-Lactamase Evolution Is Driven by Low β-Lactam Concentrations. *mSphere* 2021, *6* (2), e00108-21.